



REFERENCE ONLY

UNIVERSITY OF LONDON THESIS

Degree PhD

Year 2005

Name of Author Gau AT

**COPYRIGHT**

This is a thesis accepted for a Higher Degree of the University of London. It is an unpublished typescript and the copyright is held by the author. All persons consulting the thesis must read and abide by the Copyright Declaration below.

**COPYRIGHT DECLARATION**

I recognise that the copyright of the above-described thesis rests with the author and that no quotation from it or information derived from it may be published without the prior written consent of the author.

**LOANS**

Theses may not be lent to individuals, but the Senate House Library may lend a copy to approved libraries within the United Kingdom, for consultation solely on the premises of those libraries. Application should be made to: Inter-Library Loans, Senate House Library, Senate House, Malet Street, London WC1E 7HU.

**REPRODUCTION**

University of London theses may not be reproduced without explicit written permission from the Senate House Library. Enquiries should be addressed to the Theses Section of the Library. Regulations concerning reproduction vary according to the date of acceptance of the thesis and are listed below as guidelines.

- A. Before 1962. Permission granted only upon the prior written consent of the author. (The Senate House Library will provide addresses where possible).
- B. 1962 - 1974. In many cases the author has agreed to permit copying upon completion of a Copyright Declaration.
- C. 1975 - 1988. Most theses may be copied upon completion of a Copyright Declaration.
- D. 1989 onwards. Most theses may be copied.

*This thesis comes within category D.*

☒

This copy has been deposited in the Library of UCL

☐

This copy has been deposited in the Senate House Library, Senate House, Malet Street, London WC1E 7HU.



**Mechanisms of contrast formation in  
Non-Contact Atomic Force Microscopy (NC-AFM)  
on insulating surfaces**

**The PhD thesis of Andrei Yu. Gal**

**Supervisor: Professor Alexander L. Shluger**

**Condensed Matter and Materials Physics Group  
University College London**

UMI Number: U591997

All rights reserved

INFORMATION TO ALL USERS

The quality of this reproduction is dependent upon the quality of the copy submitted.

In the unlikely event that the author did not send a complete manuscript and there are missing pages, these will be noted. Also, if material had to be removed, a note will indicate the deletion.



UMI U591997

Published by ProQuest LLC 2013. Copyright in the Dissertation held by the Author.  
Microform Edition © ProQuest LLC.

All rights reserved. This work is protected against  
unauthorized copying under Title 17, United States Code.



ProQuest LLC  
789 East Eisenhower Parkway  
P.O. Box 1346  
Ann Arbor, MI 48106-1346



# Mechanisms of contrast formation in Non-Contact Atomic Force Microscopy (NC-AFM) on insulating surfaces

## Abstract

This work considers the problem of the prediction and interpretation of atomic resolution in NC-AFM images of ionic surfaces and adsorbed molecules, and the relation between atomic resolution and electronic properties of the system. Several tip models were studied over the MgO(001) surface, where models giving the strongest contrast were selected. The oxide tip model and the model of a Si tip with a dangling bond were used in further investigation of clean surfaces, single adsorbed molecules, and molecular monolayers.

*Ab initio* calculations based on density functional theory were used extensively for static structural optimisation and electronic structure analysis. Atomistic simulations with pair potentials were performed where possible. Interatomic potentials between organic molecules and oxide had to be fitted from the *ab initio* results.

This study predicts that atomic and chemical resolution can be achieved on a clean surface of aluminium oxide for both tip models. It is demonstrated that using the Si tip with an apex dangling bond enables one to provide straightforward chemical interpretation of images on ionic insulating surfaces. The resolution, mechanisms of tip-surface interaction and contrast formation are explained by the study of HCOOH monolayers on a TiO<sub>2</sub>(110) surface imaged using the Si tip model. An interpretation of previous experimental data on this system is suggested based on the result of this study. The resolution within charged formate ions on MgO(001) and the effect of the adsorbate on the substrate resolution is studied using the oxide tip model. Fundamental questions regarding limits of resolution in surface-adsorbate systems are addressed. Finally, the applicability of NC-AFM techniques for the detection of ionic filling inside single-wall nanotubes, and the interplay between electronic structures of the two systems are investigated.

## Contents

Abstract .....	2
Contents .....	3
List of Figures .....	6
List of Tables.....	14
List of Acronyms .....	15
Acknowledgements.....	17
List of publications.....	18
Introduction.....	19
1 Theoretical framework of modelling NC-AFM.....	32
1.1 Experimental NC-AFM setup and its model.....	33
1.1.1 The principle of operation.....	33
1.1.2 The electronics .....	34
1.1.3 The model of the FM-AFM operation .....	35
1.1.4 An illustration .....	38
1.2 Modelling of the tip-surface interaction.....	40
1.3 Theoretical methods of total energy/force calculation.....	44
1.3.1 DFT (SIESTA).....	44
1.3.2 Embedded Cluster Method (GUESS) .....	48
1.3.3 Molecular Mechanics (GULP, MARVIN, SCIFI).....	52
1.4 Electronic Structure of Substrates.....	55
1.4.1 Aluminium oxide $\text{Al}_2\text{O}_3$ .....	55
1.4.2 Magnesium oxide $\text{MgO}(001)$ .....	57
1.4.3 Titanium dioxide $\text{TiO}_2(110)$ .....	58
1.5 Structure of the tip apex .....	65
1.5.1 Model of oxidized Si tip.....	67
1.5.2 Pure Si tip model.....	68
1.6 Summary .....	72
2 Contrast formation on clean surfaces of ionic insulating crystals.....	73
2.1 Atomic resolution on $\alpha\text{-Al}_2\text{O}_3(0001)$ surface with an oxide tip.....	74
2.1.1 Tip related surface properties from <i>ab initio</i> calculations .....	74
2.1.2 Imaging clean $\alpha\text{-Al}_2\text{O}_3(0001)$ with an oxidized tip .....	77
2.2 Probing clean oxide surfaces with a “dangling bond” tip.....	84

2.3	Effect of Si tip contamination on the tip-surface interaction.....	88
2.4	Summary .....	90
3	Contrast formation in imaging of HCOO <sup>-</sup> anion on MgO(001) .....	92
3.1	Ab initio calculations of the formate anion on MgO(001).....	94
3.1.1	Adsorption of the formate anion on MgO(001) .....	95
3.1.2	Fitting interatomic potentials .....	102
3.2	Imaging a single HCOO <sup>-</sup> anion using the rigid oxide model.....	104
3.2.1	Construction of the tip-surface forcefield .....	104
3.2.2	Interpretation of the NC-AFM image .....	106
3.2.3	Contrast dependence on the tip-surface separation.....	109
3.3	Limits on surface resolution in the presence of adsorbate .....	111
3.3.1	The simplified model of macroscopic interaction.....	111
3.3.2	Favourable range of macroscopic interaction .....	112
3.3.3	Atomic resolution on the substrate in the presence of HCOO <sup>-</sup> .....	113
3.3.4	Implications for the experiment .....	114
3.4	Discussion .....	115
3.5	Summary .....	116
4	Contrast formation in imaging of molecular monolayers on TiO <sub>2</sub> (110).....	117
4.1	Adsorption of molecular monolayers on TiO <sub>2</sub> (110) .....	119
4.1.1	Methane on TiO <sub>2</sub> (110) .....	119
4.1.2	Formate on TiO <sub>2</sub> (110).....	125
4.2	Imaging HCOO <sup>-</sup> +H monolayer on TiO <sub>2</sub> (110) .....	128
4.2.1	Modelling of the tip-surface interaction.....	128
4.2.2	Comparison with experimental data .....	139
4.3	Summary .....	142
5	Characterisation of KI-filled SW-CNT .....	143
5.1	The model of KI-filled SW-CNT .....	145
5.2	Electronic structure of subsystems.....	146
5.2.1	Electronic structure of the single-walled carbon nanotubes (10,10).....	146
5.2.2	Electronic structure of potassium iodide.....	149
5.3	Electronic structure of filled SW-CNT .....	155
5.3.1	Electronic structure of filled SW-CNT with defects in the filling.....	158
5.3.2	Role of nanotube electronic structure in tube-chain interactions.....	161
5.4	Vibrational analysis of the KI filled SW-CNT .....	162

5.5	Discussion .....	165
5.5.1	KI-SWNT interactions .....	165
5.5.2	Defects in the free and encapsulated KI chains .....	165
5.5.3	Experimental characterisation of the KI filling inside SWNT .....	166
5.6	Summary .....	168
Conclusions .....		169
Reference List .....		171

## List of Figures

Figure 1. ( <i>left</i> ) AFM image of $\alpha$ -alumina (0001) surface annealed to 1300°C shows monosteps and double steps on the surface. ( <i>right</i> ) The profile of the stepped surface perpendicular to the step edges as observed with the AFM <sup>15</sup> .....	20
Figure 2. Atomically resolved AFM image of the KBr(001) surface in the contact mode. a) image of the plain terrace with indications of atomic resolution. Area marked with a red rectangle is scanned in a smaller frame and shown in b). The structure of the surface and characteristic distances are shown in c). The small and large protrusions in b) are attributed to the K <sup>+</sup> and Br <sup>-</sup> atoms respectively <sup>21</sup> . .....	21
Figure 3. SEM image of a typical microcantilever (NT-MDT). The atomistic model of tip-surface interaction consists of the “nanotip” cluster representing the apex of the tip and the model of the surface. Both the nanotip and the surface slab are split into two regions: with fixed and relaxed atoms <sup>31</sup> .....	22
Figure 4. Comparison of experimental NC-AFM images on CaF <sub>2</sub> (111) with simulated theoretical data obtained using the oxide tip model with a positive tip potential. ( <i>left</i> ) (a-c) experimental images are taken, as the tip approaches the surface with increasing of the mean detuning (-121, 127, and -140 Hz). (d-h) theoretical images simulated at 0.500 nm, 0.375 nm, 0.325 nm, and 0.250 nm. ( <i>right</i> ) experimental (a-c) and theoretical (d-h) scanlines to the second nearest bright spot in the image <sup>42</sup> .....	25
Figure 5. The block scheme of an NC-AFM instrument with a phase-locked loop (PLL). The adjustment of the tip-surface distance is made via automatic distance control (ADC). The oscillations are maintained by the automatic gain control.....	34
Figure 6. Hypothetical force- and frequency-distance curves for sites A and B. Negative values of the force correspond to the tip-surface attraction. The attraction is also manifested in the negative values of the frequency shift. ....	38
Figure 7. Scanning electron microscope image of a regular etched silicon tip. ( <i>left</i> ) large scale image of the cantilever with the tip. ( <i>right</i> ) SEM image of the tip apex illustrates that the tip radius of an as-produced tip apex is less then 10 nm. ....	41
Figure 8. Atomistic model of tip-surface interaction consists of the “nanotip” cluster representing the apex of the tip and the model of the surface. Both the nanotip and the surface slab are split into two regions: with atomistic and continuous description <sup>31</sup> .....	43

Figure 9. (left) quantum mechanical cluster used in the simulation with formate anion in the relaxed geometry. Bonds are specified in Å, angle in degrees; (right) Schematics of the embedded cluster method used in this work <sup>82</sup> .....	49
Figure 10. The density of states (DOS) of MgO(001) with a formate molecule using different exchange functionals. a) pure MgO(001) – DFT-GGA result (SIESTA); b) free QM cluster and free molecule (spectrum of eigenvalues). c) QM cluster with the adsorbed molecule in the equilibrium configuration (spectrum of eigenvalues). The different colours of eigenspectra demonstrate the nature of the state (red – molecule; green-substrate). Red lines in the eigenspectra indicate the percentage of the sum of squared coefficients of a state attributed to basis functions centred on the atoms of the molecule.....	51
Figure 11. <i>left</i> : side view of the atomic structure of the Al <sub>2</sub> O <sub>3</sub> (0001) surface, Al atoms are grey, O atoms are black. Lattice period and depth of first 4 atomic layers are indicated; <i>right</i> : coordination of Al ions in the top layer. The projection of the Al-O distance on the surface plane is 0.17 nm.....	54
Figure 12. Comparison of the force acting on the 64-atom Mg-terminated MgO tip over magnesium and oxygen surface sites of MgO(001) surface calculated from <i>ab initio</i> (red data points) and in pair potentials (solid line). The dotted line connecting <i>ab initio</i> data points is just a guideline. A major discrepancy in the description of the tip-surface interaction is observed over Mg site. ....	55
Figure 13. Calculated density of electronic states for bulk and (0001) surface of α-Al <sub>2</sub> O <sub>3</sub> . Surface spectrum is shifted to match the position of lower valence band. ....	56
Figure 14. Partial density of states (PDOS) in the MgO-Si system. Si tip is 10 Å from the surface. Red and green lines are Mg, O states respectively, dashed blue lines correspond to the total DOS. Bandgap in MgO states is 3.6 eV.....	58
Figure 15. Unit cell of titanium dioxide TiO <sub>2</sub> bulk <sup>101</sup> . Red spheres represent oxygen atoms, light green – titanium.....	59
Figure 16. Supercell of 3-layer TiO <sub>2</sub> (110) slab with 8 row oxygen atoms per cell. Red circles are oxygens, grey circles are Ti atoms. a) side view of the system; b) top layers of TiO <sub>2</sub> (110) system as in a) with one oxygen vacancy created in the oxygen row; c) top view of the defective system with the position of the oxygen vacancy marked with a hollow circle.....	60

Figure 17 Relaxed structures of $\text{TiO}_2(110)$ slab models (red spheres – O, light green - Ti) with a single vacancy marked by a blue sphere. The bottom of the unit cell is not shown.....	62
Figure 18 Electrostatic potential of the perfect $\text{TiO}_2(110)$ surface at 3.0 Å compared with electrostatic potential of the surface containing oxygen vacancies. Four types of vacancies are considered according to Figure 17(a-d). Values of the potential over defective surfaces are taken with respect to the maximum (over bridging oxygen row). Contours are drawn in the same scale with step 0.1 eV.....	63
Figure 19. Rigid oxide tip model is represented by a $4 \times 4 \times 4$ cube made of wide bandgap magnesium oxide. The cube is oriented with its $\langle 111 \rangle$ axis parallel to the surface normal and, therefore can be used to represent both positive- and negative-terminated atomically sharp tips depending on the sign of the atom on the apex. In our simulation the upper half of the cluster is kept fixed.....	67
Figure 20. ( <i>left</i> ) structure of the $\text{Si}_{10}\text{H}_{15}$ cluster. ( <i>right</i> ) Cross-section of the HOMO orbital of pure Si tip. This orbital is mainly associated with the unsaturated orbital of the apex Si atom. Shaded circles denote the projected position of other Si atoms. ....	70
Figure 21. Z-dependence of maximal/minimal value of total (blue solid line) and electrostatic potential (black dashed line), electronic density (red line) and magnified surface tails of these quantities are presented for the slabs of (a, c) $\text{MgO}(001)$ and (b, d) $\text{Al}_2\text{O}_3(0001)$ .....	75
Figure 22. Total force (microscopic + Van der Waals) acting on “negative” (left) and “positive” (right) potential tips at the level of macroscopic interaction characterised by a tip radius $R = 200 \text{ Å}$ and Hamaker constant $H = 1 \text{ eV}$ .....	78
Figure 23. Frequency-distance curves calculated over sites of the primitive surface cell of $\text{Al}_2\text{O}_3(0001)$ for two chosen macroscopic radii: (a) $R = 200 \text{ Å}$ and (b) $R = 2000 \text{ Å}$ . ....	79
Figure 24. Constant height NC-AFM images of the $\text{Al}_2\text{O}_3(0001)$ surface and normalised scanlines in the $[1\bar{1}00]$ direction for two different polarities of the $\text{MgO}$ tip. (a,c) negative potential tip image and scanlines; (b,d) positive potential tip image and scanlines. Distances in scan-lines along the surface are in nm. Both constant height images correspond to a minimum tip-surface separation of 0.3 nm. ....	81



- Figure 25. Contrast dependence in the modelled NC-AFM image as a function of the minimal tip-surface distance (in Constant Height mode, *left* ) and preset frequency shift (in Constant Frequency Shift mode, *right*). The images are calculated for  $k = 3 \text{ N/m}$ ,  $A = 70 \text{ \AA}$ ,  $f_0 = 100 \text{ kHz}$ , assuming a macroscopic interaction described by a tip radius  $R = 2000 \text{ \AA}$ . ..... 82
- Figure 26. The map of the total energy surface of the tip in the vicinity of the  $\text{Al}_2\text{O}_3(0001)$  surface is plotted for different orientations of the MgO tip apex with respect to the surface. (a) A scheme illustrating the projection of the tip apex atoms onto the surface and the tip tilt with respect to the normal. The total energy of the system as a function of the tip position at a tip-surface separation of  $2.5 \text{ \AA}$ : (b) for the original tip orientation and tilt used in calculations above (corresponding to the forcefield in Figure 22); (c) tip rotated by  $20^\circ$  with respect to the original position; (d) tip tilted by  $20^\circ$  with respect to its original orientation perpendicular to the surface. .... 83
- Figure 27. Force-distance curves for the interaction of the Si dangling bond tip ( $\text{Si}_{10}\text{H}_{15}$  cluster) with MgO (001) and  $\text{Al}_2\text{O}_3$  (0001) surfaces calculated above characteristic surface sites. The upper section (shaded in green) of each graph presents charge transferred to the tip as the tip-surface distance is reduced. The left axis corresponds to the force-distance curve, the right axis - to the charge transfer to the tip. Negative force corresponds to attraction to the surface. .... 86
- Figure 28. *Ab initio* forces acting at  $3.0 \text{ \AA}$  on tips positioned over the oxygen site of MgO(001) surface for different tip models: pure silicon tip with a dangling bond, rigid oxide tip with positive apex potential (front view), Si tip with the dangling bond saturated by an OH or H. The force acting on the Si tip with a dangling bond over the Mg site of MgO(001) surface is presented for a comparison. (Table 6 is reproduced here for the sake of the reader's convenience). .... 89
- Figure 29. The eigenspectra of QM cluster of MgO(001) with a formate molecule. a) free QM cluster and free molecule (spectrum of eigenvalues). b) QM cluster with the adsorbed molecule in the equilibrium configuration (spectrum of eigenvalues). The different colours of eigenspectra demonstrate the nature of the state (red – molecule; green-substrate). Red lines in the eigenspectra indicate the percentage of the sum of squared coefficients of a state attributed to basis functions centred on the atoms of the molecule. .... 96

- Figure 30. Relaxed configuration of an adsorbed HCOO<sup>-</sup> anion on the MgO(001) surface calculated within Embedded Cluster Method. The schematic on the right shows the height of the atoms of the molecule and the displaced Mg atoms of the surface with respect to the equilibrium z-position of oxygen atoms on the clean perfect terrace (surface level). The isosurface of the HOMO orbital of the system is presented in the picture for the isolevel of  $0.05 |e|/(\text{Bohr})^3$ . ..... 98
- Figure 31. Typical low-lying vibrational modes of the HCOO-MgO(001) system with eigenvectors primarily related to the molecular motion. The images show atomic displacements from equilibrium position along the following modes: (a) bending modes in range 79-223 cm<sup>-1</sup>, (b) sliding modes in range 90-191 cm<sup>-1</sup>, and (c) a “swinging” mode at 146 cm<sup>-1</sup> ..... 101
- Figure 32. The schematic view of a possible diffusion path for the “swinging” mode. The shaded squares represent the Mg sites, white squares – O sites; red circles identify oxygen atoms of the formate. In this mode O1 moves to the site previously occupied by O2, O2 moves to the new site. The positive C-H group bends over the surface oxygen ion O<sup>s</sup> during the motion..... 102
- Figure 33 Distribution of z-component of the force acting on the Mg-terminated oxide tip 5.0 Å over formate anion on MgO(001) surface. Lateral dimensions of the cross-section are 10x10 Å. Force on the colorbar is given in nN. Positive values correspond to the attraction to the surface. .... 105
- Figure 34. (left) Force curves for the oxide tip with positive potential.; (right) zoom into the region for tip-surface distance 4.5-6 Å. Dashed blue line indicates the closest tip-surface distance, where no jumps in force are observed. .... 105
- Figure 35. NC-AFM images of a single formate ion on MgO(001) surface modelled in Constant Frequency Shift (CFS) mode. a)-d) images obtained for various frequency shifts expressed via the normalized frequency shift  $\gamma = 0.28 \div 0.58 \text{ fNm}^{0.5}$ . The minimal distance between the tip and MgO(001) surface, achieved during acquisition of the image ( $Z_{\text{min}}$ ), is specified for each image. Positions of the substrate ions and average positions of formate are shown in colour in a). In images b)-d) only the positions of formate ions are shown. Macroscopic Van der Waals interaction is evaluated for tip radius  $R = 500 \text{ Å}$ . Corrugation scale for images a)-c) is 0.1 Å, 0.14 Å, 0.16 Å, 0.4 Å respectively. .. 107
- Figure 36. a) The relationship between chosen frequency shift and the minimal tip-surface distance achieved during acquisition of the image of a formate anion on

MgO (001) surface; b) Distance dependence of the of the contrast in the constant frequency shift image for the two tip radii.....	109
Figure 37. Interaction dependence of corrugation in CFS image of formate-MgO(001) system. The apparent height of the molecule on the surface is plotted as a solid line, corrugation on the MgO(001) surface is shown as dashed line. Solid and dashed lines of the same colour correspond to the same strength of macroscopic interaction. The value of tip radius, used to characterize the strength of interaction, is also shown in corresponding colour. ....	113
Figure 38. a) The energy-distance dependence for a methane molecule over the titanium oxide surface. Values of the energy do not account for relaxation of the molecule and the surface. b) The structure of the unit cell used in calculation and the orientation of the methane molecule CH <sub>4</sub> . Arrows indicating position of CH <sub>4</sub> molecule on the surface have the same colours as corresponding adsorption curves. ....	121
Figure 39. Methane adsorption curves over Ti and vacancy sites on reduced TiO <sub>2</sub> (110) surface are calculated for the molecule in a “dipod” position over Ti site and two “dipod” positions over the oxygen vacancy site: across and along the oxygen row. The absorption energy is calculated with respect to the energy at a separation of 10 Å. Surface and molecular relaxation is not included in the calculation.....	123
Figure 40. Relaxed geometries of formate-TiO <sub>2</sub> (110) submonolayer systems at intermediate $\theta = 0.125, 0.25, 0.375$ ML(a-c) and maximal $\theta = 0.5$ ML (d) coverage. This system is assumed to have formed by dissociation of the formic acid on the surface. Red, light green, green and grey circles correspond to O, Ti, C, H atoms respectively. ....	126
Figure 41. Two possible configurations (a,b) of the arrangement of the products of dissociation of the formic acid (formate anions and protons) at $\theta = 0.25$ ML coverage. The clear preference to fill rows rather than scatter over different rows is attributed to the change in dipole –dipole interactions between the two molecules; Red, light green, green and grey circles correspond to O, Ti, C, H atoms respectively. ....	127
Figure 42. Side and top views of the surface unit cell used for generation of NC-AFM image of formate monolayer on TiO <sub>2</sub> (110) surface. Mesh points used to acquire the force-distance curves are shown in the inset as white circles. Oxygen atoms and cations of the TiO <sub>2</sub> are red and big grey circles correspondingly, hydroxylated	

- oxygen is yellow, oxygens of the formate molecule are blue; carbon is shown green; smaller grey circles are hydrogen atoms..... 129
- Figure 43. Force-distance curves obtained with the Si tip approaching the  $\text{TiO}_2(110)$  surface covered by a formate monolayer. Numbers by each of the force curves correspond to the mesh point numbers in Figure 42..... 130
- Figure 44. Modelled NC-AFM image of formate monolayer on  $\text{TiO}_2(110)$  surface. The tip radius is  $500 \text{ \AA}$ ,  $\gamma=3.5 \text{ fNm}^{0.5}$ , cantilever stiffness is  $35 \text{ N/m}$ , peak-to-peak oscillation amplitude is  $10 \text{ nm}$ . Coloured circles draw correspondence between atomic sites and areas of the image. Red, magenta, yellow and blue circles represent bridging, surface, hydroxyl and formate oxygen atoms respectively.... 133
- Figure 45. Relaxed geometry structure of the Si tip over selected points (#13, #2, #8 as in Figure 42) of the formate monolayer on  $\text{TiO}_2(110)$ . The interaction between the tip and the molecule induces significant displacements. a) retraction of formate oxygen in a Ti-O bond, b) bending of the formate molecule, c) bending of OH group. .... 135
- Figure 46. Schematic representation of displacements induced in the  $\text{TiO}_2$  surface and adsorbed formate monolayer by the Si tip with dangling bond approaching (a) at row oxygen site (#16); (b) at hydroxylated row oxygen (#8); (c) at (#2) site next to the formate molecule; (d) at (#13) site next to the formate molecule. Bold dashed line indicates the level of bridging oxygen atoms as the reference for the height of the tip..... 137
- Figure 47. (a) NC-AFM image of the  $(2 \times 1)$  monolayer of formate ( $\text{HCOO}^-$ ) on  $\text{TiO}_2(110)-(1 \times 1)$  ( $13.3 \times 13.3 \text{ nm}^2$ ). Acquired with positive bias  $1.2 \text{ V}$  at normalized frequency shift  $46.5 \text{ fNm}^{0.5}$ . b) NC-AFM image of dilute monolayer ( $7.1 \text{ nm} \times 7.1 \text{ nm}$ ). Arrows indicate positions of formate molecules. Acquired with positive bias  $1.3 \text{ V}$  at normalized frequency shift  $16.5 \text{ fNm}^{0.5}$ . (Parameters:  $df = 80 \text{ Hz}$ ,  $f = 295 \text{ kHz}$ ,  $A_p-p = 30 \text{ nm}$ ,  $k = 33 \text{ N/m}$ )<sup>228,32</sup>..... 139
- Figure 48. Density of states for the  $(10,10)$  carbon nanotube calculated in periodic model with elementary unit cell and 6 (dashed green line) and 16 (red line) unequivalent k-points. The gap closes within smearing resolution for 16 k-points calculation, however, consideration with 6 k-points results in  $1.0 \text{ eV}$  gap between valence and conduction bands..... 147
- Figure 49. Band structure of metallic  $(10,10)$  SWNT, calculated for unit cell of 40 atoms with 16 inequivalent k-points. The Fermi level is  $\epsilon_F = -4.71 \text{ eV}$ . The small

(less 0.1 eV) gap remains between conduction band and valence band due to the finite number of k-points used. ....	148
Figure 50. Electronic band structure of the KI system along the $\Gamma$ -X direction (b) in the bulk KI, and (c) in the KI chain. The dispersion curves are calculated for the eight-atom unit cell. ....	150
Figure 51. (a) Dispersion relation for normal modes of vibration of the potassium iodide crystal from the neutron diffraction data <sup>262</sup> ; (b) Calculated dispersion relations of the KI chain calculated in the 8-atom unit cell. ....	151
Figure 52. Density of states in the perfect KI bulk (blue) and in the presence of divacancies (green) calculated in the 64-atom supercell. ....	153
Figure 53. Profile of the force acting on the positive probe charge in the vicinity of the KI chain. The profile is calculated from the ab initio electrostatic potential and plotted along the edge of KI in the (110) plane. a) potential of the perfect KI chain; b) potential of the KI chain with divacancy along the chain direction. Blue, green and red lines describe the force at 5.0 Å, 7.0 Å, and 10 Å distance from the centre of the chain. The view of the perfect chain in the (110) plane in a) illustrates the definition of the distance. ....	155
Figure 54. Structure of “ideal” and “defective” KI filling obtained as result of relaxation within the SWNT. (a) no defects; (b) divacancy along the symmetry axis; (c) “perpendicular” divacancy; (d) “parallel” divacancy. Potassium (K) atoms are blue, iodine (I) atoms are red. ....	156
Figure 55. Projected Density of States (PDOS) plotted for C(blue), K(green) and I(iodine). a) KI-filled nanotube with defects; b) KI-filled nanotube with perfect filling. ....	157
Figure 56. Schematic picture showing the atomic vibrations for (a) the RBM and (b) the G band modes <sup>286</sup> ....	163
Figure 57. Density of states of the vibrational spectra for the empty and KI-filled individual SWNT(10,10) . Left and right graphs zoom into the low and high-frequency regions of the spectrum. ....	164
Figure 58. Contour map of the modulus of electrostatic force acting on a probe charge near the edge of the perfect free 2×2 KI chain, free 2×2 KI chain with a vacancy pair, encapsulated 2×2 KI chain with a vacancy pair. The map is constructed from the ab initio electrostatic potential. Contour levels start at zero but have different step sizes for the free and for the encapsulated chains: for the free chains the step is 0.08 nN, for the encapsulated chain the step is 0.0016 nN for contours outside the nanotube and 0.16 nN for the contour inside. ....	167

## List of Tables

Table 1. SIESTA basis sets used for calculations of substrate electronic structure.....	47
Table 2. Deprotonation energy calculated in Gaussian basis sets within B3LYP exchange functional .....	50
Table 3. Comparison of surface relaxation in the $\alpha$ -alumina surface, obtained from GIXD experiment, DFT calculations and pair potentials static relaxation. ....	53
Table 4 Comparison of vacancy formation energy for the considered models of oxygen vacancies calculated with respect to a neutral oxygen atom. Total energies $E^{TX}$ (spin-polarized calculations) denote energy of a $\text{TiO}_2$ system with vacancy (T1-T4). The second column lists the total energy of T1-T4 with respect to T1. Total energy of an ideal surface and an oxygen atom calculated in the same supercell are (-56446.318 eV) and (-438.900 eV) correspondingly.....	64
Table 5. Positions of the top of the valence band $E_{VB}$ , bottom of the conduction band $E_{CB}$ and molecular orbital associated with the dangling bond $E_{DB}$ and the highest “fully occupied” orbital. Inset: Scheme of eigenvalue’s structure for a tip with a dangling bond. $\epsilon_F$ is the Fermi level of the system. ....	69
Table 6. Comparison of the strength of interaction with $\text{MgO}(001)$ surface for the Si-based and oxide tip models. The forces of attraction acting on the tip apex, z-displacements in the surface, tip and change in the actual tip-surface separation are shown. ....	71
Table 7. Frequencies of molecular vibrations of formate anion on $\text{MgO}(001)$ surface. Values obtained in this work are compared with available experimental data <sup>167</sup> .....	100
Table 8. The potential parameters describing the molecule-tip interaction obtained by fitting of QM data.....	104
Table 9. Total energy of $\text{CH}_3$ and $\text{CH}_4$ molecules in neutral and negatively charged states. Calculations are performed using the PBE GGA functional <sup>217</sup> .....	125
Table 10. Energy of formation for a neutral divacancy in KI-based systems. Divacancy formation energy is calculated with respect to ideal chain (bulk) and a KI molecule. Results are presented for smaller supercell (small SC) and larger supercell (large SC). For KI-SWNT system the results for the larger cell could not be calculated but estimates are provided, based on the relaxation of KI system in large SC. Energies are presented in eV.....	160

## List of Acronyms

ADC	Automatic Distance Control (in NC-AFM setup)
AFM	Atomic Force Microscopy
B3LYP	Name of an exchange-correlation functional
BFGS	Broyden-Fletcher-Goldfarb-Shanno      Quasi-Newton      optimization algorithm
C-AFM	Contact mode Atomic Force Microscopy
CFS	Constant Frequency Shift (NC-AFM mode)
CH	Constant Height (NC-AFM mode)
CHARMM	Set of interatomic potentials
D-AFM	Dynamic mode Atomic Force Microscopy
DFT	Density Functional Theory
DOS	Density Of States
ECM	Embedded Cluster Method
EELS	Electron Energy-Loss Spectroscopy
EPR	Electron Paramagnetic Resonance
FM-AFM	Atomic Force Microscopy
GGA	General Gradient Approximation
GIXD	Grazing Incidence X-ray Diffraction
GULP	Software for structural optimization and MD using interatomic potentials
HF	Hartree-Fock
HREELS	High Resolution Electron Energy-Loss Spectroscopy
HRTEM	High Resolution Transmission Electron Microscopy
IINT	Inorganic Insulating NanoTubes
KPFM	Kelvin Probe Force Microscopy
LCAO	Linear Combination of Atomic Orbitals
LDA	Local Density Approximation
LEED	Low-Energy Electron Diffraction
MARVIN	Software for structural optimization and MD using interatomic potentials
MD	Molecular Dynamics
MERLIN	Software package for global/local optimization
MIES	Molecular-Induced Excitation Spectroscopy



MM	Molecular Mechanics
NAO	Numeric Atomic Orbitals
NC-AFM	Non-Contact mode Atomic Force Microscopy
NEMS	Nano-Electro-Mechanical Systems
NPA	Natural Population Analysis
NPT	Negative-terminated tip
PBC	Periodic boundary conditions
PBE	Name of an exchange-correlation functional (a flavour of GGA)
PDOS	Projected Density Of States
PPT	Positive-terminated tip
QM	Quantum Mechanics (Mechanical)
RT	Room Temperature
SAM	Self-Assembled Monolayers
SCIFI	Software structural optimization and MD using interatomic potentials
SEM	Scanning Electron Microscopy
SFG	Second Frequency Generation
SFM	Scanning Force Microscopy
SIESTA	<i>Ab initio</i> package for electronic structure calculation. (Spanish Initiative Electronic Simulation with Thousands Atoms)
SPM	Scanning Probe Microscopy
SWNT	Single-Wall NanoTubes
SXRD	Surface X-Ray Diffraction
TEM	Transmission Electron Microscopy
TOF	Time-Of-Flight
TPD	Temperature Programmed Desorption
TZP	Triple- $\xi$ with Polarization (a basis set used in SIESTA)
UHF	Unrestricted Hatree-Fock
UHV	Ultra High Vacuum
XPS	X-rays Photoemission Spectroscopy

$$1 \text{ \AA} = 10^{-10} \text{ m} = 0.1 \text{ nm}$$

$$1 \text{ eV/\AA} = 1.60217653 \times 10^{-9} \text{ N} = 1.60217653 \text{ nN}$$

## **Acknowledgements**

I felt honoured to work in the Condensed Matter and Material Physics group of UCL, not only because of the high standards of the research, but also because of the attitude towards colleagues, full of respect. I'm grateful to the senior staff who were open to questions and ready to help, in particular, Marshal Stoneham, Tony Harker, John Harding, Jacob Gavartin and Peter and Maria Sushko. I personally thank my dear fellows in C101, - Charles, Sarah, Che, Sukina, Sasha, Rathin, Verity and Dan whose help would often come before I asked. I was very pleased to receive your welcome, and appreciate your tolerance to my infrequent going out.

I'm infinitely grateful to my supervisor Alexander Shluger for his support and wise guidance during my project. I am particularly indebted for the time and effort he spent planting seeds of Research in my mind. I can hardly overestimate the help of Adam Foster, Jacob Gavartin and Lev Kantorovich, who were constantly a source of knowledge and experience.

Finally, I acknowledge ORS, ESF and EPSRC for the financial support during my PhD project.

This work would be absolutely impossible without the encouragement and support of my wife and our parents.

### List of publications

1. **A.Y. Gal**, A.L. Shluger "Theoretical simulation of non-contact atomic force microscopy imaging of the  $\alpha$ -alumina(0001) surface", *Nanotechnology*, (2004), vol. 15, S108-S114
2. S. Foster, **A. Y. Gal**, J. D. Gale, Y. J. Lee, R. M. Nieminen, and A. L. Shluger, "The interaction of silicon dangling bonds with insulating surfaces", *Phys. Rev. Lett.*, (2004), vol. **92**, p. 036101.
3. S. Foster, **A. Y. Gal**, J. M. Airaksinen, O. H. Pakarinen, Y. J. Lee, J. D. Gale, A. L. Shluger and R. M. Nieminen "Towards chemical identification in atomic resolution NC-AFM imaging with silicon tips", *Phys. Rev. B*, (2003), vol. **68**, pp.195420.
4. S. Foster, **A. Y. Gal**, J. D. Gale, Y. J. Lee, R. M. Nieminen, and A. L. Shluger "Dependence of the tip-surface interaction on the surface electronic structure", *Applied Surface Science*, (2003), vol. **210**, pp. 146-152
5. S. Foster, **A. Y. Gal**, R. M. Nieminen, and A. L. Shluger "Probing Organic Layers on the  $\text{TiO}_2(110)$  Surface", *J. Phys. Chem.* (2005), vol. **109**, p.4554

## Introduction

Characterisation of insulating surfaces with high resolution of the order of 1 nm is essential for studies in heterogeneous catalysis, corrosion and in the emerging field of nanofabrication. A number of sensitive techniques, such as temperature programmed desorption<sup>1</sup>, sum-frequency generation<sup>2</sup> or the surface diffraction of particles and high energy photons<sup>3-6</sup> are used for surface characterisation. However, the measurements obtained from these techniques are averaged over the surface area and do not provide high spatial resolution locally. Hence the development of techniques providing high resolution in real space is important.

Scanning Probe Microscopy (SPM) is a vast field of techniques producing real space maps of surface properties at scales below 1  $\mu\text{m}$ . Surface Force Microscopy (SFM) is a subset of such techniques, where the strength of interaction between tip and surface is mapped. Therefore, SFM allows characterization of heterogeneous and microscopically rough surfaces. SFM techniques tailored to measure the tip-surface interaction with high resolution (approximately of 1 nm) are often described as Atomic Force Microscopy (AFM). These techniques are used to study adsorption, friction, wear and surface properties, which can be deduced from the measurement of the force exerted on the tip. The typical values of forces measured in such experiment are approximately 1-100 nN<sup>7-10</sup>.

One of the main advantages of SFM compared to Scanning Tunnelling Microscopy (STM), which is used for characterisation of conductive surfaces, is the ability to characterise the structure of insulating surfaces. Although STM has been used successfully to study the properties of thin insulating films<sup>11-14</sup>, the interpretation of the images obtained remains controversial. Therefore, SFM is the dominant SPM method for the study of atomic structure and defects on insulating surfaces.

In SFM the surface is scanned by the tip in a raster fashion, analogously to the way a TV display is scanned by the e-beam, i.e. the probe is displaced by the positioning system in two dimensions across the surface. However, in SFM there may be a significant thermal surface drift, which distorts the scanning area from a perfect rectangle. A pixel of the SFM image is formed on the basis of the tip-surface interaction, which is measured directly or indirectly by the probe over a period of time. A sequence of pixels is mapped onto the trajectory of the probe handler and presented

as a set of forward and backward *scanlines* constituting an image. The intensity level of a pixel represents the tip-surface interaction in a broad sense, because the way it is measured and interpreted varies between different types of SFM instruments.

Experimental AFM setup. Typically, a probe is mounted on a flexible Si microcantilever, and the AFM measures the displacement of the cantilever induced by the tip-surface interaction. Most instruments do not output the measured signal directly, but use a feedback system to keep the value of the signal at a preset constant value. For instance, the z-position of the surface can be adjusted continuously to maintain a preset value for the force exerted on the cantilever. The image in this case is a map of the adjusted z-position of the substrate relative to the position of the tip. It can be also interpreted as a measure of interaction. One of the advantages of such a feedback system is the ability to image highly corrugated surfaces or surfaces with adsorbed molecules.

The speed of reaction of the feedback loop is an important concern and can be regulated by the value of the *gain* in the feedback loop. For the image to be produced in a steady state, the speed of reaction of the feedback should be greater than the scanning speed.

An example of an AFM image<sup>15</sup> of an  $\text{Al}_2\text{O}_3(0001)$  surface, which attracts experimentalists due to its multiple technological applications<sup>16-20</sup>, is presented in Figure 1. The output signal in the image is the variation in the z-position of the surface (*corrugation*), which is required to maintain the preset force on the cantilever as a function of the lateral tip position.

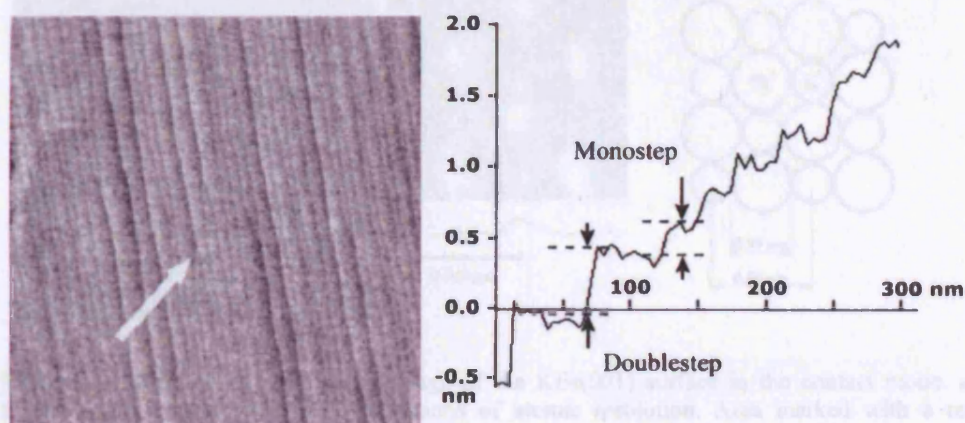


Figure 1. (left) AFM image of  $\alpha$ -alumina (0001) surface annealed to 1300°C shows monosteps and double steps on the surface. (right) The profile of the stepped surface perpendicular to the step edges as observed with the AFM<sup>15</sup>.



It is important to note that the actual distance between the tip and the surface is not measured in the experiment and its evaluation is one of the problems of the interpreting the image.

The interpretation of the AFM image is based on the fact that the chosen preset value of the force applied to the cantilever guarantees that the apex of the tip is constantly “in contact” with the surface. According to this interpretation, the image presents a number of wide terraces on the surface and steps between them<sup>15</sup> (Figure 1). The apparent height of the steps is 0.2 nm, so most likely they are monoatomic, according to the experimentalist’s opinion<sup>15</sup>. This is an example of high topographic resolution, while no corrugation is measured on the individual terraces.

There are some examples where the high resolution of the image does not mean that positions of the atoms are identified. For instance, some of the images of alkali halides surfaces made with AFM in “contact” mode (C-AFM) resulted in patterns with periods of the order of the lattice constant<sup>21</sup>. These patterns were first identified as those providing “atomic resolution”. However, the theoretical analysis of contact mode imaging demonstrates<sup>22</sup> that the correspondence between the “bright” and “dark” spots in the experimental image (Figure 2) and the positions of the ions is often a coincidence, although the period of the scanline may well correspond to the periodicity of the substrate.

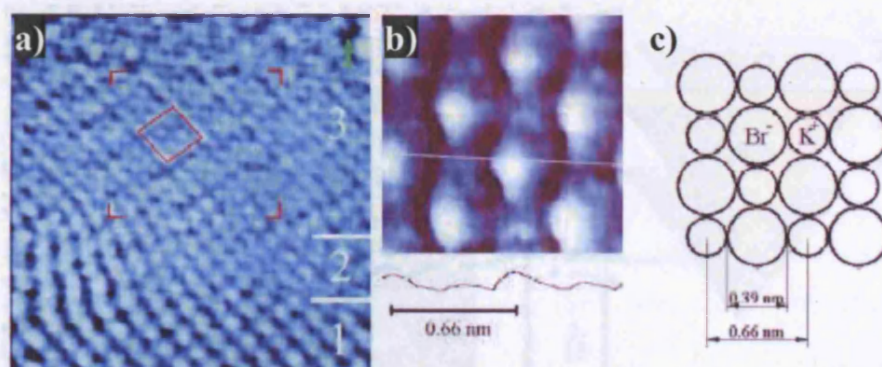


Figure 2. Atomically resolved AFM image of the KBr(001) surface in the contact mode. a) image of the plain terrace with indications of atomic resolution. Area marked with a red rectangle is scanned in a smaller frame and shown in b). The structure of the surface and characteristic distances are shown in c). The small and large protrusions in b) are attributed to the  $K^+$  and  $Br^-$  atoms respectively<sup>21</sup>.

The periodicity seen in Figure 2 arises as a “steady state” of the dynamic reconstruction of the tip accommodating itself to the change in the underlying substrate<sup>23</sup>. Therefore, the shape of the scanline is determined for a perfect lattice by the scan direction, scan speed<sup>24,25</sup>, tip properties and the shape of the substrate potential<sup>26</sup>.

In the presence of defects, the signal depends strongly on the history of the scanline, i.e. it has a “memory effect”, which significantly complicates the detection, interpretation and comparison of C-AFM images with corrugations of atomic scale. Hahn<sup>27</sup>, for instance, demonstrated that C-AFM gives a “perfect” atomic pattern, while STM showed evidences of the presence of atomic size defects. However, a C-AFM image might allow detection of an atomic defect for certain combinations of surface and tip apex<sup>28</sup>.

Since the “memory” effects and the tip reconstruction are the results of strong tip-surface interaction, the “straightforward” way to avoid these effects is to reduce the typical force of the tip-surface interaction and increase the precision and sensitivity of the measurement.

The Dynamic Atomic Force Microscopy (D-AFM)<sup>29</sup> technique developed<sup>30</sup> a few years after conventional AFM, provided the means for precise measurement of the tip-surface interactions over a range of weaker forces of typically 0.01-10 nN. In this technique, the improvement has been made by the introduction of an *oscillating* probe (Figure 3), rather than a statically bent cantilever. The high sensitivity of the force

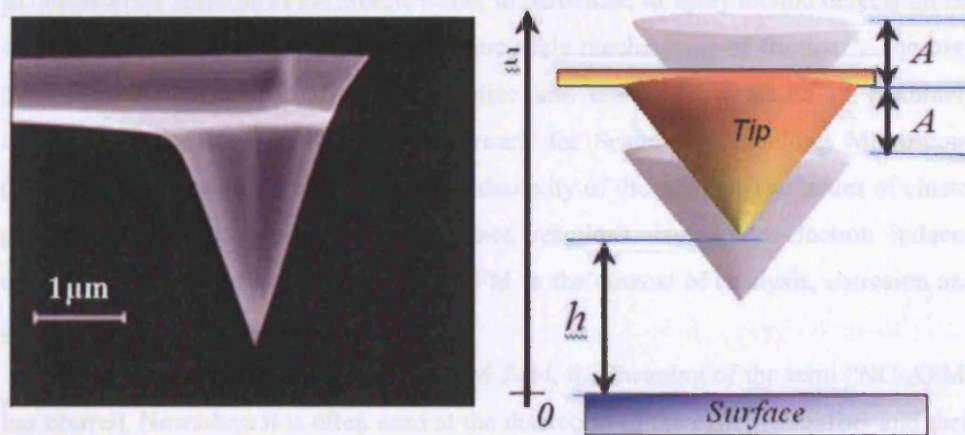


Figure 3. SEM image of a typical microcantilever (NT-MDT). The atomistic model of tip-surface interaction consists of the “nanotip” cluster representing the apex of the tip and the model of the surface. Both the nanotip and the surface slab are split into two regions: with fixed and relaxed atoms<sup>31</sup>.



measurement can be explained by the sensitivity of the period of an oscillator to perturbations in the potential near the turning point and the high precision with which frequency can be measured ( a detailed description is given in the section 1.1).

The frequency modulation mode of D-AFM (FM-AFM) is specifically tailored for high precision measurements with atomic resolution<sup>9</sup>. In this mode the amplitude of the oscillation is maintained constant, the phase of the driving signal is adjusted to maintain resonance, while the change in the frequency (“detuning”) is used in the feedback system as a measure of the tip-surface interaction.

The issues of surface drift and the relationship between the scan speed and the speed of the reaction of the feedback loop are very important in this mode. For *high* scan speed and *low* values of the feedback gain, the preset value of the frequency shift is not achieved and the image of the error results in a complementary image of “detuning”. In the ultimate limit of *very low* gain and *very high* speed, the feedback is not able to adjust the z-position of the surface to the fast variations in the interaction during the scan and the “detuning” image becomes the primary source of information. The ultimate modes with *high* gain, *slow* speed and *very low* gain, *very high* speed are termed as the Constant Frequency Shift (CFS) mode and the Constant Height (CH) mode respectively.

FM-AFM is often referred to as “Non-Contact” Atomic Force Microscopy (NC-AFM), because the measurement normally probes the 1-nm region close to the surface, and works predominantly in the attraction regime. NC-AFM is used to characterize surfaces at the atomic scale, in particular, to study atomic defects on the surface<sup>32</sup>, molecular adsorption<sup>33</sup> and atomic scale mechanisms of friction<sup>34</sup>. The high precision of this technique achieves atomic and chemical resolution of genuinely insulating surfaces<sup>35</sup>, which are out of reach for Scanning Tunnelling Microscopy (STM) which demands at least surface conductivity of the sample. The issues of cluster growth<sup>36</sup>, molecular adsorption and surface reactions, laser- and electron induced desorption are also addressed using NC-AFM in the context of catalysis, corrosion and general surface chemistry<sup>37,38</sup>.

With the expansion of the FM-AFM field, the meaning of the term “NC-AFM” has blurred. Nowadays it is often used at the discretion of the experimentalists and their perception of the model for imaging. According to a recent review book<sup>39</sup>, an imaging mode of D-AFM is “non-contact” when “neither tip nor sample suffer permanent deformations or wear during the imaging process” no matter what is the sign of the

force acting on the tip or the apex atom. In this work we will use the term “non-contact” in this sense.

We also require definitions of different degrees of resolution in an AFM image. Importantly, the “resolution” is used in the sense of “resolved information” and therefore is achieved not only by the experimental work, but from the joint application of theory and experiment.

An image with *true atomic resolution* is the result of an experiment, where a match between the features of the image and the atomic positions in surface can be made in principle. This distinguishes it from an image with features of atomic size as shown in Figure 2b. When different species of the surface structure can be resolved in the image with “true atomic resolution” and the identity of the atom can be proved - we talk about *chemical resolution*<sup>40</sup>.

In the general case, when atoms, groups of atoms or molecules can be resolved in the image “truly”, in the sense mentioned above, we will refer to the image as a “high resolution image”. The procedure of developing the correspondence between a surface structure and the image will be termed in this work as *interpretation* of the image.

*Interpretation of NC-AFM images* of  $\text{CaF}_2(111)$  performed in our group in the past provides a basis<sup>41,42</sup> for further studies. It is not the only work in the field but is an example of the productive joint application of theoretical and experimental developments that have been built up over many years<sup>23,43,44</sup>. The work<sup>41,42</sup> shows that an understanding of a realistic model of the tip and tip-surface interaction, as well as both tip and surface relaxation are required for “unambiguous” interpretation of the experimental images. It has also been demonstrated that having a single NC-AFM image is not sufficient for interpretation of the underlying system.

The comparison of a high resolution NC-AFM image of the clean  $\text{CaF}_2(111)$  surface with simulated NC-AFM images of the same surface is presented in Figure 4. Both experimental and simulated images correspond to the Constant Height mode and show detuning in the oscillations of the cantilever, as it moves along the surface. For this particular surface several types of pattern are observed in the experimental images, as the tip approaches the surface.

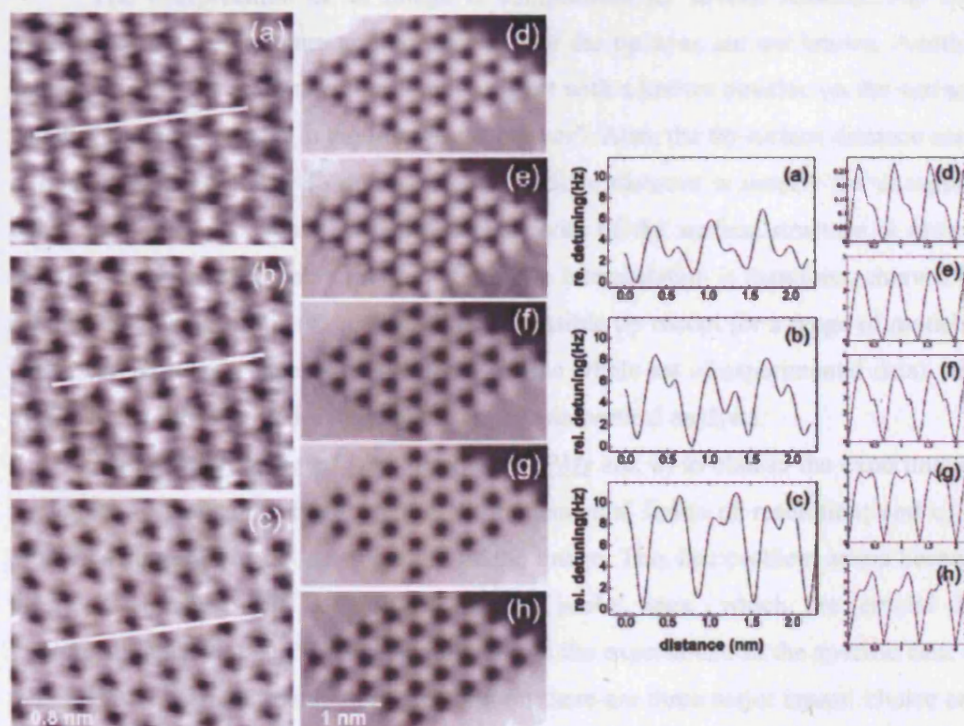


Figure 4. Comparison of experimental NC-AFM images on  $\text{CaF}_2(111)$  with simulated theoretical data obtained using the oxide tip model with a positive tip potential. (*left*) (a-c) experimental images are taken, as the tip approaches the surface with increasing of the mean detuning (-121, 127, and -140 Hz). (d-h) theoretical images simulated at 0.500 nm, 0.375 nm, 0.325 nm, and 0.250 nm. (*right*) experimental (a-c) and theoretical (d-h) scanlines to the second nearest bright spot in the image<sup>42</sup>.

The theoretical image modelled with a positively terminated oxide tip is able to reproduce the patterns qualitatively. The theory explains the mechanisms, which led to the change in the pattern on the basis of the atomistic simulation. A model interpretation built on the basis of this comparison allows the association of the centres of the dark spots in the images (a) and (d) in Figure 4 (left) with the equilibrium positions of the positive  $\text{Ca}^{2+}$  ions. Importantly, the tip model and the assignment of the “dark spots” are deduced simultaneously, so that one could potentially change the tip model and the image interpretation at once. Therefore, further analysis and comparison with other experimental data had to be made before the authors of that work were able to conclude that in this case an “unambiguous” interpretation was possible<sup>42</sup>. The work has demonstrated that the contrast formation in the image is governed by 2 factors: a strong electrostatic potential of the oxide tip model and displacements in a soft surface.

The interpretation of an image is complicated for several reasons. The first problem is that the structure and composition of the tip apex are not known. Another complication is the absence of a reference object with a known position on the surface, which is uniquely present in the image – a “marker”. Also, the tip-surface distance scale is relative and the ability to determine the absolute distance is usually the exception rather than the rule. Finally, a geometrical model of the surface structure is always required in advance to enable interpretation. The interpretation is therefore achieved by solving the inverse problem, i.e. by finding a feasible tip model (or a range of models), which can reproduce experimental images (or the whole set of experimental data) with maximal “likelihood”, and so requires extensive theoretical analysis.

*The main problems of high resolution SPMs* are: a) to choose the experimental parameters for imaging; b) to foresee the fundamental limits of resolution; and c) to provide a straightforward interpretation of the image. This last problem arises because the size, structure and composition of the probe apex, which are crucial for interpretation, cannot be characterised directly in the experiment. In the specific case of the D-AFM experiment with atomic resolution there are three major issues: choice and preparation of the tip, choice of parameters of the imaging, and interpretation of the image.

During recent years, significant theoretical effort has been made in this field contributing to all three questions. The choice of imaging parameters proved to be very important due to instabilities in the Amplitude Modulation (AM) mode of D-AFM and this has been analyzed theoretically<sup>29</sup>. In FM-AFM mainly experimental efforts have been made to improve the setup<sup>45,46</sup>, which has led to unprecedented force sensitivity. The issue of interpretation of the AFM image pattern has been in question for a decade<sup>47</sup>, however a qualitative interpretation of FM-AFM image required either tailoring the theoretical tip model to the particular experiment<sup>42</sup> or preparing the tip experimentally<sup>42</sup> to match the established theoretical tip model<sup>42,48</sup>. Based on the information available from an experiment, the problem of choosing a tip model could not so far be solved deterministically. Therefore, the problem of the tip model appears to be closely related to the problem of image interpretation and has to be addressed simultaneously. Cases of “unambiguous” interpretation with atomic resolution are quite rare and require either using unambiguous markers on the surface, such as adsorbed molecules<sup>37</sup>, or an extensive theoretical study with several tip models<sup>42</sup>.

Due to the wide range of surfaces available for NC-AFM, models of the tip apex and, correspondingly, understanding of the mechanisms of contrast formation are not universal. However, although they have been developed for particular systems, the interpretation of the image has proved to be transferable for some tip models within a class of similar systems such as in the case of typical semiconductors (Si, InP, GaAs) and alkali halides (NaCl, KBr, KI).<sup>49,50</sup> These models capture the major mechanisms of contrast formation rather than offer a particular model of the tip apex structure: interaction with unsaturated “dangling” bonds on the tip results in instantaneous charge transfer onto semiconducting surfaces, and interaction with a strong electrostatic tip potential results in ionic polarization and relaxation. Roughly, the models correspond to the clean Si tip and Si tip covered with oxide.

It has been recognised that the tip apex can be contaminated by the surface material and that the structure of the tip apex can be modified before or during high resolution imaging<sup>51</sup>. Some experimentalists exploit this idea and intentionally immerse (“softly crash”) the tip into the surface to cover the tip apex with surface material<sup>52</sup>. In the case of a binary compound surface, adsorption of either element is possible on to the apex, which allows us to use the oxide tip model, but leads to a two-fold model, and often does not result in chemical resolution. The extension of this idea to an arbitrary heterogeneous system, including defective surfaces or adsorbed molecules, makes the interpretation complicated.

Meanwhile, systems that are more complex have been imaged already: self-assembled monolayers (SAMs) of thiols on gold, monolayers of unsaturated fatty acids on TiO<sub>2</sub>, large (1-2 nm) organic molecules and DNA bases on insulating and metallic surfaces. The lateral resolution within the adsorbed species is generally worse than on the clean surface, which is usually produced by a tip convolution effect. The variety of systems, however, implies the introduction of a variety of tip models.

The alternative direction is to collect a minimal toolkit of tip apexes, with known mechanisms of contrast formation for each of them. These tips would differ in their strength of adhesion, rigidity and reactivity on typical classes of surfaces, and sensitivity to the typical surface species. Such a toolkit would rely on the available experimental evidence and the conceptual theoretical proof.

The problems addressed in this work. This work was initiated within the Material Chemistry EPSRC project “Prohibition of corrosion on the alumina surface”, aiming to combine material science methods with NC-AFM measurements and theory in the study of the adsorption of fatty acids on the surfaces of natural aluminium oxide and model systems representing the natural aluminium oxide surface.

The project was inspired by the success of NC-AFM imaging surfaces of alkali halides,  $\text{CaF}_2(111)$  and  $\text{TiO}_2(110)$  and assumed implicitly that successful imaging with atomic resolution would be possible on other oxide surfaces. Therefore, initially, the mission of the theory was to interpret the atomic resolution images, produced experimentally on the model surfaces, and move soon afterwards to the interpretation of molecular NC-AFM imaging of fatty acids on alumina with high resolution. However, until very recently<sup>35</sup>, no new oxide surfaces have been resolved with atomic resolution although the majority of simple alkali halide surfaces have been imaged with “true atomic resolution” using NC-AFM<sup>50</sup>.

This distinctive difference between oxides and alkali halides is not yet understood, since many factors, such as the choice of the tip, surface preparation, tip treatment procedure and the tip-surface interaction affect the result. The experimentalists, however, are not able to distinguish whether absence of atomic resolution on the studied surfaces arises from problems in surface preparation or because it is fundamentally unachievable. Also, one cannot exclude the possibility that lower quality surface, i.e. a higher density of defects, may result in a different regime of tip-surface interactions at smaller distances and lead to a different tip model.

The difficulties faced by the experimentalists in imaging oxide surfaces with high resolution redefined the questions to be addressed by the theoretical analysis:

- 1) Do we lose the resolution because of the imperfection of the experiment or because it can not be obtained at all on the  $\alpha$ -alumina surface with an oxidized Si tip?
- 2) Is it possible to choose a tip (and/or) tip preparation procedure, which yields high contrast on ionic surfaces and requires only minimal theoretical analysis?
- 3) What are the mechanisms of contrast formation and the limits of resolution in the imaging of molecules on insulating surfaces?
- 4) Is chemical characterisation of adsorbed molecules possible with NC-AFM?
- 5) For individual molecules adsorbed on insulating surfaces, is it possible to observe molecules and surface sublattices simultaneously? Can they be used as the markers of surface defect sites and/or sublattices?

6) Introduction of the continuous layer of molecules effectively creates a new, typically very soft, surface, which differs in its properties from the oxide. A large number of degrees of freedom, including the possibility of lateral diffusion of the molecule, could be excited by the tip-surface interaction in the NC-AFM mode. The concepts of “strong” and “weak” tip-surface interaction and the perception of the “non-contact” regime could be different on these surfaces. Ultimately, what is the impact of the imaging process on the molecules, the surface and on the tip apex? Can we use AFM for molecular manipulation on an insulating surface?

7) In the interpretation of NC-AFM images of thin molecular monolayers the tip-substrate interaction may compete with the tip-molecule interaction. Therefore, it becomes essential to distinguish the contribution of the ionic surface to the image, from the contribution of the monolayer itself. This problem challenges the fundamental sensitivity of the method in the case of a screened object.

Objectives of the work can be summarized as the following:

1. Study the mechanisms of contrast formation on ionic surfaces, such as MgO(001) and Al<sub>2</sub>O<sub>3</sub>(0001), using models of the tip with an unsaturated/saturated chemical bond at the apex
  - a. Provide characterisation of the site-dependent interaction in the case where atomic resolution is possible;
  - b. Choose the tip apex model which enables “unambiguous” identification of the ionic sublattices on the basis of theoretical modelling of the tip-surface interaction;
  - c. Identify the factors adversely affecting atomic resolution on the  $\alpha$ -alumina surface.
2. Investigate the mechanisms of contrast formation in NC-AFM imaging of adsorbed molecular systems, such as HCOO<sup>-</sup> on MgO(001) and HCOOH on TiO<sub>2</sub>(110), and the effect of the system parameters on the apparent corrugation
  - a. Study the possibility of using the HCOO<sup>-</sup> ion as a marker of the sublattice on the MgO(001) surface;
  - b. Study mechanisms for physisorption and chemisorption of molecules on the TiO<sub>2</sub>(110) surface. Analyse contrast formation mechanisms for a complete thin monolayer on the ionic surface. Investigate the tip-monolayer



interaction and the effect of the macroscopic tip-surface interaction on the contrast formation.

3. Investigate the properties of potassium iodide(KI) - filled single-walled carbon nanotubes (SWNT) such as KI:SWNT(14,0) and KI:SWNT(10,10) and explore the opportunities of using AFM techniques to characterise such systems.

*The plan of the thesis.* Within this work, we have addressed the possibility of atomic resolution in NC-AFM images of alumina and the applicability of the Si tip model to dielectric surfaces. Mechanisms of contrast formation for adsorbed single molecules and molecular monolayers on ionic surfaces are addressed theoretically for the first time. In particular, the effect of the adsorbant on high resolution in the ionic substrate is investigated. A study of encapsulated 1D potassium iodide (KI) chains in a single-walled nanotube addresses the ultimate limit of a thin ionic chain coated by a carbon nanotube.

Two tip models are used intensively in this work: the rigid oxide tip model and the model of a Si tip with a dangling bond, although other models of a Si tip are considered. The range of systems investigated in this work includes clean oxide surfaces of MgO(001) and Al<sub>2</sub>O<sub>3</sub>(0001), charged formate ions on MgO(001) and an adsorbed monolayer of formic acid on TiO<sub>2</sub>(110). A feasibility study on single-walled carbon nanotubes filled with potassium iodide concludes the work reported in the thesis.

The text of the thesis is organized in five chapters, so that models, methods and miscellaneous calculations are presented in Chapter 1, while Chapters 2-5 present the original results obtained in this work, although they often refer to the data presented in Chapter 1.

**Chapter 1** illustrates the principles of operation of the D-AFM instrument and approaches to modelling NC-AFM images, describes the theoretical methods used in this work and explains the choice of parameters.

**Chapter 2** compares two tip apex models of a Si-based tip: the rigid oxide tip model and the Si dangling bond models, applied to the imaging of the wide bandgap ionic oxides MgO(001) and  $\alpha$ -Al<sub>2</sub>O<sub>3</sub>(0001). We discuss the possibility of atomic and chemical resolution on Al<sub>2</sub>O<sub>3</sub>(0001) and highlight the limitations observed with each of the models. The full NC-AFM imaging process is studied using the oxide tip model; the analysis and interpretation of the characteristic image profiles are presented for both signs of the tip potential. The conditions for chemical resolution and the limits of spatial

resolution are discussed. The analysis of *ab initio* force-distance curves, simulated using the dangling bond tip model, allows us to explain the basic mechanisms of contrast formation on insulating surfaces with a tip carrying a dangling bond at the apex.

**Chapter 3** continues the study of the MgO(001) surface with the oxide tip model. This chapter addresses the problems arising in NC-AFM imaging of an ideal insulating surface covered with a dilute monolayer of adsorbed molecules. The charged formate molecule ( $\text{HCOO}^-$ ) and a positively terminated oxide tip were chosen for this study. We address questions about the effect of the macroscopic tip-surface interaction on the contrast in the image and the possibility of using the molecule as a marker of one of the sublattices on the surface. The possibility of simultaneous imaging of the surface and molecules with high resolution is investigated. An image of the anion adsorbed on the MgO(001) surface is calculated using the oxide tip model; the mechanisms of contrast formation are analyzed taking into account the flexibility and mobility of the adsorbed molecule. This required an *ab initio* study of the systems using an Embedded Cluster Method (ECM) and developing interatomic potentials between atoms of the formate and the MgO(001) surface.

**Chapter 4** discusses the adsorption of weakly physisorbed and chemisorbed monolayers of methane and formic acid onto the  $\text{TiO}_2(110)$  surface. On the basis of the available experimental images, the formate monolayer is chosen as a starting point from which to simulate the full NC-AFM image using static *ab initio* calculations. The typical interactions responsible for contrast formation in NC-AFM image of a formate monolayer on  $\text{TiO}_2(110)$  are compared with an analogous study on an acetate monolayer. Finally, we discuss the way the  $\text{TiO}_2(110)$  substrate displays itself in the NC-AFM image and force-distance curves.

**Chapter 5** concludes the work with a feasibility study, which was prompted by experimental efforts to characterise single wall carbon nanotubes (SW-CNT) filled with ionic insulating material, specifically potassium iodide (KI). Similarly to the previous chapter, we study whether atomic order or defects of the ionic crystal can be detected in the presence of the carbon nanotube shielding. We analyse the electronic structure of the quasi-1D KI structures and the formation of divacancy defects. The effect of the KI-CNT interactions on the electronic structure of the combined system and its vibrational spectrum is investigated using *ab initio* methods. The possibility of detecting the filling and the defects in the filling of SW-CNT using NC-AFM techniques is discussed.

## 1 Theoretical framework of modelling NC-AFM

This chapter introduces the models and concepts used in this work. The first section of the chapter gives details of the NC-AFM setup and describes the key parameters of tips and substrates. It also illustrates the major experimental foundations utilised in the construction of the tip models. It describes in detail the procedure for deriving the NC-AFM image, as well as the approaches to its analysis. The methods used in the calculation of the electronic structure, geometry optimization and forcefield construction are outlined here. The electronic structure of the surfaces studied in this work is discussed.

The interpretation of NC-AFM images and mapping them to the surface structure has proved to be a complex problem, which led to the development of theoretical methods of interpreting NC-AFM images<sup>43</sup>. Previous works in this field have considered imaging of insulating and semiconducting surfaces with insulating and semiconducting tips respectively<sup>44,49</sup>. Ideal surfaces and defects have been considered<sup>53</sup> and the nature of the site-dependent forces acting on the tip in such systems has been analyzed. It has also been demonstrated that agreement between the theory and experiment can be obtained for clean insulating surfaces of alkali halides<sup>42</sup>. However, new models of NC-AFM imaging and interpretation need to be developed to cover a wider range of surfaces of interest. To interpret the NC-AFM image four models are considered: a model of the surface, a model of the AFM cantilever with a tip, a model of the tip-surface interaction and a model of the rest of the experimental instrument.

The model of the surface incorporates the structure of the ideal surface and models of the most common defects and surface structures, usually provided by other methods including scattering techniques, surface spectroscopy and theoretical calculations. The model of the cantilever includes the shape and composition of the cantilever together with possible compositions and the structures of the tip apex. Since the tip apex may undergo a preparation procedure, this procedure should be included into the model.

The model of the tip apex, in general, depends on the composition of the tip, its treatment in an ultra high vacuum (UHV) chamber and the surface with which it interacts. However, there is a lack of experimental information to validate the effect of these factors on a particular tip. Direct information about the tip apex is only available from the image, while indirect information is obtained from *ex situ* studies of materials similar to the tip. Very recently, efforts have been made to combine NC-AFM experiments with the time-of-flight technique (ToF)<sup>54</sup> allowing one to monitor the

composition of the tip apex after the experiment. This technique may give the crucial information about the few atoms on the apex of the tip, which is currently lacking in conventional experiments and prevents direct interpretation of the image. The nature of the tip apex and the way its properties are manifested in the image has only been addressed theoretically so far.

The model of the instrument comprises the behaviour of NC-AFM electronic equipment. Several such models have been developed recently<sup>55-58</sup> to describe appropriately the different regimes of FM-AFM and the effect of key parameters, like the gain parameter of the feedback loop or the scan speed.

## **1.1 Experimental NC-AFM setup and its model**

This work considers only “non-contact” regimes of imaging and therefore the description is limited to the frequency modulated acquisition mode of dynamic AFM (FM-AFM), which was used in the experiments discussed in the work. I will attempt to limit the discussion to the elements which are essential for qualitative interpretation of the NC-AFM experiments.

### **1.1.1 The principle of operation**

AFM is based around the sensitive measurement of the interaction between the surface and the apex of a sharp tip mounted onto the force sensor. The force sensor is usually a bar (cantilever) with dimensions  $20\mu\text{m} \times 200\mu\text{m} \times 5\mu\text{m}$  made of silicon (Si) or silicon nitride ( $\text{Si}_3\text{N}_4$ ) mounted onto a piezo element attached to a positioning system. The back side of the cantilever is reflective, which allows one to detect deflections of the cantilever using a laser beam and a photodiode (Figure 5).

The piezo element drives oscillations of the cantilever near its eigenfrequency. The oscillations are monitored by the current in the position sensitive photodiode monitoring the laser beam reflected off the cantilever. The amplitude of the excitation signal is regulated so as to maintain a constant amplitude. The frequency of the cantilever oscillations and its phase shift with respect to the excitation signal are monitored by the electronics.

The low amplitude oscillations of the cantilever can be described by a harmonic potential given the bending spring constant of the cantilever. Due to the shape of the cantilever the bending mode of the cantilever is the softest mode and it can be considered to be decoupled from other modes like torsion or lateral bending.

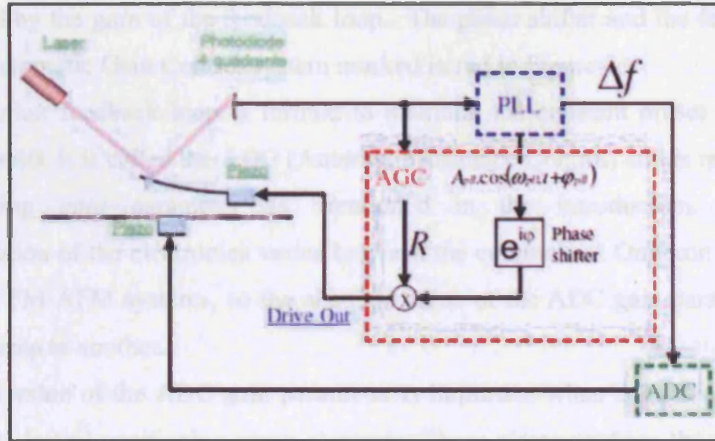


Figure 5. The block scheme of an NC-AFM instrument with a phase-locked loop (PLL). The adjustment of the tip-surface distance is made via automatic distance control (ADC). The oscillations are maintained by the automatic gain control.

As the tip of the cantilever approaches to the surface, the harmonic potential of the free cantilever is disturbed by the interaction with the surface. This perturbation shifts the eigenfrequency of the combined system “cantilever + surface”.

The electronics adjusts the frequency of the excitation signal so as to maintain the phase shift at a constant value near the resonance. The shift of the frequency from the eigenfrequency of the free cantilever is the measure of the perturbation potential and therefore the measure of the tip-surface interaction. This is the most common approach, although alternative approaches exist<sup>29,59</sup>

### 1.1.2 The electronics

The schematic representation of the electronics of a D-AFM operating in the FM-AFM regime is sketched in Figure 5. It shows how the lateral (x,y) positions of the oscillating cantilever and the z-position of surface are controlled by separate piezo elements. The detector reads the change in the position of the tip from the deflection of the laser beam.

The signal from the detector is processed by the phase-locked loop<sup>60</sup>, which outputs two values. The first is the difference between the preset (target) frequency of the cantilever and the currently measured value. This difference is commonly termed the “detuning”. The second output is the phase shift between the oscillations of the cantilever and the driving force. This value is automatically adjusted in the *phase shifter* (Figure 5) so to maintain the system near the resonance.

The filtered signal from the detector is also fed back into the cantilever piezo element in order to maintain a positive feedback loop. The proportion which is fed back

is regulated by the *gain* of the feedback loop. The phase shifter and the feedback loop form the Automatic Gain Control system marked in red in Figure 5.

Another feedback loop is formed to maintain the constant preset value of the frequency shift. It is called the ADC (Automatic Distance Control) and is regulated by a corresponding *gain* parameter as mentioned in the introduction. The actual implementation of the electronics varies between the commercial Omicron systems and home-built FM-AFM systems, so the absolute value of the ADC gain parameter varies from one setup to another.

The value of the ADC gain parameter is important when compared to the scan speed of the lateral positioning piezo elements. These elements drive the tip along the scanline with constant speed. Over the characteristic time necessary to adjust the z-position of the surface the tip travels a certain distance  $D$ . If, over that distance, the tip-surface interaction did not change faster than the feedback loop could track, the feedback loop maintains the preset (target) value of the frequency shift. As a result, the z-position of the surface changes accordingly with the change in the tip-surface interaction and produces a “topographic image” when mapped onto the displacements of the positioning system. This regime of imaging is called the Constant Frequency Shift (CFS) mode.

However, if the feedback loop is not able to track changes in the interaction at the atomic scale, the z-position does not adjust fully to the changes in the tip-surface interaction at this scale. Nevertheless it is still able to respond to the slow changes in the tip-surface interaction e.g. due to a slight tilt of the surface with respect of the plane of the scan, or to a significant change in the tip-surface interaction, like one due to a step. When scanning a plane terrace in this mode, the z-position of the surface is virtually constant, but the detuning signal carries the information about the change in the tip-surface interaction. This regime is called the Constant Height (CH) mode.

### 1.1.3 The model of the FM-AFM operation

Here we concentrate on a simplified mathematical description of the technique. The motion of the tip in the vicinity of the substrate can be approximately described by the equation for a harmonic oscillator driven by an external force  $F_{ext}(t)$  in the presence of a perturbing potential due to the tip-surface interaction  $F_{t-s}(z)$ .

$$m^* \ddot{z} + \alpha \dot{z} + kz - F_{t-s}(z) = F_{ext}(t) \quad (1)$$

where  $m^* = \omega_0^2/k$ ,  $k$  is the spring constant of the cantilever and  $\alpha$  is an empirical friction coefficient. In the Frequency Modulated (FM) operation mode, a further simplification

of the equation is made by introducing a positive feedback system which maintains the oscillation at a constant amplitude,  $A$ , and delays the phase of the excitation signal by approximately  $\pi/2$  with respect to the phase of the cantilever motion. This is achieved by tuning the frequency of the driving signal on the basis of the relationship between the quality factor  $Q$ , cantilever eigenfrequency and driving signal frequency  $f_{\text{ext}}$ .

$$\varphi = \arctan \left[ \frac{f_{\text{ext}}}{Q f_0 (1 - [f_{\text{ext}}/f_0]^2)} \right].$$

Such a phase shift formally cancels the dissipation term with the driving force in the equation above, so that the system can be described via the following Hamiltonian:

$$H = \frac{p^2}{2m^*} + \frac{1}{2} k z^2 + V_{t-s}(z) \quad (2)$$

where the expression for the period is the following:

$$T = \int_{z_{\min}}^{z_{\max}} \frac{2 dz}{\sqrt{\frac{2}{m} \left[ E - \left( \frac{1}{2} k z^2 + V_{t-s}(z) \right) \right]}}.$$

The tip-surface potential enters both into the expression under the integral and into the integral limit, so that overall it results in an increase in the period if the potential is attractive. At the turning points the expression under the square root equals zero and the function under the integral diverges. The integral, however is still well defined but its value is significantly affected by small variations in  $V_{t-s}(z)$  close to the turning point. This formula highlights the sensitivity of the oscillator to a small variation of the tip-surface potential.

The actual calculations in this work are performed in the frequency domain. In this approach the tip-surface interaction has an effect on the main frequency of the system. To the first order with respect to the tip-surface interaction, the frequency shift  $\Delta f(h)$  of the cantilever with an equilibrium tip height  $h$  above the surface is <sup>48</sup>:

$$\Delta f(h) = f(h) - f_0 = -\frac{1}{k A^2} \int_0^{1/f_0} F_{t-s}(z(t) + h) z(t) dt, \quad (3)$$

where  $z(t)$  is the trajectory of the tip apex given by  $z(t) = \sum_{m=0} a_m \cos(2\pi[mf_0]t)$ . The

amplitudes of the Fourier harmonics are calculated via the following expressions:

$$a_0(h) = \langle F_{ts} \rangle / k$$

$$a_m(h) = \frac{f_0}{k(1-m^2)} \int_0^{1/f_0} F_{t-s}(h + A \cos(2\pi[mf_0]t)) \cos(2\pi[mf_0]t) dt. \quad (4)$$

For the experiments with high lateral resolution described in the work, the typical values of the parameters are  $A = 10\text{-}100$  nm,  $k = 0.01\text{-}10$  N/m,  $f_0 = 10\text{-}1000$  kHz,  $Q = 10^4\text{-}10^5$ ,

$F_{t-s} < 10$  nN. Under these conditions the energy of oscillation exceeds the energy of the tip-surface interaction by at least 3 orders of the magnitude. As result, the observed change in the frequency is a small ( $10^{-3}$ - $10^{-4}$ ) fraction of the eigenfrequency. Given the typical sensitivity of an instrument in FM mode to changes of 0.1 Hz in the frequency and of 10 pm in height, such instrument can routinely detect forces of order 1.0 nN and detect differences of 0.1 nN at room temperature.

In the frequency modulation (FM) operation mode of NC-AFM, the lower limit on the frequency shift due to thermal noise<sup>61</sup> depends on the cantilever parameters: stiffness  $k$ , main cantilever frequency  $f_0$ , quality factor  $Q$ , and detection bandwidth  $B$ :

$$\frac{\delta(\Delta f)}{f_0} = \sqrt{\frac{k_B T B}{2\pi f_0 k Q \langle z_{osc}^2 \rangle}} = \sqrt{\frac{1}{\pi} \frac{B}{Q} \frac{k_B T}{f_0 k A_0^2}} \leq 10^{-6}.$$

Here  $\langle z_{osc}^2 \rangle$  is the mean-square amplitude of the driven cantilever vibration, and  $k_B T$  is the thermal energy at temperature  $T$ . The bandwidth  $B$  is a measure of the scanning speed. Operating at small  $B$  implies a low scanning speed and long acquisition times. The bandwidth approximately represents the number of recorded pixels per second. A conventional demodulator is able to measure a frequency shift of 0.01 Hz at a main frequency of 50 kHz with a 75 Hz bandwidth. Later, fully digital electronics based on the phase-locked loop principle<sup>45</sup> has been developed allowing resolution down to 5 mHz with a 500 Hz bandwidth. This development increases the sensitivity of the experiment and reduces the acquisition time.

The noise in the corrugation signal is determined by the slope of the frequency-distance curve and the frequency noise which drops as  $A^{-3/2}$  for larger amplitudes. Therefore, the minimal error in the corrugation signal as a function of the amplitude is

$$\delta z = \frac{1 + (A/\lambda)^{3/2}}{A},$$

where  $\lambda$  is the range of the tip-surface interaction<sup>62</sup> so the optimal conditions are fulfilled if the amplitude is of the order of  $\lambda$ .

Finally, it is important to mention basic criteria for stable imaging with respect to jump-to-contact and dissipation, i.e. that the spring should be stiff enough  $k * A > \max(F_{t-s})$  to overcome surface attraction near the turning point and the dissipation over cycle  $\Delta E_{t-s}$  should be negligible compared to the energy of the oscillation:  $\frac{kA^2}{2} \frac{2\eta}{Q} > \Delta E_{t-s}$ <sup>62</sup>.



#### 1.1.4 An illustration

Finally, I illustrate the above discussion by a study of the behaviour of the NC-AFM instrument in imaging a surface with two characteristic sites – A and B (Figure 6). Suppose that the force-distance curves above these sites are the extremes and all other force curves are in between those for A and B. We consider NC-AFM operation with high amplitude of the order of 10 nm or more and therefore the conversion from the force-distance curve to frequency-distance curve is virtually independent of the amplitude. The parameters of the setup are chosen so that the energy of oscillation is significantly larger than the potential of the tip-surface interaction. The spring constant exceeds the value of the second derivative of the attractive part of the tip-surface potential at all points, so that jump-to-contact is not considered. The force-distance curves are intentionally chosen so that both the positions and values of the minima in the two force-distance curves differ significantly.

First, consider the Constant Frequency Shift imaging mode (CFS mode) of the hypothetical surface (Figure 6) with sites A and B. Imagine that it is possible to acquire the frequency shift curves over those sites. If CFS imaging is performed with a value for the preset frequency shift (FS) of  $\Delta f_1$ , then the corrugation in the image is 1.5 Å and the site B is seen as a “bright” spot. The preset FS value is achieved over B at larger tip-surface separations than over A, therefore the B site is associated with a stronger tip-surface interaction. Although this imaging mode is often called “topographic mode”, the measured quantity is the tip-surface interaction and a conclusion about the height cannot be drawn on the basis of mere consideration of a single image.

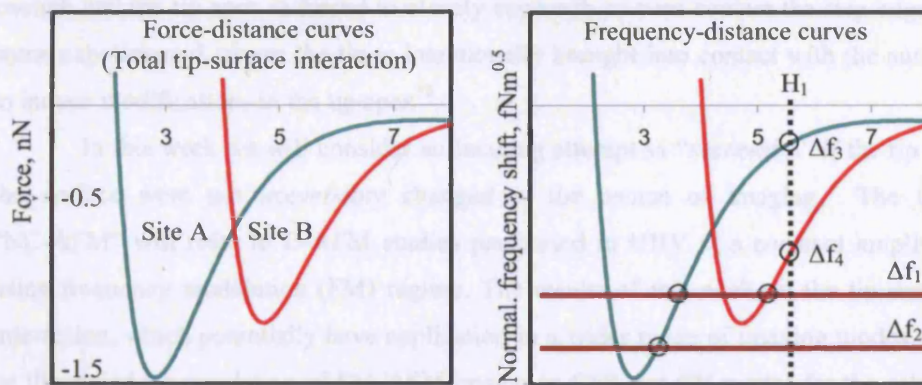


Figure 6. Hypothetical force- and frequency-distance curves for sites A and B. Negative values of the force correspond to the tip-surface attraction. The attraction is also manifested in the negative values of the frequency shift.

If the value of FS is less than  $\Delta f_1$ , the corrugation decreases, and eventually ceases, because the two frequency-distance curves coincide at about 8 Å (Figure 6). The atomic scale image is lost at small frequency shifts. They are typically used to observe larger areas of the surface.

If the absolute value of the FS is instead increased further to  $\Delta f_2$ , the ADC loop is able to find the appropriate z-position of the surface for the site A. For the site B, the loop may reach the position of the minima in the frequency-distance curve, but since the preset value is not achieved, the ADC continues approaching the surface to the tip, because a conventional ADC is not sensitive to the second derivative, but only to the difference between the preset and measured frequencies. As a result, the tip starts “hammering” the surface at the frequency of the oscillation i.e. in the order of 100,000 times per second. It is important that such behaviour from the ADC does not lead us to the conclusion that FM-AFM samples only the range of attractive tip-surface interactions – the forces acting on the apex of the tip might be repulsive, while the macroscopic interaction is strongly attractive.

Operation in the Constant Height mode is similar to the CFS, but the output information is different. In this mode the atomic scale image is formed by the variation in the frequency shift (“detuning”). The site B will be seen as “bright”, because it is associated with a more significant frequency shift.

This regime of imaging can also be dangerous to the tip, especially when scanning an extended area with topographic defects such as steps. If the scanning speed is fast, an ADC with a low gain cannot adjust the z-position of the surface quickly enough and the tip apex is forced to closely approach or even contact the step edge. In some experimental groups the tip is intentionally brought into contact with the surface to induce modifications in the tip apex<sup>52</sup>.

In this work we will consider an imaging attempt as “successful” if the tip and the surface were not irreversibly changed in the course of imaging. The term “NC-AFM” will refer to D-AFM studies performed in UHV at a constant amplitude using frequency modulation (FM) regime. The results of this work on the tip-surface interaction, which potentially have application in a wider range of imaging modes, will be illustrated by simulation of FM-AFM images in CFS and CH modes for the sake of consistency and comparison with experiment.

## 1.2 Modelling of the tip-surface interaction

The first stage of the NC-AFM image simulation is modelling of the tip-surface interaction. We consider the interaction at two scales: (1) macroscopic, based on a continuous model, and (2) microscopic, based on an atomistic model. The sum of micro and macroscopic contributions to the tip-surface interaction, calculated on a 3D mesh, comprises the tip-surface forcefield.

At this point it is essential to distinguish between interactions which are potentially site-dependent at the atomic scale and those which are site-independent by nature or by definition. “Macroscopic” interactions are essentially site-independent, since they are modelled in a continuous model, while microscopic interactions may have both site-independent and site-dependent components, and the latter eventually lead to the formation of contrast in the image at the atomic scale. The total tip-surface forcefield includes the following terms in general:

1. Chemical interaction and bond formation between atoms of the tip and surface;
2. Interaction due to Capacitance Forces (in the presence of a potential difference);
3. Interaction due to the electrostatic Image Force<sup>63</sup> (if  $\sigma_{\text{tip}}$  or  $\sigma_{\text{surf}} \neq 0$ );
4. Dispersion interaction between the tip and the surface.

In a particular application, some of the terms can be neglected due to the choice of contacting materials or because of the methods used to calculate the tip-surface forcefield. For instance, considering the atomistic problem with a pair potentials approach usually prohibits the description of bond formation. Another example is not considering the Image force when both contacting systems are insulators. To simplify the description further and reduce the number of parameters of the model, in this work we represent the cumulative effect of various tip-surface macroscopic interactions by a single term in the Van der Waals interaction as illustrated in Figure 8.

The tip is modelled as a semi-infinite object of conical shape with a rounded apex. The cone is described by an angle and the apex by its radius  $R$  (Figure 7). In this case, an analytical solution is available<sup>64</sup> for the Van der Waals force  $F(z, R)$  between the tip and a plane surface:

$$F_z(Z) = \frac{HR^2(1 - \sin\gamma)(R\sin\gamma - Z\sin\gamma - R - Z)}{6Z^2(z + R - R\sin\gamma)^2} + \frac{-H\tan\gamma[z\sin\gamma + R\sin\gamma + R\cos(2\gamma)]}{6\cos\gamma(Z + R - R\sin\gamma)^2}, \quad (5)$$



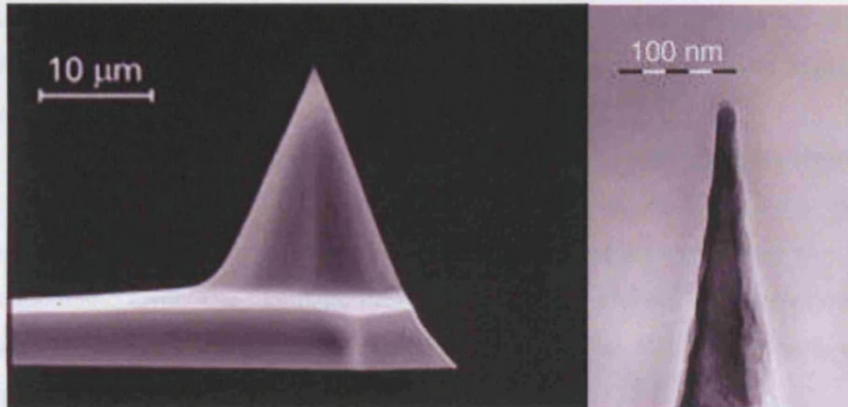


Figure 7. Scanning electron microscope image of a regular etched silicon tip. (left) large scale image of the cantilever with the tip. (right) SEM image of the tip apex illustrates that the tip radius of an as-produced tip apex is less than 10 nm.

where  $Z$  is the distance between the apex of macroscopic tip and the surface plane, and  $R$  is the radius of the tip. The dependence of the strength of the interaction on the materials of the tip and the surface is integrated in the Hamaker constant  $H$ . The value of the constant does not vary much among the ionic insulators and a typical value of  $H = 1.0 \text{ eV}$  is usually used.

To compare the results of the model with the experimentally measured macroscopic force in the vicinity of the surface, we change the interpretation of the tip radius  $R$ . In the absence of other macroscopic interactions in the model the radius does not only describe the shape of the tip apex, but is a measure of the macroscopic tip-surface interaction. The larger the radius is, the stronger the interaction is.

At a surface with a considerable density of charge, for instance, the strength of the macroscopic tip force acting on a  $R = 5 \text{ nm}$  tip may be approximated by the force acting on a tip with  $R = 500 \text{ nm}$  in the absence of defects at the same distance.

The functional form of the Van der Waals interaction, however, may not match the long range behaviour of the realistic macroscopic interaction. This difference essentially affects the precise values of simulated frequency shift, but is not considered important for analysing the contrast formation in this work, because:

- a) the contrast in the image is determined by the forcefield in the vicinity of the surface;
- b) the value of the frequency shift is much less sensitive to the values of the force away from the turning points of the tip;
- c) the experiment cannot provide parameters for a precise definition of the interaction.

Over short ranges (3-4 Å), where the site-dependent forces are distinguishable, the effect of the macroscopic interaction, can therefore be described by the magnitude and the slope of the macroscopic site-independent interaction.

The chemical interaction (1) is considered atomistically using *ab initio* methods or interatomic potentials. Consequently, the tip apex is modelled by a nanocluster (“nanotip”) in an atomistic simulation. The top layers of the surface are also treated at the atomistic level. The atomistic description does not include the interaction with the macroscopic parts of the system and the size of the atomistic region is chosen appropriately.

The size of the atomistic system has to be chosen appropriately to reproduce the change in the force as a function of the tip position rather than the absolute value of the force. Previous theoretical work<sup>48</sup> suggested considering  $1 \times 1 \times 1 \text{ nm}^3$  as the characteristic dimension of the nanocluster representing the tip apex and using about  $2 \times 2 \times 1 \text{ nm}^3$  to model the surface using the slab model with periodic boundary conditions (PBC). The bottom layers of the surface slab are kept fixed at the calculated bulk value, while top atoms of the “slab” are allowed to relax. The major concern in this case is the artefact due to the interactions between PBC images of the tip. This problem can be eliminated by using the finite cluster representation of the surface, when the atoms at the border of the cluster are fixed at the relaxed position obtained in the slab calculation. However, this imposes artificial boundary conditions and also requires a unit cell size of the order of  $2 \times 2 \times 1 \text{ nm}^3$ . The computational advantage of this technique is elimination of the time-consuming Ewald summation from the calculation.

The microscopic force acting on the nanotip is calculated for every position of the tip with respect to the surface at a range of tip-surface distances. The maximal distance is determined by the decay of the site-dependent tip-surface interactions in the system. The value of the force is obtained by summation of the normal component of forces over all fixed atoms of the nanotip after full relaxation of the system.

It is important to highlight for later reference the two variables which arise here. One is the actual distance between the apex atom of the tip and the surface level, which, at least currently, is not measurable. The other is the distance  $z_{t-s}^{\min}$  (Figure 8b) between the surface and the apex atom of the tip in its unrelaxed position. This variable cannot be measured either, but its variation is available directly from the piezo element regulating the height of the substrate.



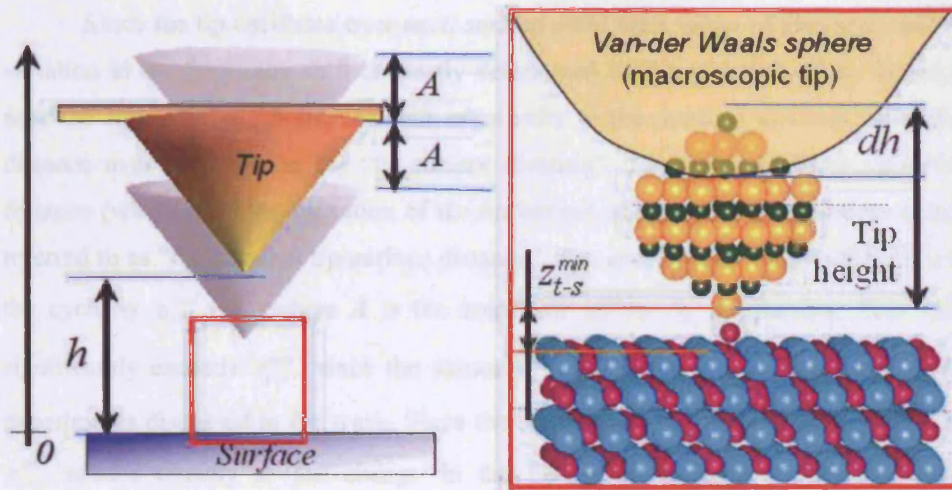


Figure 8. Atomistic model of tip-surface interaction consists of the “nanotip” cluster representing the apex of the tip and the model of the surface. Both the nanotip and the surface slab are split into two regions: with atomistic and continuous description<sup>31</sup>.

Although the frequency shift is mostly determined by the force acting on the tip at the turning point, the frequency shift is an integral over the whole range of the tip oscillations. The two simulation scales are put together in a following way:

- The surface of the atomistic model coincides with the surface of the continuous model for the substrate;
- The macroscopic tip only partially overlaps with the “nanotip”. The gap between the macro- and microscopic- approaches is required to prevent divergence of the VdW interaction at small distances and to reduce double counting;
- The “tip-surface distance” for large tip-surface separations, when the relaxations of the nanotip are negligible is defined as the height of the apex atom of the tip with respect to the surface level. (The surface level is usually defined as the height of an atom in the first layer of the substrate. The choice of the atom may depend on the system);
- For small tip-surface separations the tip-surface distance is defined as the height of the apex atom for the *unrelaxed position* of the tip with respect to the surface level. This is motivated by the fact that it is the relative position of the surface and the cantilever and not of the tip apex that is measured in an experiment.

These rules (a)-(d) allow calculation of the total forcefield by summing the micro- and macroscopic interactions with an appropriate shift which depends on :

- the overlap  $dh$  between the macroscopic tip and the “nanotip”
- the z-dimension of the tip at large tip-surface separations

Since the tip oscillates over each surface point for a range of distances, and the variation in the frequency shift is mostly determined by the variation of the forcefield near the lower turning point, we will often refer to the nominal minimal tip-surface distance over the cycle as the “tip-surface distance”. The actual minimal tip-surface distance (which includes relaxation of the tip but not of the surface) will be sometimes referred to as “the minimal tip-surface distance”. The *average* tip-surface distance over the cycle is  $z_{t-s}^{\min} + A$ , where  $A$  is the amplitude of the tip oscillations. This value significantly exceeds  $z_{t-s}^{\min}$ , since the values of  $A$  are in the range 5-100 nm for the experiments discussed in the work. Since the amplitude is kept constant, the change in  $z_{t-s}^{\min}$  relates directly to the change in the tip-surface separation measured in an experiment.

The total tip-surface forcefield produced in this way is converted into a frequency forcefield using the steady state solution for the driven oscillator in an anharmonic potential based on the equations (3-4) in section 1.1 above. Every point of the forcefield is characterised by the lateral position of the “nanotip” and the tip-surface distance  $x, y, z_{t-s}^{\min}$ .

The resulting frequency field  $f(x,y,z)$  can be processed to produce images for the two NC-AFM modes discussed in the work – constant frequency shift (CFS) and constant height (CH) images (section 1.1). They are obtained by taking a cross-section through the volumetric frequency field  $f(x,y,z)$  either at a constant value of the frequency  $f(x,y,z)=f_0-df$  or at constant height  $z'$ . The image is given by the *corrugation*  $z_{t-s}^{\min}(x,y)$  or *detuning*  $\Delta f_{image}(x,y)=f(x,y,z=z')-f_0$ .

Although other NC-AFM modes exist<sup>29</sup>, further discussion will be focused on the constant frequency shift (CFS) and constant height modes (CH), which are more conventional for imaging with atomic resolution<sup>39</sup>.

### 1.3 Theoretical methods of total energy/force calculation

#### 1.3.1 DFT (SIESTA)

The SIESTA package<sup>65</sup> was chosen for density functional theory (DFT) calculations of electronic structure and geometry relaxation. This implementation of the Linear Combination of Atomic Orbitals (LCAO) approach, is advantageous for sparse 3D systems, and allows traditional DFT calculations to be performed within the

LDA/GGA approximation using an efficient real space technique. It provides an opportunity to adjust speed/precision by varying the real space mesh, basis set or diagonalisation routine.

Using pseudopotentials in LCAO calculations is convenient for the expansion of pseudocharge density on a uniform real space grid. Pseudopotentials  $V_l(r)$  are generated for every value of the angular momentum  $l$ . The solution of the relativistic atomic problem<sup>66-68</sup> results in a relativistic pseudopotential. Normally the Troullier-Martin parameterisation<sup>69</sup> is used in the fully non-local form proposed by Kleinman and Bylander (KB)<sup>67</sup>. Since the local part  $V^{local}$  of the pseudopotential is arbitrary to an extent, the pseudopotential was optimized for smoothness by making it equal to potential created by the following charge distribution<sup>70</sup>

$$\rho^{local}(r) \propto \exp\left[-(\sinh(abr)/\sinh(b))^2\right].$$

Parameters  $a$  and  $b$  were selected by the potential generating program to achieve better convergence.

In this work we used basis sets built from Numerical Atomic Orbitals (NAOs). Each NAO is obtained from the solution of the Schrödinger equation for an atom given a cutoff radius for the wavefunction. Smooth extension of the potential beyond the cutoff radius is provided by an analytic potential. The number of NAOs per angular momentum channel may be varied, starting from 1 for a single- $\zeta$  basis set (cheap, qualitative calculations) to 3 for the triple- $\zeta$  basis set. This method of assigning basis functions correlates with the split valence methodology in Quantum Chemistry, where less contracted Gaussians are added to increase accuracy. To include excited atomic states into the basis set, the Schrödinger equation is solved for an atom in a weak electrical field, or with an additional fictitious charge on the core, which gives polarized basis orbitals. The details of NAO generation are extensively described in the literature<sup>71,72</sup>.

The total energy of valence electrons in the field of a periodic ionic lattice can be written in the following form:

$$\hat{H} = \hat{T} + \sum_l V_l^{local}(r) + \sum_l \hat{V}_l^{KB} + V^H(r) + V^{xc}(r).$$

Since pseudowavefunctions, generated for these pseudopotentials, are non-zero only for  $r < r_{cut}$ , the potential  $V_l^{atom}$  created by the atomic electron density  $\rho^{atom}(r)$ , which is produced by populating basis functions with valence electrons, would be zero for



$r > r_{\text{cut}}$ . The difference  $\delta\rho(r)$  between the self-consistent density  $\rho(r)$  and  $\rho^{\text{atom}}(r)$  would produce an electrostatic potential  $\delta V^H$ . Now the Hamiltonian can be rewritten in these terms

$$\hat{H} = \hat{T} + \sum_I \hat{V}_I^{KB} + \sum_I V_I^{NA}(r) + \delta V^H(r) + V^{xc}(r),$$

$$\text{where } V_I^{NA} = V_I^{\text{local}} + V_I^{\text{atom}}.$$

Here the first two terms involve only two-centre integrals, which are calculated in reciprocal space and tabulated for different interatomic distances. The remaining terms are calculated by integration on the real space grid.

Although the program was written for large systems assuming  $\Gamma$ -point calculations, the k-space integration is facilitated by the expansion of the unit cell into a larger auxiliary cell. Such an auxiliary cell consists of a number of image cells and the original unit cell. Image cells are obtained by an elementary translation  $\vec{R}_j$  of the original unit cell. An image cell is included in the auxiliary cell if there is at least one atom with a non-zero value of the basis functions inside the unit cell. Matrix elements are evaluated on the real space grid according to the following formula:

$$\langle \phi_\mu | V(r) | \phi_\nu \rangle = \sum_{(\vec{R}_i, \vec{R}_j \in \text{Aux.cell})} \langle \hat{T}(\vec{R}_i) \phi_\mu | V(r) f(r) | \hat{T}(\vec{R}_j) \phi_\nu \rangle,$$

$$\text{where } f(r) = \begin{cases} 1, & \text{inside unit cell,} \\ 0, & \text{outside unit cell.} \end{cases}$$

The operator  $\hat{T}(\vec{R}_i)$  is the translation operator along  $\vec{R}_i$ , which is a linear combination of translational vectors of the unit cell with integer coefficients. The summation is performed for all overlapping basis functions within the auxiliary cell. Every matrix element of the Hamiltonian,  $H_{\mu\nu}(k)$ , is expressed for a given k-point as a sum of matrix elements calculated in the auxiliary cell with the corresponding phase factor

$$H_{\mu\nu}(k) = \sum_{\nu \equiv \nu'} H_{\mu\nu'} e^{-ik(R_\mu - R_{\nu'})}.$$

Finally, the Kohn-Sham functional<sup>73</sup> takes the following form:

$$E^{KS} = \sum H_{mn} \rho_{nm} - \frac{1}{2} \int V^H(r) \rho(r) d^3r + \int (\epsilon^{xc}(r) - V^{xc}(r)) \rho(r) d^3r + \sum_{I < J} \frac{Z_I Z_J}{R_{IJ}},$$

where  $I, J$  are atomic indices,  $Z_I$  is the valence pseudoatom charge,  $\epsilon^{xc}(r)\rho(r)$  is the exchange-correlation energy density, and  $V^H(r)$  and  $V^{xc}(r)$  are the Hartree and

exchange-correlation functionals correspondingly. Further details of numerical realizations, benchmarks and examples of applications of this package can be found elsewhere<sup>65,72,74</sup>.

The method is often referred to as “*ab initio*”, but several degrees of freedom exist, such as the choice of the exchange functional, basis set and optimization method. These choices will be discussed in this section and referred to in following chapters.

In this work DFT is used within the Generalised Gradient Approximation (GGA) using the Perdew, Burke and Ernzerhof (PBE) functional for exchange-correlation. The Troullier-Martins pseudopotentials for the silicon, aluminium, oxygen, magnesium, carbon and titanium atoms are generated for the electronic configurations [Ne] 3s<sup>2</sup> 3p<sup>2</sup>, [Ne] 3s<sup>2</sup> 3p<sup>1</sup>, [1s<sup>2</sup>] 2s<sup>2</sup> 2p<sup>4</sup>, [Ne] 3s<sup>2</sup>, [1s<sup>2</sup>] 2s<sup>2</sup> 2p<sup>2</sup>, [Ne] 3s<sup>2</sup> 3p<sup>4</sup> 3d<sup>2</sup>, respectively. Square brackets denote the core electron configurations. The pseudopotentials are constructed on the basis of the solution for a free atom/ion using the PBE functional.

The basis set is formed from numerical atomic orbitals (NAOs) obtained by numerical solution of the Schrödinger equation. In most cases, the basis is chosen in the “double- $\xi$ ” form with polarization orbitals (Table 1). This results in 2 NAOs for each projection of the orbital momentum ( $m$ ), while the use of polarization NAOs adds a set of orbitals with symmetry characterised by an orbital number ( $l+1$ ).

Following previous studies of the TiO<sub>2</sub>(110) surface, atoms representing the deepest TiO<sub>2</sub> layer of the slab are described with “single- $\xi$ ” to reduce computational effort. The basis set includes s- and p-, or s- and d-orbitals for both O and Ti ions. In the case of alumina, a small additional positive or negative charge  $Q_{\text{gen}}$  is added to the charge of nucleus to obtain contracted or expanded orbitals<sup>75</sup>. The precision of the real space mesh is characterised by the energy cutoff of 150 Ry, which corresponds to a real mesh step of 0.16 Å.

Table 1. SIESTA basis sets used for calculations of substrate electronic structure.

<i>Parameters</i>	<i>TiO<sub>2</sub>(110)-HCOO</i>						<i>Al<sub>2</sub>O<sub>3</sub></i>		<i>MgO</i>	
	<i>H</i>	<i>C</i>	<i>O</i>	<i>Ti</i>	<i>O<sup>s</sup></i>	<i>Ti<sup>s</sup></i>	<i>Al</i>	<i>O</i>	<i>Mg</i>	<i>O</i>
<i>Basis functions per orbital (l)</i>	2	2	2	2	1	1	2	2	2	1
<i>Total number of basis functions (per atom per spin)</i>	5	10	10	12	4	6	10	10	12	6
<i>Energy Shift, E<sub>shift</sub>, meV</i>	20						300		15	
<i>Energy cutoff, E<sub>cutoff</sub>, Ry</i>	150						150		100	

### 1.3.2 Embedded Cluster Method (GUESS)

In this work formate ( $\text{HCOO}^-$ ) adsorption on  $\text{MgO}(001)$  is studied with the Embedded Cluster Method (ECM)<sup>76,77</sup> using *Gaussian 98*<sup>78</sup> as an engine for quantum mechanical *ab initio* calculations. This method is implemented in the GUESS computer code, developed in our group. It provides a quantum mechanical treatment of atoms surrounding a bulk or surface defect, while the rest of the system is represented using the shell model<sup>79</sup> and point ions.

Importantly, this method enables relaxation of both atoms treated quantum mechanically and classically, produces a consistent Madelung potential at the site of interest and accounts for both ionic and electronic contributions to the polarization of defect's environment. The method has proved to be effective for insulators with purely ionic and ion-covalent bonds<sup>76,80,81</sup> according to studies of the electronic structure of bulk and surface defects<sup>82</sup>.

In this work the embedded cluster approach is chosen to describe the adsorption of the charged ion on  $\text{MgO}(001)$  surface, because *Gaussian 98* provides<sup>78</sup> us with a choice of exchange-correlation functionals, while the cluster model avoids the problem of interaction between the periodically translated images of the charged molecule.

The surface is represented by a neutral  $\text{MgO}$  cluster of 3200 ions divided in two regions (518 ions in Region I and 2682 ions in Region II) (Figure 9). A quantum mechanical (QM) description is applied to 42 atoms of 518 atoms in the Region I. The remaining 476 atoms are described by the shell model using the formal charge. Positions of QM atoms, cores and shells in the Region I are optimized while ions in region II are fixed. The ions in Region II serve to create a proper Madelung potential in the Region I.

The shell model<sup>79</sup> is used to incorporate the polarizability of ions into the description. Within the shell model an ion is represented as the combination of a charged core and a shell linked by a spring. Charges on the cores and shells and the elasticity of the spring are chosen to reproduce properties of the bulk crystal. Interactions between ions are described by pair potential functions<sup>83</sup>.

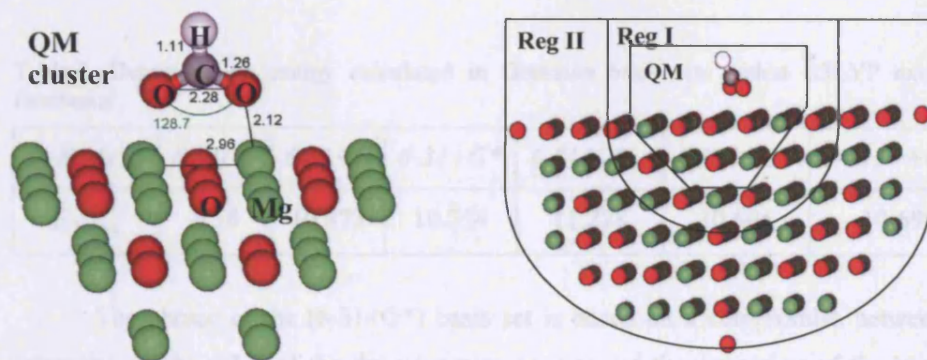


Figure 9. (left) quantum mechanical cluster used in the simulation with formate anion in the relaxed geometry. Bonds are specified in Å, angle in degrees; (right) Schematics of the embedded cluster method used in this work<sup>82</sup>.

The advantage of the method is the consistence of the force and relaxation calculations in the QM cluster and in the rest of Region I. The sizes of Region I and Region II are chosen so that the electrostatic potential in the region of the QM cluster does not deviate significantly ( $<6.10^{-3}$  V/nm) from the value calculated using periodic boundary conditions. The division of the region I into QM and non-QM parts is simplified by the high ionicity of MgO and the ionic character of the Mg-O bond, so that no covalent bonds are broken when Region I is split into classical and quantum subsystems.

The QM cluster is terminated with  $\text{Mg}^{2+}$  ions described with a pseudopotential and 2 Gaussian functions with large exponents ( $\alpha = 1000$ ). The choice of Mg as a terminating atom is advocated by the fact that  $\text{Mg}^{2+}$  has low polarizability and is better described by a bare pseudopotential. The details of the choice of the cluster and the atoms on the boundary of the QM cluster have been described in previous work conducted by our group<sup>22,82</sup>.

For the modelling of the adsorption of formate anion on MgO(001) the QM cluster included 29  $\text{Mg}^{2+}$  and 13  $\text{O}^{2-}$  ions with total charge of  $+32|e|$  (Figure 9) due to the unequal number of Mg and O atoms included. All electrons were taken into consideration due to the relatively small size of the ions.

To test the convergence with respect to the basis set, the deprotonation energy of the formic acid was calculated using the B3LYP exchange-correlation functional.

Table 2. Deprotonation energy calculated in Gaussian basis sets within B3LYP exchange functional

<i>Basis</i>	<i>6-31G</i>	<i>6-31+G</i>	<i>6-31+G*</i>	<i>6-311G*</i>	<i>6-311+G*</i>	<i>6-311++G*</i>
$E_{\text{deprot}}$	4.58	10.873	10.754	11.228	10.696	10.696

The choice of the (6-31+G\*) basis set is based on a compromise between the saturation of the value of the deprotonation energy and the expansion of the basis set (Table 2). The detailed study of excitations in the bulk and on the (001) surface of MgO by Peter Sushko<sup>77</sup> and later investigations using this method<sup>82</sup> have demonstrated that ECM method gives an adequate description of the electronic structure of the system.

In this study we have also compared the electronic structure of the clean MgO(001) surface as it is reproduced by the ECM and GGA calculations with periodic boundary calculations. Figure 10 shows the superposition of the partial density of states (PDOS) of the MgO(surface) obtained in GGA calculations and DOS for the ECM calculation. The eigenvalues used to build the ECM DOS are also shown on the graph. Analysis of the eigenfunctions confirms that the states at the top of the valence band are primarily localised on O atoms while states at the bottom of the conduction band are associated with Mg atoms. The graph shows that the bandgap is underestimated in GGA by 3.0 eV, while the ECM predicts 6.0 eV bandgap, which agrees qualitatively with EELS<sup>84,85</sup> and MIES<sup>86</sup> experiments on MgO(001) surface yielding the energy of the surface exciton as about 6.2-6.7 eV.

The Mulliken analysis was performed in both calculations. The SIESTA DFT calculations resulted in Mulliken charges of +0.4 |e|, -0.4 |e| on Mg and O ions correspondingly. For ECM Mulliken analysis gave the following atomic charges on the central Mg and O: +1.48 |e|, -1.3 |e| in the second layer and +0.8 |e|, -1.0 |e| in the first layer. However, the natural population analysis within ECM gives -1.67 |e| and +1.63 |e| for O and Mg in the first layer of the perfect MgO surface, which indicates that Mulliken charge is just not the optimal measure of the charge on the ion. However, we were bound to use it in SIESTA since no other charge analysis method was available in this code.



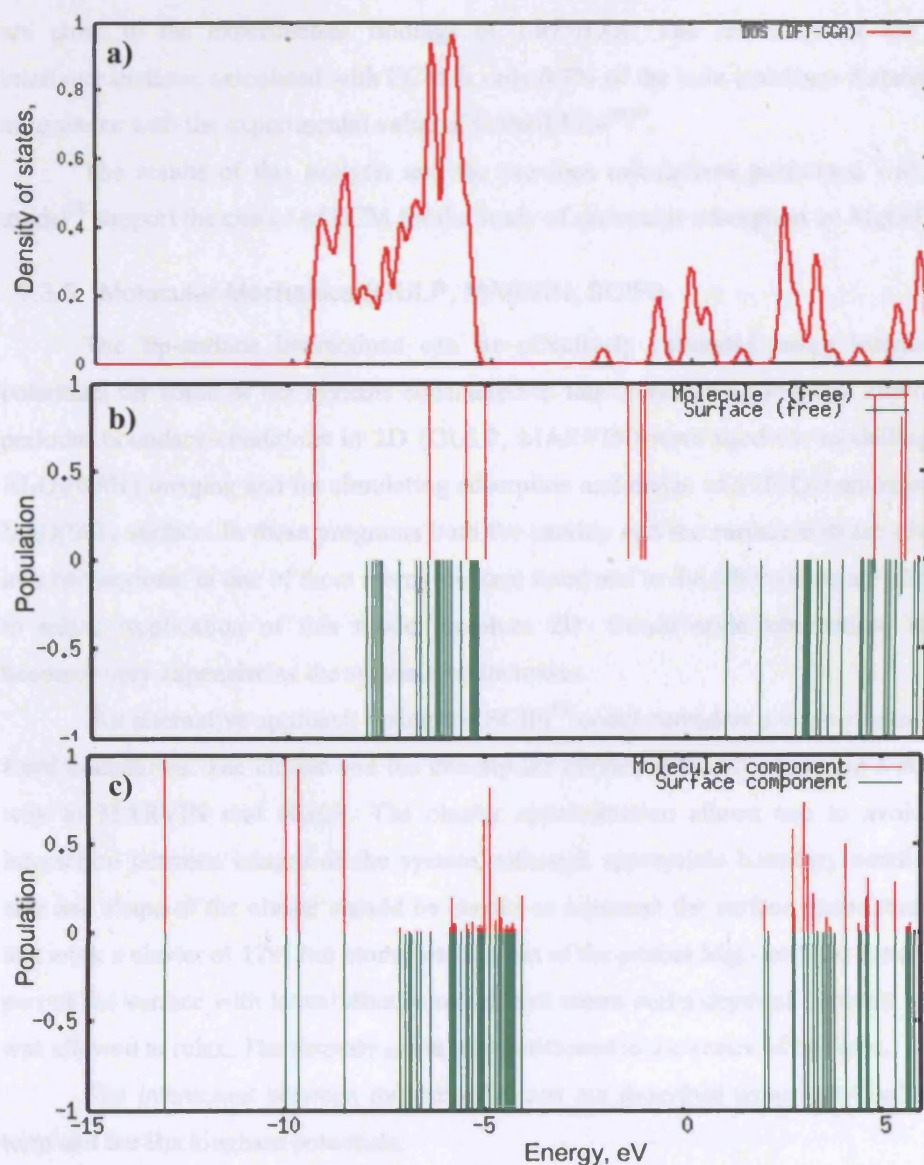


Figure 10. The density of states (DOS) of MgO(001) with a formate molecule using different exchange functionals. a) pure MgO(001) – DFT-GGA result (SIESTA); b) free QM cluster and free molecule (spectrum of eigenvalues). c) QM cluster with the adsorbed molecule in the equilibrium configuration (spectrum of eigenvalues). The different colours of eigenspectra demonstrate the nature of the state (red – molecule; green-substrate). Red lines in the eigenspectra indicate the percentage of the sum of squared coefficients of a state attributed to basis functions centred on the atoms of the molecule.

The optimized atomic positions of the clean surface were compared with available experimental and theoretical data<sup>87,88</sup>. In this calculation the relative displacement of Mg and O ions in the z-direction, termed “rumpling”, is 1.2% of the interlayer distance; SIESTA, for comparison gave a close value of 1.6%. Both numbers are close to the experimental findings of  $1.07 \pm 0.5\%$ . The relaxation of the first interlayer distance calculated with ECM is only 0.7% of the bulk interlayer distance, in accordance with the experimental value of  $0.56 \pm 0.35\%$ <sup>89,90</sup>.

The results of this analysis and the previous calculations performed with this model<sup>88</sup> support the choice of ECM for the study of molecular adsorption on MgO(001).

### 1.3.3 Molecular Mechanics (GULP, MARVIN, SCIFI)

The tip-surface interactions can be effectively estimated using interatomic potentials for some of the systems considered in this work. Two programs exploiting periodic boundary conditions in 2D (GULP, MARVIN) were used for modelling the Al<sub>2</sub>O<sub>3</sub>(0001) imaging and for simulating adsorption and image of a HCOO anion on the MgO(001) surface. In these programs both the nanotip and the surface slab are divided into two regions: in one of them atoms are kept fixed and in the other atoms are allowed to relax. Application of this model involves 2D ‘Ewald’-style summation, which becomes very expensive as the system size increases.

An alternative approach (using the SCIFI<sup>91</sup> code) considers a large cluster with fixed boundaries. The cluster and the nanotip are divided into two regions in a similar way to MARVIN and GULP. The cluster approximation allows one to avoid the interaction between images of the system, although appropriate boundary conditions, size and shape of the cluster should be chosen to represent the surface under study. In this work a cluster of 12x12x6 atoms was cut out of the perfect MgO surface; the central part of the surface with lateral dimensions of 8x8 atoms and a depth of 3 atomic layers was allowed to relax. The formate anion was positioned in the centre of this area.

The interaction between monoatomic ions are described using the Coulombic term and the Buckingham potentials:

$$V(r) = Z_1 Z_2 / r + A \exp(-r/B) - C/r^6, \quad (6)$$

where  $r$  is the interatomic distance,  $Z$  is the charge of the ion and  $A$ ,  $B$ ,  $C$  are the empirical parameters of the potential.

To account for the polarizability of anions, a shell-core model was applied. This model describes an atom by two point charges bound via a soft spring. For a free atom

Table 3. Comparison of surface relaxation in the  $\alpha$ -alumina surface, obtained from GIXD experiment, DFT calculations and pair potentials static relaxation.

<i>Interlayer distance</i>	<i>DFT-GGA, Å<sup>92</sup></i>	<i>DFT-GGA, Å (this work)</i>	<i>Interatomic potentials, Å</i>	<i>Exp. data, Å<sup>93</sup></i>
Al1-O1	0.12	0.14	0.17	0.413
O1-Al2	0.88	0.91	0.81	0.974
Al2-Al3	0.35	0.27	0.43	0.346
Al3-O2	0.98	1.02	0.89	1.007
O2-Al4	0.89	0.88	0.8	

the positions of charges coincide, but they split if an external electrostatic potential “polarises” the system. The parameters for the Buckingham interaction, partial charges and spring constants for the shell-core model were taken from Ref.<sup>48,94,95</sup>.

The formate anion is described by two forcefields: the internal degrees of freedom are described by parameters of the CHARMM forcefield<sup>96</sup>, while the interaction of the molecule with the surface is given in the form of the Buckingham potential. The parameters of the latter are fitted to reproduce the *ab initio* energy-distance dependence for the formate molecule approaching the MgO(001) surface. The fitting procedure was performed using the MERLIN<sup>97</sup> software package.

The choice of interatomic potentials is crucial to avoid misinterpretation of the results. The potential parameters chosen for modelling AFM images should reproduce the correct structure and relaxation of the surface.

In the case of the Al<sub>2</sub>O<sub>3</sub>(0001) surface, most of the available pair potentials are able to reproduce the bulk structure. However they were fitted for highly coordinated Al sites, while the coordination is reduced for surface Al ions. As a result, some of them are not able to reproduce the relaxation of the surface structure. Therefore, a set of potentials able to describe Al ions in both octahedral and tetrahedral coordination was used<sup>95</sup>. These potential parameters were originally fitted to reproduce both spinel and corundum structures and are able to reproduce surface relaxation at least qualitatively.

The results of the relaxation of the  $\alpha$ -Al<sub>2</sub>O<sub>3</sub> (0001) surface using the chosen pair potentials are compared in Table 3 with the grazing incident X-ray diffraction (GIXD) data and theoretical calculations. According to the experimental data the Al<sub>2</sub>O<sub>3</sub>(0001) surface is Al-terminated (Figure 11). The strong relaxation at the surface



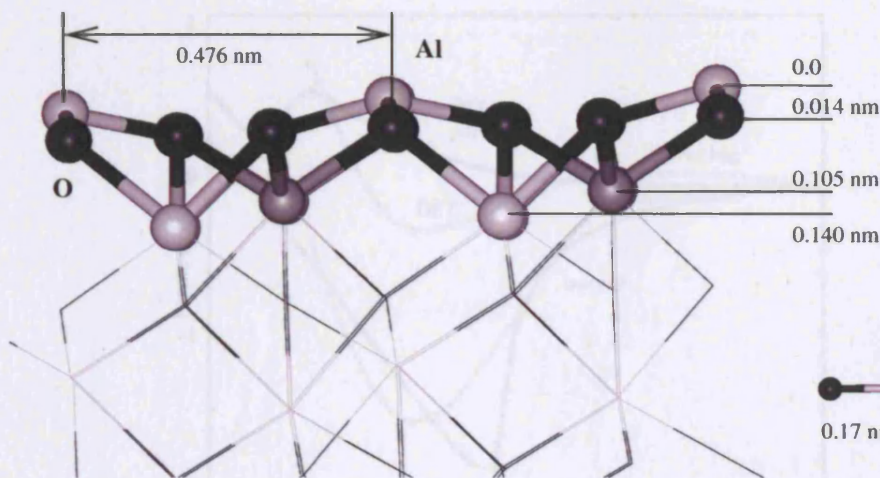


Figure 11. *left*: side view of the atomic structure of the  $\text{Al}_2\text{O}_3(0001)$  surface, Al atoms are grey, O atoms are black. Lattice period and depth of first 4 atomic layers are indicated; *right*: coordination of Al ions in the top layer. The projection of the Al-O distance on the surface plane is 0.17 nm.

pushes Al atoms almost into the O layer. The experimental distance between the Al layer(0001) and the nearest O layer in the bulk of  $\text{Al}_2\text{O}_3$  is 0.80 Å. On the surface the aluminium atom relaxes towards the bulk by a significant fraction of the bulk interlayer distance  $(\text{Al-O})_{\text{bulk}}$ . The relaxation estimated in GIXD experiments reduces the distance between first Al layer and first O layer of the surface (Al1-O1) to 0.413 Å, which is 48% of the bulk value. *Ab initio* DFT calculations predict relaxations of the order of 78-82% of the bulk distance. The result depends strongly on the chosen exchange-correlation potential<sup>98</sup>. The relaxation of the first interlayer distance calculated using the pair potentials<sup>95</sup> is 79% which corresponds to an interplane distance (Al-O) of 0.17 Å. This is in fair agreement with the result of our *ab-initio* calculations (Table 3) performed using DFT-GGA and SIESTA code and similar calculations with a plane wave basis set<sup>92</sup>. The discrepancy between the experimental data and the results of static theoretical calculation is ascribed to a soft vibrational mode on the surface leading to high amplitude anharmonic vibrations of Al atoms in the surface layer<sup>99,100</sup>.

For MgO, the interatomic potentials are available from previous work<sup>48</sup>. The validity of these potentials for modelling NC-AFM images is tested by comparing the force acting on the 64-atom MgO cluster in the vicinity of a MgO(001) surface calculated using DFT and the pair potentials calculations. Figure 12, which will be discussed in more details in chapter 2, demonstrates that pair potentials give only a qualitative description of the tip-surface interaction.

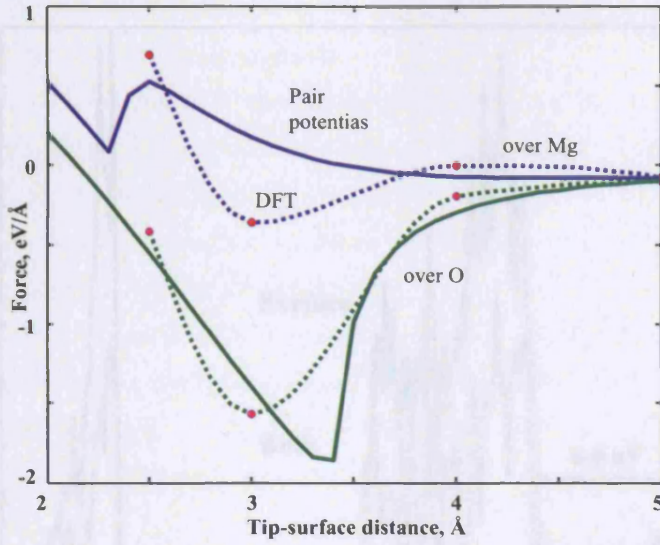


Figure 12. Comparison of the force acting on the 64-atom Mg-terminated MgO tip over magnesium and oxygen surface sites of MgO(001) surface calculated from *ab initio* (red data points) and in pair potentials (solid line). The dotted line connecting *ab initio* data points is just a guideline. A major discrepancy in the description of the tip-surface interaction is observed over Mg site.

#### 1.4 Electronic Structure of Substrates

In this section I summarise the results of electronic structure calculations for substrates which are discussed in subsequent chapters. The calculations were performed with SIESTA using periodic boundary conditions with a periodic slab model for the surfaces. The basis sets used in these calculations are listed in Table 1. The atomic positions in the bottom layers of the slab are fixed at the bulk positions, unless stated otherwise.

##### 1.4.1 Aluminium oxide $\text{Al}_2\text{O}_3$

Bulk calculations are performed with the crystal structure and primitive cell of  $\alpha$ -alumina taken from Wyckoff<sup>101</sup>. The geometry optimisations with a  $4 \times 4 \times 4$  Monkhorst-Pack grid and a 10-atom unit cell reproduces the lattice parameter ( $a=b=c=5.13$  Å) with less than 1% error. Mulliken<sup>102</sup> charge analysis gives  $+1.92|e|$  on aluminium and  $-0.8|e|$  on the oxygen. The calculated value of bandgap (6.0 eV) is only 60 % of the experimental value (10 eV) in accordance with previous results for DFT-GGA calculations<sup>103</sup>. The Bulk density of states (DOS) is presented in the Figure 13.



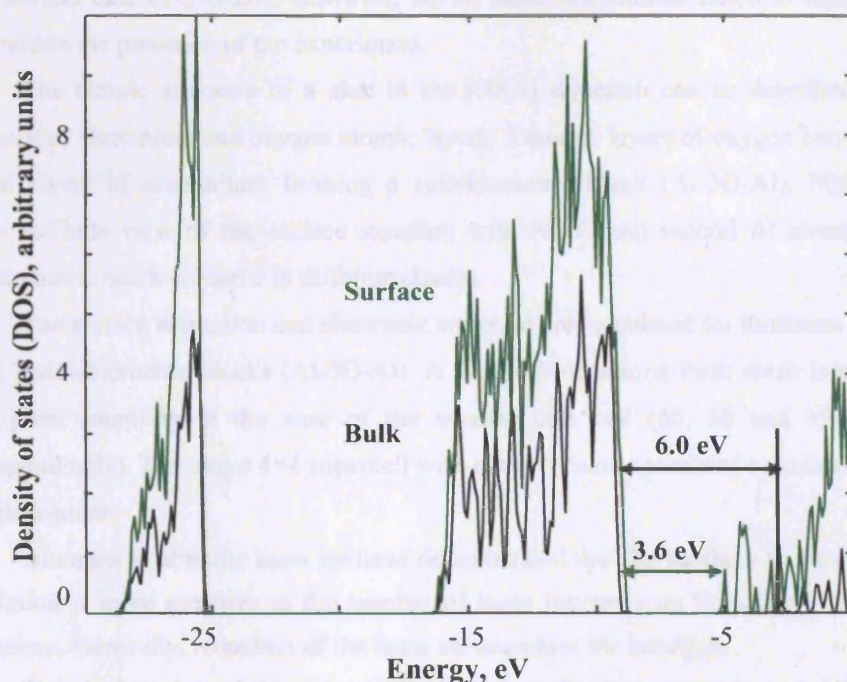


Figure 13. Calculated density of electronic states for bulk and (0001) surface of  $\alpha$ -Al<sub>2</sub>O<sub>3</sub>. Surface spectrum is shifted to match the position of lower valence band.

For surface calculations, there is a trade-off between qualitative reproduction of the properties of the system and the slab thickness. Calculation of the tip-surface interaction with periodic boundary conditions requires large supercell to avoid the strong interaction between the tip and its copy in the next supercell. An extension (4x4) of the primitive surface cell of the (0001) surface is used to minimize the interactions between periodic images of the tip.

Several slab models are tested to ensure that the electronic structure of the slab does not change drastically on the reduction of the slab thickness. It was shown for MgO(001) surface<sup>104,105</sup> that a slab with 3 layers is sufficient to reproduce the surface electronic structure qualitatively.

To model the (0001) surface of alumina the conventional Al-termination<sup>93</sup> was employed. A significant relaxation of the top Al atom was predicted theoretically<sup>103,106</sup> and observed experimentally<sup>93,100,107</sup>. DFT-GGA result tends to overestimate the relaxation, while the Hatree-Fock calculation underestimates it. Calculations with a mixed exchange-correlation functional<sup>103</sup> were also attempted in order to reproduce the

experimental data of SXRD<sup>93</sup>. However, all *ab initio* calculations failed to reproduce them within the precision of the experiment.

The atomic structure of a slab in the [0001] direction can be described as a sequence of aluminium and oxygen atomic layers: 3 atomic layers of oxygen between 2 atomic layers of aluminium, forming a stoichiometric block (Al-3O-Al). Figure 11 shows the side view of the surface structure with Al, O and second Al atoms of a stoichiometric block coloured in different shades.

The surface relaxation and electronic structure are calculated for thickness of 12, 6 and 3 stoichiometric blocks (Al-3O-Al). A  $7 \times 7 \times 1$  Monkhorst-Pack mesh is chosen for k-point sampling in the case of the smaller unit cell (60, 30 and 15 atoms correspondingly). The larger  $4 \times 4$  supercell with extra vacuum space was calculated with a single k-point.

Attempts to alter the basis set have demonstrated that the bandgap in the surface calculation is more sensitive to the number of basis functions on the oxygen than on aluminium. Generally, reduction of the basis set decreases the bandgap.

The thicker slab of 60 atoms (12 blocks) qualitatively reproduces width and shape of the valence band although the bandgap (3.6 eV) is significantly lower than experimental values 7.8 - 8.5 eV for a thin film<sup>108</sup> since the GGA-PBE functional is used. Charges are  $1.8-2.1 |e|$  and  $(-1.23)-(-1.26) |e|$  on the Al and O “bulk” atoms correspondingly. The topmost Al atoms and Al atoms of second Al layer tend to decrease ionicity by  $0.2 |e|$ .

In the calculation described above, all atomic positions are relaxed so one of the slab’s surfaces cancels the dipole moment of its counterpart. To economise on the computation time, half (6-block) and quarter (3-block) slabs are cut off from the 12-block slab and all the atoms positions were fixed at the positions found in relaxation of 12-block slab except for the atoms in the first stoichiometric layer. The 3-block system was later used to represent (0001) surface in the calculations of the tip-surface calculations.

#### 1.4.2 Magnesium oxide MgO(001)

The electronic structure of the magnesium oxide was first studied with SIESTA to test the basis and analyse the band structure. The band gap was reduced from the experimental value of 10.0 eV to 6.0 eV, which compares well with the previous plane wave calculations<sup>105</sup>. The reduction is attributed to the lack of exchange in the PBE-DFT description of the inhomogeneous electron gas. The three-layer slab is used in simulation of the electronic structure of the surface in accordance with the previous

work<sup>105</sup>. The bandgap is further reduced in two dimensions to 3.6 eV and the system remains highly ionic.

The partial density of states (PDOS) in Figure 14 details oxygen and magnesium states in the total DOS, which is plotted with a blue dashed line. It also illustrates the overlap between the electronic structure of Si tip and the MgO(001) surface. The discrete spectrum of the Si cluster is distinctively displayed between the MgO bands. The top of the valence band resides at -6.2 eV, which is about 1 eV below position of the top of the valence band in bulk Si (-4.8 eV) as calculated with SIESTA. In the combined system, the HOMO of the tip shifts towards the MgO valence band even at a significant separation of 10 Å.

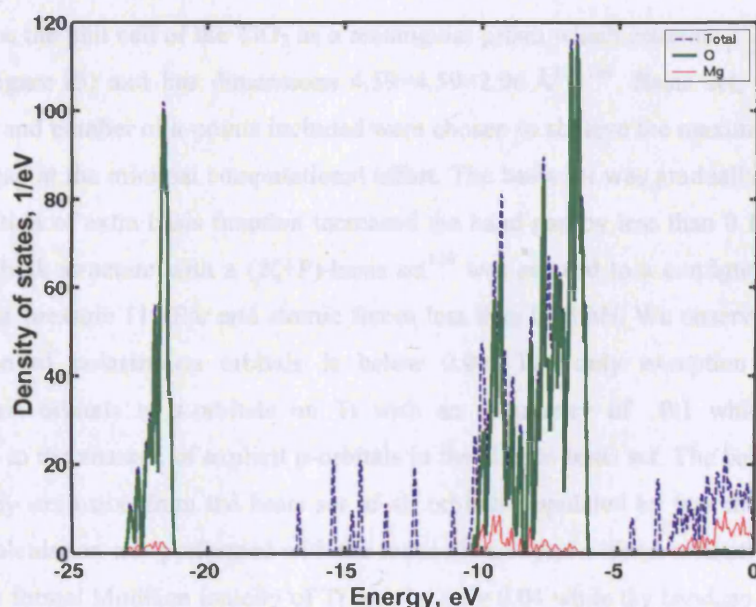


Figure 14. Partial density of states (PDOS) in the MgO-Si system. Si tip is 10 Å from the surface. Red and green lines are Mg, O states respectively, dashed blue lines correspond to the total DOS. Bandgap in MgO states is 3.6 eV.

### 1.4.3 Titanium dioxide TiO<sub>2</sub>(110)

In this section we assess the quality to which SIESTA is able to characterize a titanium oxide surface. For this purpose we calculate the electronic structure and geometry of bulk rutile (TiO<sub>2</sub>) and the (110) surface. The results are compared with available experimental data and other *ab initio* calculations. The choice of basis sets, electronic configuration of pseudopotentials and size of the unit cell is discussed.



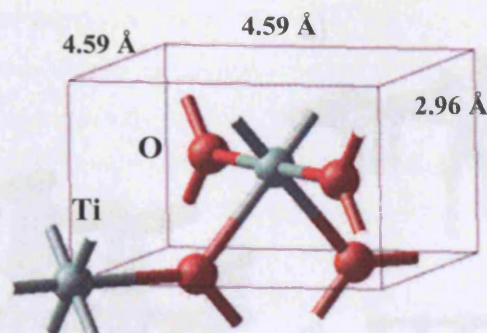


Figure 15. Unit cell of titanium dioxide  $\text{TiO}_2$  bulk<sup>101</sup>. Red spheres represent oxygen atoms, light green – titanium.

We choose the unit cell of the  $\text{TiO}_2$  as a rectangular prism which contains 2 Ti and 4 O atoms (Figure 15) and has dimensions  $4.59 \times 4.59 \times 2.96 \text{ \AA}$ <sup>101,109</sup>. Basis set, mesh grid (Table 1) and number of k-points included were chosen to achieve the maximal value of the bandgap at the minimal computational effort. The basis set was gradually increased until addition of extra basis function increased the band gap by less than 0.1 eV. First, the  $\text{TiO}_2$  bulk structure with a  $(2\zeta+\text{P})$ -basis set<sup>110</sup> was relaxed to a configuration with hydrostatic pressure 11 kBar and atomic forces less than 0.08 nN. We observed that the occupation of polarization orbitals is below 0.01. The only exception were the polarization orbitals of s-orbitals on Ti with an occupancy of 0.1 which can be attributed to the absence of explicit p-orbitals in the chosen basis set. The basis set was reduced by exclusion from the basis set of all orbitals populated by less than 0.01. A  $\Gamma$ -point calculation was performed with the reduced basis and without relaxation. As the result, the formal Mulliken ionicity of Ti rose by only 0.04 while the bandgap (1.34 eV) didn't change more than by 0.02 eV. The hydrostatic pressure in the unit cell, however, changed from -11.6 kBar to +12.8 kBar. A noticeable change was obtained in the population of the basis functions obtained when all polarization orbitals are removed from the basis set, but this can also be viewed as reassignment of the density between basis functions rather than charge redistribution since the bandgap did not shrink (1.30 eV). Further contraction of the oxygen basis set results in a reduction of the bandgap to (1.12 eV). The parameters of the optimal basis set for  $\text{TiO}_2$  are presented in Table 1.





#### 1.4.3.1 Oxygen vacancies in TiO<sub>2</sub>(110)

We consider here the electronic structure of the oxygen vacancies because it is one of the systems which we were going to include in the work as a realistic model of the TiO<sub>2</sub>(110) surface. The study presented here convinced us that we may not be able to provide any decisive answers about the system by the means of methods we use (section 1.3) and within the time of the PhD project. The results of the consideration may be however of use for others interested in the question.

The most frequent defect on the TiO<sub>2</sub> surface is the oxygen vacancy in the oxygen bridging row (Figure 16c) studied by SPMs as well as by conventional spectroscopies and theoretical analysis<sup>115</sup>. There are convincing models of what the vacancy may look like but no experimental proof yet. A charged vacancy with one electron ( $F^+$ ), which was also observed in titania, is associated with a 1.53 eV band in near-infrared photoluminescence<sup>116,117</sup> and a feature about 1.0 eV from the Fermi level in photoemission spectroscopy<sup>118</sup>. The semiconducting properties of TiO<sub>2</sub>(110), according to the available data, suggest the formation of an “empty” vacancy ( $F^{2+}$ ) with electrons hopped onto Ti ions. The reduction of the Ti ion is also often associated with enhanced catalytic activity of the defective surface. There is also a nontrivial proposal to explain this enhancement by a hydrogen atom/ion being captured into the O vacancy in the oxygen bridge. The bond formed in this process is claimed to have a Ti-H flavour<sup>119</sup> although the question is still under discussion. Remarkably, STM observes defects of two types and one of them cannot be removed from the surface by a 20 eV electron beam, which exceeds 14 eV, the energy necessary to break an O-H bond.

There is no full model about defects on the surface, but neutral oxygen vacancies are conventionally associated with dominating active centres on terraces. Moreover, the TiO<sub>2</sub> samples used in STM are always slightly non-stoichiometric to make them conducting and other experiments are also using oxygen-deficient samples. This fact brings into consideration the effect of bulk and subsurface vacancies on the catalytic and transport properties<sup>115</sup>. In this work several single vacancy models were considered (Figure 17, Figure 18). The same slab model was used as for clean surface calculations, however a deeper models with up to 5 Ti layers were constructed and compared to the conventional model with 3 Ti layers.

It is also known that the electronic structure of the defect and the degree of its localization may depend strongly on the exchange-correlation functional used. The result of our study is compared to available results from the literature to estimate the predictive power of the method with respect to systems with a F-center on TiO<sub>2</sub>(110).



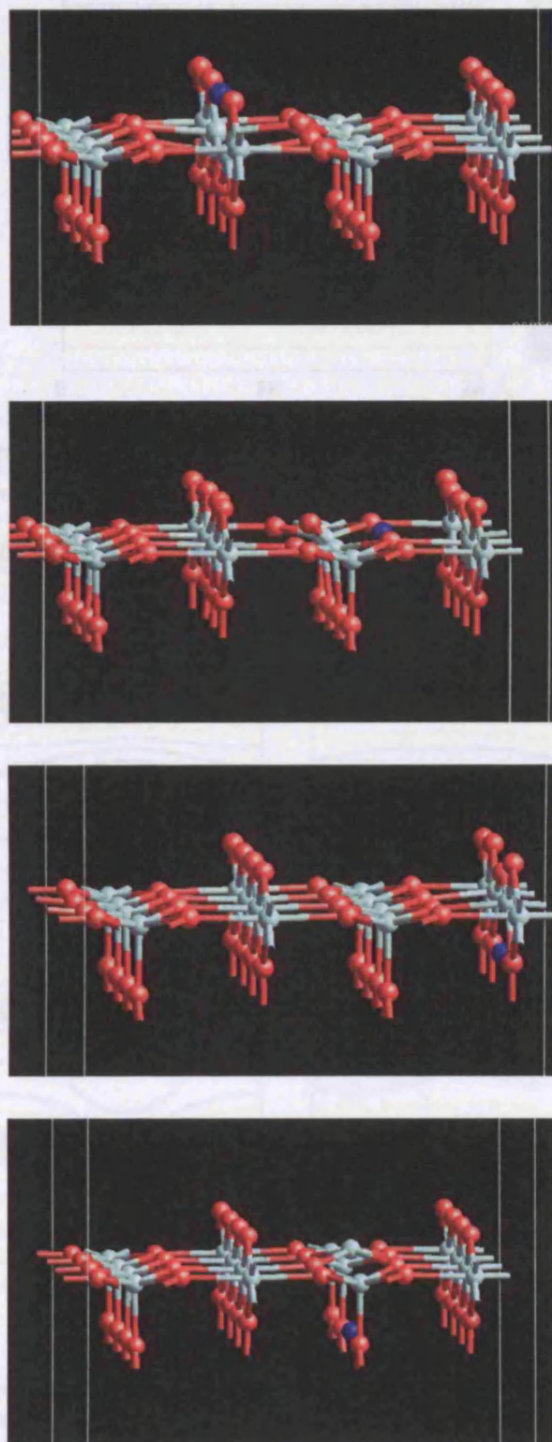


Figure 17 Relaxed structures of TiO<sub>2</sub>(110) slab models (red spheres – O, light green - Ti) with a single vacancy marked by a blue sphere. The bottom of the unit cell is not shown.

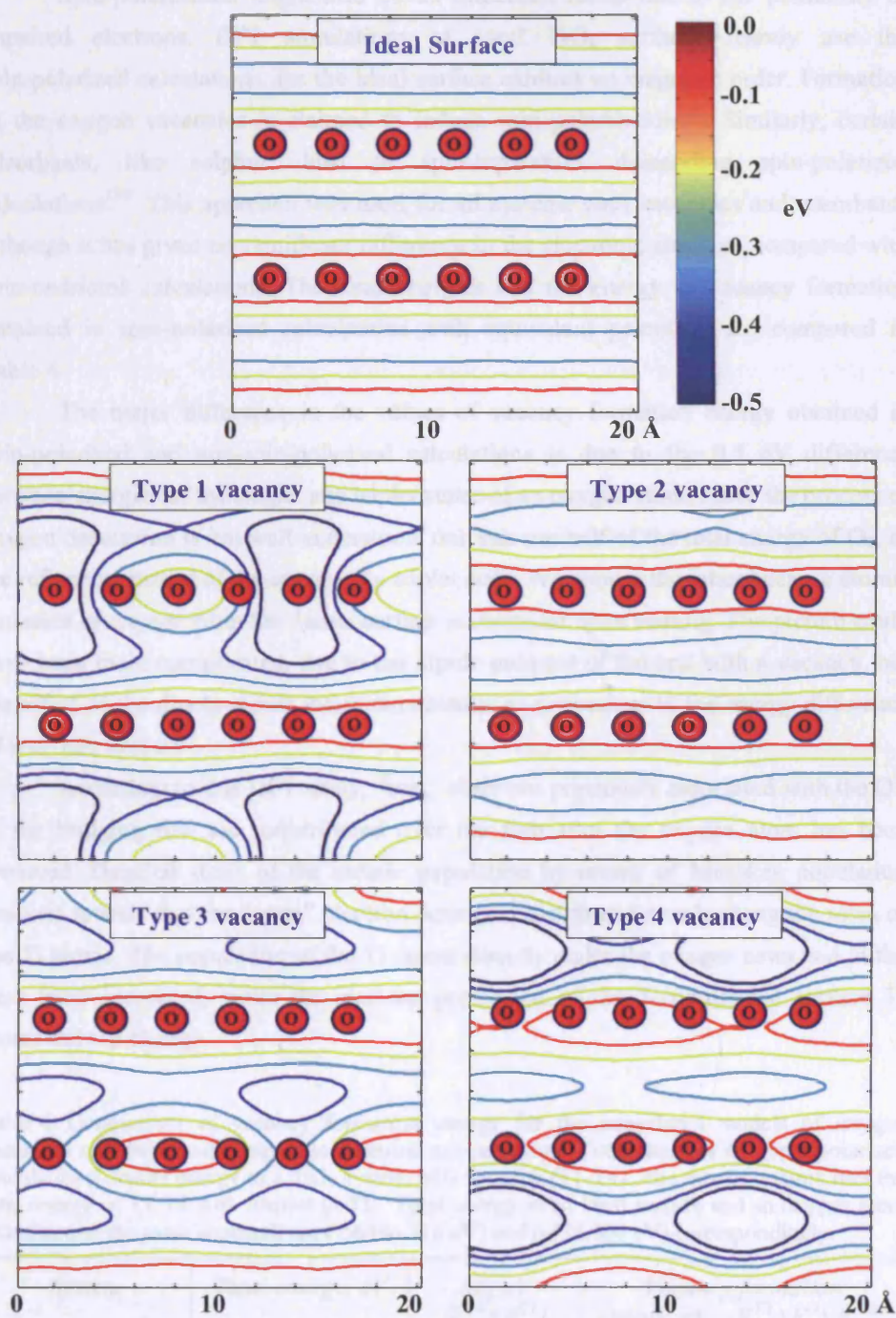


Figure 18 Electrostatic potential of the perfect  $\text{TiO}_2(110)$  surface at 3.0 Å compared with electrostatic potential of the surface containing oxygen vacancies. Four types of vacancies are considered according to Figure 17(a-d). Values of the potential over defective surfaces are taken with respect to the maximum (over bridging oxygen row). Contours are drawn in the same scale with step 0.1 eV.

Spin-polarization might also be an important factor due to the possibility of unpaired electrons. DFT simulations of ideal  $\text{TiO}_2$  surfaces rarely use the spin-polarized calculations, for the ideal surface exhibits no magnetic order. Formation of the oxygen vacancies is claimed to induce spin polarization<sup>112</sup>. Similarly, certain adsorbants, like sulphur, lead to spin-separation, demanding spin-polarized calculations<sup>120</sup>. This approach was used for all systems with vacancies and adsorbants although it has given no significant difference in the electronic structure compared with spin-restricted calculations. The total energies and the energy of vacancy formation obtained in spin-polarized calculations with equivalent potentials are compared in Table 4.

The major difference in the values of vacancy formation energy obtained in spin-polarized and non-spin-polarized calculations is due to the 0.5 eV difference between energies of the singlet and triplet states of an oxygen atom. Since the process of oxygen desorption is not well understood, one can use half of the total energy of  $\text{O}_2$ , as the reference instead of the energy of a triplet state. We choose the latter because atomic emission of oxygen from the titania surface is observed upon heating. The picture could have been more complicated, due to the dipole moment of the cell with a vacancy, but the effect of the dipole-dipole interaction results in corrections to the energy difference of less than 0.02 eV.

According to this DFT study, “two” electrons previously associated with the  $\text{O}^{2-}$  in the bridging row are redistributed over the slab after the oxygen atom has been removed. Detailed study of the atomic population by means of Mulliken population analysis reveals that the “extra” electron density is distributed evenly along the rows of the Ti atoms. The population of the Ti atoms directly under the oxygen rows and in the next layer increased, while the electron population of the 5-coordinated surface Ti atoms did not change.

Table 4 Comparison of vacancy formation energy for the considered models of oxygen vacancies calculated with respect to a neutral oxygen atom. Total energies  $E^{TX}$  (spin-polarized calculations) denote energy of a  $\text{TiO}_2$  system with vacancy (T1-T4). The second column lists the total energy of T1-T4 with respect to T1. Total energy of an ideal surface and an oxygen atom calculated in the same supercell are (-56446.318 eV) and (-438.900 eV) correspondingly.

<i>System</i>	<i>Total energy, eV</i>	<i><math>\Delta E</math>, eV (<math>E^{TX}+E^{Tl}</math>)</i>	<i>Vacancy formation energy, eV. (<math>E^{TX}+E^O</math>)-<math>E^{Ideal}</math></i>
T1	-56002.619	0.0	4.80
T2	-56000.788	1.83	6.63
T3	-56002.294	0.32	5.12
T4	-55999.160	3.46	8.26



This result is similar to the previous DFT predictions stating that the excess electrons are injected into the conduction band of the surface<sup>112</sup> and can be attributed to the neighbouring five- and six coordinated atoms. Results of previous studies<sup>121</sup>, as well as work conducted in our own group<sup>122</sup>, illustrate that the degree to which the defect wave function is distributed between the two Ti atoms depends strongly on the exchange functional used. Use of HF, for instance, results in an electron wave function localized “in the vacancy” between the 5- and 6- coordinated Ti, but an admixture of correlation (30% or more) resulted in a state localized in both Ti sites. The spin polarisation also differs with the change in the correlation functional: there is no polarization using HF, but the solution becomes spin polarized when correlation is added to the functional.

According to a recent review, there is no experimental data available on the subject<sup>115</sup>, although it is known that two types of defects are present on the surface. Further studies of rutile single crystals in UHV are necessary with an emphasis on the spin separation on the surface. Hence, currently it is difficult to draw a conclusion about the vacancy model on the basis of the DFT calculation of subsurface vacancies because the vacancy formation energy is strongly affected by the choice of exchange functional. It may still serve as an illustration if the DFT scenario is acceptable. On the other hand, the comparison of the results with previous theoretical calculations have shown that the DFT method used in this work describes well the electronic structure of the clean  $\text{TiO}_2(110)$  surface.

Defect states are described in accordance with previous theoretical results. Assuming that DFT correctly describes the electron distribution, the less frequently observed defect in STM images can be attributed to the second layer oxygen vacancy. However, combined experimental and theoretical efforts are necessary to resolve the nature of F-centres in  $\text{TiO}_2(110)$ , their charge state and the hierarchy of oxygen vacancy formation energies in the subsurface layers, and on the surface.

### **1.5 Structure of the tip apex**

The image obtained in high resolution NC-AFM imaging is essentially a nonlinear 2D mapping of tip-surface interactions, and cannot be limited to the surface topography in its interpretation. Therefore, the pattern for a given surface strongly depends on the nature of the tip. From this perspective, information available about the tip apex and the ability to control it becomes the key for image interpretation.

NC-AFM tips on cantilevers are normally produced using conventional Si-based microfabrication techniques and made of n-doped Si. Maximal sharpness, as measured

in scanning electron microscope (SEM) immediately after fabrication, is characterised by a radius of curvature of 5 nm. The cantilever can have a metallic coating (e.g. Pt/Ir alloy) to increase its conductivity and corrosion resistance. In high resolution UHV studies of insulators, an uncoated Si tip is used more frequently since the coating also reduces the sharpness of the tip. The larger tip radius is normally avoided, because it is often regarded as a factor that reduces the resolution.

The tip of the cantilever is exposed to ambient air during transportation and mounting, hence, it is always covered by at least 1 nm of amorphous silicon oxide. Therefore, using a Si cantilever with a tip does not mean, however, that a Si nanocluster can model the apex of this tip.

In an experiment the tip can be heated, annealed or sputtered after it has been mounted and placed into the UHV chamber. Heating a Si surface up to 200°C applied to a Si surface is expected to remove water from the SiO<sub>x</sub> layer, while sputtering with an Ar<sup>+</sup> beam is supposed to recover pristine Si. As the precision of the sputtering is questionable when the actual tip is treated and also may result in charging of the tip, heating and annealing are usually chosen for the tip cleaning.

Contamination of the tip apex is also possible during the imaging process. The transfer of an atom/ion between tip and surface at small distances has been predicted theoretically<sup>51</sup>, observed in transmission electron microscopy (TEM)<sup>123</sup>, and evidenced from the change in contrast during NC-AFM image acquisition<sup>124</sup>.

When the substrate is an insulating surface, experimentalists often do not remove the oxide<sup>52,125</sup> from the tip apex. Moreover, some of them actually perform a “soft” contact with the surface. This leads to mass transfer between the tip and the surface and eventually results in a tip configuration, which remains stable during an intermediate contact. If the oxide was removed from the tip then incidental contact between the tip and the surface would result in jump-to-contact with significant tip contamination due to the strong adhesion between bare Si and ionic surfaces.

On semiconducting surfaces, imaging with a Si tip apex is favourable because contamination of the tip by the surface material does not affect significantly the tip-surface interaction strength.

Here we consider models for both scenarios: clean Si tip and oxidized Si tip in application to insulating surfaces.

### 1.5.1 Model of oxidized Si tip

The fact that the tip can be contaminated by the surface material led to a theoretical model of a rigid oxide tip, widely used for the interpretation of NC-AFM images of ionic insulators. This simple model<sup>48</sup> captures the essence of experimental practice and represents an atomically sharp tip with either a positive or negative overall electrostatic potential. For the sake of comparison, we use the same model of the tip.

Historically a  $\text{Mg}_{32}\text{O}_{32}$  cluster was used to represent the tip potential<sup>31,42,48,51,124</sup> (Figure 19). This cluster is a MgO cube which is oriented with  $\langle 111 \rangle$  axis along the surface normal and points towards the surface with either Mg or O ion. These two modes will be referred to as a positive-terminated and negative-terminated tip. In both cases, the top half of the cube is kept fixed, while the lower is allowed to relax. In this work we chose this tip model for the study of mechanisms of contrast formation on the  $\text{Al}_2\text{O}_3$  surface and on  $\text{MgO}(001)$  in the presence of an adsorbed formate molecule.

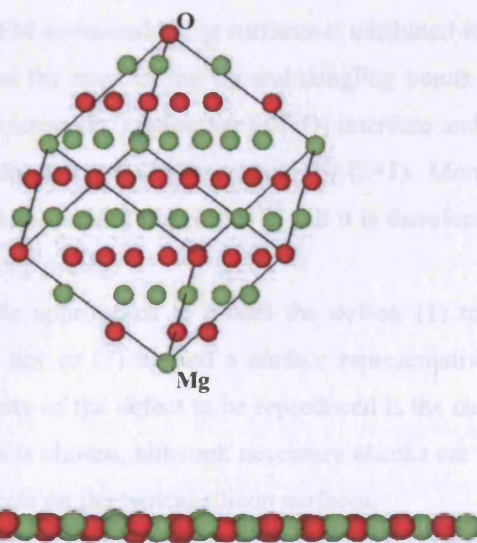


Figure 19. Rigid oxide tip model is represented by a  $4 \times 4 \times 4$  cube made of wide bandgap magnesium oxide. The cube is oriented with its  $\langle 111 \rangle$  axis parallel to the surface normal and, therefore can be used to represent both positive- and negative- terminated atomically sharp tips depending on the sign of the atom on the apex. In our simulation the upper half of the cluster is kept fixed.

### 1.5.2 Pure Si tip model

The major distinctive feature of using an oxidized tip is that the tip may have positive or negative polarity – consequently one expects to obtain two distinctive images and/or two distinctive interpretations of the image. There is a belief that if the apex of the tip is made of pure Si than a dangling Si bond will form on the apex and such tip will produce images with high contrast and enable straightforward unambiguous interpretation. There is experimental<sup>38</sup> and theoretical<sup>49,126</sup> support for this idea on a semiconducting surface, but no thorough proof as yet. We will use this tip model to study other surface types, but remain conscious of the high reactivity of the dangling bond and presence of contaminants in the residual gas.

The major requirement for the structural tip apex model is to reproduce the features of a Si surface, that are responsible for contrast formation. The essential technical requirement is to reduce the computational load, since a detailed forcefield is usually required for image production. To reduce the computation time, we accept an error in the electronic structure calculation due to the small distance (3 Å) between the tip images in calculations with periodic boundary conditions.

The contrast in NC-AFM semiconducting surfaces is attributed to the interaction between the dangling bond on the apex of the tip and dangling bonds on the surface. The dangling bond is a well known ( $P_b$ ) defect on Si/SiO<sub>2</sub> interface and exists on ideal Si surfaces like Si (111) (5×5), Si (111) (7×7) or Si (110) (2×1). Moreover, it is the most prominent defect on interfaces with dielectrics<sup>127</sup> and it is therefore appropriate to consider it as the basis for the tip model.

There are two possible approaches to model the defect: (1) to find a cluster representing the apex of the tip; or (2) to find a surface representative of the Si tip surface. Since the main property of the defect to be reproduced is the dangling bond on the apex, the cluster approach is chosen, although necessary checks are made to ensure that it is representative of defects on the typical silicon surfaces.

Previous studies of silicon clusters have demonstrated<sup>128</sup> that most stable clusters have no dangling bonds on the surface. Correspondingly a different approach can be taken: a cluster can be cut from a surface and every broken Si-Si bond can be “saturated” with a hydrogen atom. Clusters of this type have already been constructed in studies of NC-AFM on semiconductors<sup>49</sup>, so the largest of them is adopted in this work. The question, first addressed here, is whether this cluster is able to reproduce the electronic properties of surface dangling bonds.



We have compared the electronic structure of the cluster with the electronic structure of Si (111) (5×5) and Si (110) (2×1) surfaces in order to assess the quality of the model. The problem of the tip-surface interaction is quite relevant to the interface problem, which is discussed in corrosion science<sup>108,129-132</sup> and electronics<sup>17,127</sup>. Correspondingly, since charge redistribution and bond formation are expected, an analysis of the “band offset” between the Si tip and the substrate should be performed.

In the case of the Si dangling bond, it appears to be the HOMO orbital of the system. The position of the top of the valence band is monitored across the various systems (Table 5). The structure of the energy levels for a system with a dangling bond is outlined in the inset in Table 5 showing a pair of states split by the Fermi level between the valence and conduction bands. States drawn in red are occupied, those in black are not. The analysis shows that the HOMO energy varies only by 0.05 eV between the two Si surfaces, while the position of the valence band differs by 0.16 eV. The electronic structure of the cluster is different due to the confined nature of the system: the gap is twice as large (2 eV) in the cluster than in either of slab systems (1 eV). Since the difference in the position of doubly occupied states between the cluster and Si(2×1) surface (0.15 eV) is of the same order as between Si(2×1) and Si(5×5) one can consider the cluster as a prototype of a Si nanotip.

The absolute position of the dangling bond does depend on the choice of exchange-correlation potential, but if the distance between fully occupied and unoccupied states shrinks, the dangling bond state is pressed towards the bottom of the valence band. The dependence of the absolute position of the dangling bond state on the choice of exchange-correlation functional was verified with Gaussian 98 calculations of the Si<sub>10</sub>H<sub>15</sub> cluster using UHF and B3LYP functionals.

Table 5. Positions of the top of the valence band  $E_{VB}$ , bottom of the conduction band  $E_{CB}$  and molecular orbital associated with the dangling bond  $E_{DB}$  and the highest “fully occupied” orbital. Inset: Scheme of eigenvalue’s structure for a tip with a dangling bond.  $\epsilon_F$  is the Fermi level of the system.

System	$E_{DB}-E_{VB}$ eV	$E_{CB}-E_{VB}$ eV	
Si(111) (5x5)	0.05	0.17	
Si(110) (2x1)	0.34	1.0	
Si <sub>10</sub> H <sub>15</sub> (GGA)	0.77	0.85	
Si <sub>10</sub> H <sub>15</sub> (B3LYP)	1.54	4.24	



Inclusion of the exchange functional in the cluster calculations increased the split between fully occupied and fully unoccupied states, while the distance between the highest occupied states and the dangling bond state decreased from 1.0 eV for DFT-GGA within SIESTA to 0.9 eV for B3LYP and to 0.5 eV for UHF with Gaussian 98. The added exchange has also shifted all the eigenvalues of the  $\text{Si}_{10}\text{H}_{15}$  cluster downwards and resulted in  $E_{\text{DB}} = -5.53$  eV, which is 0.25 eV below the value on  $\text{Si}(111)$  (5x5).

The demonstrated sensitivity of the cluster to the choice of exchange functional should be taken into account in the interpretation of the result since the value of  $E_{\text{DB}}$  will affect charge redistribution when the cluster contacts an insulating surface.

To develop understanding of the dangling bond model used in this study in real-space, a cross-section of the HOMO orbital of the tip is plotted in Figure 20(right). The plane of the cross-section passes through the apex atom and at an equal distance between two of its nearest neighbours. Grey circles on the contour plot represent projections of the position of the nearest Si atoms onto the cross-section plane. The width of the HOMO at 4.0 Å from the surface is about 3 Å (Figure 20) at the level of the last contour (0.01 e/Å). The shape of the distribution implies that noticeable interference to the force is expected from the neighbouring atoms when interatomic distances between tip and surface are of order 4.0 Å.

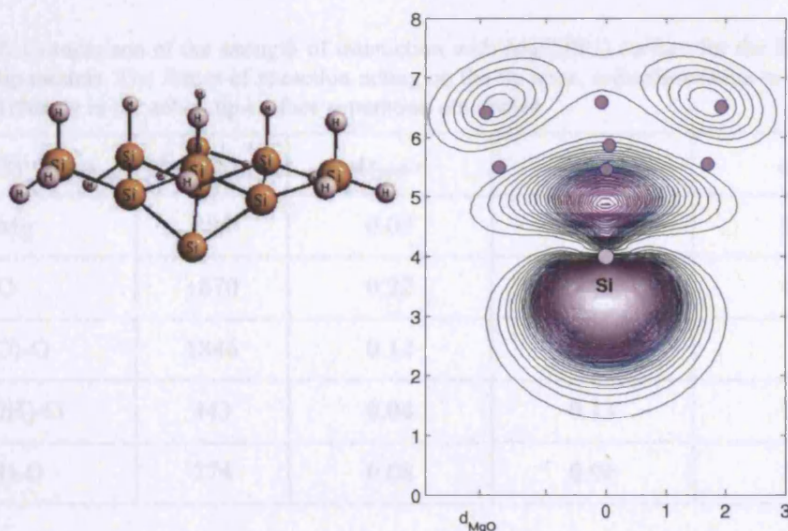


Figure 20. (left) structure of the  $\text{Si}_{10}\text{H}_{15}$  cluster. (right) Cross-section of the HOMO orbital of pure Si tip. This orbital is mainly associated with the unsaturated orbital of the apex Si atom. Shaded circles denote the projected position of other Si atoms.

The Si tip model can be extended to account for the saturation of the Si dangling bond by active surface species. Two typical types of Si surface contamination are considered: hydrogenation and hydroxylation. To compare these models we position all of them: MgO oxide tip, pure Si tip and two Si contaminated tips over the oxygen site of a MgO(001) surface at 3.0 Å distance and perform relaxation of the surface and apex atoms of the model. The distance here is defined as the distance between the apex of the tip and the oxygen plane of the surface. In relaxation the upper part of the oxide tip is fixed, and the top of the Si tip, including hydrogen atoms saturating broken Si bonds and their first neighbours, are kept fixed.

As a result of the relaxation, displacements are observed in both the tip and the surface. The resulting force is calculated as the sum of the z-components of the forces acting on all the atoms of the tip. This force was found to be attractive in every instance. The magnitude of the force over the oxygen site is about 1.8 nN for the oxide and the Si tip. This is several times larger than the force on the contaminated Si tip with a saturated dangling bond. The full comparison including relaxation of the tip-surface distance and comparison with the Si-Mg interaction is outlined in Table 6. Based on this data, models of the Si tip with a dangling bond and a rigid ionic tip will be used, and the corresponding mechanisms of contrast formation will be studied. This choice should not undermine the importance of the contaminated tips, which may also find their application as a more robust model.

Table 6. Comparison of the strength of interaction with MgO(001) surface for the Si-based and oxide tip models. The forces of attraction acting on the tip apex, z-displacements in the surface, tip and change in the actual tip-surface separation are shown.

<i>(Tip)-Atom</i>	<i>Force, pN</i>	$\Delta z_{surf}, \text{\AA}$	$\Delta z_{tip}, \text{\AA}$	$\Delta d, \text{\AA}$
(Si)-Mg	484	0.07	0.05	0.12
(Si)-O	1870	0.22	0.16	0.38
(MgO)-O	1846	0.12	0.18	0.3
(Si-OH)-O	443	0.04	0.13	0.17
(Si-H)-O	274	0.08	0.06	0.14

## **1.6 Summary**

This chapter was meant to absorb the majority of the technical details in order to make lighter and more transparent presentation of the material in the following chapters.

Comparison of the electronic structure of the Si tip model with the electronic structure of surface silicon systems demonstrates that the description of the Si dangling bond is qualitatively correct.

The combination of the DFT-GGA technique for treatment of periodic systems, the Embedded Cluster Method for study of electron localization, the MM methods for calculation of the tip-surface forcefield and the macroscopic theory for the description of the long-range tip-surface interactions is optimal for the theoretical study of NC-AFM imaging of insulating surfaces with atomic resolution.

## 2 Contrast formation on clean surfaces of ionic insulating crystals

In this chapter we apply the rigid oxide tip model and the Si dangling bond models to the imaging MgO(001) and  $\alpha$ -Al<sub>2</sub>O<sub>3</sub>(0001). The possibility of obtaining atomic and chemical resolution on Al<sub>2</sub>O<sub>3</sub>(0001) is discussed with emphasis on the limitations observed within each of the models. A full NC-AFM image of  $\alpha$ -Al<sub>2</sub>O<sub>3</sub>(0001) is obtained with the oxide tip model and the possibility of atomic resolution is demonstrated. The conditions for chemical resolution and the limits of spatial resolution are presented. The analysis of *ab initio* force-distance curves over both surfaces, simulated using the tip model with an unsaturated bond at the apex, explains the basic mechanisms of contrast formation on insulating surfaces using a pure silicon tip. A possible explanation of the difficulties in obtaining atomic resolution on Al<sub>2</sub>O<sub>3</sub>(0001) is suggested.

It is known that for a given surface, the tip-surface interaction depends on the nature and structure of the tip apex. The properties of the tip apex depend on the choice of the tip and surface materials, preparation of the tip and the scanning regime<sup>43</sup>. Moreover, there is no direct access to the information regarding the tip apex at the atomic scale during the experiment, which altogether often leads to the uncertainty in the interpretation of NC-AFM images<sup>43</sup>.

In this chapter, the problem of interpreting NC-AFM images of clean surfaces of ionic insulators is considered. Interpretation of the atomic scale resolution image involves drawing a correspondence between the pattern of the image and the atomic sublattices of the surface<sup>124</sup>. In some cases ions or groups of ions, occupying sublattices, can be distinguished<sup>133</sup> but rarely identified<sup>42</sup>. Therefore, it is essential to understand the nature of the tip-surface interaction, which in most cases requires developing a particular model of the tip apex.

In this chapter we focus on the two tip models most widely accepted among experimentalists<sup>38,46,50,124,134</sup>: the model of the tip with a dangling bond and the model of an oxide tip. While the oxidized tip model has already been used to interpret NC-AFM images of insulating ionic materials<sup>42,48,51</sup>, the application of the “dangling bond” model has been restricted to semiconducting systems<sup>135,136</sup>. On these systems the “dangling bond” allowed chemical identification, which makes it a promising model to implement for insulating ionic systems, where chemical identification of the sublattices has so far been complicated<sup>42</sup>.

The aim of this study is to reveal whether the success of the dangling bond model, which offers unambiguous interpretation on semiconducting surfaces, can be

transferred onto ionic surfaces. For the trial we consider two classic oxide surfaces -  $\text{Al}_2\text{O}_3$  and  $\text{MgO}$ , which are currently the focus of experimental NC-AFM studies<sup>35,125,131,137,138</sup>. We study these surfaces using both an oxide tip model and a model of a Si tip with a “dangling bond”. These two tip models are based on different assumptions about the tip and the surface experimental preparation (see section 1.5). So, it is important to discuss the technical problems associated with preparation of the tips and maintaining during the imaging process.

Since experimental studies have so far been unsuccessful in obtaining atomic resolution imaging of the  $\text{Al}_2\text{O}_3(0001)$  surface, we also address whether it is possible to resolve ionic sublattices on these surfaces.

## **2.1 Atomic resolution on $\alpha\text{-Al}_2\text{O}_3(0001)$ surface with an oxide tip**

The aim of this section is to provide experimentalists with a complementary theoretical insight by attempting to resolve the following questions:

- Is atomic resolution on  $\alpha$ -alumina (0001) at low temperatures possible in principle?
- What are the main obstacles to obtaining atomic resolution on the surface?
- Is chemical resolution possible at this surface?

This section addresses these questions by studying the tip-surface interaction using the oxidized tip model<sup>44</sup> and modelling of the NC-AFM image for both possible terminations of the oxide tip (positive and negative). The details of the tip construction within the oxide tip model and properties of the tip are discussed in section 1.5.1.

### **2.1.1 Tip related surface properties from *ab initio* calculations**

There are two issues, which one has to be aware of in the use of the pair potentials for modelling the tip-surface interaction, even if the geometric structure of the surface structure is well reproduced. First, the potential has been fitted to reproduce the interatomic distances and interaction in particular environments, which are different from those occurring during the imaging process when the tip is contacting the surface. Second, the strength of interatomic interaction can be exaggerated at small distances, because of the use of formal charges in an unconventional environment. This has a particularly strong impact on the force between two cations; for instance, with the close approach of the “positive” tip ( $\text{Mg}^{2+}$ ) to a cation ( $\text{Al}^{3+}$ ) on the alumina surface.

Until recently, most simulations of NC-AFM images of insulating surfaces have been conducted in the framework of atomistic static optimisation using pair potentials. The main properties in this case are electrostatic potentials of the tip and surface.



*Ab initio* modelling of the tip-surface interaction allows comparison of the range and behaviour of this electrostatic potential with those of the total electronic potential close to the surface. In our DFT calculations the total potential also incorporates exchange and correlation components, which are a significant fraction of the binding energy.

In the case of  $\text{Al}_2\text{O}_3(0001)$  surface, the bonding in the crystal and the bonding between the oxide tip apex and the surface, are not purely ionic. The detailed account of contribution of covalent bonding becomes more important as the tip-surface distance approaches the bond length.

To characterise the contribution of the exchange-correlation to the total electronic potential at the  $\text{Al}_2\text{O}_3(0001)$  surface, the profiles of electrostatic and total electronic potential are plotted in Figure 21 and compared with those of  $\text{MgO}(001)$ , a

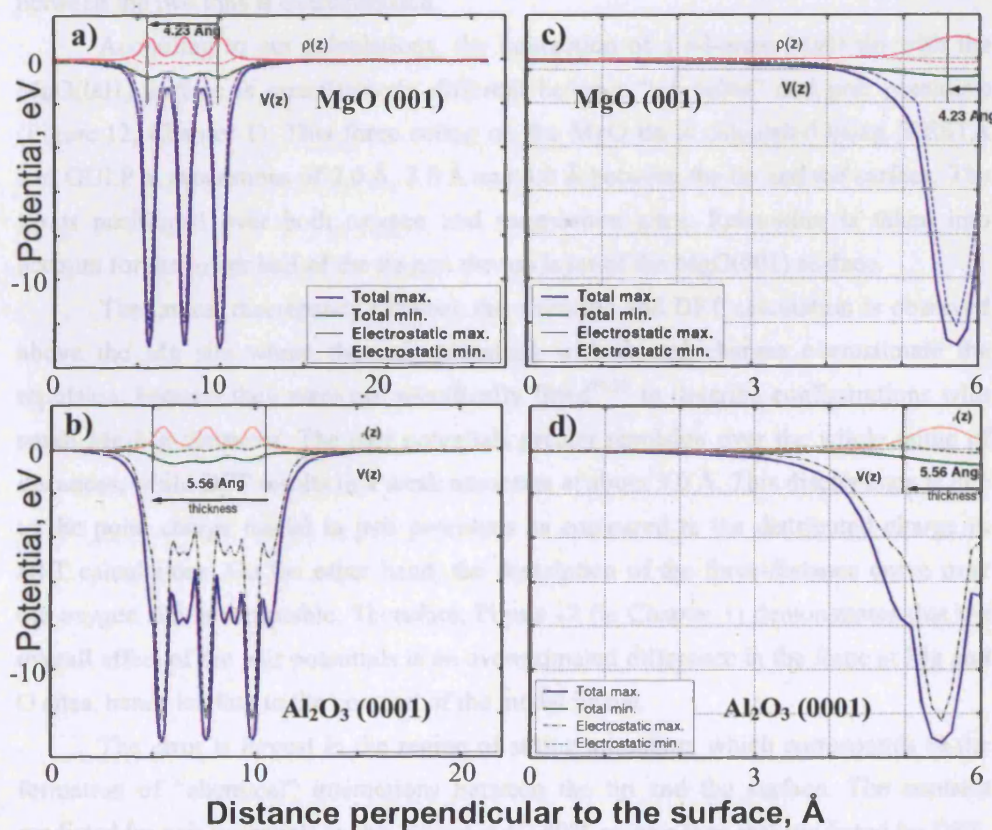


Figure 21. Z-dependence of maximal/minimal value of total (blue solid line) and electrostatic potential (black dashed line), electronic density (red line) and magnified surface tails of these quantities are presented for the slabs of (a, c)  $\text{MgO}(001)$  and (b, d)  $\text{Al}_2\text{O}_3(0001)$ .

classic ionic insulator. The calculations are made using DFT methods (SIESTA) and parameters described in section 1.3.1 above.

Comparison of the profiles for MgO and Al<sub>2</sub>O<sub>3</sub> shows that the electrostatic potential in MgO is the dominant part of the total potential (Figure 21), while for alumina it is just a significant fraction. This is yet another way to highlight that care should be taken in interpreting any results obtained with pair potentials. Figure 21 also demonstrates that the range of the electrostatic potential is shorter than range of the total potential, while comparison of the decay length of the total potential shows that it is about the same (3 Å) for both MgO and Al<sub>2</sub>O<sub>3</sub>.

The most typical drawback of pair potentials fitted to empirical data is the poor reproduction of the cation-cation interaction. The potential functions are usually fitted to the calculated or measured properties of the oxide's polymorphs, where a cation can hardly have another cation in its first coordination shell. As a result, the repulsion between the two ions is overestimated.

According to our calculations, the interaction of a 64-atom MgO tip with the MgO(001) surface is quantitatively different between “*ab initio*” and pair potentials (Figure 12, Chapter 1). This force acting on the MgO tip is calculated using SIESTA and GULP at separations of 2.0 Å, 3.0 Å and 4.0 Å between the tip and the surface. The tip is positioned over both oxygen and magnesium sites. Relaxation is taken into account for the lower half of the tip and the top layer of the MgO(001) surface.

The largest discrepancy between the atomistic and DFT calculation is observed above the Mg site where the pair potentials with formal charges overestimate the repulsion, because they were not specifically fitted<sup>94,95</sup> to describe configurations with small Mg-Mg distances. The pair potentials predict repulsion over the whole range of distances, while DFT results in a weak attraction at about 3.0 Å. This discrepancy is due to the point charge model in pair potentials as compared to the distributed charge in DFT calculations. On the other hand, the description of the force-distance curve over the oxygen site is acceptable. Therefore, Figure 12 (in Chapter 1) demonstrates that the overall effect of the pair potentials is an overestimated difference in the force at Mg and O sites, hence leading to the contrast of the model image.

The error is largest in the region of strong attraction, which corresponds to the formation of “chemical” interactions between the tip and the surface. The contrast predicted by pair potentials in this region is 60-80% greater than that predicted by DFT. However, given the difference in CPU consumption between these methods, pair potentials are chosen to construct the force field for a MgO tip over the aluminium oxide surface. This choice also enables one to draw a direct comparison with the work



conducted with pair potentials in the past. The knowledge about the overestimation of the cation-cation repulsion is important at the stage of quantitative image interpretation.

### 2.1.2 Imaging clean $\alpha$ -Al<sub>2</sub>O<sub>3</sub>(0001) with an oxidized tip

The major steps in the construction of the NC-AFM image of  $\alpha$ -alumina (0001) surface are calculation of the microscopic force-distance curves on a mesh and the transformation of the force field into a frequency field. The analysis of the images includes the search for the possibility of atomic resolution and identification of the sublattices and a study of the effect of the macroscopic tip-surface interaction on the resolution.

#### 2.1.2.1 Forcefield construction

The tip-surface forcefield necessary for simulating AFM images is calculated for the  $\alpha$ -alumina (0001) surface using both positive and negative tip terminations of the MgO cube, as detailed in Chapter 1 (section 1.1). At short distances (below 5.0 Å), the interaction between the tip and the surface may result in surface/tip contamination and a change in the tip polarity. Contamination of the tip with the surface material with close approach of the tip to the surface was recently observed in NC-AFM<sup>50</sup> as well as in real-time TEM film<sup>123</sup> and attributed to the minimal distance of 2.0-4.0 Å between the opposing surfaces. The precision of this estimate is limited by the resolution of the TEM and adequacy of the theoretical model for NC-AFM tip.

In this work the MgO tip approaches the surface as close as 1.8 Å and “scratches” the surface at constant height. This method is similar to the work on self-lubrication of the tip<sup>51</sup> but uses a static relaxation technique at every point, rather than MD. The interactions between the tip and the surface are represented by the pair potentials described above (1.3.3). In contrast to the alkali halide surface LiF<sup>51</sup>, the alumina surface “unzipped” the MgO cluster, and the string pulled from the tip cluster formed a chain of small 4-6 atom clusters on the alumina surface. This simulation clearly demonstrates that preparation of the tip apex by “soft contact” is not the appropriate procedure for the corundum surface and even occasional contact with the surface may damage the tip apex.

To avoid generation of data unrelated to the interpretation of stable NC-AFM images, following criteria are applied to the forcefield: (a) only purely “non-contact” trajectories are considered, i.e. points of close approach, where atoms are transferred between the tip and the surface, are excluded from consideration; (b) 0.1 Hz and 0.01 Å are chosen as realistic limits of NC-AFM resolution in constant height (CH) and

constant frequency shift (CFS) modes, respectively. The values are chosen on the basis of recent review of progress in the development of the NC-AFM instrument<sup>38</sup>.

The force field of the tip-surface interaction is derived from the results of structural relaxation using static simulation of the system for each chosen height of the tip. The choice of this technique, rather than molecular dynamics (MD) simulation is based on the experience of previous AFM modelling performed in our group<sup>44,51</sup> and is justified by the relatively small amplitude and simplicity of the relaxations observed on a softer crystal (LiF) in the field of the same tip.

In this work we consider interactions at tip-surface distances of 3-6 Å which is defined as the distance between the tip apex and the topmost cation of the surface before relaxation (see section 1.2).

Trial calculations revealed that for a typical AFM setup<sup>42,50,131</sup> the frequency corrugation in the constant height (CH) image is less than 0.1 Hz if the distance is greater than 5 Å. At distances closer than 2.8 Å the negatively terminated tip breaks over the Al site. By “breaking” the tip we mean that the apex atom of the tip is transferred to the surface. Since the pair potentials are not fitted to reproduce such a process, we exclude corresponding data from the force field. Therefore, the tip-surface interactions are sampled in the 2.8-5.0 Å range of tip-surface separations in order to construct the “microscopic” tip-surface force field above the area of the primitive unit cell for the surface. We stress that the range of distances that gives information relevant to “true atomic resolution” is only within 2.2 Å from a rigid surface of ionic insulator.

The parameters of the macroscopic tip-surface interaction are chosen to reproduce typical experimental conditions. For the sake of simplicity, the strength of the macroscopic interaction is characterised by the tip radius only, while the other parameters are kept fixed. The Hamaker constant is 1.0 eV, which is an estimate for the typical oxides and insulating ionic materials<sup>41,64,139</sup>.

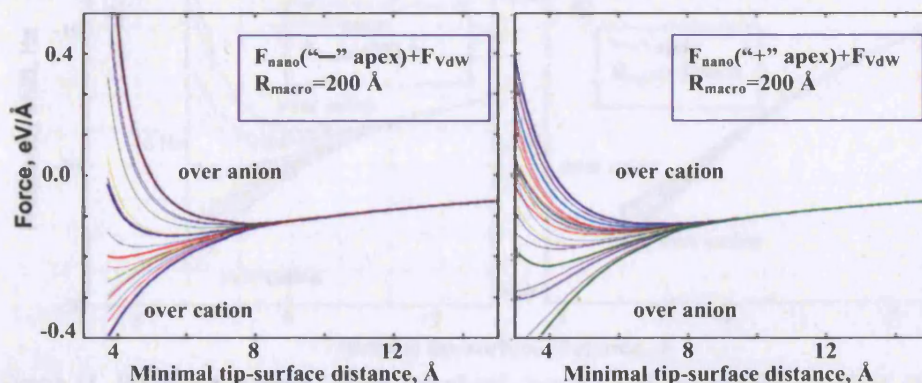


Figure 22. Total force (microscopic + Van der Waals) acting on “negative” (left) and “positive” (right) potential tips at the level of macroscopic interaction characterised by a tip radius  $R = 200$  Å and Hamaker constant  $H = 1$  eV.



The choice of a tip radius of 200 Å, results in an attractive force of 0.06 eV/Å acting at a distance of 15 Å. Figure 22 shows the individual force-distance curves for all inequivalent nodes of the mesh. The force in Figure 22 is the sum of the macroscopic Van der Waals force and the site-dependent microscopic force acting on the positive- or negative-terminated tip. The strength of the macroscopic interaction is not enough to overcome repulsion at smaller distances, i.e. the force becomes positive (repulsive) as the tip approaches the surface.

The frequency-distance curves calculated on the basis of these force-distance curves for the negative-terminated (O-terminated) oxide tip (Figure 22a) are shown in Figure 23a. The frequency-distance curves over the cation and over the centre of anionic group  $[3O^2]$  are plotted with bold lines. For all distances the strongest and the weakest detuning is achieved over  $Al^{3+}$  site and in the centre of  $[3O^2]$  site respectively (see the description of the surface geometry in section 1.4.1). Similarly to the previous calculations<sup>133</sup>, displacements of the tip and surface ions play a significant role in the contrast formation. However, the displacements of atoms of the first surface layer do not exceed 0.15 Å.

The large orange mark in the Figure 23a corresponds to the largest value of tip-surface separation where the derivative of the frequency detuning with respect to the tip-surface distance equals zero at one of the positions of the tip. The corresponding value of the tip-surface separation determines the point of the closest approach available in the conventional NC-AFM setup, because the feedback loop used in CFS mode assumes that tip-surface interaction is attractive.

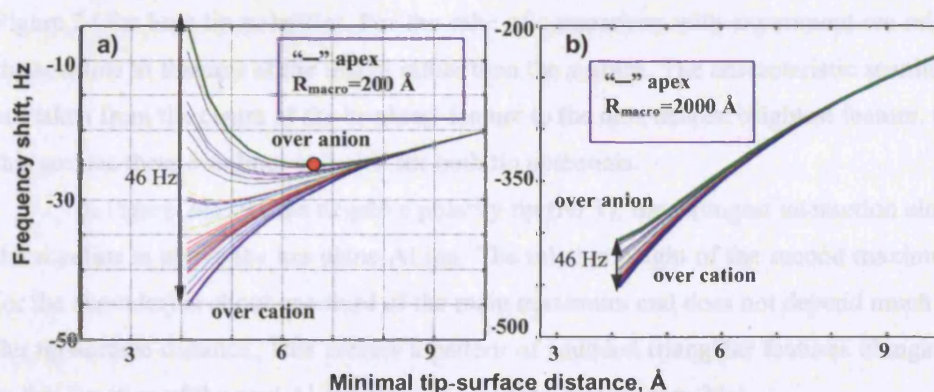


Figure 23. Frequency-distance curves calculated over sites of the primitive surface cell of  $Al_2O_3(0001)$  for two chosen macroscopic radii: (a)  $R = 200$  Å and (b)  $R = 2000$  Å.

If the modulus of the preset frequency shift passes through the minimum (Figure 23a), the feedback mechanism will shift the cantilever tip closer to the surface in an attempt to increase the value of frequency shift, until the tip crashes into the surface. The orange mark defines, therefore, the maximum detuning available in CFS mode for the given level of macroscopic interaction ( $R = 200 \text{ \AA}$ ). This sets a limit on the corrugation in the image, which can be overcome only by increasing the macroscopic component of the tip-surface interaction (Figure 23b). The increased macroscopic interaction is always attractive and therefore eventually compensates the short-range repulsion for the 3-6  $\text{\AA}$  range of tip-surface separations. In this work we chose a larger radius of  $R = 2000 \text{ \AA}$ . At this radius, the frequency-distance curve is monotonic (Figure 23b), and therefore the range of imaging is extended for the CFS mode.

Importantly, increasing the radius does not change the absolute value of the contrast (detuning signal) in the constant height (CH) image since the contribution of the macroscopic force is laterally homogeneous at each given height. Further increases of the macroscopic interaction in CFS mode will, however, reduce the corrugation, due to the increased slope of the bunch of curves (Figure 23a). Therefore, a distinctive property of the constant height (CH) mode is the independence of the contrast from the level of macroscopic interaction, which is not the case in CFS imaging, where a search for the optimal level of macroscopic interaction is required.

### 2.1.2.2 NC-AFM image analysis

The modelled NC-AFM images of the (0001) alumina surface in the constant height (CH) acquisition mode and corresponding normalised scanlines are presented in Figure 24 for both tip polarities. For the sake of comparison with experiment we relate the scanline to features of the image rather than the surface. The characteristic scanlines are taken from the centre of the brightest feature to the next nearest brightest feature. On this surface these scanlines coincide for both tip potentials.

In Figure 24a, for the negative polarity tip (NPT), the strongest interaction along the scanline is above the top plane Al ion. The relative height of the second maximum (or the shoulder) is about one third of the main maximum and does not depend much on the tip-surface distance. This creates a pattern of rounded triangular features elongated in the direction of the next Al ion along the surface axis (Figure 24a).



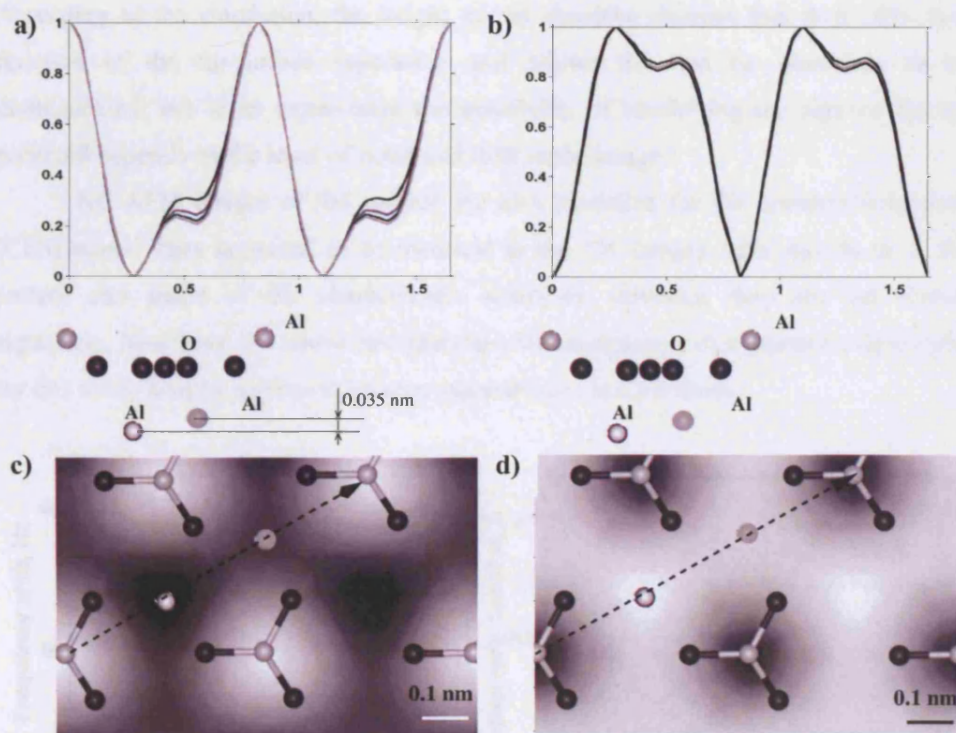


Figure 24. Constant height NC-AFM images of the  $\text{Al}_2\text{O}_3$  (0001) surface and normalised scanlines in the  $[1\bar{1}00]$  direction for two different polarities of the MgO tip. (a,c) negative potential tip image and scanlines; (b,d) positive potential tip image and scanlines. Distances in scan-lines along the surface are in nm. Both constant height images correspond to a minimum tip-surface separation of 0.3 nm.

These elongations merge at very small tip-surface distances. The degree to which the second maximum is pronounced, depends on the details of the atomic arrangement in the apex of the tip. The orientation of the MgO tip ions with respect to the surface ions, as shown below, also affects the maximum.

The positively terminated tip (PPT) demonstrates strongest detuning above the centre of the three oxygen ions (Figure 24b) forming two different types of triangles in the image (Figure 24d). As it can be seen in Figure 24b, the corresponding scanline has two almost equivalent maxima. The individual oxygen ions are not resolved, but the image is a collection of interconnected triangles. The image pattern and the shape of scanlines do not depend significantly on the tip-surface separation. The height of the shoulder distinguishes PPT scanlines from NPT scanlines. Given the stability of the scanline shape, the difference between the two types of scanlines (Figure 24a,b) can be used to learn about the sign of the tip potential.

According to the simulation, the height of the shoulder changes less than 10% as a function of the tip-surface separation and allows the two tip potentials to be distinguished, but in an experiment the possibility of identifying the sign of the tip potential depends on the level of noise and drift in the image.

NC-AFM images of the surface are also modelled for the constant frequency (CFS) mode. They appeared to be identical to the CH images with regards to in the pattern and shape of the characteristic scanlines; therefore they are not shown separately. Moreover, the above interpretation and assignment of sublattices, developed for CH mode images, applies to images and scanlines in CFS mode.

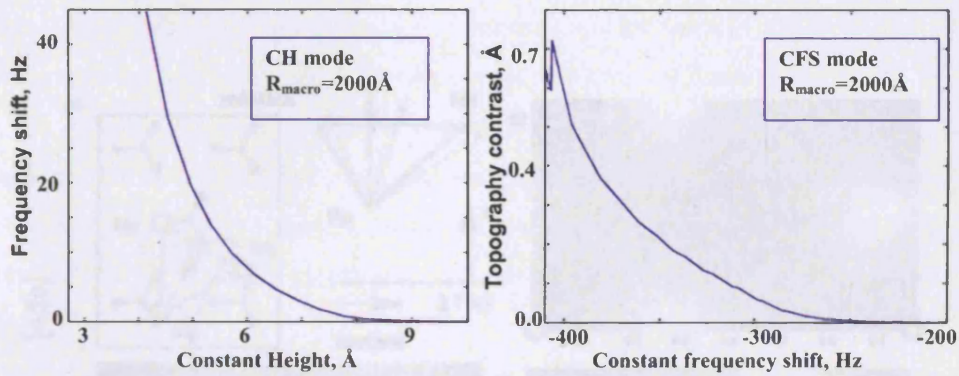


Figure 25. Contrast dependence in the modelled NC-AFM image as a function of the minimal tip-surface distance (in Constant Height mode, *left*) and preset frequency shift (in Constant Frequency Shift mode, *right*). The images are calculated for  $k = 3$  N/m,  $A = 70$  Å,  $f_0 = 100$  kHz, assuming a macroscopic interaction described by a tip radius  $R = 2000$  Å.

The contrast in the pattern monotonically increases with the rise of the tip-surface interaction in both CFS and CH mode (Figure 25). We do not observe a change of the pattern with the distance, which distinguishes  $\text{Al}_2\text{O}_3(0001)$  from  $\text{CaF}_2(111)$ . The difference can be explained by the significant rigidity of the  $\text{Al}_2\text{O}_3$  surface compared to  $\text{CaF}_2$ , which agrees well with the small displacements of oxygen atoms ( $< 0.1$  Å) compared to the displacements of fluorine atoms (1.0 Å) in  $\text{CaF}_2$  which lead to a sequence of different patterns observed without altering the tip.

The study conducted in this chapter considers a very particular shape of the MgO tip apex. Moreover, only one tip-surface arrangement has been considered. However, it is important to illustrate that several different patterns can be produced on the same surface using the same tip model. The triangular feature of the Al ions and of the three surrounding O ions (Figure 24) is very similar to the structure of the tip apex, which also has three-coordinated Mg or O ions next to the apex. It is expected that by changing tip-surface orientation it is possible to affect the image pattern.



In order to study this “convolution” effect, the MgO cube is rotated with respect to the z-axis perpendicular to the surface, and in this way changes the registry of the tip and surface ions. It can also be tilted with respect to the z-axis (Figure 26a). The total energy of the system is calculated as a function of the tip position with respect to the surface at a constant tip-surface separation of 2.5 Å for the tip and surface geometries with no relaxation (Figure 26).

“Breaking” the symmetry demonstrates that there are two types of oxygen triangles on the surface. Both tip rotation and tip tilting significantly change the relative strength of the interaction above these sites. Although the NC-AFM images are not calculated, these results clearly demonstrate that the tip-surface convolution can affect the image on the atomic scale.

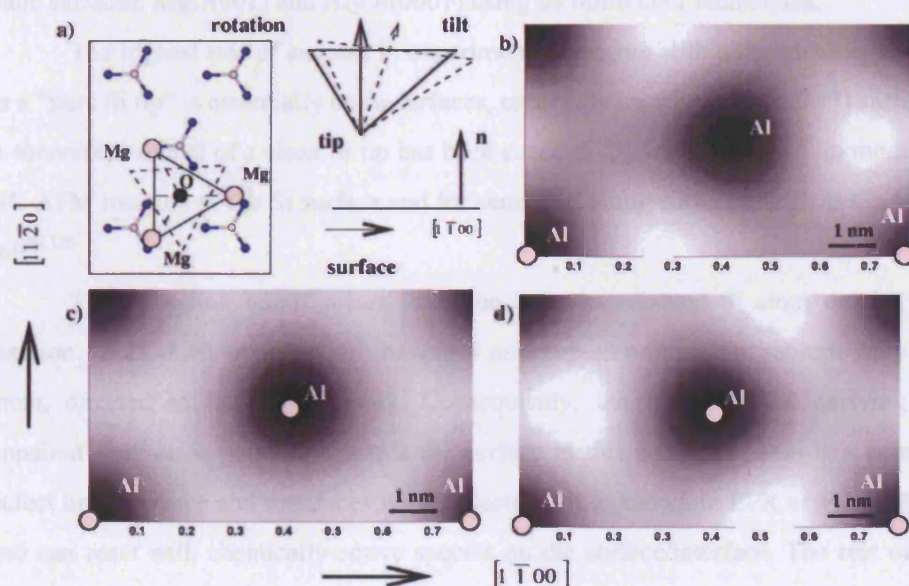


Figure 26. The map of the total energy surface of the tip in the vicinity of the  $\text{Al}_2\text{O}_3(0001)$  surface is plotted for different orientations of the MgO tip apex with respect to the surface. (a) A scheme illustrating the projection of the tip apex atoms onto the surface and the tip tilt with respect to the normal. The total energy of the system as a function of the tip position at a tip-surface separation of 2.5 Å: (b) for the original tip orientation and tilt used in calculations above (corresponding to the forcefield in Figure 22); (c) tip rotated by 20° with respect to the original position; (d) tip tilted by 20° with respect to its original orientation perpendicular to the surface.



## 2.2 Probing clean oxide surfaces with a “dangling bond” tip

The Si tip model with a dangling bond (section 1.5.2) is an example of a different probe: although the tip has a weak overall electrostatic potential, the unsaturated “dangling bond” on the apex of the tip acts as the actual probe. On semiconducting surfaces this model allows unambiguous interpretation due to the strong interaction with unsaturated bonds of the surface reconstruction<sup>46</sup>. Such a possibility is a desirable property lacking on insulating surfaces where an oxide tip is usually used. To analyse the nature of the tip-surface interaction and the applicability of the “dangling” bond tip for imaging oxide surfaces, we consider contact between the Si tip and two ionic surfaces: MgO(001) and Al<sub>2</sub>O<sub>3</sub>(0001) using *ab initio* DFT techniques.

The highest rate of success in experimental imaging with a tip which is claimed as a “pure Si tip” is essentially on Si surfaces, especially on the Si (111) (7×7) surface<sup>46</sup>. A theoretical model of a clean Si tip has been successfully implemented<sup>49</sup> in modelling NC-AFM imaging of the Si surface and for semiconducting surfaces, such as GaAs and InP<sup>49,136</sup>.

The “dangling bond” arises from the three-coordinated Si atom on the apex (section 1.5.2). A Si atom (sp<sup>3</sup>-Si) having 4 unoccupied orbitals can saturate only 3 of them, directed to its 3 neighbours. Consequently, the fourth orbital carrying one unpaired electron is pointing towards the surface in this geometry. This is a common defect on Si surface and interfaces with dielectrics. It is known in EPR as P<sub>b0</sub> or P<sub>bi</sub><sup>127</sup>, and can react with chemically active species on the surface/interface. The rest of this section is devoted to pure Si tips, while the section (2.3) considers the effect of tip contamination.

The strength of the interaction between the Si dangling bond tip and ionic surfaces<sup>42,140</sup> is determined by the onset of ion-covalent bonding between the tip apex Si atom and the surface oxygen atoms. The SIESTA code is used to calculate the force acting on the tip, electronic structure and Mulliken population.

The distance dependence of the force acting on the tip is calculated above several surface sites, taking into account the surface and tip relaxation. Following the results of classical calculations described in section 2.1, we have chosen the Al site and the centre of the triangle formed by 3 surface oxygens, denoted by 3O in the following

discussion, as representative sites with cationic and anionic characters, respectively. The individual oxygen sites are also considered to ensure consistency with previous studies.

Figure 27 shows the site-dependent forces acting on the Si tip with a dangling bond over the characteristic sites of the MgO(001) and Al<sub>2</sub>O<sub>3</sub>(0001) surfaces. The two insets detail the structure of the top layer of these surfaces. The graphs on the green background present the estimates of the charge redistribution between the tip and the surface on the basis of the Mulliken analysis.

The force vs. distance curves in Figure 27 represent only the short-range “chemical” component of the tip-surface interaction, and do not include the long-range van der Waals forces. Figure 27 demonstrates that the interaction above both the Al and oxygen sites is attractive at large distances ( $> 2.5$  Å). At the distances smaller than 2.5 Å, we observe the onset of repulsion.

The interaction above the 3O site is the strongest one ( $F_{\min} = -7.0$  nN) over the alumina surface. Moreover, there is an overall attraction even at distance of 2.0 Å. The latter is due to the interaction of the Si apex atom with the group of three oxygen ions, which effectively may lead to the Si atom being removed from the tip and being adsorbed onto the surface. This is manifested by a 0.55 Å displacement of the tip Si atom from its stable position in the free tip at a tip-surface distance of 3 Å.

The interaction above Al sites with a Si tip is also attractive, although weaker than that above oxygen sites (Figure 27). The attractive force acting on the tip at this site reaches 1.0 nN at 3.5 Å and remains at this level at 3.0 Å, but switches into repulsion at 2.5 Å. Very similar behaviour over the same range of interatomic distances is observed over the Mg site in MgO(001). We compared this behaviour with the interaction of an identical Si tip with cations in CaF<sub>2</sub> and TiO<sub>2</sub><sup>141</sup>. The force curves allow us to suggest that the position and depth of the minimum of the force-distance curves qualitatively correlates with the length and strength of the corresponding Si-Me bond (Me=Al, Mg, Ca, Ti) in a diatomic molecule. For instance, we observe a particular large force over Al, which correlates with the large value of the enthalpy of formation of the Al – Si molecular bond (about  $229.3 \pm 30.1$  kJ/mol)<sup>142</sup> compared to other metals, such as Mg, Ca and Ti<sup>143</sup>.

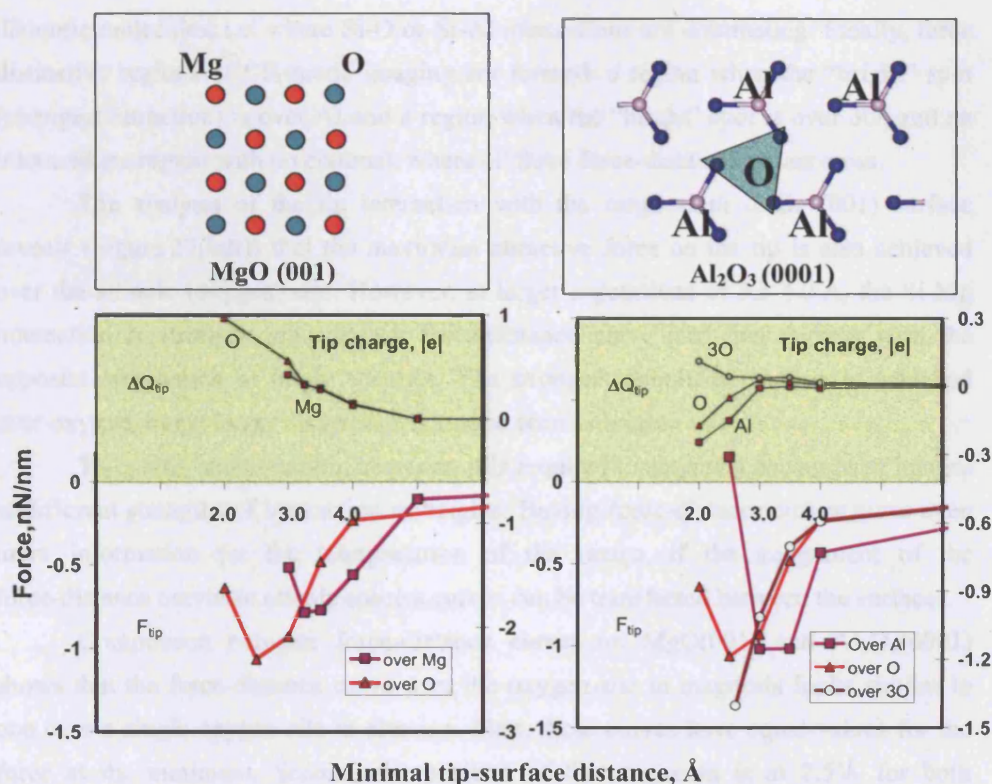


Figure 27. Force-distance curves for the interaction of the Si dangling bond tip ( $\text{Si}_{10}\text{H}_{15}$  cluster) with  $\text{MgO}$  (001) and  $\text{Al}_2\text{O}_3$  (0001) surfaces calculated above characteristic surface sites. The upper section (shaded in green) of each graph presents charge transferred to the tip as the tip-surface distance is reduced. The left axis corresponds to the force-distance curve, the right axis - to the charge transfer to the tip. Negative force corresponds to attraction to the surface.

The increase in the force acting on the tip correlates with the displacements of surface atoms and a significant charge redistribution between the tip and the surface according to the Mulliken population analysis (Figure 27). The surface displacements of the Al atoms are larger than those of the surface oxygens by an order of magnitude, which correlates with soft vibrational modes involving the surface Al ions proposed for the  $\alpha$ -alumina (0001) surface on the basis of LEED analysis<sup>144</sup>.

From the perspective of NC-AFM imaging, the study demonstrates the feasibility of atomic scale resolution: the difference in the force acting on the tip over 3O and Al varies between 0.2-1.2 nN (Figure 27). Therefore, the atomic sites of Al and sites corresponding to  $[\text{3O}^2]$  groups can be clearly distinguished over two ranges of distances once it has been proved that neither the surface nor the tip are contaminated. At the “intermediate” distance of 3 Å, however, the forces are equal for all three sites under consideration, which means that the contrast diminishes. The two regions (below and above 3 Å) are roughly defined by the interatomic distances in the corresponding

diatomic molecules, i.e. where Si-O or Si-Al interactions are dominating. Finally, three distinctive regions of CH mode imaging are formed: a region when the “bright” spot (strongest attraction) is over Al and a region when the “bright” spot is over 3O, and an intermediate region with no contrast, where all three force-distance curves cross.

The analysis of the tip interaction with the magnesium oxide (001) surface reveals (Figure 27(left)) that the maximum attractive force on the tip is also achieved over the anionic (oxygen) site. However, at larger separations of 3.5-4.0 Å, the Si-Mg interaction is stronger, splitting the force-distance curve into two regions with the opposite assignment of bright features. The strongest overall interaction is achieved over oxygen, but at larger distances Mg can be seen as bright.

To enable interpretation, however, it is required to acquire a sequence of images at different strengths of interaction or heights. Having force-distance curves gives even more information for the interpretation of the image, if the assignment of the force-distance curves to atomic species curves can be transferred between the surfaces.

Comparison between force-distance curves on MgO(001) and Al<sub>2</sub>O<sub>3</sub>(0001) shows that the force-distance curve over the oxygen site in magnesia looks similar to one over a single oxygen site in alumina. First, these curves have equal values for the force at the minimum. Second, the position of the minimum is at 2.5 Å for both surfaces. Finally, the shape of the force-distance curve over oxygen is almost identical for the two surfaces. This indicates that in spite of the differences in the atomic environment and less ionic bonding in alumina, the Si tip “sees” these oxygen ions as similar species, according to Figure 27.

If similar distinctive footprints can be obtained for oxygen on other surfaces, it will allow chemical identification of the oxygen O<sup>2-</sup> ions on a surface with a Si tip with a dangling bond. Experimental confirmation of such a result is most likely to come from low-temperature NC-AFM studies, where site-specific force-distance curves are currently being developed as a standard, while preparation, maintenance and identification of the Si dangling bond on the apex of the tip is a great challenge for oxide surface studies.

In this section we have investigated the interaction between the dangling bond Si tip and the ionic surfaces of MgO and Al<sub>2</sub>O<sub>3</sub>. The Si tip allows one to discriminate anionic and cationic sites on insulating oxide surfaces from a sequence of NC-AFM images. The significant contrast in the image arises due to the instantaneous charge redistribution between the tip and the surface when the dangling bond approaches an anion on the surface. The strength of the force at a given tip-surface separation is larger over ions, which form stronger bonds with Si. The strongest overall interaction for oxides, therefore, is over anionic groups. The similarity of the force-distance curves

over the oxygen sites of the two surfaces does not guarantee transferability of the force curves, but calls for extra study into this topic. Importantly, NC-AFM imaging with a Si dangling bond allows straightforward interpretation of atomic scale resolution images from a sequence of images or site-dependent force-distance curves.

### **2.3 Effect of Si tip contamination on the tip-surface interaction**

In the previous section it was shown that the Si dangling bond strongly interacts with the oxide surface. The interaction at a small distance may also result in the tip damage. However, an alternative scenario of interaction is the interaction of the tip with adsorbants, which may result in tip contamination. In this section we assess the effect of tip contamination on the strength of the tip-surface interaction.

In this study we use the classical ionic MgO(001) surface as a substrate contacted by a range of tips including where the apex dangling bond is contaminated by hydrogen (Si-H) or a hydroxyl group (Si-OH) and a fully oxidized tip modelled by a MgO cube (section 1.5.1). The choice of the contaminants is dictated by the presence of water vapour in the UHV chamber. The calculations are performed at the DFT level (section 1.3.1) and compared with DFT results for a pure Si tip with a “dangling” bond (section 2.2).

To distinguish between a “weak” and “strong” interaction we first define the scale and sensitivity of the method. With a NC-AFM probe one can measure forces of the order of 0.1 nN while a difference in force of 0.01 nN between two sites can be detected. In constant frequency shift (CFS) mode, corrugations of a few picometers are measurable. The presence of noise often decreases the sensitivity of the method by an order of magnitude. However, a further improvement of the precision can be achieved in purpose-built low temperature devices. The stability of the experiment at low temperatures allows measurement of site-dependent force-distance curves routinely<sup>43</sup>.

To compare the strengths of the tip-surface interaction provided by the tip models and yet avoid calculation of the full force-distance curve, we position the tips at the characteristic distance ( $z = 3.0 \text{ \AA}$ ) from the surface to characterise the strength of the interaction. The distance is chosen from previous theoretical investigations of NC-AFM imaging of the oxide surfaces as reviewed in references<sup>38,43</sup>.


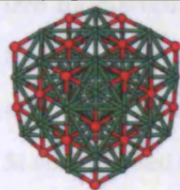


To study the tip-surface interaction, full relaxation is applied to 2 surface layers and the 4 outermost Si atoms of the tip. Finally, the z-component of the force acting on the whole tip is calculated by summation of the z-components of the force acting on individual atoms of the tip. Since we aimed to study the qualitative effect of contamination, the tip models are positioned above the site where the strongest



interaction is expected, which, for the chosen tip models and the ideal MgO(001) surface, is the O site.

The results of the *ab initio* calculations are presented in Figure 28. The atomic structure of the Si-based tip and the fully oxidized Si tip models is shown in the lefthand column. The values of the force and of the values of the displacements in the tip and in the surface are listed in the table (Figure 28). All numbers presented in this table are calculated for a tip-surface separation of 3.0 Å, where the separation distance is defined as the distance between the apex atom of the tip and the nearest atom of the surface. The numbers in the table detail the relaxation of the tip apex atom and the corresponding surface atom along the normal to the surface. The last column of the table summarizes the total change in the distance between the two atoms due to the relaxation.

Figure 28 shows that the strongest tip-surface interaction (1870 pN and 1846 pN respectively) over O is observed with a pure Si tip and a Mg-terminated  $\text{Mg}_{32}\text{O}_{32}$  tip. The interaction of the oxide surface with a tip apex carrying a dangling bond is as strong as the interaction with a completely oxidised tip. Both tip apexes are able to produce measurable (1-1.4 nN) force contrast on the surface. The strongest interaction in the case of the contaminated tip apexes (-H, -OH) is several times less than that of a pure Si tip with a “dangling bond” tip or an “oxidized” tip.

					
Si					
					
MgO					
					
Si-OH					
					
Si-H					

(Tip)-Atom	Force, pN	$\Delta z_{\text{apex}}, \text{\AA}$	$\Delta z_{\text{tip}}, \text{\AA}$	$\Delta d, \text{\AA}$
(Si)-Mg	484	0.07	0.05	0.12
(Si)- <u>O</u>	1870	0.22	0.16	0.38
(MgO)- <u>O</u>	1846	0.12	0.18	0.3
(Si-OH)- <u>O</u>	443	0.04	0.13	0.17
(Si-H)- <u>O</u>	274	0.08	0.06	0.14

Figure 28. *Ab initio* forces acting at 3.0 Å on tips positioned over the oxygen site of MgO(001) surface for different tip models: pure silicon tip with a dangling bond, rigid oxide tip with positive apex potential (front view), Si tip with the dangling bond saturated by an OH or H. The force acting on the Si tip with a dangling bond over the Mg site of MgO(001) surface is presented for a comparison. (Table 6 is reproduced here for the sake of the reader's convenience).

The three last columns of the table display the magnitude of relaxation in these systems. This ranges from 0.04 to 0.22 Å in the tip and 0.05 to 0.18 Å at the surface. Systems with weaker forces exhibit smaller relaxations, while the largest relaxations of 0.38 Å and 0.3 Å are observed in the case of pure Si and oxidised tips.

Comparison of the considered models highlights the weak reactivity of the contaminated tips compared to a pure Si tip with a dangling bond or a oxidized tip. Models of a pure Si tip and an oxidized tip give a higher degree of contrast, i.e. the difference in the force over Mg and O sites, but these tips are also more easily contaminated in the vicinity of the surface.

The major experimental problem is that the image is often the only source of information about the structure and chemical composition of the tip apex<sup>145,146</sup>. This again leads to an ambiguity in the interpretation, because it is not known whether the oxide tip with positive/negative potential contacts the surface or the pristine Si tip does. Differentiation between a pure Si apex and one of the polarities of an oxide tip might be possible if site-dependent force-distance curves can be acquired. These curves enable the direct comparison of the difference in the interaction over the characteristic sites between experiment and DFT calculations. The site-dependent force-distance curves are rare for conventional UHV NC-AFM at room temperature (RT), because of the high level of noise and thermal drift. However, a sequence of images with resolved ionic sublattices, obtained with no tip change, may also allow the differentiation between pure Si and oxidised tips.

## **2.4 Summary**

Two models of the tip are implemented to study NC-AFM contrast formation on hard oxide surfaces; one with a dangling bond on the apex (Si tip model) and the other with a strong electrostatic potential (oxide tip model). The pure Si tip model of the AFM tip apex has been applied to the study of oxide surfaces for the first time.

According to the DFT results the strength of the site-dependent interaction over the oxide surfaces studied using a dangling bond at the apex of a Si tip is determined by reversible charge redistribution between the dangling bond and atoms of the substrate.

This redistribution depends on the chemical nature of the surface site and, therefore, allows straightforward chemical interpretation of the image. The maximum overall interaction is achieved over anions or group of anions ( $[3O^{2-}]$  for  $Al_2O_3$ ). However, the interpretation may also become ambiguous, for instance, for a certain range of heights over the  $Al_2O_3$  surface. In this case, site-dependent force-distance curves or a sequence of images taken over a representative range of interactions could allow experimentalists to distinguish between cationic and anionic sites.

It was demonstrated that using the oxide tip model of an atomically sharp tip,  $Al^{3+}$  ions and oxygen  $[3O]^{6-}$  groups can be resolved in CFS and CH modes on the clean unreconstructed  $\alpha-Al_2O_3(0001)$  surface with realistic parameters for the NC-AFM setup. Identification of the cationic and anionic sublattices and of the sign of the oxide tip potential could be possible on the basis of a detailed scanline analysis.

It is shown that for an atomically sharp ionic tip rotation and tilt of the tip apex change the image pattern. It was also demonstrated that for the atomically sharp oxide tip model that the pattern of the image depends on the orientation of the tip apex with respect to the surface ions due to the asymmetrical shape of the electrostatic potential of the tip.

At small nominal distances of below 2.0 Å between the tip and the oxide surface the apexes of both tip models considered in this work adhere strongly to the surface. This may result in an irreversible change to the tip apex. There are two possibilities: material is transferred from the surface to the tip or vice versa. In the latter case this effect undermines the success of the “gentle contact” technique, used by experimentalists to sharpen the tip via contact with the surface. Such behaviour is one possible explanation for the experimental difficulties in obtaining atomic resolution on the  $\alpha-Al_2O_3(0001)$  surface.

### 3 Contrast formation in imaging of HCOO<sup>-</sup> anion on MgO(001)

The chapter discusses NC-AFM contrast formation on the MgO(001) surface in the presence of an adsorbed HCOO<sup>-</sup> formate anion. The adsorption of the molecule onto the surface is studied using the Embedded Cluster Method. The results of this study are used to fit the parameters of the potential functions for the MgO-HCOO system. The tip-surface forcefield is calculated by means of static structural optimisation using these potential functions. The study of NC-AFM contrast formation in a “*molecule + surface*” system assesses resolution within the formate molecule, the effect of the tip-molecule interaction on imaging of a surface with a dilute monolayer, the effect of the macroscopic tip-surface interaction on the contrast in CFS mode and looks into the possibility of atomic resolution on the surface in the presence of adsorbed molecules.

The interpretation of molecular NC-AFM images is not well developed. The approach to image interpretation is often borrowed from NC-AFM imaging at larger scale or even from contact mode AFM. The field of high resolution molecular imaging also lacks empirical understanding - we do not know from experiment for which systems high resolution can be produced and what information about the system an image can provide. In particular, there is very little consideration of the optimal experimental parameters required for imaging adsorbed molecules.

The development of NC-AFM instruments has led to high resolution imaging of surfaces with molecular adsorbates, such as carboxylic acids (R-COOH)<sup>147</sup>, biphenyls<sup>148</sup> on TiO<sub>2</sub>(110), thiols on gold<sup>149,150</sup>, and C<sub>60</sub> on silicon<sup>151</sup> and gold<sup>152</sup>. However it proved to be difficult to resolve individual atoms within adsorbed molecules using AFM. Therefore we discuss “high” resolution, which here refers to resolution of features within the molecule with sizes below 1 nm<sup>33,153</sup>. The size of resolved species is comparable with the distance between bright features on atomically resolved surfaces with large lattice constants, such as KBr(001) or KI(001), where the distance between the bright spots is of the order of 0.7 nm<sup>50</sup>.

From an experimental perspective, the detection of an adsorbed molecule with a distinctive shape or size on the ionic lattice could make it possible to distinguish between sublattices, which cannot be discriminated otherwise, such as Mg and O sublattices on MgO(001) when observed with an “oxide” tip. This approach has been applied to the experimental study of TiO<sub>2</sub>(110) surface – the presence of oxygen vacancies in the bridging oxygen row allows Ti rows from O rows to be differentiated on this surface<sup>32</sup>.

The utility of introducing molecules as markers is determined by the ability to experimentally resolve the substrate sublattices and individual adsorbate molecules

simultaneously. The  $C_{60}/KBr^{152}$  system is a rare example where high resolution is achieved simultaneously on clusters of the adsorbate and on the substrate. However, the results for formate ( $HCOO^-$ ) on  $TiO_2(110)$  have demonstrated that the quality of the image is generally much lower in the presence of a dilute monolayer of formate<sup>147</sup> compared to the clean surface or monolayer at full coverage.

The limit of NC-AFM resolution within an adsorbed molecule is also an open question which lacks experimental data. For planar ionic surfaces, it has been shown that resolution can be obtained between lattices with interatomic distances down to  $2.1 \text{ \AA}^{35}$ , which is in accordance with theoretical simulations using the rigid oxide tip model<sup>48</sup>. However, such a level of resolution has not yet been achieved with NC-AFM of molecules on insulating surfaces.

On insulating surfaces, high resolution is available because of the significant force contrast provided by the interaction between the strong electrostatic potential of the oxide tip and charges of the opposite sign on the surface<sup>42,154</sup>. If there is no significant variation in the interaction, the contrast can be lost. In the previous chapter, for instance, it was shown that O atoms separated by a distance of  $2.7 \text{ \AA}$  cannot be resolved on the  $Al_2O_3(0001)$  surface using an oxide tip. This fact highlights that it is not atoms, but the variation in interaction that is being resolved<sup>155</sup>.

In this chapter we consider a rigid oxide tip model and choose a formate anion as the trial molecule, which combines a polar ( $COO^-$ ) and less polar group ( $C-H$ ). This anion is relevant to the study of carboxylic acid ( $R-COOH$ ) adsorption, formation of SAMs on ionic surfaces<sup>156</sup>, and has been widely studied as a product of formate dissociation on ionic surfaces<sup>114,157,158</sup>. As an anion, the molecule interacts electrostatically with the oxide tip; therefore we chose a tip with positive tip potential to increase the tip-molecule attraction.

We use modelling to develop the main principles of contrast formation in an NC-AFM image of the molecule and its vicinity, and to identify the critical parameters which determine the resolution of the molecule. We compare the interpretation of the image in the presence of an adsorbed molecule to the interpretation of clean atomically resolved surfaces. The resolution of individual sublattices of the surface is studied in the presence of the molecule to validate the possibility of using small molecules as “markers” of sublattices on the surface. Finally we take the experimentalist’s viewpoint to analyze simulated images and assess the effect of the tip radius on the contrast in the image.



To set up the model, we study the adsorption of a formate anion on the MgO(001) surface. The Embedded Cluster Method is used to eliminate the artificial interaction between images of charged formate molecules and to employ a DFT exchange-correlation functional with an admixture of the exact exchange. The adsorption study includes the analysis of the vibrational frequencies of the system and soft modes related to the lateral motion of the molecule. The results of the *ab initio* adsorption study are used to fit interatomic potential functions describing the interaction between atoms of the molecule and of the surface. The potentials developed allow us to increase significantly the speed of calculating the NC-AFM image.

The chapter is organized as follows: the system is first characterised in the *ab initio* adsorption study (3.1); the tip-surface forcefield is calculated on the basis of the developed potential functions and existing potential sets for the surface and for the molecule (3.2); the analysis and interpretation of simulated NC-AFM images are presented in (3.2.2). The effect of the presence of the molecule on the surface resolution is addressed in (3.3). The discussion of the result concludes the chapter and draws links with experiment.

### 3.1 *Ab initio* calculations of the formate anion on MgO(001)

In this section we study the formate-MgO(001) interaction at the *ab initio* level and propagate the results to the level of molecular mechanics (MM). Such approach is necessary because there is lack of force fields that can tackle both organic molecules and ionic solids. Although there are new force fields describing combined systems, they are still at the stage of development<sup>159</sup> hence a new purpose-built forcefield was required to carry out an effective study of NC-AFM contrast formation in this system.

We study adsorption of a single charged molecule ( $\text{HCOO}^-$ ) on the surface, in contrast to the previous works<sup>157,160</sup> which considered the electrostatically bound  $\text{HCOO}^- - \text{H}^+$  pair. The single  $\text{HCOO}^-$  system serves as an example of a charged adsorbate on the surface, which has not been discussed theoretically in the context of NC-AFM imaging.

Experimentally, the dissociative adsorption of formate on MgO(001) has been investigated at room temperature (RT) in desorption studies (TPD) combined with electronic structure investigation using XPS studies<sup>161,162</sup>. Its vibrational spectrum is known from experiments with infrared-visible vibrational sum-frequency generation (SFG)<sup>161,163</sup> and HREELS studies<sup>164</sup>. The studies agree on the preferentially “bridging”

adsorption of the dissociated formate anion on the MgO(001) surface, although modes identified as those of monodentate are also present.

The detailed study of polarization analysis within SFG suggests a broad distribution for the tilt angle<sup>160</sup> around the normal direction, which was confirmed by theoretical work done in the same group. That theoretical work demonstrated the dissociative adsorption of formic acid in an embedded cluster model and found the heat of adsorption to be 1.56 eV. Hopping of the proton between surface oxygens is characterised by a barrier of 3.88 eV, which halves in the vicinity of the formate anion. The orientation of the molecule and the softness of the tilt obtained in the experiment was explained<sup>165</sup> by the interaction with the neighbouring oxygen ion of the surface.

### 3.1.1 Adsorption of the formate anion on MgO(001)

The calculations for the formate adsorbed on MgO were performed using the embedded cluster approach to avoid periodic boundary conditions and to access B3LYP exchange-correlation functional, which reproduces better the wide bandgap of MgO. It is important to reproduce the bandgap correctly, to describe appropriately the bonding in adsorbate-substrate system. In particular, artificial charge transfer from the charged molecule to unoccupied surface states is overestimated if the width of the bandgap is reduced. The details of the Embedded Cluster Method, implemented in the GUESS code<sup>76,77</sup>, are discussed in the first chapter of this thesis (section 1.3.2). The quantum mechanical part of the calculations is performed using Gaussian 98<sup>78</sup>.

The calculations include: (1) static energy optimisation of the combined system HCOO<sup>-</sup> on MgO(001), and (2) calculation of several profiles of the adiabatic potential, which correspond to trajectories relevant to the study. The following molecular trajectories were calculated: retraction from the surface, tilt of the molecular plane and rotation in the plane with respect to one of the oxygens, so that another one is lifted upwards. The calculated energy profiles have been used to fit interatomic potentials for the molecule-surface interaction and should give a qualitative description of molecular behaviour near the equilibrium state. Our focus on non-contact AFM studies allows us to limit the number of configurations and energy profiles. We choose only those which are relevant to minor displacements from the equilibrium position.

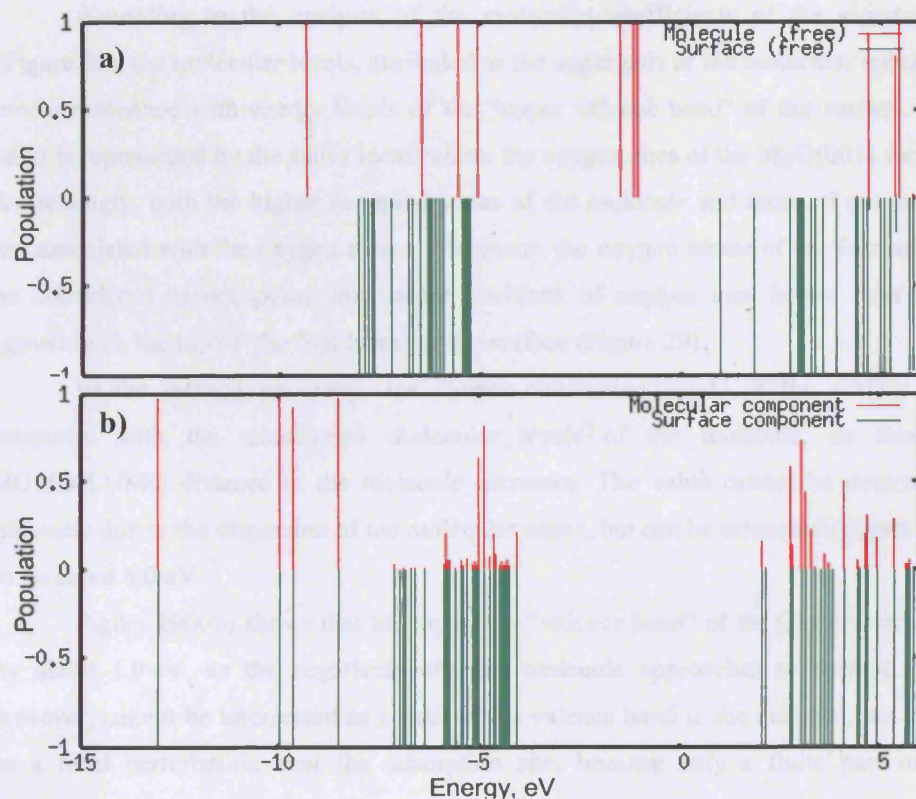


Figure 29. The eigenspectra of QM cluster of MgO(001) with a formate molecule. a) free QM cluster and free molecule (spectrum of eigenvalues). b) QM cluster with the adsorbed molecule in the equilibrium configuration (spectrum of eigenvalues). The different colours of eigenspectra demonstrate the nature of the state (red – molecule; green-substrate). Red lines in the eigenspectra indicate the percentage of the sum of squared coefficients of a state attributed to basis functions centred on the atoms of the molecule.

First, the total energy of the system was fully optimized starting with the formate anion in the “bridging” position above the two Mg atoms in the centre of the quantum cluster. According to the data obtained from the vibrational spectroscopy<sup>161,163,164</sup> study, this binding configuration is the most stable one. As a result of the optimization, the adsorbed formate molecule remained in the “bridging” upright position; with an adsorption energy of 2.1 eV.

The analysis of the electronic structure of the QM cluster with the adsorbed anion shows (Figure 29) an increase in the difference between the eigenvalues of HOMO and LUMO levels  $E_{O-U}$ , as the molecule approaches to the surface. At the large distance of 10 Å between the molecule and the cluster, the  $E_{O-U}$  is determined by the HOMO-LUMO split of the molecule – 4.3 eV. At the equilibrium distance, the value of  $E_{O-U}$  is determined by the “bandgap” of the surface (6.0 eV).

According to the analysis of the molecular coefficients of the eigenvalues (Figure 29), the molecular levels, attributed to the upper part of the molecular spectrum, are in resonance with energy levels of the “upper valence band” of the surface. This band is represented by the states localized on the oxygen sites of the MgO(001) surface. Interestingly, both the higher occupied states of the molecule and those of the surface are associated with the oxygen atoms. Moreover, the oxygen atoms of the formate can be considered as occupying the vacant positions of oxygen ions in the next layer (growing on the top of the first layer) of the surface (Figure 29).

In the relaxed geometry, the “lower conduction band” of the surface also resonates with the unoccupied molecular levels of the molecule, so that the HOMO-LUMO distance in the molecule increases. The value cannot be determined precisely due to the dispersion of the molecular states, but can be estimated (Figure 29b) to be about 6.0 eV.

Figure 29(a-b) shows that the top of the “valence band” of the QM cluster shifts by about 1.0 eV, as the negatively charged molecule approaches to surface. This, however, cannot be interpreted as a shift of the valence band in the material, but rather as a local perturbation near the adsorption site, because only a finite part of the electronic subsystem is taken into account.

The flavour of the bond formed between the molecule and the surface is a crucial question. In particular, it determines the choice of the functional form to be used in the interatomic potentials describing the interaction between the atoms of the molecule and the surface. According to Figure 29, molecular basis functions contribute significantly to the eigenvectors of states in the valence band when the molecule is adsorbed. However, we interpret it as an artefact of the localized basis set.

We have selected several eigenfunctions in the spectrum (Figure 29b) with a significant admixture of the molecular states for visual analysis. The criterion for selecting these eigenfunction is following: the sum ( $S$ ) of the squared coefficients attributed to the basis functions centred on the atoms of the molecule should be greater than 10%. The shape of the wavefunctions is assessed visually by drawing isosurfaces and cross-sections. The cross-sections passing through plane ( $\text{Mg}^{\text{surf}}\text{-O}^{\text{mol}}\text{-C}$ ) or ( $\text{O}^{\text{surf}}\text{-C-O}^{\text{surf}}$ ) and isosurfaces at values in the range  $(-0.05)\text{-(}+0.05\text{)} |e|/(\text{Bohr})^3$  are considered. However, no covalent molecule-surface “bonding” states were found among the wavefunctions considered. Figure 30 shows an example of an eigenfunction with a significant contribution from the molecule: the sum of squared coefficients is 20% for the HOMO orbital of the system.



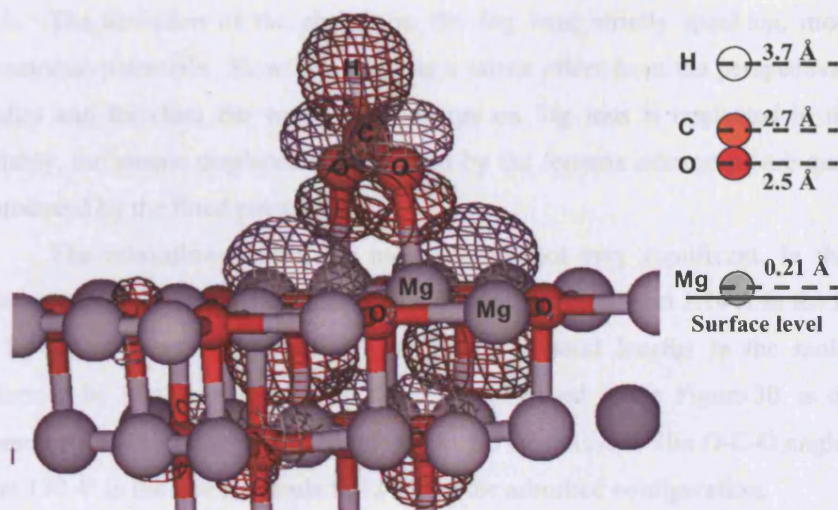


Figure 30. Relaxed configuration of an adsorbed  $\text{HCOO}^-$  anion on the  $\text{MgO}(001)$  surface calculated within Embedded Cluster Method. The schematic on the right shows the height of the atoms of the molecule and the displaced Mg atoms of the surface with respect to the equilibrium z-position of oxygen atoms on the clean perfect terrace (surface level). The isosurface of the HOMO orbital of the system is presented in the picture for the isolevel of  $0.05 |e|/(\text{Bohr})^3$ .

The results of the eigenspectrum analysis are strongly supported by the population analysis. Natural population analysis (NPA) gives charges of  $-0.85 |e|$  for the  $\text{O}^{\text{mol}}$  atoms,  $+0.66 |e|$  and  $+0.1 |e|$  for C and H atoms respectively (Figure 30), so that the total charge on the molecule amounts to  $-0.94 |e|$  in this calculation. The value of the charge on the formate anion is not affected significantly by the surface and remains about  $-0.9 |e|$  at all distances. In a free formate ion, the charges on oxygen, carbon and hydrogen atoms are  $-0.82 |e|$ ,  $0.58 |e|$  and  $0.06 |e|$  respectively.

Comparison of the numbers above and the analysis of the electronic structure show that charge redistribution between the molecule and the surface can be neglected in the construction of potential functions. Hence, we use standard Buckingham-type potentials to describe the interaction between ions of the surface and ions of the molecule.

As the result of the relaxation, magnesium ions located directly underneath the molecule are displaced towards the molecule by  $0.24 \text{ \AA}$  in the equilibrium configuration (Figure 30). The NPA charges of the substrate Mg atoms beneath the molecule decreased by  $0.02 |e|$ , as the molecule has approached and by the  $0.1 |e|$  as the Mg atoms moved upwards. The changes in the atomic charges on other atoms of the surface compensate the change on Mg ions, while individual charges do not change by more than  $0.02 |e|$ .



The deviation of the charge on the Mg ions, strictly speaking, modifies the interatomic potentials. However, this has a minor effect from the perspective of AFM studies and therefore the variation in charge on Mg ions is neglected in this study. Notably, the atomic displacements induced by the formate adsorption are qualitatively reproduced by the fitted potentials.

The relaxations within the molecule are not very significant. In the relaxed geometry the C-H bond of the adsorbed molecule shortens from 1.14 Å in the free anion to 1.11 Å, and stands almost upright. The C-O bond lengths in the molecule are deformed by less than 0.5 %. The slight tilt, observed in the Figure 30, is due to the asymmetry of the molecular position within the QM cluster. The O-C-O angle changes from 130.4° in the free molecule to 128.7° in the adsorbed configuration.

The overall deformation is characterised by the “relaxation energy” of the molecule, which is defined as the difference between the total energy of standalone molecule, calculated in the adsorbed geometry, and the total energy of a free molecule. The value of the relaxation energy is 0.01 eV, which means that the adsorbed molecule is virtually not deformed. Therefore, we can describe the mechanics of the adsorbed molecule using conventional force fields.

An important implication of the symmetry of the relaxed molecule is a soft tilting potential of the molecule arising from the attraction between the two nearest negative O ions of the substrate and the positive charge distributed over carbon and hydrogen. As a result, the molecular tilt of 60 degrees with respect to the surface normal costs only 0.4 eV.

According to the experimental interpretation of the vibrational spectrum<sup>161,163,164</sup>, the bidentate configuration (i.e. both oxygen atoms of the formate bond to the same cation) should also be present on the surface. We performed an ECM relaxation for the molecule in the bidentate configuration for the same cluster as discussed before. The carbon atom of the formate molecule was fixed laterally over an Mg ion; all other atoms of the molecule were allowed to relax. The relaxation demonstrated that the bidentate configuration is 0.8 eV less favourable than “bridging” the position. This calculation rules out the possibility of adsorption of formate on the perfect terrace in the bidentate position, but still allows it near a defect.

Unfortunately, the calculated adsorption energies for the *formate ion* do not compare directly with the previous theoretical studies of the adsorption of the *formic acid molecule*. The values of the adsorption energy, calculated in this work, do not contradict, but at the same time cannot be directly compared to the experimental TPD

results on HCOO<sup>-</sup> because of the dehydration reaction taking place at 500-700 K. Otherwise, the stability of the “bridging” configuration fits well into the simple description of the bonding as dominated by the interaction between the positive Mg<sup>2+</sup> cations of the surface and the negative oxygens of the formate anion.

To conclude with the *ab initio* description of the system and characterize the degree of the discrepancy with the experiment, we perform vibration frequency analysis within the ECM. The frequencies, calculated for the free molecule and for the adsorbed molecule+cluster system, are compared (Table 7) with the available experimental data for the free anion<sup>166</sup> and adsorbed formate on MgO(001) surface<sup>167</sup>. The eigenvectors were limited to the displacements of the atoms within the QM cluster.

The most significant discrepancy is observed for the C-H stretching mode of the molecular ion. A similar tendency for the formate anion was reported in reference<sup>166</sup>, where a change from HF to post-HF methods decreased the stretch frequency of the C-H bond for an extensive range of basis sets. In this work the 6-31+G\* basis was used and our HF value for the C-H stretch of 2722 cm<sup>-1</sup> matches well the theoretical<sup>166</sup> value of 2795 cm<sup>-1</sup>.

This qualitative description is useful for visualisation of the low energy vibrational modes, which highlight the dynamic behaviour of the molecule expected on the surface. Figure 31 shows some characteristic motions, found in the vibrational spectrum of the system. While the bending modes (79-223 cm<sup>-1</sup>) (Figure 31a) can be expected

Table 7. Frequencies of molecular vibrations of formate anion on MgO(001) surface. Values obtained in this work are compared with available experimental data<sup>167</sup>.

<i>Frequencies, (cm<sup>-1</sup>)</i>						
<i>Type</i>	<i>Stretch</i>	<i>Out-of plane Bending</i>	<i>Symmetric stretch</i>	<i>In-plane bending</i>	<i>Asymmetric Stretch</i>	<i>Stretch</i>
<i>Bond</i>	<i>C-O</i>	<i>C-H</i>	<i>C-O</i>	<i>C-H</i>	<i>C-H</i>	<i>C-H</i>
Free molecule ( <i>experiment</i> )	773	1069	1352	1386	1584	2825
Adsorbed on MgO(001) ( <i>experiment</i> )	761	1081	1340	1395	1630	2907
Free molecule	735	1048	1301	1432	1679	2585
Adsorbed on MgO(001)	738	1054	1333	1425	1590	2988

because of the soft tilt potential, the sliding mode with frequency ( $90\text{-}191\text{ cm}^{-1}$ ) (Figure 31b) or “swinging” mode ( $146\text{ cm}^{-1}$ ) (Figure 31c) give an insight into the dynamics of the molecule. These modes can be closely related to the diffusion of the formate on the surface because extrapolation of the mode motion transfers the molecule into an equivalent position.

Among the eigenmodes, where the molecular motion is significantly involved, only a few modes are likely to result in the diffusion of the molecule. For instance, the rolling of the molecule, extrapolated from the bending mode, is unlikely, since it requires about  $2.1\text{ eV}$  to break the bond. The sliding of molecule along the rows of Mg atoms only stresses bonds but does not require bond breakage.

The “swinging” mode can be extrapolated into a diffusion path, which involves spinning, translation and tilt of the molecule. Figure 32 illustrates the transition from the initial to final positions of the formate molecule with respect to the matrix of surface sites. The shaded sites are sites of adsorption (Mg) which attract O ions of formate; clear rectangles correspond to the oxygen sites, which attract the C-H group and repel O ions of the molecule.

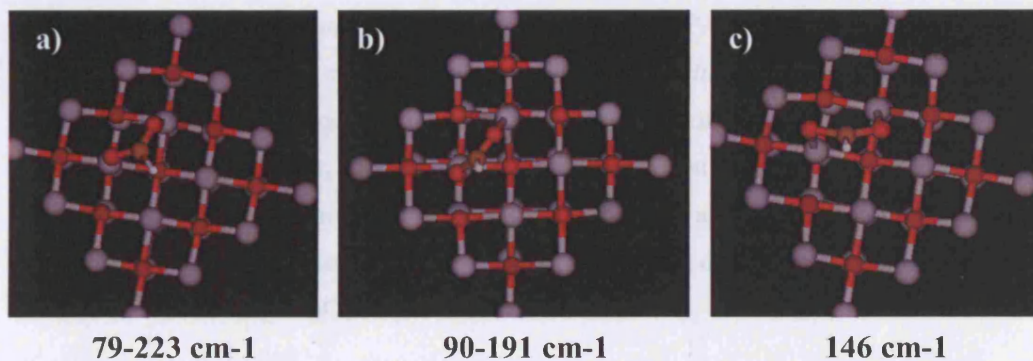


Figure 31. Typical low-lying vibrational modes of the  $\text{HCOO-MgO}(001)$  system with eigenvectors primarily related to the molecular motion. The images show atomic displacements from equilibrium position along the following modes: (a) bending modes in range  $79\text{-}223\text{ cm}^{-1}$ , (b) sliding modes in range  $90\text{-}191\text{ cm}^{-1}$ , and (c) a “swinging” mode at  $146\text{ cm}^{-1}$ .



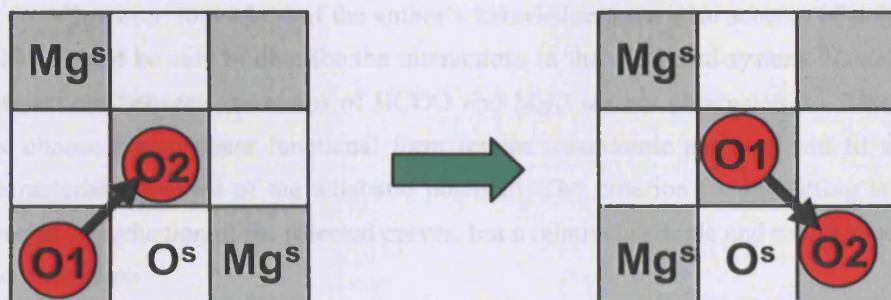


Figure 32. The schematic view of a possible diffusion path for the “swinging” mode. The shaded squares represent the Mg sites, white squares – O sites; red circles identify oxygen atoms of the formate. In this mode O1 moves to the site previously occupied by O2, O2 moves to the new site. The positive C-H group bends over the surface oxygen ion  $O^s$  during the motion.

For the NC-AFM studies we need an estimate of the lateral mobility of the molecule on the surface, to ensure that the molecule will remain on its site during the imaging. According to the *ab initio* vibrational analysis, the softest mode which could be related to the lateral diffusion, is the sliding mode. For this mode we can easily identify the configuration, which corresponds to the crossing of the barrier between the two equilibrium configurations. Luckily, this configuration coincides with the bidentate configuration studied above. Therefore, the diffusion barrier for the formate molecule on the surface can be estimated as 0.8 eV, which means that the molecule is likely to remain on its sites at the room temperature i.e. for  $kT \approx 0.025$  eV.

In conclusion, the chosen precision of the *ab initio* calculation does not reproduce the molecular frequencies quantitatively, nor the shift in molecular frequency due to adsorption. However, it gives a qualitative description of adsorption, diffusion barriers, vibrational eigenfrequencies and eigenvectors. It also allows us to derive interatomic potentials used later in this work in the modelling of NC-AFM imaging of a formate molecule on the MgO(001) surface.

### 3.1.2 Fitting interatomic potentials

An atomistic description of the interactions in the formate-MgO system via interatomic potentials is required to speed up the calculation of the tip-surface force field, essential for the construction of NC-AFM images. The interatomic potential functions already exist for the molecule and for the MgO crystal. To describe the interactions between the atoms of the molecule we use the CHARMM forcefield; the surface and the tip are described by Buckingham-type potentials and the shell model (1.3.3).

However, to the best of the author's knowledge there is no scheme of potentials which would be able to describe the interactions in the combined system. Namely, the interactions between the atoms of HCOO and MgO are not parameterised. Therefore, we choose a convenient functional form for the interatomic potential and fit several characteristic profiles of the adiabatic potential. The criterion for the fitting is not a precise reproduction of the selected curves, but a relatively simple and robust model for the interaction.

Only basic profiles of the adiabatic potential are chosen for the fit: the adsorption curve, tilt and rotation of the molecule with respect to one of the formate oxygens. The interaction between the HCOO<sup>-</sup> and the positive potential tip was also fitted. The interaction between Mg ion on the tip and C-H group of the molecule is fitted to reproduce the sequence of *ab initio* data corresponding to the approach of the free rigid molecule to the positive corner of MgO cluster representing a tip apex with a positive potential.

According to the results of the previous section (3.1.1), strong adsorption of the formate on the MgO(001) is determined by the electrostatic attraction between the negative oxygens of the formate and the positive ions of the substrate. Since no charge transfer of covalent bonding was detected, the Buckingham potentials functions are used to describe the interaction (1.3.3). The parameters of the interaction of four atomic pairs are used in the fitting: Mg-O<sup>f</sup>(formate); C-O<sup>s</sup> (surface), Mg-H<sup>f</sup> and Mg-C<sup>f</sup>.

The optimization of the parameters of these potential functions is performed with MERLIN – a powerful optimization software package available under a GNU license<sup>97,97</sup>. The software can search for the local minimum using BFGS, conjugate gradients, or steepest descent methods. It also enables global search on a mesh of points with an optional local search in the neighbourhood of each point. The cost function used in the fitting of the parameters is constructed as a weighted sum of squared deviations from the *ab initio* values. Weights are chosen empirically with large weights assigned to the configurations closer to the equilibrium. The total energies of the systems represented by the atomic potentials are calculated with GULP (1.3.3).

Three parameters enter into the expression of each interaction, which makes 12 parameters in total. Thorough optimization in this 12-dimensional parameter space is difficult to perform with a local optimisation method and is time consuming using available global search methods<sup>97,97</sup>. Therefore, the optimization was made in an hierarchical manner: first, global optimisation is performed for the most significant data; then the rest of parameters are fitted to the complete set of data using local optimisations. As the last step, all unknowns are fitted simultaneously using local minimization methods. The resulting potential parameters are listed in the Table 8.



Table 8. The potential parameters describing the molecule-tip interaction obtained by fitting of QM data

<i>Interaction</i>	<i>A, eV</i>	<i><math>\rho</math>, 1/Å</i>	<i>C eV/Å<sup>6</sup></i>
O-C(formate)	16.7397	0.6865	17.96
Mg-H(formate)	8359.876	0.211419	80.56
Mg-O(formate)	1778.47	0.263	0.0
O-H(formate)	145.840	0.425	37.61

### 3.2 Imaging a single HCOO-anion using the rigid oxide model

#### 3.2.1 Construction of the tip-surface forcefield

The set of potentials constructed in the previous section (3.1.2) is used here to build the tip-substrate forcefield for an oxide tip interacting with the formate anion on the surface. By analogy with our previous simulations using a MgO tip (section 2.1.2), the top of the tip cluster and the bottom part of the surface are kept fixed. Here, however, we use a cluster model (implemented in SCIFI) to represent the surface. Removing the periodicity speeds up the calculation since there is no more need to calculate the Ewald sum.

We chose an MgO cluster of 500 atoms (10x10) in 5 layers to represent the (001) surface of magnesium oxide. Two atomic layers along the boundaries of the cluster are kept frozen to avoid boundary effects during the optimisation. The tip-surface forcefield is calculated near the site where the molecule is adsorbed and covers an area of 10x10 Å. A fine grid with a 0.625 Å step in the  $x$  and  $y$  directions, resulting in 289 points per image was used. At every ( $x,y$ ) grid point the tip approaches the surface in small steps of 0.05 Å from a distance of 15 Å. The small step is chosen due to the soft bending mode of the adsorbed molecule. All approach curves used to construct the NC-AFM image are presented in Figure 34.

A close-up view of the surface with the adsorbed molecule and the tip is presented in Figure 34. The right image shows the schematic map of the surface close to the adsorption site: the red circles are Mg ions i.e. sites of possible adsorption, green sites are surface oxygens. The atoms of the molecule are denoted by two blue ions representing oxygens, grey and small green ions represent carbon and hydrogen respectively. In the absence of the tip, the equilibrium direction of the C-H bond is upright.

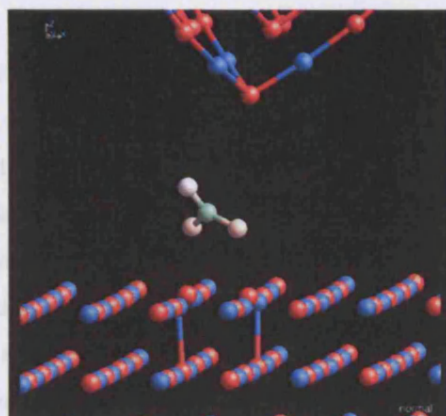


Figure 33 Distribution of z-component of the force acting on the Mg-terminated oxide tip 5.0 Å over formate anion on MgO(001) surface. Lateral dimensions of the cross-section are 10x10 Å. Force on the colorbar is given in nN. Positive values correspond to the attraction to the surface.

As was indicated in section 3.1.1, the molecule has a very soft bending potential. When the tip approaches the surface in the vicinity of the molecule the molecule bends aside (Figure 34 (left)).

Figure 34 (right) conveniently illustrates the jumps in the force that happen as the tip approaches the surface. For different lateral positions of the tip, the jump is seen at various tip-surface separations. The jumps are attributed to the molecule binding to the Mg atom at the apex of the tip. Such behaviour is not observed at separations above 5.0 Å in the static simulation, and therefore the image is constructed for heights above this threshold. The site-dependent contrast in the force-distance curves above the threshold decays within 1-1.5 Å. However, the threshold for “safe” imaging may also vary with temperature.

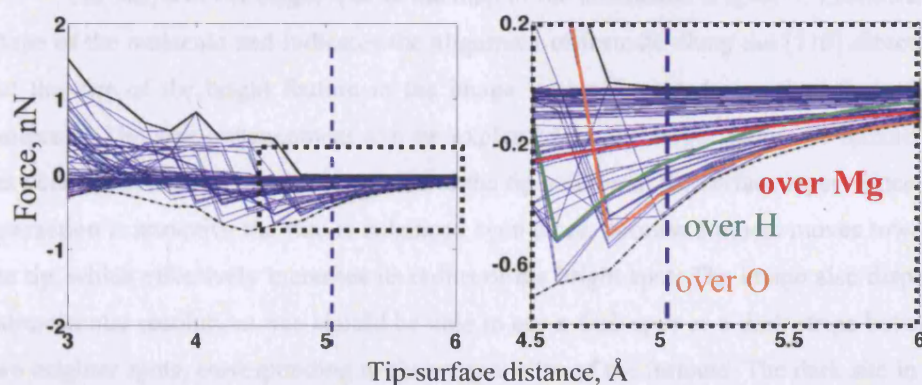


Figure 34. (left) Force curves for the oxide tip with positive potential.; (right) zoom into the region for tip-surface distance 4.5-6 Å. Dashed blue line indicates the closest tip-surface distance, where no jumps in force are observed.

To observe the effect of the temperature on the distance when the molecule jumps to the surface, a molecular dynamics simulation was run for 10.0 ps at constant temperature  $T = 300$  K with the formate molecule on the surface both in the presence of the tip at 5.0 Å and in the absence of the tip. The same code (SCIFI) and geometry are used as for the static simulation. A time step of 0.5 fs and a 1.0 ps equilibration period are used. The 10 ps duration of the simulation is sufficient to illustrate the instability of the system: the molecule jumps to the positive  $\text{Mg}^{2+}$  ion at the end of the tip and binds to it with both oxygen atoms. In the interpretation of the images it is assumed that they are recorded at low temperatures.

This MD simulation serves as an illustration that a molecule can be easily picked up by the tip potential at room temperature.

The cross-section of the forcefield calculated at 5.0 Å demonstrates that the interaction with the molecule is already measurable (of the order of 0.5 nN) at this distance, while no atomic contrast is seen on the  $\text{MgO}(001)$  surface. This means that constant height (CH) imaging mode can be applied to locate the anions adsorbed on the surface. The absence of contrast in the surface at this distance could have been attributed to the screening by the anion, but tests for the bare surface confirm that no measurable contrast over a terrace can be observed in a NC-AFM image in constant height mode over an ideal  $\text{MgO}(001)$  surface at this distance. The absence of contrast is in accordance with previous theoretical studies of NC-AFM imaging on the  $\text{MgO}(001)$  surface<sup>53,91</sup>.

### 3.2.2 Interpretation of the NC-AFM image

The shape of the bright spot in the map of the interaction (Figure 35) follows the shape of the molecule and indicates the alignment of formate along the [110] direction, but the size of the bright feature in the image is significantly larger than that of the molecule. The size enhancement can be explained by the larger radius of interaction between the anion and the tip, compared to the tip and ion in the surface layer. Since the interaction is attractive the size is enhanced even more, because formate moves towards the tip, which effectively increases its radius of the bright spot. The image also displays submolecular resolution: one should be able to see a dark spot or a dark stripe between two brighter spots, corresponding to the oxygen sites of the formate. The dark site in the centre corresponds to the centre of the molecule.

The tip-surface forcefield was used to simulate NC-AFM images for a range of setup parameters. Figure 35 shows the Constant Frequency Shift (CFS) image built



using the following parameters for the tip:  $R=100 \text{ \AA}$ ,  $H=1 \text{ eV}$ ,  $\alpha=20^\circ$  tip with  $k=35 \text{ N/m}$ . The frequency shift is quoted here as a normalized frequency shift to enable comparison between experiments using different imaging parameters. One can deduce the real world frequency shift by imagining an apparatus with the most convenient values for the parameters. For instance, a normalized frequency shift of  $\gamma=4 \text{ fNm}^{0.5}$  corresponds  $4 \times 10=40 \text{ Hz}$  frequency shift in a system with a stiff cantilever:  $k=10 \text{ N/m}$ , frequency  $f_0=10^5 \text{ Hz}$  and amplitude  $A=100 \text{ \AA}$ .

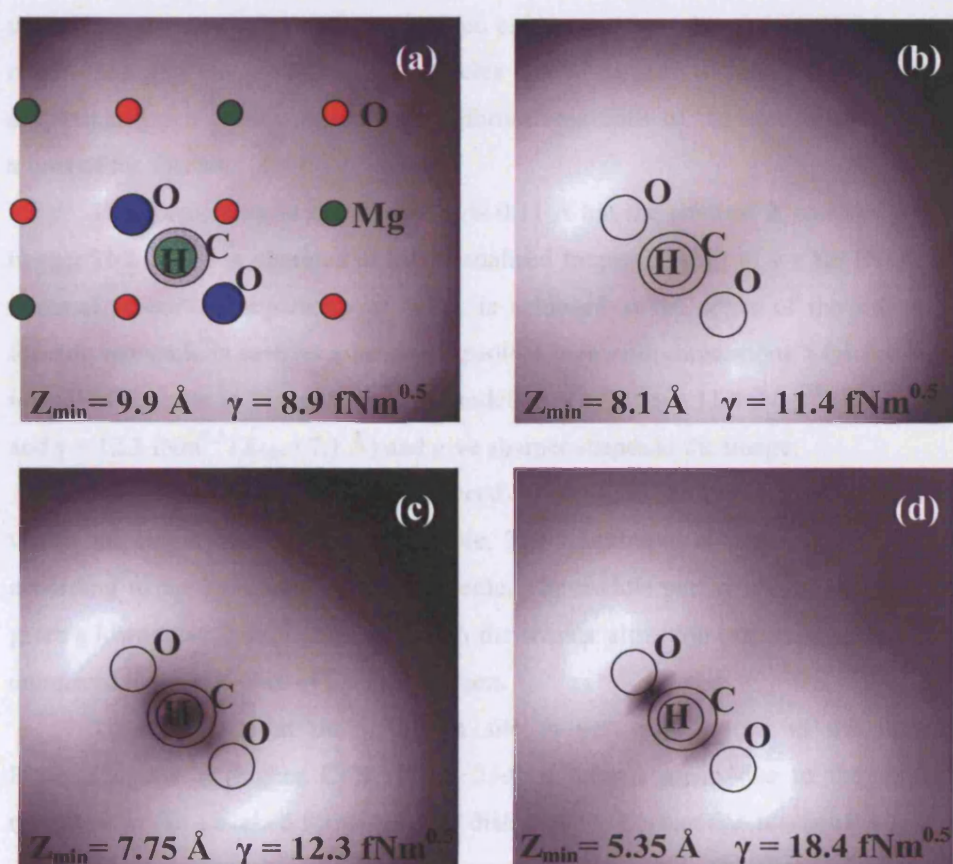


Figure 35. NC-AFM images of a single formate ion on MgO(001) surface modelled in Constant Frequency Shift (CFS) mode. a)-d) images obtained for various frequency shifts expressed via the normalized frequency shift  $\gamma = 0.28 \div 0.58 \text{ fNm}^{0.5}$ . The minimal distance between the tip and MgO(001) surface, achieved during acquisition of the image ( $Z_{\min}$ ), is specified for each image. Positions of the substrate ions and average positions of formate are shown in colour in a). In images b)-d) only the positions of formate ions are shown. Macroscopic Van der Waals interaction is evaluated for tip radius  $R=500 \text{ \AA}$ . Corrugation scale for images a)-c) is  $0.1 \text{ \AA}, 0.14 \text{ \AA}, 0.16 \text{ \AA}, 0.4 \text{ \AA}$  respectively.

The pattern of the image changes as the frequency shift is increased and the minimal tip-surface separation, correspondingly, decreases. This can be exploited provided the signal-to-noise ratio (SNR) is high. The evolution of the image pattern, as the tip approaches the surface, is shown in Figure 35a-d. The images are shown only for the blunter tip with  $R = 500 \text{ \AA}$  because the sequence of observed patterns was the same for every tip radius, although the normalized frequency shift depends on the macroscopic tip radius. Therefore, the minimal tip-surface distance is added to characterize the pattern.

Figure 35a demonstrates the correspondence between the modelled image and underlying atomic structure. Green and red circles represent the positions of the surface magnesium and oxygen atoms, blue circles denote formate oxygen atoms, large grey and bright green circles show the equilibrium positions of the carbon and hydrogen atoms of the formate.

The corrugation in the image (a) is  $0.11 \text{ \AA}$  but the contrast is smeared over the image. This image is obtained at the normalised frequency shift of  $\gamma = 8.9 \text{ fNm}^{0.5}$ . The minimal tip-surface separation of  $9.1 \text{ \AA}$  is achieved at the edges of the image. The formate molecule is seen as a bright ellipsoidal blob with dimensions  $5.0 \times 8.0 \text{ \AA}$ . The images of formate in Figure 35b-c are modelled for CFS  $\gamma = 11.4 \text{ fNm}^{0.5}$  ( $Z_{\min} = 8.1 \text{ \AA}$ ) and  $\gamma = 12.3 \text{ fNm}^{0.5}$  ( $Z_{\min} = 7.1 \text{ \AA}$ ) and give sharper shapes in the image.

The width of the ellipse is reduced to  $4.4 \text{ \AA}$ . In addition, a structure is seen within the bright blob over the molecule. The bright spot is divided into two parts according to the symmetry of the molecule. The middle part of the molecular image gives a lower corrugation associated with the weaker attraction over the hydrogen atom compared to the two sites of formate oxygen.

The minimum at the hydrogen site is very pronounced in the image in Figure 35c, but at higher CFS (Figure 35d) it smears again due to the enhanced relaxation in the adsorbed formate at this distance. The corrugation reaches  $0.4 \text{ \AA}$  in this image, which is the maximum value of contrast for  $R = 500 \text{ \AA}$ . The shape of the formate in the image also changes from elliptical to a dual lobe shape at the smaller distance. In Figure 35c-d one can distinguish two bright lobes attributed to the oxygen atoms of the formate. However, they are not centred over the oxygen atoms, because of the repulsion over H. The distance between the centres of the lobes exceeds significantly the distance between oxygen atoms in the adsorbed anion and may confuse experimentalists. The position of the oxygen atom with respect to the features of the image is the edge of the lobe on the symmetry axis as shown in Figure 35.



### 3.2.3 Contrast dependence on the tip-surface separation

Two tip radii were used to model the macroscopic Van der Waals interaction: one with  $R = 200 \text{ \AA}$  representing a sharp tip, and a slightly blunt tip with  $R = 500 \text{ \AA}$ . Since the hydrogen-magnesium interaction is repulsive, the height restrictions in the constant frequency mode are the same as in the constant height regime, where the tip cannot come closer than  $5.0 \text{ \AA}$  to the  $\text{MgO}(001)$  surface, because of the instability of the molecule. The minimal distance between the tip and the surface achieved in the imaging in constant frequency shift (CFS) mode varies with the preset frequency shift (Figure 36a). The ranges of valid frequency shifts are different between the considered tip radii, because of the change in the scale of interaction with respect to height. The increase in the radius from  $R = 200 \text{ \AA}$  to  $R = 500 \text{ \AA}$  results in non-overlapping curves.

The absolute value of the frequency shift at which the atomic resolution is achieved, increases as the tip radius increase. The range of the frequency shifts where the resolution can be obtained in CFS mode decreases slightly with an increase in the macroscopic interaction, but contracts even greater when the macroscopic interaction decreases and a minimum develops in the force-distance curve (section 1.1.3).

In the case considered in Figure 36a, the tip with  $R = 200 \text{ \AA}$  gives a three times more narrow range of high resolution imaging than the range for the tip with  $R = 500 \text{ \AA}$  with the same driving frequency. The extension of the frequency shift range is

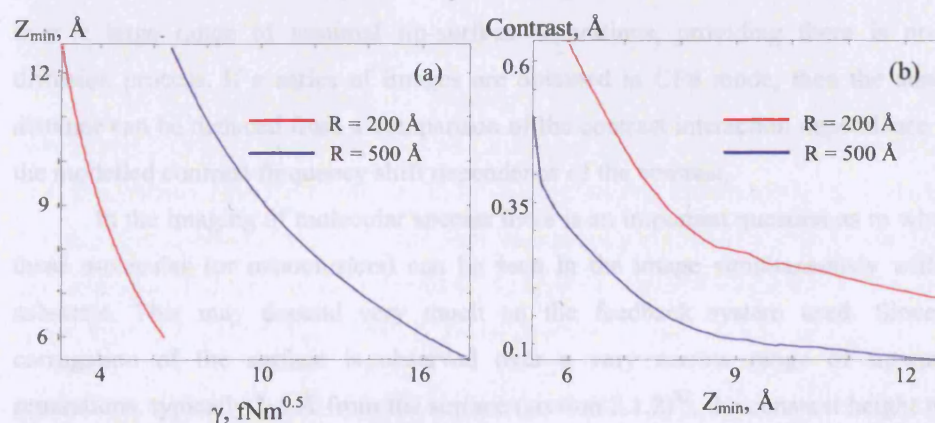


Figure 36. a) The relationship between chosen frequency shift and the minimal tip-surface distance achieved during acquisition of the image of a formate anion on  $\text{MgO}(001)$  surface; b) Distance dependence of the contrast in the constant frequency shift image for the two tip radii.

accompanied by a decrease in the observed corrugation, because the fraction of the site-specific interaction is decreased compared to the total interaction (section 1.1).

The corrugation in the image obtained with different tip radii is plotted in Figure 36b as a function of the minimal tip-surface distance. The figure shows that the corrugation drops systematically for the blunter tip. However, the figure demonstrates that a 200 Å tip is sufficiently good to produce high resolution images with measurable corrugation. Both curves in Figure 36b demonstrate two distinct areas in the distance dependence of the contrast. For the tip with  $R = 500$  Å, for instance, the dependence is linear with slope 0.01 at tip-surface separations larger than 8.5 Å. But at smaller distances the average slope increases 10 times and the dependence can be better described as  $C^2/(r - r_0)^2$  ( $C = 2.1$ ;  $r_0 = 2.5$ ). This indicates that different interactions or processes can be responsible for contrast formation at different distances. Here the onset of higher contrast during the approach is attributed to the displacements of the formate atoms in the tip potential, and bending of the formate in particular. Similar behaviour is discussed in previous chapters on the interaction of the oxide tip with  $\text{Al}_2\text{O}_3$ , and was experimentally confirmed in case of  $\text{CaF}_2$ <sup>42,42</sup>.

Altogether, Figure 36 gives a twofold perspective for understanding the imaging of the formate anion. On one hand, it gives the intervals of frequency shift and estimates the contrast that one can obtain using an oxidized tip with a macroscopic interaction described by a tip radius of 200-500 Å. On the other hand, it highlights the fact that the formate anion can be routinely detected on the  $\text{MgO}(001)$  terrace with conventional tips over a large range of minimal tip-surface separations, providing there is no fast diffusion process. If a series of images are obtained in CFS mode, then the absolute distance can be deduced from a comparison of the contrast interaction dependence with the modelled contrast-frequency shift dependence of the contrast.

In the imaging of molecular species there is an important question as to whether these molecules (or nanoclusters) can be seen in the image simultaneously with the substrate. This may depend very much on the feedback system used. Since the corrugation of the surface is observed over a very narrow range of tip-surface separations, typically 3-5 Å from the surface (section 2.1.2)<sup>42</sup>, the constant height mode (weak feedback) would scratch or move molecules on the surface. The use of feedback on the constant current is apparently not suitable for insulating surfaces. This study is focused on the constant frequency shift feedback system, which is most frequently used to study adsorbates<sup>39</sup>. The preliminary analysis with a tip of a conventional sharpness ( $R = 500$  Å) shows that the atoms of the  $\text{MgO}(001)$  surface cannot be resolved with the

oxide tip model according to the images (Figure 35b,c) taken at  $\gamma = 11.4 \text{ fNm}^{0.5}$  (8.1 Å), 12.3  $\text{fNm}^{0.5}$  (7.75 Å).

Normally, the constant frequency shift mode is thought to be advantageous due to its ability to adjust the tip-surface distance in accordance with a preset frequency shift, so that highly corrugated surfaces can be imaged. For the considered range of macroscopic tip-surface interactions, however, the flexibility of the CFS mode is not sufficient to see an atomically resolved surface in the presence of formate.

The clean magnesium oxide surface alone can be measured with atomic corrugation above 0.1 Å in the range of the tip-surface distances 3-4 Å, which for  $R = 500 \text{ Å}$  corresponds to  $\gamma = 20\text{-}25 \text{ fNm}^{0.5}$ . Therefore,  $Z_{\min}$  is less than 5.0 Å, and consequently the frequency shift, which is dominated at this distance by Van der Waals forces over the clean surface, is larger than those used to achieve resolution on the adsorbed formate.

It should be mentioned, however, that an experimentalist could move a few nanometres away from the position of the formate molecule, adjust the imaging frequency and be able to image with atomic resolution. It is only claimed that observing formate and atoms of the surface in the same image requires extremely sharp tips and very small noise. This problem is implicit to the constant frequency shift mode and might be overcome with a weaker macroscopic interaction. This possibility is analysed below in further detail.

### **3.3 Limits on surface resolution in the presence of adsorbate**

The following question is frequently asked: “What is the strength of the macroscopic tip-surface interaction, which allows atomic resolution of the molecules and the surface simultaneously, without damage to the molecules?” In the case of formate, the jumping of the molecule onto the oxide tip at distances closer than 5.0 Å is considered as “damage” to the molecule. The analysis is based on the force fields for the oxide tip over MgO(001) (section 1.3.3) and over the formate ion on MgO(001).

#### **3.3.1 The simplified model of macroscopic interaction**

The calculation of the frequency-distance curves in this work is based on the model of macroscopic interaction (1.2) governed by the three parameters defining the shape of the AFM tip apex: (1) the conical angle of the cantilever, (2) the product of the tip radius with the Hamaker constant and (3) the position of the bottom of the macroscopic tip with respect to the apex of the microscopic tip. For the sake of the

qualitatively illustrating the effect of the macroscopic interaction on the possibility of having simultaneous resolution of both the MgO(001) surface and adsorbed formate in the NC-AFM mode, we reduce the number of parameters. First, the Hamaker constant is fixed at 1 eV since it enters as a product with the tip radius (section 1.1)

The cantilever conical angle is also kept fixed at a typical value of 20 degrees. Therefore, the model has two parameters: a tip radius representing the strength of the macroscopic interaction and the shift between microscopic and macroscopic descriptions of the tip. In the current model, the shift can be interpreted as the height of a protrusion on the tip surface and describes the “sharpness” of the protrusion.

This parameter can be important in revealing details of the tip shape by fitting the experimental force-distance curves obtained for a wide range of distances (10-100 nm). For the range of short (1-10 Å) distances the effect of the position of the reference plane can hardly be distinguished from the effect of the tip radius. Therefore the position of the reference plane is chosen to be 3 Å, representing a locally blunt tip (section 1.1). As the result, the tip radius  $R$  becomes the single parameter describing the strength of macroscopic tip-surface interaction in the vicinity of the surface.

### 3.3.2 Favourable range of macroscopic interaction

Figure 37 gives the experimentalist’s viewpoint by plotting corrugations in the CFS image as a function of the frequency shift. Notably, it shows the range of the frequency shift, where a high-resolution image can be obtained. The upper limit of this range is defined by the tip-surface separation where the tip, molecule or substrate is damaged. The distance where the accuracy of the experiment or calculation is not sufficient to distinguish atomic-size features defines the lower limit of interaction. With the scheme used here, the data, which were obtained by extrapolation of the force curves, are regarded as not sufficiently reliable to judge the limits of resolution over the formate anion.

According to Figure 37, CFS corrugation over the MgO(001) surface strongly depends on the strength of the macroscopic interaction and is greater than 0.2 Å for sharp tips with radii less than or equal to 200 Å. The range of the normalized frequency shifts, where atomic resolution is observed, increases with increasing tip radius. The corrugation in the CFS image of the formate anion has a similar behaviour: corrugation in the image decreases 3 times if the macroscopic interaction increases from 50 Å to 400 Å.



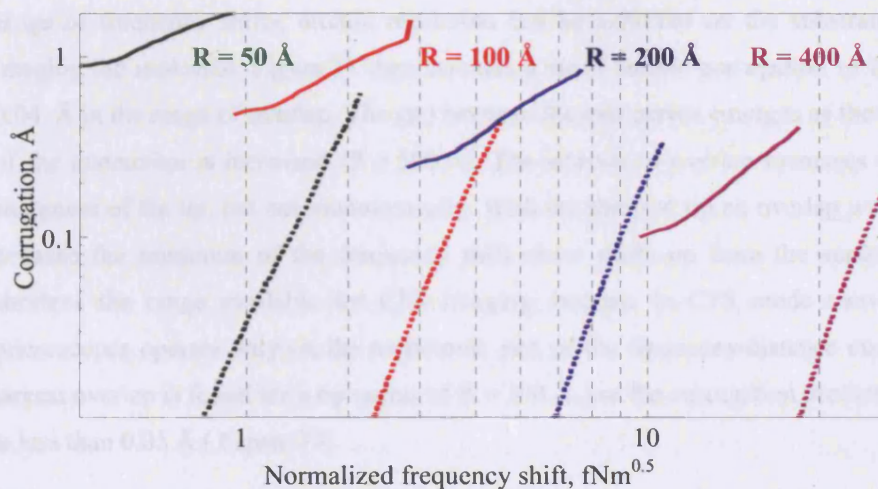


Figure 37. Interaction dependence of corrugation in CFS image of formate-MgO(001) system. The apparent height of the molecule on the surface is plotted as a solid line, corrugation on the MgO(001) surface is shown as dashed line. Solid and dashed lines of the same colour correspond to the same strength of macroscopic interaction. The value of tip radius, used to characterize the strength of interaction, is also shown in corresponding colour.

This demonstration is very instructive since the apparent height of a surface nanostructure in a CFS image is often related to its real dimensions by experimentalists. The corrugations over the H and O atoms of the formate are an example, where their relative apparent height is counterintuitive and the higher site (H) can be imaged as a protrusion.

### 3.3.3 Atomic resolution on the substrate in the presence of $\text{HCOO}^-$

The comparison between the two interaction dependencies of the corrugation is plotted in Figure 37. Dashed lines and solid lines correspond to the corrugation over the adsorbed molecule and the corrugation in the image of a clean MgO (001) surface, respectively. Plotting the data on a log-log scale allows more clear presentation.

The interaction dependence of the contrast over the MgO(001) surface is represented by a straight line on the graph. Therefore, it demonstrates the exponential decay of the contrast with the tip-surface interaction. According to previous studies of  $\text{CaF}_2$ , and  $\text{Al}_2\text{O}_3$ , this behaviour is typical for the region of interaction strength with no significant deformations in either tip or the surface. It is worth noting for clarity, that due to the log-log scale, the minimal limits on the X and Y axes are not zeros but  $0.1 \text{ fNm}^{0.5}$  and  $0.01 \text{ Å}$ , respectively. The limit of corrugation is chosen as a lower estimate of the feasible resolution with conventional apparatus. If there is overlap between the ranges of dashed and solid lines of the same colour, it means that, in this



range of frequency shifts, atomic resolution can be achieved on the substrate, while imaging the molecule. Figure 37 demonstrates a small atomic corrugation of less than 0.04 Å in the range of overlap. The gap between the two curves emerges as the strength of the interaction is increased ( $R = 500$  Å). The interval of overlap increases with the sharpness of the tip, but not monotonically. With the sharpest tip no overlap was found, because the minimum of the frequency shift curve shifts up from the surface. This shortens the range available for CFS imaging, because in CFS mode conventional microscopes operate only on the monotonic part of the frequency-distance curve. The largest overlap is found for a tip radius of  $R = 100$  Å, but the corrugation predicted there is less than 0.05 Å (Figure 37).

### 3.3.4 Implications for the experiment

It is important to point out that the effective tip radius, used to describe macroscopic tip-surface interactions, can be different from the physical radius of the tip. Therefore, the problem of “too small a radius” can be eliminated by applying a potential on the tip, which adds an additional capacitance force to the macroscopic interactions. Sometimes, for instance, if the tip and surface material have different workfunctions, tuning the tip voltage will allow reduction of the macroscopic interaction.

Experimentally, the strength of the macroscopic interaction can be estimated, using Figure 37, from a sequence of images with atomic resolution for either system. The figure links together the contrast, normalised frequency shift and strength of the macroscopic interaction characterised by the effective tip radius. The images should be taken at different frequency shifts and the relationship between the corrugation in the CFS image and the normalized frequency shift should be identified. The comparison of the dependence against the calculated set of curves gives an estimate of the parameters of the model notably the effective radius of the tip.

To summarize, the inability to image formate on the MgO(001) surface with atomic resolution is a fundamental problem, which is due to the gradient of the macroscopic force. Atomic resolution is available separately on the surface and over the molecule for a range of constant frequency shifts. The two ranges do not overlap due to the presence of a strong gradient in the macroscopic force between the tip and the surface. For ultra-sharp tips the lack of macroscopic interaction, necessary to obtain a monotonic frequency-distance curve, can be compensated by the capacitance force due to the applied voltage.

### 3.4 Discussion

The results presented in this chapter identify the possible problems emerging during imaging of the MgO(001) surface with an adsorbed charged formate ( $\text{HCOO}^-$ ) ion. Interatomic potentials for the formate-MgO system are developed from the *ab initio* results. Using the interatomic potentials developed, imaging of the formate anion on the MgO(001) surface is modelled using the oxide tip model with a positive potential.

The molecule can be seen in constant frequency shift mode (CFS) with sub-molecular resolution: two blobs in the image can be associated with the O atoms of the formate. The size of the bright feature has dimensions almost twice those of the molecule. The pattern changes from a homogeneous ellipse to a pair of distinguishable blobs with an increase of the frequency shift. Surface atoms cannot be resolved simultaneously with the molecule, i.e. in the same image.

The range of the tip-surface distances is also limited from below, because an oxide tip with a positive potential picks up the molecule from the surface if the tip is closer than 5.0 Å from the surface, according to static and dynamic atomistic simulations.

The maximal corrugation in the image obtained in the constant frequency shift (CFS) mode depends on the strength of the macroscopic interaction. A sequence of experimental images of MgO(001) can be used to estimate the strength of the macroscopic interaction in terms of the tip radius using graphical tables developed in this chapter.

The possibility of obtaining simultaneous resolution on the substrate and adsorbate within the “safe” regime is predicted for tips of intermediate sharpness and for ultra sharp tips in the presence of other macroscopic interactions, such as a capacitance force. To resolve the substrate one has to approach closer to the surface, i.e. use a high preset frequency shift value. To resolve the molecule one has to be at a distance  $>5.0\text{Å}$  from the surface when the tip is over the molecule, i.e. the high CFS value should be achieved at this distance. The major problem is that the decrease in the tip-surface distance usually results in an increase of the frequency shift due to the gradient of macroscopic tip-surface interaction.

Simultaneous imaging could be possible with ultrasharp tips if there was very small gradient of the macroscopic tip-surface interaction. Alternatively, it could also be possible, if there was a strong attraction between the apex of the tip and the end group of the molecule to compensate the macroscopic tip-surface attraction over the bare surface.

The study reports two observations applicable to the general system:

- a) when repulsion dominates the interaction of the tip at some site over the molecule, atomic resolution in a typical ionic substrate beneath is very unlikely, unless the minimal anion-cation distance on the surface exceeds the height of the molecule;
- b) simultaneous atomic resolution both in the substrate and in the molecule can be prevented by more general violations of imaging conditions that prevent sampling of stronger interactions, such as a strong negative gradient in the force-distance curve over the molecule.

### 3.5 Summary

Interatomic potentials for the formate-MgO(001) system have been developed in this work from *ab initio* data for the purpose of building the NC-AFM image.

The study demonstrates that the molecule can be observed in the CFS mode with corrugations from 0.1 Å to 1.0 Å depending on the strength of the macroscopic interaction. The submolecular features, less than 0.5 nm, can be also observed in the modeled image of the formate. The lateral size of the molecule in the image is affected by two factors: molecular relaxation due to the proximity of the tip and a convolution effect caused by the interaction with the tip at larger separations.

Results of the simulation show that the presence of the molecule on the surface significantly reduces the possibility of simultaneous resolution of the molecule and atomic structure of the substrate in the same NC-AFM image. In the presence of the formate, the maximal contrast between the O and Mg ions on the MgO(001) surface is expected to be at the limit of the experimental resolution (0.04 Å). Attempting to increase the frequency will result in irreversible processes such as picking up the molecule with the tip apex. The application of this result can be extended to a range of similar systems, for instance, small metal clusters on the oxide surfaces.

## 4 Contrast formation in imaging of molecular monolayers on TiO<sub>2</sub>(110)

In this chapter we combine several systems discussed in the previous chapters: we use the model Si tip with a dangling bond (section 2.2) and formic acid (Chapter 3) to model NC-AFM imaging of a molecular monolayer of formic acid (HCOOH) on an ideal TiO<sub>2</sub>(110) surface (section 1.4.3). For the sake of comparison we also study monolayers of methane (CH<sub>4</sub>) on an ideal rutile surface and in the presence of oxygen vacancies. The characterisation of the two molecular monolayers - HCOOH and CH<sub>4</sub> is followed by *ab initio* modelling of the interaction of the “pure Si” tip with HCOOH-TiO<sub>2</sub>(110) and comparison with available experimental data. We also analyse the impact of the substrate on the image contrast and the tip-induced motion of the adsorbed molecules. On the basis of these results we provide an interpretation of the experimental pattern with the assumption of the “pure Si” tip model.

This study was motivated by the expanding field of experimental NC-AFM studies of molecular monolayers, including self-assembled monolayers (SAMs)<sup>32,148-150,168-175</sup>. Interest in these systems has been increasing among different disciplines due to the application of molecular monolayers in biological sciences, technology and medicine as substrates, templates, anti-adhesive and anti-corrosive coatings<sup>176-180</sup>. The NC-AFM is thought of as an advanced technique able to provide high resolution in the monolayers and enable the study of local defects.

On conventional solid surfaces, such as semiconductors and insulators<sup>29,38,43</sup> considerable theoretical and experimental effort has been spent in achieving high resolution using NC-AFM. Molecular monolayers demonstrate a very different set of surface properties<sup>156,181-184</sup>. Therefore, it is necessary to understand to what degree the interpretation, built for NC-AFM images on conventional surfaces, can be used for interpretation of images of molecular monolayers. Currently, there is very limited NC-AFM theoretical information to support the interpretation of high-resolution images of molecular monolayers and to provide insight into the performance of specific types of AFM tips. Experiment often relies on the concepts developed for low-resolution wide area imaging<sup>172,174,185,186</sup> in the interpretation of high resolution imaging.

Previous theoretical studies<sup>187,188</sup> studying contact between molecular monolayers and an AFM tip used interatomic potentials and addressed the problem of friction phenomenon rather than imaging itself. A very recent work<sup>185</sup> on the modelling of NC-AFM images of molecular monolayers uses the ultimate “coarse-graining” provided by the empirical “united atom model”. This approach neglects intramolecular degrees of freedom and imposes empirical values for the tip-surface interactions.

However, this pioneering work highlights the importance of theoretical development for the interpretation of NC-AFM images of a molecular monolayer.

In this work, we adopt as a hypothesis that the success of the qualitative interpretation of NC-AFM images<sup>43</sup> on ionic surfaces and semiconductors can be transferred to the “softer” surfaces of molecular monolayers. It has been demonstrated experimentally<sup>38</sup> that such an interpretation is feasible on semiconducting surfaces. The study of the transferability of the image interpretation between ionic surfaces (Chapter 2) supports the application of the Si tip with a dangling bond to studies of molecular monolayers of HCOOH-TiO<sub>2</sub>(110).

As an initial step of our analysis, we assume that the models of the tip and NC-AFM imaging described in Chapter 1 are still valid for the softer surfaces. However, we must note the qualitative difference between the dynamics of the hard surfaces studied previously and those of the relatively “soft” molecular monolayers<sup>189</sup>. Experiment focus on the preparation and maintenance of a tip with a dangling bond, while the main focus of theory is to study the interaction of the dangling bond with different classes of surfaces and provide consistent interpretations of existing NC-AFM images with high resolution.

In this work we choose the static relaxation approach for modelling NC-AFM imaging of molecular monolayers using an *ab initio* DFT method with periodic boundary conditions. This technique does not capture the dynamic properties of a long-chain or sparse SAM system<sup>190</sup>. Therefore we focus on the study of the tip-surface interaction on surfaces with a short-chain molecular monolayer at high coverage.

As a preliminary step, we explore the adsorption of molecular monolayers on an ionic surface. The TiO<sub>2</sub>(110) surface was chosen as a substrate because both the clean surface and one with molecular monolayer of formic acid (HCOOH) have been experimentally studied with high resolution using NC-AFM<sup>32,169</sup>.

Formic acid is known to dissociate on the TiO<sub>2</sub>(110) surface into a proton and formate anion (HCOO<sup>-</sup>). The process of dissociation has been investigated already both theoretically<sup>157,158</sup> and experimentally<sup>191,192</sup> and we use this data to validate the results obtained in our study.

The choice of the “pure Si tip” model is supported by experimental NC-AFM work<sup>169</sup> conducted on monolayers of formic acid at full coverage with a “cleaned silicon tip”. This claim that the silicon tip was “clean” was based, however, on the treatment given to the tip rather than on characterisation of the tip apex. Moreover, there is a



significant probability that the tip apex is contaminated by the surface material during image acquisition.

The direct application of the interpretation based on this tip model therefore requires detailed experimental characterization of the tip apex. Nevertheless, we choose the pure Si tip with a dangling bond as a model of the tip in our study. Therefore, this work encourages experimental efforts towards the preparation of well defined tips, as well as continues the theoretical study of the mechanisms of NC-AFM contrast formation started in Chapter 2.

## **4.1 Adsorption of molecular monolayers on $\text{TiO}_2(110)$**

### **4.1.1 Methane on $\text{TiO}_2(110)$**

According to the extensive theoretical<sup>193-195</sup> and experimental studies<sup>196-198</sup> methane weakly adsorbs on clean oxide surfaces. The typical physisorption energy on a perfect oxide surface is of the order of a fraction of an electron-volt. Oxygen vacancies, however, have been shown to lead to dissociation of  $\text{CH}_4$ <sup>199-201</sup> on some oxide surfaces. As for the stoichiometric rutile surface, no work on  $\text{CH}_4$  molecular adsorption has been done in UHV conditions, although there are works on both polycrystalline material and in ambient conditions<sup>198</sup>.

There is also very little *ab initio* work on weakly adsorbed  $\text{CH}_4$  molecules or monolayers although results of forcefield simulations are available<sup>202,203</sup>. The main reason is the sensitivity of the total energy to the choice of the exchange functionals, which leads to uncertainty in the energy of adsorption. This problem was not avoided in this work. However, the target of the current study is to locate approximately the minimum (or a plateau) of the adsorption energy-distance curve and to study its repulsive part as a function of the lateral position of the molecule. This distinguishes our study from conventional works on adsorption, which are often focused on the attractive part of the energy-distance curve. We consider a molecule pressed to the surface as opposed to a molecule attracted by the surface in the typical adsorption studies. The acquired adsorption data can be useful to analyse and model three systems:

- i)  $\text{CH}_4$  molecule is pushed down to the surface by an AFM tip;
- ii)  $\text{CH}_3^-$  group of a larger molecule is pressed down to the surface by means of an AFM tip acting on the larger molecule;
- iii)  $\text{CH}_3^-$  group of a larger molecule is pressed down to the surface due to the strong binding of the larger molecule to the surface.

The energy-distance curve obtained for CH<sub>4</sub> can be also used in the construction of forcefield of the molecule-surface interactions. One can use this forcefield to investigate contrast formation in NC-AFM images acquired with a tip contaminated by organics with a CH<sub>3</sub> at the end<sup>204</sup>.

This study considers the adsorption of CH<sub>4</sub> molecules on clean TiO<sub>2</sub>(110) surface as well as in the presence of an oxygen vacancy in the bridging row, which is claimed to be the most common defect on the reduced TiO<sub>2</sub>(110) surface<sup>115</sup>. The study is conducted solely in the DFT framework (section 1.3.1) using periodic boundary conditions (PBC). However, the results are being constantly compared to those obtained in our group with various exchange functionals<sup>78</sup> using a cluster model for the surface. The choice of the cluster model has been justified by the high dielectric constant of TiO<sub>2</sub>(110) and the proper choice of the cluster geometry. The surface was modelled using PBC calculations with a (2×1) surface unit cell incorporating 3 stoichiometric layers. The spacing between slabs is at least 20 Å. Although a (2×1) model was primarily used, the results were also compared with the data for a larger (4×2) unit cell with a 4-layer slab. The details of the choice of parameters for the SIESTA DFT calculations are discussed in section 1.4.3.

The energy vs. distance curve (“adsorption curve”) was first calculated over the 5-coordinated Ti site with two of the hydrogen atoms of CH<sub>4</sub> pointing to the nearest oxygen atoms – the “dipod” configuration (Figure 38a). The height of the molecule is determined by the difference in the z-coordinates of the carbon atom of the molecule and topmost Ti atom of the surface. The C-Ti separation was varied between 2.0 and 4.0 Å, while neither the molecule nor the surface were relaxed. The adsorption curve is shown in blue at Figure 38a. The energy values are calculated with respect to the energy of the system at 10 Å separation. The maximum value of adsorption energy along this trajectory, 0.4 eV, was found at a C-Ti separation of 3.1 Å. This value compares with the embedded cluster result of 0.1 eV for CH<sub>4</sub> on MgO(001)<sup>205</sup> and the experimental observation that methane molecules adsorb at the clean MgO(001) surface below 75K<sup>206,207</sup>.

Other characteristic sites were tested in a configuration where two hydrogen atoms of the molecule were directed towards the surface. The approach curves for the methane molecule positioned over a bridging row O and over a second layer O, are shown in Figure 38a as magenta and orange lines, correspondingly. The lateral positions of the molecule are marked in Figure 38b with arrows of corresponding colour. They demonstrate that the minima of the approach curves are situated further from the surface and are shallower, so that adsorption at these sites is still possible.

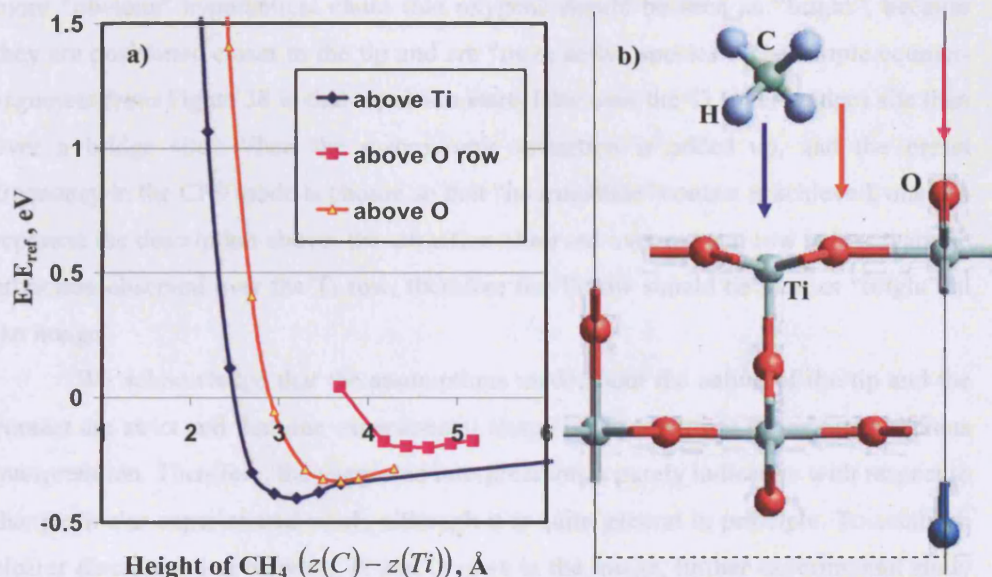


Figure 38. a) The energy-distance dependence for a methane molecule over the titanium oxide surface. Values of the energy do not account for relaxation of the molecule and the surface. b) The structure of the unit cell used in calculation and the orientation of the methane molecule  $\text{CH}_4$ . Arrows indicating position of  $\text{CH}_4$  molecule on the surface have the same colours as corresponding adsorption curves.

The same applies to a methyl  $\text{CH}_3$ - group of a larger molecule in contact with the surface. For all points considered, we found weak adsorption energies (Figure 38). This is also supported by the Mulliken population analysis which suggests that no charge transfer occurs as the molecule approaches the surface.

Let us consider a functionalised tip that touches a  $\text{TiO}_2(110)$  surface with a methyl group. Such a tip can be fabricated by depositing a hydrophobic SAM thiol monolayer on the oxidized silicon tip. The results in Figure 38a provide a rough guide for interpretation of an image acquired with such a tip. Such experiments have been done very recently<sup>204</sup> with a SiOx tip coated by an alkyl-terminated SAM and demonstrated bright stripes on the  $\text{TiO}_2(110)$  in the direction of the bridging oxygen rows, but no interpretation was suggested. We can propose an interpretation on the basis of following assumptions: (i) the image was acquired in “intermediate contact” regime; (ii) only a single  $\text{CH}_3$  group was responsible for the image; (iii) the effect of the variation in the macroscopic interaction on the contrast is negligible (the effect due to the adjustment of the tip-surface distance in CFS mode).

In this case, the analysis of the slope of calculated energy-distance curve (Figure 38) demonstrates that the Ti row should be imaged as “bright”, rather than the

more “obvious” hypothetical claim that oxygens should be seen as “bright”, because they are positioned closer to the tip and are “more active species”. The simple counter-argument from Figure 38 is that repulsion starts later over the Ti (inter-bridge) site than over a bridge site. When the macroscopic attraction is added up, and the preset frequency in the CFS mode is chosen so that “intermediate” contact is achieved, one can rephrase the description above: the attraction observed over oxygen row is less than the attraction observed over the Ti row, therefore the Ti row should be seen as “bright” in the image.

We acknowledge that the assumptions made about the nature of the tip and the contact are strict and that one experimental image is not sufficient for an unambiguous interpretation. Therefore, the suggested interpretation is purely indicative with respect to that particular experimental work, although it is quite general in principle. To establish clearer discrimination between Ti and O rows in the image, further experimental study is required as well as related theoretical modelling and analysis.

Apart from the relatively low adsorption energy of the methane (less than 0.4 eV), the shallow shape of the curve suggests weak coupling of methane to the ideal surface and high mobility of the molecule in the vicinity of the surface, because no deep potential minima were found for the molecule on the surface. As a result, the methane molecule is not expected to form stable monolayers at room temperature, so that imaging of methane monolayer might be practical only at extremely low temperatures.

On some surfaces introduction of defects, e.g. oxygen vacancies results in a stronger coupling of the methane to the surface. These vacancies in magnesium oxide, gallium and chromium oxide have been related to the onset of strong methane coupling and oxidation of methane<sup>205,208-211</sup>. In the case of the magnesium oxide, for example, presence of oxygen vacancies and impurities is essential for the decomposition of methane<sup>212</sup>.

For titanium oxide experiment<sup>198</sup> suggests high chemical activity for nanocrystalline TiO<sub>2</sub>, which is associated with the reduced phase of the oxide. However, no theoretical work detailing this mechanism was found.

Unfortunately, the models of defects developed for MgO<sup>82,83,213-215</sup> as well as the models of methane adsorption on this surface<sup>193,210</sup> cannot be transferred to TiO<sub>2</sub> surface, firstly, because of the difference in the chemical properties of the surface<sup>216</sup>, and secondly due the lack of knowledge about electron localisation on the reduced TiO<sub>2</sub> surface. In the case of a terrace oxygen vacancy on MgO(001), the electron is well localised in the vacancy, while the current consensus about vacancies on TiO<sub>2</sub>(110)



suggests that both electrons go to the conduction band or are possibly localized at the Ti atoms around the vacancy.

Recent theoretical work<sup>121</sup> on  $\text{TiO}_2$  has demonstrated that significant variation in electron localization is obtained as the admixture of exchange is varied in the exchange-correlation functional. This brings a parameter into the first principle calculations of oxygen vacancies.

In this work the PBE (GGA-DFT) functional<sup>217</sup> is used (1.4.3), which has proved to be effective in describing probe-surface interactions on reduced  $\text{TiO}_2(110)$  and produced results in accordance with STM and NC-AFM<sup>218</sup> experiments. This density functional approach allows us to reproduce electronic structure and surface relaxation on an ideal  $\text{TiO}_2(110)$  surface. The bandgap of the system (1.0 eV) is reduced, due to the lack of exchange in the chosen exchange-correlation functional. The electrons donated to the system by the vacancy are attributed to the titanium ions. The degree of the localization of these states is still arguable since the result depends on the choice of the functional. The details of the calculations as well as comparison with previous calculations and experimental data are reported in section 1.4.3.

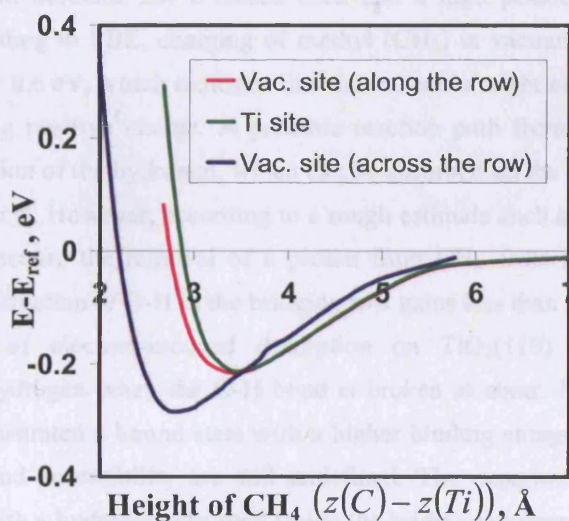


Figure 39. Methane adsorption curves over Ti and vacancy sites on reduced  $\text{TiO}_2(110)$  surface are calculated for the molecule in a “dipod” position over Ti site and two “dipod” positions over the oxygen vacancy site: across and along the oxygen row. The absorption energy is calculated with respect to the energy at a separation of 10 Å. Surface and molecular relaxation is not included in the calculation.



In the presence of neutral oxygen vacancies the strength of interaction with the methane has been reduced over all sites. The adsorption over Ti site became half as favourable. The deepest well of 0.3 eV for the methane is over the vacancy site when the molecule approaches the site in “dipod” position with 2 hydrogens perpendicular to the row. This is also the closest approach to the surface: the Ti-C height in the point of minimum of the adsorption curve is 2.8 Å. Figure 39 demonstrates the adsorption curves and highlights an observation that the values of the energy and slope of the adsorption curves at the height above 3.5 Å are similar for the considered adsorption points, which means that in an NC-AFM image taken with a methyl terminated tip the vacancy sites and Ti sites would look identically. Therefore, entry into the repulsive regime is again required to distinguish these surface sites.

For a better understanding of the adsorption in the chosen model methane-TiO<sub>2</sub> charge transfer and the electron affinity of the molecule were analyzed. According to the Mulliken analysis the charge on the molecule in the presence of oxygen vacancies on the surface changes less than 0.01e, which can be neglected.

The possibility of charge transfer is analyzed by the study of electron affinity of CH<sub>4</sub> and CH<sub>3</sub> molecules as summarized in Table 9. These two systems differ in number of hydrogen atoms and, therefore, in number of electrons, which makes their electron affinity different. Methane has a closed shell and a high penalty (4 eV) to electron trapping. According to PBE, charging of methyl (CH<sub>3</sub>) in vacuum with an electron is unfavourable by 0.6 eV, which indicates that the molecule might become charged in the field of a strong positive charge. A possible reaction path from CH<sub>4</sub> to CH<sub>3</sub> would involve abstraction of the hydrogen, which can be absorbed on the bridging oxygen row to form a hydroxyl. However, according to a rough estimate such a path is energetically unfavourable because the removal of a proton from CH<sub>4</sub> costs more than 19 eV (in PBE) while the creation of O-H in the bridging row gains less than 14 eV (PBE).

Studies of electron-induced desorption on TiO<sub>2</sub>(110) have observed the desorption of hydrogen when the O-H bond is broken at about 14 eV. However they have also demonstrated a bound state with a higher binding energy of about 21 eV<sup>219</sup>, but its origin and accessibility are still undefined. The experimentalists suggested a configuration with a hydrogen adsorbed inside the bridging oxygen vacancy, but within the PBE approach it was found to be unfavourable compared with hydroxylation of the bridging oxygen. A wider range of surface models incorporating more defects, such as a Ti interstitial, might be needed to explain the experimental result. As for the molecule, the choice of the exchange functional also influences the calculated electron affinity and absolute position of energy levels.

Table 9. Total energy of CH<sub>3</sub> and CH<sub>4</sub> molecules in neutral and negatively charged states. Calculations are performed using the PBE GGA functional<sup>217</sup>.

<i>System</i>	<i>CH<sub>4</sub></i>	<i>CH<sub>4</sub><sup>-</sup></i>	<i>CH<sub>3</sub></i>	<i>CH<sub>3</sub><sup>-</sup></i>
<i>Energy(PBE), eV</i>	-223.06	-219.07	-204.84	-204.20

The study of methane adsorption addressed the weak molecule-surface interaction on ideal and reduced (110) surfaces of titanium oxide. The data obtained was used to support the development of methane-TiO<sub>2</sub> atomistic pair potentials. Periodic calculations in SIESTA proved to be computationally less effective than quantum mechanical calculation within a cluster model and also less flexible with respect to the choice of exchange functional. Analysed adsorption curves (Figure 39) for a dipod configuration allow the prediction of the ability to resolve oxygen rows with NC-AFM using a methyl-terminated tip and obtain “inverse topography” in the image. The titanium site is the site of the strongest attraction and should be seen as bright.

According to the DFT calculations, the presence of vacancies introduces a new active site, but reduces the overall adsorption energy. Moreover, this reduces the difference between site-dependent force-curves at larger distances, i.e the contrast in the image.

#### 4.1.2 Formate on TiO<sub>2</sub>(110)

In this section we look into the “bridging” adsorption of the formic acid on the TiO<sub>2</sub>(110) surface at saturation (full coverage) and fractional coverage. By “bridging” we refer to adsorption geometry where two Ti-O bonds are formed between the two oxygens of formic acid and two Ti atoms on the surface (Figure 40). The molecule of the formic acid on the titania surface is considered in its dissociated form, HCOO—, with no discussion of the dissociation process itself because this process has been discussed in the literature from both experimental<sup>191,220</sup> and theoretical<sup>114,221</sup> viewpoints. The details of the setup for the TiO<sub>2</sub>(110) slab can be found in the first chapter (section 1.4.3).

According to the experimental data on a formate monolayer<sup>115</sup>, the formate ions bind in the “bridging” position to the fivefold Ti<sup>3+</sup> ions on the surface with a maximum coverage of 1 formate per a surface area of 2 unit cells (6.02 Å × 6.7 Å). Each surface unit cell contains one five-coordinated Ti ion in the first surface layer, which essentially defines the maximum coverage possible ( $\theta = 0.5$ ) for this binding configuration. The O-C-O angle of the adsorbed formate is 126 ± 1 degrees; Ti-O distance is 2.1 ± 0.1 Å.

This data agrees well with calculated values for the angle of 127 degrees and distance of 2.11 Å, obtained in our calculations as well as in the previous theoretical studies<sup>158,221</sup>. The molecular plane is upright, perpendicular to the surface, according to both theory and experiment.

The adsorption energy is defined here as the difference in energy between two systems. In the first system, the neutral molecule of formic acid is at infinite distance from the TiO<sub>2</sub>(110) surface. In the second system the molecule has already dissociated into formate and hydrogen on the TiO<sub>2</sub>(110) surface; the formate is adsorbed in the bidentate position and hydrogen is adsorbed at the nearest bridging oxygen. This choice of hydrogen position was made on the basis of previous investigations of the role of hydrogen in adsorption and dissociation of formic acid on TiO<sub>2</sub>(110)<sup>221</sup>.

Since the calculations are made in periodic boundary conditions, the result can be interpreted as the energy of monolayer formation for the given coverage. The limit of low coverage is interpreted as an approximation to the adsorption energy of a single molecule of formic acid. The dependence of the adsorption energy versus coverage was investigated for fractional coverage  $\theta = 0.5, 0.375, 0.25, 0.125$  ML, i.e. from 4 to 1 molecules per area of 8 surface unit cells. Correspondingly, following energies of

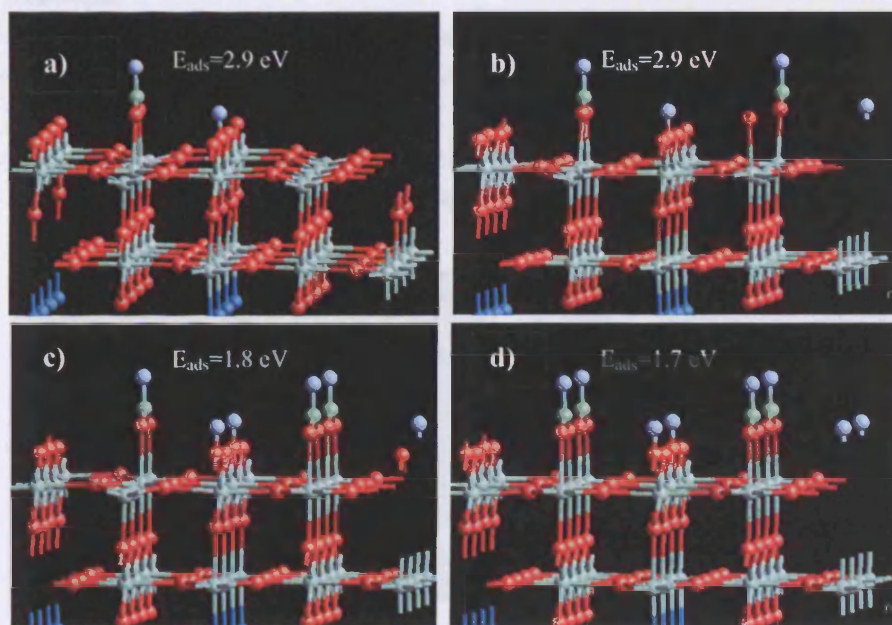


Figure 40. Relaxed geometries of formate-TiO<sub>2</sub>(110) submonolayer systems at intermediate  $\theta = 0.125, 0.25, 0.375$  ML (a-c) and maximal  $\theta = 0.5$  ML (d) coverage. This system is assumed to have formed by dissociation of the formic acid on the surface. Red, light green, green and grey circles correspond to O, Ti, C, H atoms respectively.



monolayer formation were obtained as function of coverage: 1.7 eV, 1.9 eV, 2.9 eV, 2.9 eV (Figure 40) in the expanded surface cell ( $12.08 \times 13.43 \text{ \AA}$ ). This might suggest that intermolecular interactions at 0.25 ML coverage are negligible, but favourable rearrangement of the monolayer proves the opposite.

The system with  $\theta=0.375$  ML coverage models a monolayer with high density of defects, but the adsorption energy per molecule of the system is more than 30% below than for  $\theta=0.25$  ML. There are three arrangements at  $\theta=0.25$  ML which are possible in a supercell with four adsorption sites: two with molecules along each of cell's dimension and a chessboard orientation (Figure 40). Assuming that interaction in the monolayer is mainly between dipoles formed by dissociated molecules, the most advantageous configuration is when molecules stay parallel to neighbouring rows and least favourable when formate molecules fill every second row (Figure 41b). The chessboard arrangement (Figure 41a) is in an intermediate position. This hierarchy developed in the point charges model is confirmed by the *ab initio* calculation.

The difference in energy between the "chessboard" configuration and the least favourable orientation (0.5 eV) obtained *ab initio* is reproduced by interaction of in-plane surface dipoles described by an effective charge of  $\pm 0.5 |e|$  assigned to the formate anion and the proton in the hydroxyl group respectively. Components of the dipole moments perpendicular to the surface, which are attributed to the molecule and relaxations of the surface do not affect significantly the relative energies between these structures.

Each oxygen carries  $-0.5 |e|$  while the hydrogen of the hydroxyl group and the carbon of the formate carry  $+0.5 |e|$  and the induced surface dipole is neglected. The values of charge are neither the formal charge of anion/proton nor the Mulliken charge, since the former does not take into account redistribution of the charge while the latter overestimates the effective size of the ion in calculation of the population.

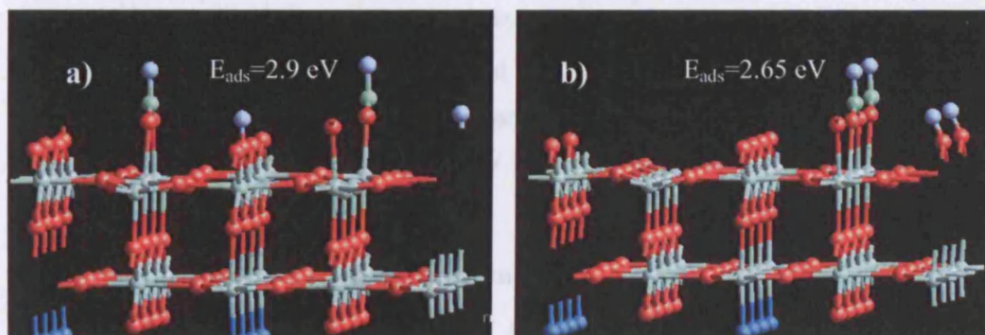


Figure 41. Two possible configurations (a,b) of the arrangement of the products of dissociation of the formic acid (formate anions and protons) at  $\theta = 0.25$  ML coverage. The clear preference to fill rows rather than scatter over different rows is attributed to the change in dipole-dipole interactions between the two molecules; Red, light green, green and grey circles correspond to O, Ti, C, H atoms respectively.

Such a crude approach, however, gives an estimate of the effective electrostatic charge on the hydrogen in the hydroxyl group on the surface. The parallel arrangement of the molecules is also seen in experimental high-resolution STM images<sup>115</sup>.

The study of formate bonding indicates the ionic-covalent nature of Ti-O bond where the covalency is due to the mixture of Ti d-states with the states of the formate oxygen, in agreement with previous theoretical analysis<sup>158</sup>. The Ti-O bond of the rutile is of  $\sigma$ -character, which is well known for rutile-type structures to be at the expense of  $\pi$ -bonding in the Ti-Ti bond<sup>222</sup>. Therefore, the adsorption energy of an HCOO<sup>-</sup> ion is determined by electrostatic attraction and formation of two Ti-O bonds since no significant relaxation is associated with the adsorption.

Adsorption mechanisms of monolayers of dissociated formic acid are studied both at full and fractional coverage. The intermolecular dipole-dipole interaction is shown to play an important role at 0.25 ML coverage. As the result of the study, formic acid on TiO<sub>2</sub>(110) was chosen for further modelling with NC-AFM since the system has been better studied both theoretically and experimentally<sup>115</sup>, including NC-AFM studies<sup>32</sup>.

## **4.2 Imaging HCOO+H monolayer on TiO<sub>2</sub>(110)**

NC-AFM images of monolayers of formic and acetic acid on TiO<sub>2</sub>(110) surface were first obtained by Y.Iwasawa's group in Tokyo University. Both images were recorded at room temperature in ultra-high vacuum conditions. According to the experimentalists, bright features in the images are molecules<sup>32</sup>. Although the molecular resolution in the formate image was reproducible, no theoretical model was suggested to support the interpretation<sup>218</sup>. The model essentially depends on the details of the tip preparation. Since experimental articles<sup>169,223</sup> claim that the oxide layer had been removed from the Si tip, we use the model of a pure Si tip with a dangling bond to interpret the contrast formation in the images. Therefore, in this section, we continue using this model, which proved to be very sensitive and informative for clean oxide surfaces (section 2.2).

### **4.2.1 Modelling of the tip-surface interaction**

A formate monolayer is simulated as a perfectly ordered monolayer at full coverage with surface cell dimensions of 6.72 Å x 6.03 Å i.e. a 2x1 extension of the primitive TiO<sub>2</sub>(110) surface unit cell (3.36 Å x 6.03 Å). The molecules are adsorbed in the bridging coordination between two Ti ions. At maximum coverage, also referred to



as “full” coverage, the number of formate molecules is half the number of Ti atoms in the top surface layer due to the bidentate adsorption.

As the tip is introduced into the system, a further (4x2) expansion of the unit cell is applied resulting in 4 formate molecules per simulation supercell. Such an expansion of the unit cell guarantees that the minimum distance between periodic images of the “tip” is at least 3 Å. The tip of the cantilever is modelled by a conical tip at macroscopic level and by a Si cluster of 10 atoms at the atomic level (the same as in the section 2.2). The properties of the tip model are discussed in section 1.5.2.

The geometry of the monolayer (Figure 42) is chosen in accordance with the previous theoretical work<sup>114,221</sup> as well as to match photoelectron diffraction data<sup>220</sup>. The structure of the monolayer is obtained by geometry optimisation with SIESTA using a force tolerance of 0.08 nN. This criterion applies for all consequent optimisations of the system with the tip used in the construction of the microscopic forcefield of the tip.

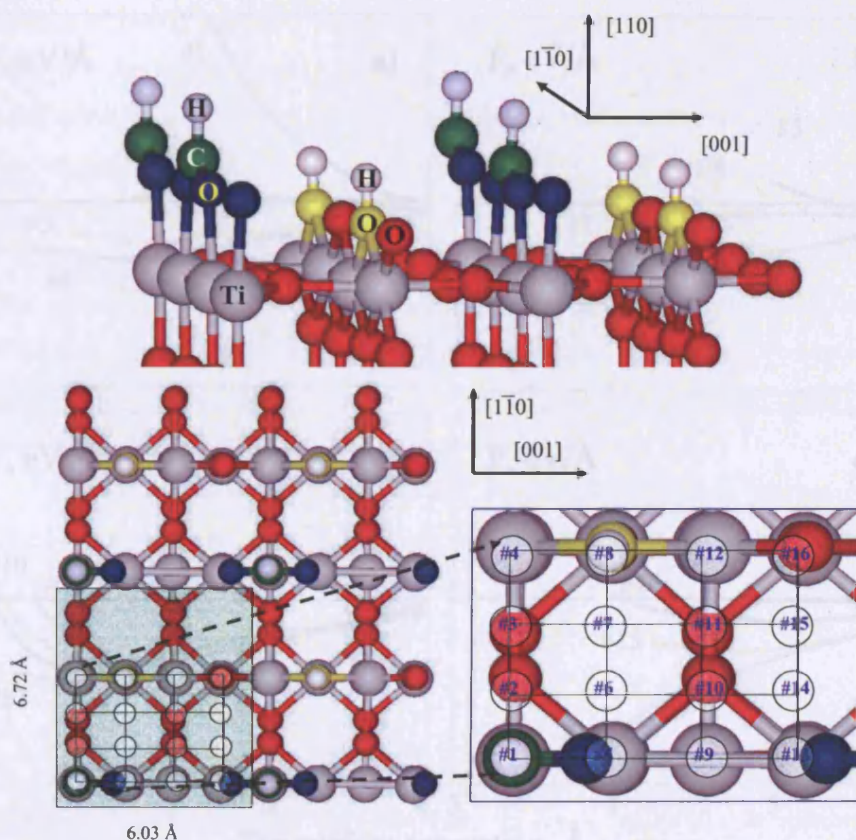


Figure 42. Side and top views of the surface unit cell used for generation of NC-AFM image of formate monolayer on TiO<sub>2</sub>(110) surface. Mesh points used to acquire the force-distance curves are shown in the inset as white circles. Oxygen atoms and cations of the TiO<sub>2</sub> are red and big grey circles correspondingly, hydroxylated oxygen is yellow, oxygens of the formate molecule are blue; carbon is shown green; smaller grey circles are hydrogen atoms.

This tip-surface forcefield is constructed on a regular x-y mesh for the surface plane and an irregular mesh in the z-direction normal to the surface. The steps in the z-direction are chosen depending on the value of the force acting on the tip at the previous step. The step decreases as the modulus of the force increases and until the modulus is less than 2.3 nN. The x-y mesh used is presented in the Figure 42.

#### 4.2.1.1 Side-dependent force-distance curves

The frequency shift was calculated for different strengths of the macroscopic Van der Waals interaction characterised by the macroscopic radius of the tip  $R = 50, 100, 200 \text{ \AA}$ . The images are, however, presented for  $R = 50 \text{ \AA}$  only, since the pattern does not visibly change with the strength of the macroscopic interaction. The conventional approach described in section 1.1 was used to model the NC-AFM image and individual force-distance curves. The resulting force-distance curves obtained over 16 meshpoints are presented in Figure 43a-d.

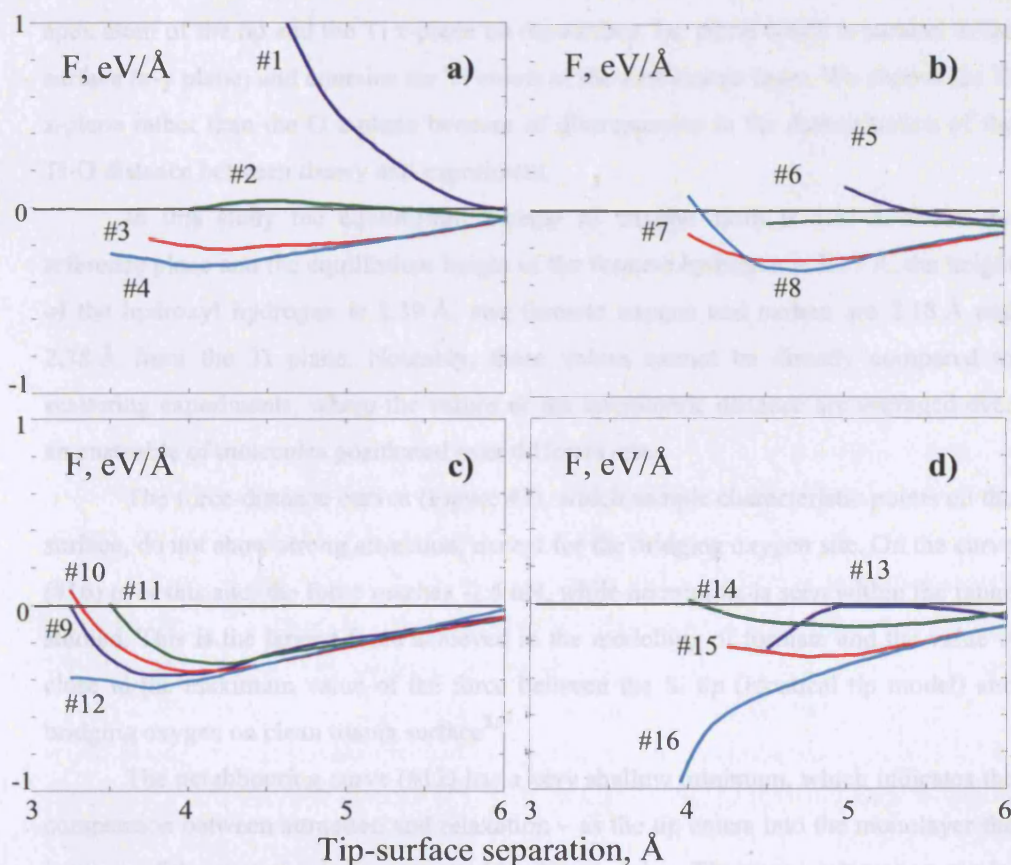


Figure 43. Force-distance curves obtained with the Si tip approaching the  $\text{TiO}_2(110)$  surface covered by a formate monolayer. Numbers by each of the force curves correspond to the mesh point numbers in Figure 42.

These curves are divided into 4 quadruplets (Figure 43a-d); each quadruplet corresponds to a line, perpendicular to the direction of the titanium/oxygen row Figure 42. These lines start at the centre of the formate (#1-#4), in the middle between neighbouring molecules (#5-#8), (#9-#12) and next to the formate oxygen (#13-#16).

The force-distance curves within each group sample the distribution of interactions, as the tip is displaced along the line. The order of the curves in Figure 43 is conserved, so that colour of the line reflects the row number of the meshpoint in Figure 42. Blue curves, for example, correspond to force curves over the Ti row populated by formate molecules. Cyan lines are obtained over the row of bridging oxygens.

An important issue in the analysis of AFM images is the choice of the definition for the distance between the tip and the surface. At large separations, where tip relaxations are negligible, we define the tip-surface distance as the distance between the apex atom of the tip and the Ti z-plane on the surface, i.e. plane which is parallel to the surface (x-y plane) and contains the Ti atoms of the first atomic layer. We choose the Ti z-plane rather than the O z-plane because of discrepancies in the determination of the Ti-O distance between theory and experiment.

In this study the equilibrium z-plane of oxygen atom is 1.31 Å above the reference plane and the equilibrium height of the formate hydrogen is 3.77 Å, the height of the hydroxyl hydrogen is 2.39 Å, and formate oxygen and carbon are 2.18 Å and 2.75 Å from the Ti plane. Notably, these values cannot be directly compared to scattering experiments, where the values of the interatomic distance are averaged over an ensemble of molecules positioned over different sites.

The force-distance curves (Figure 43), which sample characteristic points on the surface, do not show strong attraction, except for the bridging oxygen site. On the curve (#16) over this site, the force reaches -1.5 nN, while no minima is seen within the range studied. This is the largest force achieved in the modelling of formate and the value is close to the maximum value of the force between the Si tip (identical tip model) and bridging oxygen on clean titania surface<sup>218</sup>.

The neighbouring curve (#12) has a very shallow minimum, which indicates the competition between attraction and relaxation – as the tip enters into the monolayer the increase of the attraction is compensated by the repulsion. The strong interaction can be ascribed to the interaction between under-coordinated bridging oxygen atoms with the dangling bond of the tip similarly to other oxides studied in this work (section 2.2). For



the given site density, the low height of the molecules and their flexibility are crucial to enable attraction over this site, because the tip apex still can be accommodated at a close distance from the oxide surface. The shallow minimum, therefore, can be interpreted as competition between the apex Si-oxygen attraction and tip-molecule repulsion.

Well clustered attractive force curves in the Figure 43c are indicative of the valley of attraction in the landscape of this molecular monolayer. In the image, it results in a stripe along the  $[1\bar{1}0]$  direction with a small corrugation. There are two cyan lines (#16 and #8) in Figure 43b,d, taken over bridging oxygens, which are a characteristic display of the difference in interaction between the dangling bond and the two types of oxygen atoms in the system. The oxygen corresponding to the (#8) curve is hydroxylated, which results in significant repulsion starting at the nominal tip-surface separation of 4.5 Å. Notably, this is the only force curve where contribution of the hydrogen atom is evident at smaller distances, which contrasts with the long range interaction of hydrogen species observed in STM<sup>119</sup>. The difference between force-distance curves over (#16) and (#8) is not seen for tip-surface separation larger than 4.0 Å in this case. The most evident explanation of the difference is that the electrostatic field of formate effectively compensates the electrostatic field of the proton, while their states do not overlap energetically, so that the presence of the hydrogen is displayed only on close approach of the Si tip.

At the neighbouring point (#10), where the tip is approaching close to the surface and is also attracted by the oxygen, the hydroxyl-hydrogen bond is bent 53 degrees being significantly affected by the repulsive interaction with the apex Si atom. The equilibrium Si-H distance achieved in the optimisation is 2.88 Å. The overall shortest Si-H distance of 2.5 Å has been achieved at 4.0 Å in point (#4), where the competition between attraction and repulsion leads to “flattening” of the force-distance curve, which was not typical for perfect oxide surfaces.

The small magnitude of force observed in approach curves does not always mean, however, that interaction with the apex of the tip is weak. The interaction near the bridging oxygen site is an example, where strong attraction is masked by the overall repulsion. The cyan line (#12) in Figure 43c passes the minimum, but repulsion is not strong enough to compensate the Si-O attraction at the nominal separation of 3.25 Å. The actual silicon-oxygen distance is 1.72 Å, which is close to the Si-O bond length in quartz (1.61 Å).

The strong attraction of the tip over oxygen is reminiscent of the interaction of the Si tip with oxygen in the Al<sub>2</sub>O<sub>3</sub>(0001) surface (section 2.2). Similarly, there is significant relaxation both in the tip and in the surface. At the nominal distance of

3.95 Å the apex Si atom is displaced towards the surface by 0.4 Å and the oxygen atom on the surface jumps out by 0.7 Å. Therefore, the Si-O distance in the relaxed configuration is only 1.74 Å. At the same time, bonds with tip Si atoms are elongated from 2.49 Å to 2.84 Å which is indicative of strong attraction between Si and O, probably due to bond formation, and may lead to the breakage of the Ti-O bond on retraction.

Because of the weak site-dependent attraction between the tip and the surface it was at first expected that there would be a narrow range of distances where site-dependent force-distance curves could be distinguished. However the high flexibility of the surface allows significant relaxation and results in a wide range of distances where a measurable contrast can be obtained (2.0 - 3.0 Å). This range is at least as wide as the one calculated for  $\text{Al}_2\text{O}_3(0001)$  with the same tip. This illustrates that either of the two factors –relaxation and interaction - is sufficient for site-dependent contrast.

The NC-AFM image (Figure 44) has been modelled for several parameters of the macroscopic tip  $R = 50\div 500$  Å, but only  $R = 500$  Å is being discussed since no change in the pattern was found. The minimal tip-surface distance achieved is 5.0 Å. The tip-surface distance is defined as the distance from the level of Ti layer to the level of Si apex in the unrelaxed geometry.

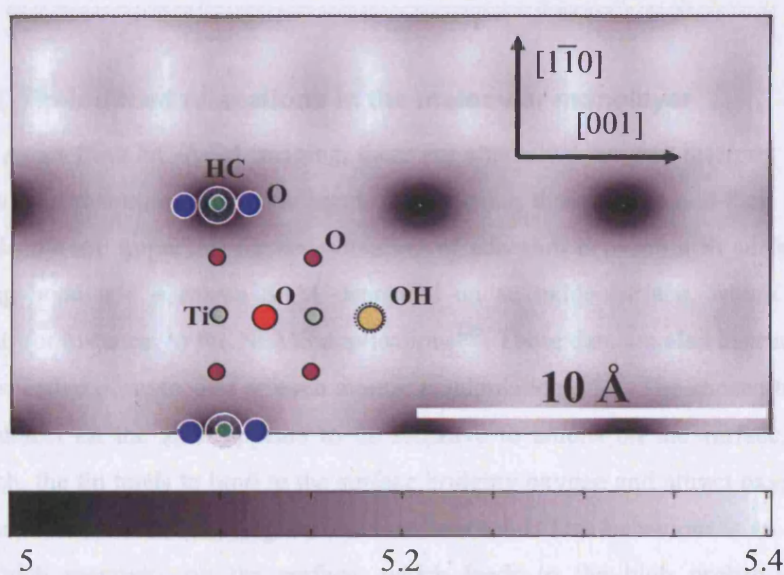


Figure 44. Modelled NC-AFM image of formate monolayer on  $\text{TiO}_2(110)$  surface. The tip radius is 500 Å,  $\gamma=3.5 \text{ fNm}^{-0.5}$ , cantilever stiffness is 35 N/m, peak-to-peak oscillation amplitude is 10 nm. Coloured circles draw correspondence between atomic sites and areas of the image. Red, magenta, yellow and blue circles represent bridging, surface, hydroxyl and formate oxygen atoms respectively.



The modelled NC-AFM image is presented in Figure 44. Dark spots elongated along [001] are centred over the formate molecule, bright stripes perpendicular [001] to the direction correspond to the bridging oxygen or hydroxyl group. These two sites can be distinguished only from the force-distance curves. The repulsion over the formate site leads to the formation of the dark spot, while bright spots over the oxygen site manifest the attraction between the Si dangling bond and surface oxygen atom. To summarize, given the strong repulsion over the formate ion, only one pattern can be observed in the ideal formate monolayer on perfect  $\text{TiO}_2(110)$  surface using the Si tip with a dangling bond.

In this pattern, the dark spot corresponds to the higher site of the surface. The bright features correspond to the atoms, which are geometrically lower. This is the opposite of conventional “topographic” AFM interpretation. The topographic interpretation is based on an assumption that interaction depends only on the distance between the apex of the tip and nearest point of the surface. When this assumption breaks down, e.g. due to significant relaxation in the system or due to a significant difference in the interaction at sites of different type, we observe a different NC-AFM pattern which is often called “inverted”. This effect is common for both conventional AFM and NC-AFM<sup>47,185,224,225</sup>.

#### 4.2.1.2 Tip-induced relaxations in the molecular monolayer

Apart from NC-AFM imaging, there are alternative ways to interpret and apply the results of this numerical experiment. In particular, these curves and their impact on the molecule are important for consideration of adhesion between a Si surface with a dangling bond and a sparse SAM deposited on an oxide surface, which might be relevant, for instance, to the NEMS applications<sup>226</sup>. These data are also instructive from the perspective of molecular or even atomic manipulation<sup>188,227</sup>. The chosen tip with an active defect on the apex appears to be sensitive to anions on the surface. At close approach, the tip tends to bind to the surface bridging oxygen and attract oxygen atoms from the formate i.e. elongating the Ti-O surface bond. This behaviour is an indication of its high reactivity on the surface, which leads to the high probability of tip contamination by the surface material.

The force-distance curves described above demonstrate that the surface is “neutral” or weakly attractive with respect to the Si tip at most of sites of the mesh, although two sites – hydrogen and oxygen of the molecule – show stronger interaction at small distances. This results in a marked repulsion over the hydrogen site and should

be treated cautiously, since the optimisation procedure used does not guarantee stability of the solution with respect to the initial geometry in the absence of periodic boundary conditions. At the neighbouring point (#2) 1.12 Å aside from the Ti row, the formate molecule bends 37 degrees (Figure 45b) and the tip experiences a smaller repulsive force of 0.1 eV/Å at a closer (4.0 Å) nominal distance compared to 1.2 eV/Å at 4.5 Å directly over the formate hydrogen. This data indicates that the rigidity of the molecule at point (#1) might be an artefact of the optimization procedure or imposed periodic boundary conditions.

An interesting situation is observed when the tip is approaching one of the oxygen atoms of the formate (#13). In this case, attraction of the oxygen to the tip is accompanied by relaxation of the monolayer and the formate molecule is bent due to the oxygen atom displacing towards the tip by 0.5 Å (Figure 45a). The Mulliken charge analysis suggests that the population of the displaced O atom increases by 0.05 e due to the proximity of the Si tip. However, the proximity of the Si tip does not always lead to relaxation. Comparison between points (#5) and (#13) is such an example.

The nominal distance between the tip and the surface is 4.5 Å in both cases, the tip is over the Ti/formate row (#5) and positioned next to the oxygen (#13). One could have suggested that the force and the response of the surface should be the same in both points. However, the tip is repelled with force  $F = 0.08$  eV/Å at point (#5) and attracted with force  $F = -0.08$  eV/Å at point (#13). The oxygen relaxation in point (#5) is only 0.16 Å compared with 0.5 Å at point (#13). The difference is due to the charge density of the covalent Si-Si bonds of the apex Si atom.

The charge density of the Si-Si bond is highest in the direction of the neighbours and smallest along the bisector of the angle between them. At the point #5 one of these Si neighbours is over the molecule and prevents it from relaxing upwards, while at the point #13 the covalent bonds of the apex atom do not obstruct the relaxation of the

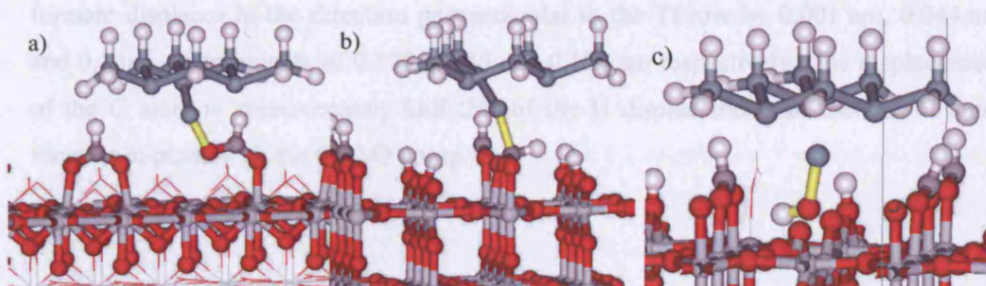


Figure 45. Relaxed geometry structure of the Si tip over selected points (#13, #2, #8 as in Figure 42) of the formate monolayer on  $\text{TiO}_2(110)$ . The interaction between the tip and the molecule induces significant displacements. a) retraction of formate oxygen in a Ti-O bond, b) bending of the formate molecule, c) bending of OH group.

molecule. This is because the tip approaches the molecule from another side so that there are no Si atoms directly over the molecule. The effect is similar to the sensitivity of the pattern of interaction over the  $\text{Al}_2\text{O}_3(0001)$  to the rotation of the apex around its axis described in section (2.1.2).

The ability to access the binding group of the adsorbed formate molecule is therefore a special case. If the molecular chain was longer, there would be no access to the binding group in the perfect monolayer on  $\text{TiO}_2(110)$  with full coverage, which is the case for the monolayer of acetic acid - no access to the binding group with the Si tip could be found using static optimisation for loads in the 2-5 nN range<sup>141</sup>.

The major risk to a “pure Si” tip apex is therefore the chance of contaminating the tip with the surface material, most likely the adsorbed molecule or an oxygen from the bridging oxygen row (Figure 45). The probability of such an event depends on the accessibility of the corresponding group in the image. The comparison of our result and the results on the modelling of the NC-AFM images of acetic acid<sup>140</sup> with the experimental images supports the observation that the quality of the acetate image is always higher and contains no “scratches” indicating a possible change of the tip apex<sup>228</sup>.

The rest of this section discusses the deformations induced by the tip in the monolayer. Deformations of the system can be split into two categories: (1) tilting of the molecule and of the OH group; and (2) displacements of tip and surface atoms.

A strong tilt of the molecule is observed when the tip is over the (#2) site. It tilts as a whole with respect to the bridging oxygen atoms (see Figure 46c). The tilt can be understood as a result of C-H group repulsion from the Si atom at the tip apex. At large distance (0.295 nm), the C-H bond is contracted by 0.002 nm due to the presence of the Si dangling bond. As the tip approaches closer to the oxygen site, the hydrogen atom of formate displaces in the direction perpendicular to the Ti row by 0.001 nm, 0.044 nm and 0.1 nm, at tip heights of 0.195, 0.145 and 0.105 nm respectively. The displacement of the C atom is approximately half that of the H displacement, so that the H atom remains in-plane with the O-C-O group.



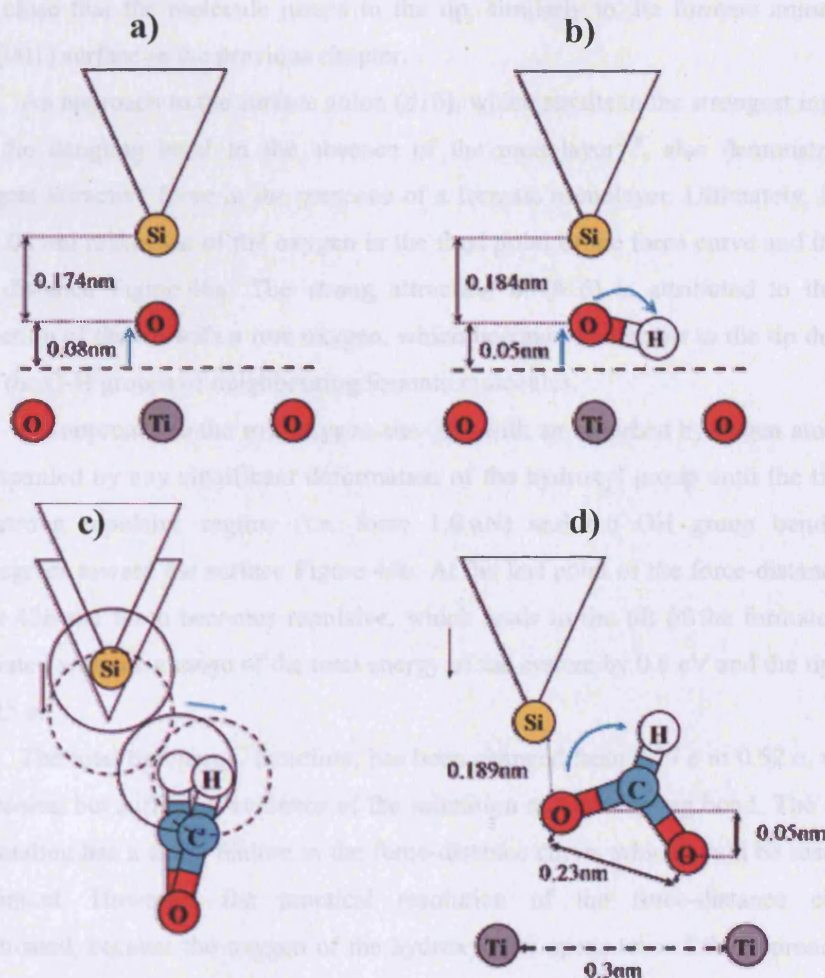


Figure 46. Schematic representation of displacements induced in the  $\text{TiO}_2$  surface and adsorbed formate monolayer by the Si tip with dangling bond approaching (a) at row oxygen site (#16); (b) at hydroxylated row oxygen (#8); (c) at (#2) site next to the formate molecule; (d) at (#13) site next to the formate molecule. Bold dashed line indicates the level of bridging oxygen atoms as the reference for the height of the tip.

Further analysis shows that the apex Si atom "pushes" the hydrogen of the formate, rather than C, making the whole molecule tilt (Figure 46c). As the tip approaches closer to H, the tilt increases. The only exception is the position directly above the hydrogen where the molecule remains in the upright position. However, if we included tilting vibrations of the molecule at finite temperature in the simulations to break the symmetry, we would expect to find a significant tilt and molecular deformation. This would affect the pattern of the image, but only quantitatively since the interaction remains strongly repulsive at this location of the tip, unless the approach

is so close that the molecule jumps to the tip, similarly to the formate anion on the MgO(001) surface in the previous chapter.

An approach to the surface anion (#16), which results in the strongest interaction with the dangling bond in the absence of the monolayer<sup>218</sup>, also demonstrates the strongest attractive force in the presence of a formate monolayer. Ultimately, it results in a 0.08 nm relaxation of the oxygen in the final point of the force curve and 0.174 nm Si-O distance Figure 46a. The strong attraction at (#16) is attributed to the direct interaction of the tip with a row oxygen, which becomes accessible to the tip due to the tilt of the C-H groups of neighbouring formate molecules.

An approach to the row oxygen site (#8) with an adsorbed hydrogen atom is not accompanied by any significant deformation of the hydroxyl group until the tip enters into strong repulsive regime (i.e. force 1.0 nN) and the OH group bends about 100 degrees toward the surface Figure 46b. At the last point of the force-distance curve Figure 43b the force becomes repulsive, which leads to the tilt of the formate, and is associated with the change of the total energy of the system by 0.8 eV and the tip charge by 0.25 e.

The total tip charge, therefore, has been changed from 0.27 e to 0.52 e, which is not precise, but sufficient evidence of the saturation of the dangling bond. The onset of OH bending has a sharp feature in the force-distance curve, which could be resolved in experiment. However, the practical resolution of the force-distance curve is complicated, because the oxygen of the hydroxyl site opens toward the approaching Si dangling bond and relaxes 0.052 nm upwards, so that Si-O distance becomes 0.186 nm. Such a short distance, is indicative of formation of a strong bond and therefore of the possibility of contaminating the tip with an oxygen atom or with an OH group.

The possibility of contamination of the tip with the adsorbed molecules is indicated by the tip-formate interaction at (#13) site. The tip apex in this configuration is shifted from (#13) oxygen by 0.045 nm towards the next molecule in the row. Descent of the tip to the height of 0.280 nm results in 11 degrees rotation of the formate in its plane around the O6 oxygen Figure 46d. The molecule is also repelled by the tip sideways and shifts 0.06 nm along the Ti row to the formate nearest molecule. As the result of the tip-molecule interaction, the C-O distance changes from 0.128 nm to 0.134 nm for the nearest oxygen and to 0.124 nm for the other oxygen.

Most importantly, the tip withdraws the nearest oxygen of COO group by 0.05 nm from the surface and the Ti-O bond length increases from 0.211 nm to 0.282 nm. The fact that a Ti atom relaxes in the direction opposite to the displacement



of the oxygen indicates that the Ti-O bond is being broken. Deformations of the molecule itself include a decrease by 2 percent in the O-C-O angle and a 10 percent deformation of C-O bonds. The full process of formate removal has not been addressed in this study because of the high computational cost and focus on imaging with the Si tip. Experimental validation of a possibility of contamination of the tip by a single molecule is complicated, but can be performed in NC-AFM combined with time-of-flight experiment<sup>145</sup>.

#### 4.2.2 Comparison with experimental data

A monolayer of formate on  $\text{TiO}_2(110)$  surface was the first monolayer on oxide surface resolved with molecular resolution (Figure 47a) using UHV NC-AFM<sup>228</sup>. The reported image reproduces 6.0 Å periodicity along the rows, but has no stable molecular resolution Figure 47b. The bright features of the image were tentatively interpreted as top sites of formate ions. This conclusion is “supported” by observation of bright features on the surface covered by formate molecules at low concentration. However, it should be noted that this argument may work only if the tip-molecule interaction, the surface chemistry of the formate and the mechanisms of contrast formation are altogether transferable between the two systems with low and high coverage.

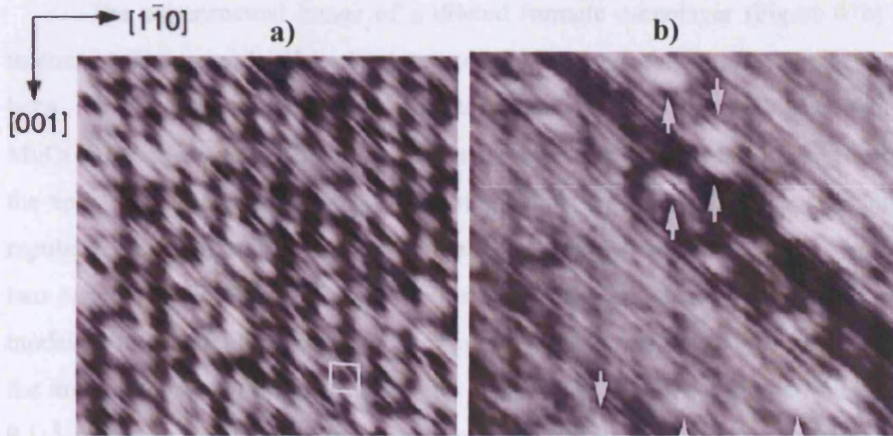


Figure 47. (a) NC-AFM image of the (2×1) monolayer of formate ( $\text{HCOO}^-$ ) on  $\text{TiO}_2(110)-(1\times1)$  ( $13.3\times13.3\text{ nm}^2$ ). Acquired with positive bias 1.2 V at normalized frequency shift  $46.5\text{ fNm}^{0.5}$ . b) NC-AFM image of dilute monolayer ( $7.1\text{ nm}\times7.1\text{ nm}$ ). Arrows indicate positions of formate molecules. Acquired with positive bias 1.3 V at normalized frequency shift  $16.5\text{ fNm}^{0.5}$ . (Parameters:  $df = 80\text{ Hz}$ ,  $f = 295\text{ kHz}$ ,  $A_p-p = 30\text{ nm}$ ,  $k = 33\text{ N/m}$ )<sup>228,32</sup>.

One can make an assumption that the missing bright spots along a row in the image identify the row as an oxygen row with oxygen vacancies. This assumption leads to a choice between two major alternatives: either the apex of the tip is pure Si during the whole experiment, as it was claimed by authors, or it is partially oxidized and carries a net positive potential.

If the tip is oxidized, it has to carry an overall positive potential, because stripes with randomly distributed spots (vacancies) seen in the image are “bright”, which corresponds to the conventional interpretation of clean  $\text{TiO}_2(110)$ <sup>115</sup>. Both chosen models would interact strongly with the oxygen row and display vacancies as dark spots, i.e. a clean titania surface with vacancies cannot differentiate at a qualitative level between those tip models.

The interpretation of an image at full coverage concludes that the tip-surface interaction is repulsive above the top sites of the molecules unless there is a specific attraction due to the interaction between the tip and the molecule. This could be due to a strong negative dipole or negative charge on the top of molecule if the tip apex was an oxide with positive tip potential. However, it was shown in section 3.2.1 that no strong attraction is observed over a bare formate anion on the more ionic  $\text{MgO}(001)$  surface. For a dissociated molecule of formic acid we have an extra proton which counteracts the formate dipole. Therefore, there is no strong interaction which would allow one to distinguish the interaction of the two tip models with a formate monolayer.

The experimental image of a diluted formate monolayer (Figure 47b) exhibits interesting features related to the results of the previous chapter. In the chapter 3 it has been demonstrated that an oxidized tip with positive potential sees formate on  $\text{MgO}(001)$  surface as bright at smaller frequencies shifts (Figure 35). As the strength of the tip-surface interaction increases, the single blob is split into two lobes because of the repulsion from the inert C-H head group. We observe a similar structure, indicated by two arrows in the Figure 47b which both have similar shape and size to the image modelled in the previous chapter. The greater diameter of the pair of bright features in the image Figure 47b is 9.2 Å while the size estimated in the formate-MgO study was 9.1 Å. Therefore, the pair of “formate” ions could well match the theoretical estimation of a single molecule imaged with an oxide tip with positive potential.

Although the comparison is not sufficient to draw final conclusions on the image; it clearly indicates that interpretation of images at atomic scale should be undertaken with care. In the particular case of dilute monolayer, further experimental investigation is required, because the publication does not contain scanlines, statistics

and values of corrugations. The fact that there are traces of the tip change, such as continuous white and black stripes (Figure 47b) and the considerable value of normalized frequency shift ( $16.4 \text{ fNm}^{0.5}$ ) suggests the regime of intermediate contact with the molecules. This value compares with the strength of interaction predicted over the MgO-formate system in the point of the closest approach with a tip of 500 Å radius.

Strictly speaking, many more experimental images of the molecular monolayer are required for unambiguous theoretical interpretation of the image. We do hope that this study will stimulate further experimental efforts in NC-AFM studies of formic acid on oxide surfaces.

A recent theoretical study of interaction of acetic acid<sup>229</sup> with a “pure Si tip” also demonstrated that CH<sub>3</sub> group is inert with respect to the dangling bond of the Si tip. The extension of the chain and the presence of a CH<sub>3</sub> “umbrella” decreases the access of the tip to the surface at the full coverage. In the area between the molecules, however, the TiO<sub>2</sub>(110) surface is still accessible. At the closest approach, penetration of the tip in these areas was predicted to induce a significant tilt (about 30°) of surrounding acetate molecules. The results for acetic acid agree well with the results of this chapter and predict the “inversed” interpretation of the experimental image, i.e. the top sites of the acetic molecule are seen as dark spots in the image.

### 4.3 Summary

The results presented above demonstrate that a Si tip carrying a dangling bond is able to resolve the positions of molecules in the monolayer. The major features of the modelled image are “dark spots” associated with the head groups of the formate. At these sites the molecules experience no significant attraction to the silicon atoms of the tip and repel the tip as it approaches. The area of significant repulsion is seen as dark in NC-AFM image and centred at the equilibrium position of the top formate site.

The high reactivity of the tip leads to contamination of the dangling bond by oxygen from the  $\text{TiO}_2(110)$  surface or by the formate molecules when the tip apex approaches to the  $\text{TiO}_2(110)$  surface closer than 0.2 nm. However, recent experiments have demonstrated that site-specific force-distance curves can be taken at low temperatures<sup>230,231</sup>. This breakthrough allows, in principle, the oxygen and hydroxyl sites of the substrate to be differentiated by NC-AFM.

It is shown that the interpretation of NC-AFM high resolution images of a perfect molecular monolayer adsorbed on an oxide surface is different from the interpretation of high resolution images of the ideal surfaces of semiconductors and insulators<sup>43</sup>. The distinctive properties of an adsorbed monolayer are the high mobility, polarity and flexibility of the adsorbed molecules. In particular, because of their flexibility, more atoms of the tip apex contribute to the force of the tip-surface chemical interaction reducing resolution in the image. The interplay between macroscopic and chemical interactions in CFS mode results in the interpretation of the dark spots in the image as positions of the highest (CH) group of the adsorbed molecule ( $\text{HCOO}^-$ ). These observations are of a general character and can be used for interpretation of high resolution NC-AFM images of molecular monolayers or other systems with similar qualities.

## 5 Characterisation of KI-filled SW-CNT

In this chapter we investigate the possibility of detecting potassium iodide(KI) filling in single wall carbon nanotubes SWNT by means of an AFM with an ionic tip. To study this, we characterise the combined system KI:SWNT, as well as each of the system's components. To analyze the influence of the carbon nanotube on the KI filling, we study the electronic structure of the KI-filled single-walled carbon nanotube using *ab initio* methods. The systems are characterised by their electronic structure, phonon spectrum, energy of defect formation and electrostatic potential. The electronic properties and phonon spectrum of the system are compared to those of an isolated KI chain. The energy of the formation of neutral divacancies in the KI chains is compared to the results obtained for the better studied bulk KI system. The interactions between the KI and SWNT are expected to be displayed in the properties of the combined system.

Nanotubes are often considered as possible building blocks for future electronic devices. The function of SWNTs in such a device<sup>232-234</sup> will be determined by the interactions between the walls of the nanotube, filling and substrate. The assembly of the CNT-based devices requires precise positioning of the CNT on the surface, which can be achieved by AFM techniques<sup>235-237</sup>. The key problem in such an experiment is to detect the presence of the filling in an individual CNT.

Currently, a range of techniques can be used to characterise individual single-walled nanotubes: HRTEM, AFM, as well as Raman, Rayleigh and fluorescence spectroscopies. However, each of these techniques suffers from various limitations. Fluorescence studies of SWNTs are limited to semiconducting SWNTs<sup>238,239</sup>. The reported approach using Rayleigh scattering spectroscopy does not allow characterisation of supported nanotubes<sup>240</sup>. HRTEM is a destructive method of characterisation<sup>241-243</sup>. Novel developments have demonstrated<sup>244</sup> that micro-Raman spectroscopy has the potential for characterising fillings in individual SWNTs, although technical challenges still exist in the collection of the Raman signal<sup>245</sup>.

Dynamic atomic force microscopy combines several advantages - it can be used to manipulate the SWNT on the surface and also can operate on all types of SWNTs. In addition, it does not depend on the conductivity of the surface and does not require extra equipment in the chamber. Moreover, this method offers unprecedented sensitivity to the force (0.1-0.01 nN) and position (0.01 nm) and allows site-dependent force spectroscopy at low temperatures. Very recently, dynamic force microscopy at low temperatures in "non-contact" mode (NC-AFM) has demonstrated resolution of the facets on the surface of a single-walled carbon nanotube<sup>246</sup>.



The structural model for the KI-filled SWNT was suggested on the basis of TEM images with “atomic” resolution<sup>243,247</sup> and supported by theoretical studies<sup>248-250</sup> (Dr. Mark Wilson, UCL) with pair potentials between K and I ions in KI. Unfortunately, no reliable potential functions are available for SWNT-KI interaction, so that SWNT atoms were not allowed to relax. These studies have yielded possible structures of the KI subsystem which agree well with the TEM experimental images.

Recent practical application of the NC-AFM technique to study the properties of KI-filled SWNT<sup>251</sup> has been undertaken in Cambridge (Dr. Adelina Ilie) in collaboration with the TEM group in Oxford. One of the ambitions of the project was to test the limits of sensitivity of NC-AFM and attempt to detect the filling of the SWNT by observation in “non-contact” mode. The important experimental result of this work was the possibility to differentiate “filled” and “unfilled” SWNTs by NC-AFM in the range of the tip-surface interaction of order 1.0-2.0 nN. In particular, it was possible to acquire local force-distance curves over the nanotube, although one cannot claim that these measurements were site-dependent due to the drift present in the setup at room temperature.

Discussions with Dr. Wilson and Dr. Ilie motivated us to undertake an electronic-structure study of the KI-SWNT system. This approach will provide a more adequate description of the KI-SWNT interaction missing in the pair potential framework. Moreover, it allows us to study electronic properties of typical defects in the KI and dynamic properties of the combined KI-SWNT system.

It has been already shown in this work (Chapter 4) that the ionic surface can be detected by NC-AFM even in the presence of an organic monolayer adsorbed on the surface. In this chapter we investigate the possibility of detecting the presence of an ionic material inside a single-walled carbon nanotube (SWNT) with a tip carrying a strong electrostatic potential.

Since this work is one of the first *ab initio* studies of the KI:SWNT(10,10) system, we also study the properties of the free KI chain and empty SWNT. In particular, we study the electronic structure of hypothetical free KI chains and compare the formation of defects in free and encapsulated KI chains. We also analyse the interaction between the SWNT and the filling both with and without defects. In addition, we investigate the effect of the filling on the electronic structure, electrostatic potential and phonon spectrum of the system to assess the applicability of NC-AFM and Raman spectroscopy for discriminating between filled and unfilled SWNTs.

The chapter starts with the definition of the model for the combined system (section 5.1), followed by an investigation of the properties of the reference systems (section 5.2), compounding (section 5.3) and combined systems (section 5.4). The analysis of the results is presented in the discussion (section 5.5).

### 5.1 The model of KI-filled SW-CNT

Atomistic modelling of the filled single-walled nanotube (SWNT) encounters problems associated with the choice of the computational methods and the model system. In particular, the nanotubes are usually bent ( $R \approx 500$  nm)<sup>252</sup> and contain defects. Moreover, the KI and SWNT subsystems are incommensurate.

In this study, the model system will exclude any CNT defects, as well as the presence of the substrate. Periodic boundary conditions (PBC) along the CNT axis are chosen to reproduce the electronic structure of an “infinite” perfect nanotube and the metallic state for (10,10) CNTs. Therefore, the bending of the nanotube and its effect on the filling is neglected in all our calculations.

Given the incommensurability between the atomic structure of the SWNT and its filling, the description of the combined system with a supercell of a realistic size, requires that one or both systems should be deformed along the translation symmetry axis. The Young modulus of the SWNT (10,10) is in the range 1-3 TPa according to experimental and theoretical evaluations<sup>253-256</sup>, which exceeds the Young modulus of the KI (30 GPa)<sup>257</sup> by two orders of magnitude. Therefore, in this study, the softer system (KI) is deformed to reduce the dimension of the supercell to a multiple of the lattice period of the nanotube ( $a_{\text{SWNT}} = 2.44$  Å).

The size of the periodic unit cell for the encapsulated KI system is chosen to minimize the misfit between the nanotube and KI structure. Starting from calculated lattice parameters in the bulk KI ( $a_{\text{KI}}^{\text{bulk}} = 7.183$  Å) and empty (10,10) SWNT ( $a_{\text{SWNT}} = 2.49$  Å) the ratio between the lattice constants of the two materials can be approximated as

$$r = a_{\text{KI}}^{\text{bulk}} / a_{\text{SWNT}} = 2.89 \leftrightarrow 14/5 = 2.8.$$

The lattice constant ratio  $r$  can be approximated as 14:5, therefore the SWNT supercell with lattice constant  $a_{\text{SC}} = 14 \cdot 2.49$  Å = 34.86 Å should accommodate 5 unit cells of the KI cell with a small strain about 2.6 % in the KI structure. However, taking

into account the relaxation of the lattice constant in the chain geometry ( $a_{KI}^{chain} = 6.88 \text{ \AA}$ ) compared to the bulk lattice constant, ( $a_{KI}^{bulk} = 7.183 \text{ \AA}$ ) the misfit in the structure amounts to 1.2 %. The resulting unit cell consists of 600 atoms ( $N_{atoms} = 40*14+8*5$ ) and occupies volume  $20 \times 20 \times 34 \text{ \AA}^3$ .

The test calculations of the combined system were performed at a single k-point ( $\Gamma$ -point). The memory requirements for this system exceeded the resources on available parallel machines, so the system size was reduced to 7:2 and 3:1 replication of CNT and KI unit cells, which gives the strain of the KI chain as 21% and 8%, respectively. The accumulated misfit is partially released due to relaxation of the KI chain inside the CNT.

The ionic filling itself, shaped by the SWNT walls into a string, formally belongs to the class of inorganic insulating nanotubules (IINT), although this term usually refers to hollow systems of larger diameter. To avoid complication, we consider the bulk-like structure for the KI filling in the nanotube, while neglecting more sophisticated “twisted” helical structures of the IINT inside the CNT that have been proposed<sup>249</sup> as a result of MD simulations and HRTEM data. This is because the shortest period of the “twisted” KI chain, which is able to fill the (10,10) nanotube, exceeds 4 nm and consequently exceeds our current computational resources.

The *ab initio* DFT framework applied in this work allows us to study the interplay between electronic structures of the nanotube and the filling material. To achieve acceptable performance for large periodic systems the SIESTA package was used<sup>74</sup>. The system possesses translational symmetry in one direction only, therefore the size of the supercell in the two other directions is chosen to be large enough to have zero matrix elements of the Hamiltonian between images of the systems. Using the localized basis set is also beneficial in this case, compared to the plane wave basis set, because the size of the basis set remains the same with increasing vacuum space. As a result, the expansion of the supercell does not affect significantly the consumption of CPU time<sup>74</sup>, although it does require more operating memory.

## 5.2 Electronic structure of subsystems

### 5.2.1 Electronic structure of the single-walled carbon nanotubes (10,10)

The atomic structure of a (m, n) nanotube can be obtained by folding the corresponding 2D layer with basis vectors  $\vec{e}_1$  and  $\vec{e}_2$  into a cylinder (in case of CNT – a

graphene sheet, and  $(\vec{e}_1, \vec{e}_2) \neq 0$ ). The indices “(m, n)” indicate the direction in which the 2D sheet is folded into the cylinder. For example, in the case of CNT (10,10) the site (0,0) should coincide with site  $10\vec{e}_1 + 10\vec{e}_2$  or (10,10), and the vector, perpendicular to (10,10), (i.e. (1,-1) on the graphene sheet) defines the direction of the translational symmetry in the CNT. The length of the (10,10) vector defines the length of the circumference of the unrelaxed nanotube.

The unit cell of SWNT (10,10) consists of 40 atoms and has a 0.244 nm period, which is equal to the period of the graphene sheet. According to the available experimental and theoretical data<sup>6,258</sup>, the SWNT (10,10) is metallic, so a fine mesh in the reciprocal space (*k*-mesh) is needed for the faithful description of its electronic structure near the Fermi level. The metallic state of the perfect nanotube and its band structure are reproduced with a  $1 \times 1 \times 32$  Monkhorst-Pack *k*-mesh using 16 non-equivalent *k*-points and TZP (triple- $\zeta$  with polarization) basis set. The values of the SIESTA parameters “energy cutoff” and “energy shift” used for these and following calculations in this chapter are 150 Ry and 15 meV respectively. The pseudopotential for the carbon atom was generated in the form  $[1s^2]2s^22p^2$  using the PBE functional.

Figure 48 compares the density of states (DOS) obtained in calculations with 16 (red line) and 6 (green line) unequivalent *k*-points. The results obtained with the reduced *k*-mesh display a gap in the DOS. This gap is purely an artefact of the choice of the *k*-points, which can be understood from the band structure of the system (Figure 49).

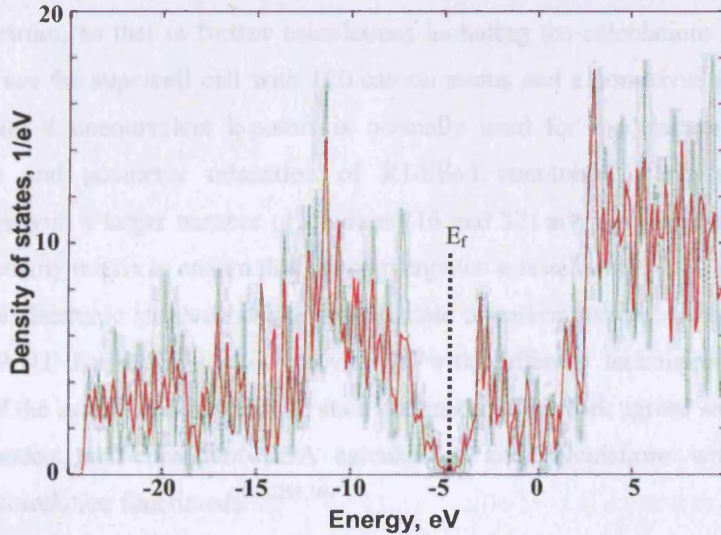


Figure 48. Density of states for the (10,10) carbon nanotube calculated in periodic model with elementary unit cell and 6 (dashed green line) and 16 (red line) unequivalent *k*-points. The gap closes within smearing resolution for 16 *k*-points calculation, however, consideration with 6 *k*-points results in 1.0 eV gap between valence and conduction bands.



Due to the 1-dimensional periodicity of the system, the Fermi surface in this system is represented by a single point of contact between the conduction and the valence bands (Figure 49). In the  $\Gamma$ -point, the gap reaches its largest value of about 7.0 eV. Therefore, the formal gap displayed in the self-consistently calculated spectrum, depends strongly on the choice of the mesh.

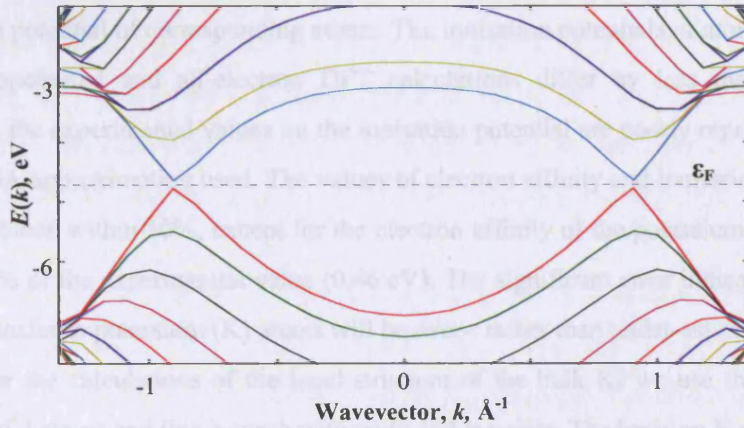


Figure 49. Band structure of metallic (10,10) SWNT, calculated for unit cell of 40 atoms with 16 inequivalent k-points. The Fermi level is  $\epsilon_F = -4.71$  eV. The small (less 0.1 eV) gap remains between conduction band and valence band due to the finite number of k-points used.

The use of a larger supercell and trivial k-mesh (only  $\Gamma$ -point) in SIESTA sometimes allows economizing the CPU time at expense of memory consumption. However, the largest supercell attempted here with 280 atoms still has a gap of 1.0 eV in the spectrum, so that in further calculations including the calculations with the KI filling we use the supercell cell with 120 carbon atoms and a non-trivial k-mesh. The k-mesh with 4 unequivalent k-points is normally used for the electronic structure calculation and geometry relaxation of KI-filled nanotubes, while single point calculations with a larger number of k-points (16 and 32) are performed starting from the same density matrix to ensure that the convergence was achieved.

The electronic structure of the ground state of carbon nanotubes, especially the (10,10) SWNT has been studied previously with different techniques. The band structure of the system and its metallic state obtained in this work agrees well with tight binding models, self-consistent LDA calculations and calculations with advanced exchange-correlation functionals<sup>234,259,260</sup>.



## 5.2.2 Electronic structure of potassium iodide

### 5.2.2.1 Bulk KI

The pseudopotentials for potassium (K) and iodine (I) were generated for  $[\text{Ar}]3p^64s^1$  and  $[\text{Kr} 4d^{10}]5s^25p^5$  electronic configurations correspondingly. We characterize the pseudopotentials by their ability to reproduce the electron affinity and ionization potential of corresponding atoms. The ionisation potentials of atoms obtained in pseudopotential and all-electron DFT calculations differ by less than 0.01 eV. However, the experimental values on the ionisation potential are poorly reproduced due to the GGA approximation used. The values of electron affinity and ionisation potential are reproduced within 10%, except for the electron affinity of the potassium ion, which is just 20% of the experimental value (0.46 eV). The significant error indicates that the charge transfer to potassium (K) atoms will be over-, rather than under-estimated.

For the calculations of the band structure of the bulk KI we use the primitive unit cell of 2 atoms and fine k-mesh with up to 144 k-points. The basis on K and I atoms is chosen in the form of the triple- $\zeta$  with polarization (TZP) basis set. For this setup, the band gap in the fully relaxed geometry is 4.0 eV. The band structure, calculated for the primitive unit cell, shows (Figure 50b) the direct bandgap with the minimum at the  $\Gamma$ -point.

This result matched the calculations of the electronic structure in the larger supercell of cubic shape with 64 atoms with 18  $k$ -points. Both calculations result in the band gap of  $E_{\text{gap}} = 4.0$  eV, which is an underestimate of the experimental value  $6.3 \text{ eV}^{261}$ , as would be expected from the DFT calculation. The charges on the ions are  $\pm 0.55 |e|$ , according to the Mulliken population analysis, which is close to the ionicity obtained for KBr surface using B3LYP in embedded cluster method calculations.

The band structure of the system along the  $\Gamma$ -X direction is presented in Figure 50b. According to the PDOS analysis, the valence band of KI is formed by the states on iodine atoms with an admixture of potassium (K) states contributing less than 10%. The percentage of K-admixture decays to zero at the edges of the valence band. The conduction band and, especially, the bottom of this band is formed by the states of the cation.

The relaxed geometry of the primitive unit cell with 2 atoms per unit cell is used to calculate the vibrational spectrum of the system. We validate the DFT result by

comparison with the results of the neutron diffraction on the system<sup>262</sup> (Figure 51a). The main criteria of the comparison are the positions of top of the optical band and the width of the acoustic band. The general trend is that the calculated crystal appears slightly softer than the real potassium iodide – the frequencies of the optical modes at the  $\Gamma$ -point and the width of the acoustic band are 20 % less than the measured values.

The previous studies have discussed the electronic structure of the system and the effect of the spin-orbital interaction on the electronic properties<sup>263,264</sup>. In the DFT framework, the choice of the exchange correlation functional is important to reproduce quantitatively the electronic properties and in particular, the band gap of the system, however this study focuses only on qualitative behaviour and therefore, uses DFT-GGA.

To summarize, for the bulk potassium iodide, the DFT description used in this chapter, overestimates the lattice constant by 1.8 % and underestimated the experimental bandgap<sup>261</sup> of the system by 36 %. This description produces qualitatively correct electronic structure of the system and the vibrational spectrum, which are in the qualitative agreement with previous theoretical and experimental studies of the system.

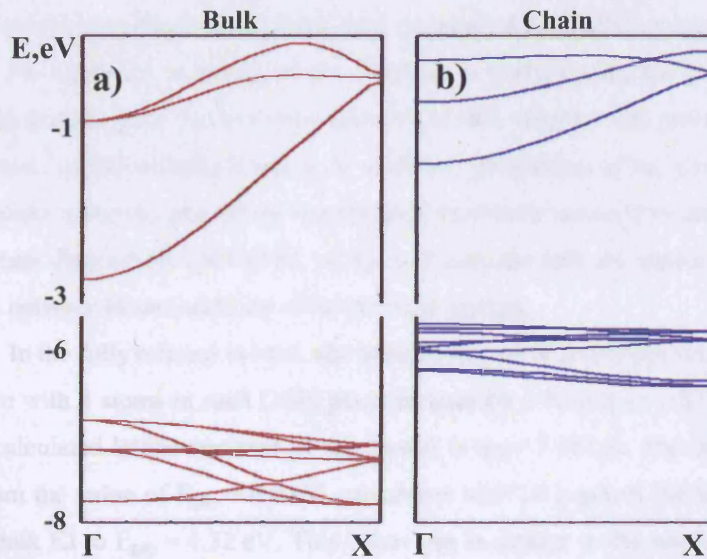


Figure 50. Electronic band structure of the KI system along the  $\Gamma$ -X direction (b) in the bulk KI, and (c) in the KI chain. The dispersion curves are calculated for the eight-atom unit cell.

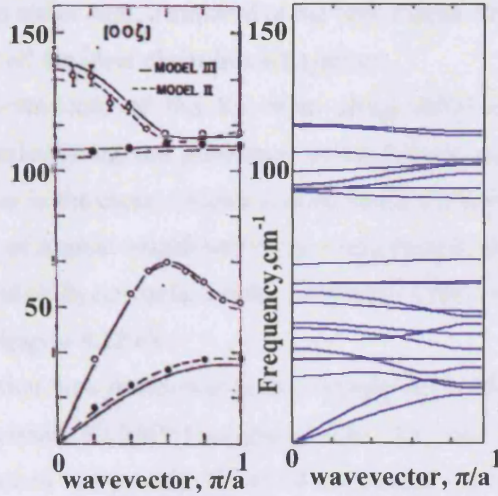


Figure 51. (a) Dispersion relation for normal modes of vibration of the potassium iodide crystal from the neutron diffraction data<sup>262</sup>; (b) Calculated dispersion relations of the KI chain calculated in the 8-atom unit cell.

#### 5.2.2.2 [001]-chains of KI

We look into properties of three  $2 \times 2$  chain structures, which represent the “ideal” KI chain. The three structures being considered are: (i) chain with the equilibrium lattice constant and relaxed atomic positions, (ii) chain with lattice constant of the KI-SWNT supercell ( $a_{\text{KI}} = 7.46 \text{ \AA}$ ) and relaxed atomic positions and (iii) chain with fixed atomic positions extracted from the relaxed KI-SWNT system ( $a_{\text{KI}} = 7.46 \text{ \AA}$ ).

The electronic structure of the KI chain is studied using the same basis set and mesh parameters as in the previous sections of this chapter. The primitive unit cell of the system, which includes 8 atoms, is used for calculations of the electronic structure. Six k-points along the axis of the translational symmetry are used to sample the k-space. The lateral dimensions ( $40 \times 40 \text{ \AA}$ ) of the 3-D periodic cell are chosen so to avoid the overlap between basis functions of the periodic images.

In the fully relaxed system, the lattice constant of an infinite unsupported  $\langle 100 \rangle$  KI chain with 4 atoms in each (100) plane reduces by 4 % to  $a_{\text{KI}} = 6.875 \text{ \AA}$  as compared to the calculated lattice constant of the crystal is  $a_{\text{KI}} = 7.183 \text{ \AA}$ . The bandgap increases 8 % from the value of  $E_{\text{gap}} = 4.0 \text{ eV}$ , calculated with 18 k-points for 64-atom supercell of the bulk KI to  $E_{\text{gap}} = 4.32 \text{ eV}$ . This behaviour is similar to the one in the bulk phase, where the largest band gap is achieved in the slightly strained crystal.

In the system with relaxed positions of atoms and lattice constant fixed at the bulk value, the band gap is  $E_{\text{gap}} = 4.11 \text{ eV}$ . According to the PDOS analysis, the nature of the states at the top of the valence band and at the bottom of the conduction band

does not change in either case, compared to the bulk PDOS. The Mulliken charge on the ions is  $\pm 0.6 |e|$  for all the ideal chain-like KI systems.

The band structure of the KI chain along [001] direction is presented in Figure 50c. The calculations are performed in the 8-atom unit cell. The dispersion is consistently weaker in the chain systems and the bands are respectively narrower, due to the lower number of nearest neighbours in the chain compared to the bulk. The position of the valence band shifts upwards, but the shrinkage of the conduction band effectively increases the bandgap to 4.12 eV.

No relaxation was performed in the system obtained by stripping the SWNT shell from the relaxed KI:SWNT configuration. The bare KI structure has similar electronic structure to the system discussed above and the bandgap of 4.11 eV. The increase in the value of the bandgap is also attributed to the reduced lattice constant. The distortion of the atomic positions in the system due to the presence of SWNT is less than 0.2 Å compared to the relaxed atomic position of the chain at the same lattice constant.

### 5.2.2.3 Divacancies in the bulk of KI

The potassium iodide is a Schottky-type crystal, i.e. Schottky defects have the smallest formation energy<sup>265-267</sup> in the bulk. These defects are also responsible for diffusion in KI<sup>268,269</sup> and play the key role in the models of KI melt<sup>270,271</sup>. We study the cation-anion divacancy defects in 3D systems and calculate the formation energy to assess the quality of the description provided by the GGA-DFT and to compare with the result for the KI chain.

The divacancy formation energy in the bulk of KI is calculated with respect to the equivalent supercell and KI molecule evaluated in the same supercell using the identical parameters of the calculation (section 5.2.2.1). The divacancy was created in the 64-atom supercell with the period of 14.37 Å, so that the distance between nearest sites of the neighbouring divacancies is 10.8 Å. The divacancy formation energy of 3.14 eV can be decomposed as a sum of 3.54 eV for the actual creation of the vacancy at the frozen positions of surrounding atoms in the cell and -0.4 eV arising from the relaxation of the atomic positions.

The divacancy introduced in the 64-atom unit cell creates a network of dipoles inside the crystal at cost of 3.54 eV per divacancy, induces ionic displacements and minor change in the electronic structure of the system. To calculate the formation energy of a dilute vacancy we estimate the correction due to the electrostatic interaction



in an array of divacancies in the calculations with PBC and for the under-relaxation constrained by the size of the unit cell.

To estimate the energy of dipole-dipole interaction, we consider a network of point charge dipoles with period equal to the period in the 64-atom KI supercell. The value of the interaction energy depends on the ionicity of the system; therefore, the value for the KI system (i.e.  $q < \pm 1.0 |e|$ ) is less than 0.14 eV.

The largest displacement found during the relaxation of the 64-atom supercell is 0.14 Å and gains 0.4 eV. At this point we borrow the result for the KI chain where the relaxation of the system on the introduction of a divacancy is substantial (1.2 eV) in the larger supercell. This gives an upper estimate of 0.8 eV for the residual relaxation energy which was not realized due to PBC. Combination of this estimate with 0.14 eV correction due to the interaction between divacancies, results in a lower estimate of the divacancy formation energy of 2.2 eV, which falls into the range of values 2.0-2.6 eV derived from the experiment<sup>272,273</sup>. The importance of the correction due to the underrelaxation is a consequence of the softness of the material, which results in the larger required radius of the relaxation around the defect.

The high concentration of divacancies in PBC also affects the electronic structure of the crystal by splitting K and I states (Figure 52) from the bottom of the conduction band (0.15 eV) and the top of the valence band respectively (0.25 eV). As a result, the HOMO-LUMO difference in the one-electron spectrum is reduced to 3.6 eV. The width of the lower valence bands of the crystal also increases in the presence of the divacancies.

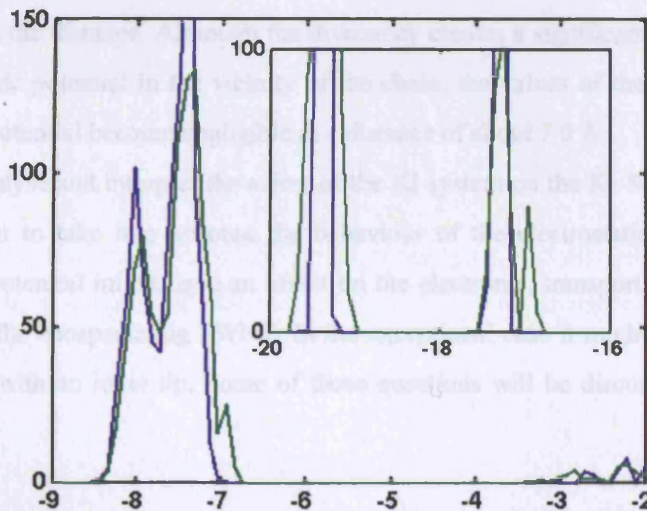


Figure 52. Density of states in the perfect KI bulk (blue) and in the presence of divacancies (green) calculated in the 64-atom supercell.



#### 5.2.2.4 Divacancy defects in the [100] chains of KI

In the case of the [001] KI chain, two types of neutral divacancies are possible: the divacancy can be oriented along the chain (the “parallel”) or perpendicular to the chain axis (the “perpendicular”). The energies of formation are calculated for both vacancy types. They amount to 3.18 eV for the divacancy oriented along the chain axis and 3.3 eV for the vacancy perpendicular to the axis.

Presence of the divacancy results in a significant relaxation of the surrounding “host” chain. The energy released on the atomic relaxation around “perpendicular” divacancy in chain with 8-atom unit cell is 0.38 eV. An increase of the supercell size to 32 atoms per single divacancy increases the relaxation energy to 1.2 eV and, consequently, reduces the formation energy to 2.0 eV. Creation of the divacancy pair along the axis (“parallel” divacancy) reduces the Madelung field and results in significant relaxation of the system. However, should the PBC conditions be removed, this system may collapse into a more compact cluster or break the chain.

The divacancy in either orientation with respect to the chain is expected to produce a significant dipole and perturbation in the electrostatic potential of the chain. To characterize the potential outside the chain, we compare the profiles of the gradient of the electrostatic potentials along the ideal [001] chain, and defective [001] chain with divacancy oriented along and perpendicular to the chain axis.

The profiles are taken along the edge of the KI chain at the distance of 5.0 Å, 7.0 Å and 10.0 Å (Figure 53a, inset) from the nearest atom of the chain in the region of the strongest potential. Figure 53a illustrates the rapid decay of the electrostatic potential with the distance. Although the divacancy creates a significant perturbation to the electrostatic potential in the vicinity of the chain, the values of the gradient of the electrostatic potential become negligible at a distance of about 7.0 Å.

To analyse and interpret the effect of the KI system on the KI-SWNT nanotube, it is important to take into account the behaviour of the electrostatic potential. The electrostatic potential might have an effect on the electronic, transport and vibrational properties of the encapsulating SWNT. In the exceptional case it might be detected by an NC-AFM with an ionic tip. Some of these questions will be discussed later in the chapter.

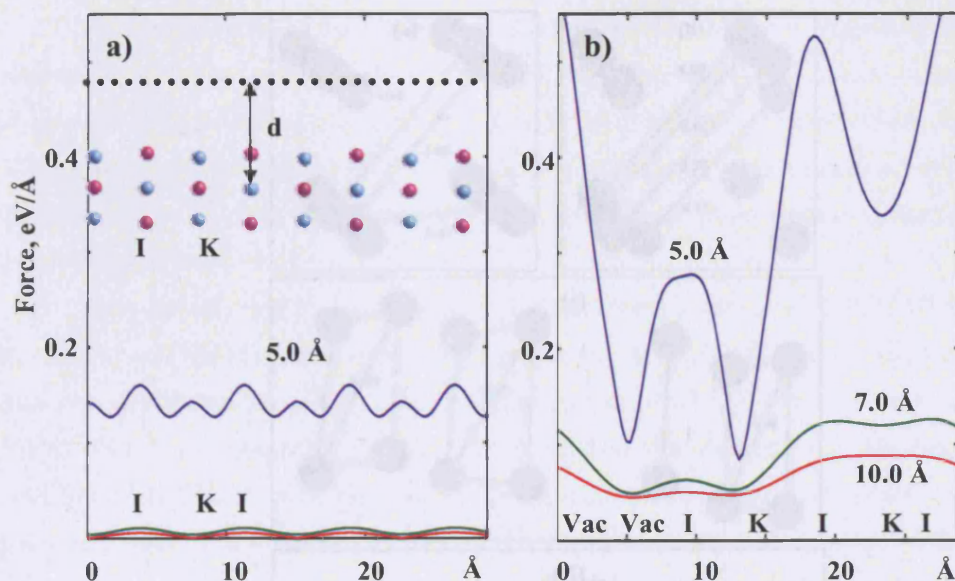


Figure 53. Profile of the force acting on the positive probe charge in the vicinity of the KI chain. The profile is calculated from the ab initio electrostatic potential and plotted along the edge of KI in the (110) plane. a) potential of the perfect KI chain; b) potential of the KI chain with divacancy along the chain direction. Blue, green and red lines describe the force at 5.0 Å, 7.0 Å, and 10 Å distance from the centre of the chain. The view of the perfect chain in the (110) plane in a) illustrates the definition of the distance.

### 5.3 Electronic structure of filled SW-CNT

Theoretical and experimental studies of CNTs predict that the presence of filling material<sup>274,275</sup> or adsorbates on the walls strongly affects the electronic properties of the combined system. Significant deformations induced in the carbon nanotube by the AFM tip also change the electronic structure of the nanotube<sup>276,277</sup>.

In this work the KI-filled SW-CNT system is described by a supercell of 120 carbon atoms containing a stack of 2 KI layers of 4 atoms each (2x2), representing the KI chain forming the filling. The atomic positions of the system are relaxed until the atomic forces are less than 0.05 eV/Å. The relaxation leads to distortion of the KI planes (Figure 54) and homogeneous expansion of the CNT. The diameter of the nanotube increases by only 0.06 Å.

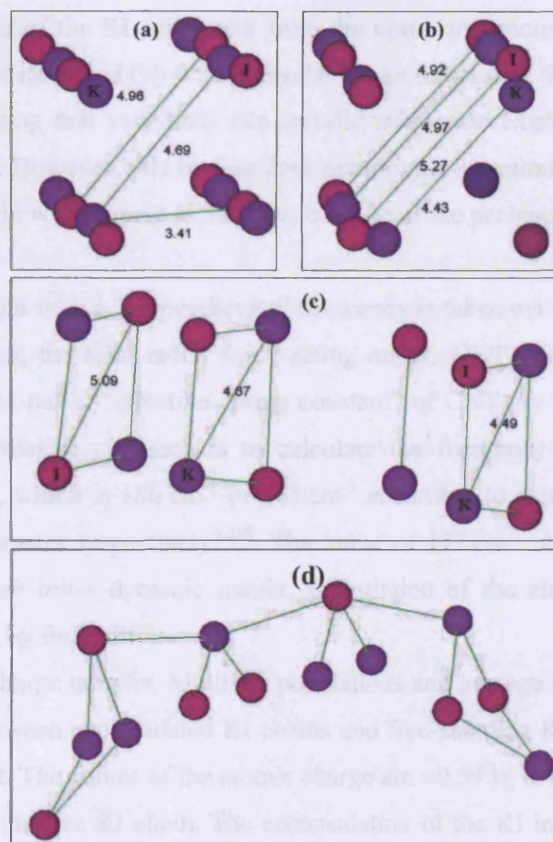


Figure 54. Structure of “ideal” and “defective” KI filling obtained as result of relaxation within the SWNT. (a) no defects; (b) divacancy along the symmetry axis; (c) “perpendicular” divacancy; (d) “parallel” divacancy. Potassium (K) atoms are blue, iodine (I) atoms are red.

Carbon atoms of the CNT displace predominantly in the radial direction. Compared to the displacements in the KI, these deformations are negligible. The displacements in the chain are also insignificant. Iodine atoms relax outwards from the chain axis, so that K-K and I-I distances in the plane perpendicular to the symmetry axis are 4.69 Å and 4.96 Å correspondingly. The structure of the KI chain structure obtained by relaxation within the nanotube is shown in Figure 54a.

The relaxation of the combined KI-SWNT system starts from the following initial geometry - the KI chain is placed into the carbon nanotube, in such a way that the axis of the chain coincides with the axis of the nanotube. As for the other degrees of freedom (rotation of the KI around the axis and shift along the axis) the position of the KI chain is not specific. Within the precision of the optimization, however, the KI chain as whole does not change its orientation with respect to the SWNT.



The displacement of the KI subsystem from the optimized geometry along the nanotube by a fraction of its period (by 0.5 Å) resulted in an increase in the total energy of only 0.06 eV, indicating that very little site-specific interaction exists between the filling and the nanotube. However, this finding does not provide an estimate of a barrier for sliding of the KI chain with respect to the tube, because of the presence of defects in the realistic CNTs.

When the KI chain with a “perpendicular” divacancy is taken out of the CNT in the relaxed configuration, the total radial force acting on the CNT is 0.35 nN. This allows us to estimate the radial “effective spring constant” of CNT per unit length as  $5.3 \times 10^9 \text{ N/m}^2$ . An alternative approach is to calculate the frequency of the radial breathing mode (RBM), which is  $186 \text{ cm}^{-1}$  or  $165 \text{ cm}^{-1}$  according to experimental and previous theoretical estimates respectively<sup>6,258</sup>. The value of  $177 \text{ cm}^{-1}$  obtained in this work is based on the *ab initio* dynamic matrix. Calculation of the elements of the dynamic matrix is made by finite differences.

To analyze the charge transfer, Mulliken populations and average ionicity of the filling are compared between encapsulated KI chains and free-standing KI chains with the same lattice constant. The values of the atomic charge are  $\pm 0.59 |e|$  in the KI:SWNT system and  $\pm 0.56 |e|$  in the free KI chain. The encapsulation of the KI into the SWNT also leads to a total charge transfer of  $-0.08 |e|$  per unit cell of the KI, according to the Mulliken analysis. The non-zero total Mulliken charge on the KI is interpreted as a result of the overlap between the basis functions of the KI and the carbon nanotube.

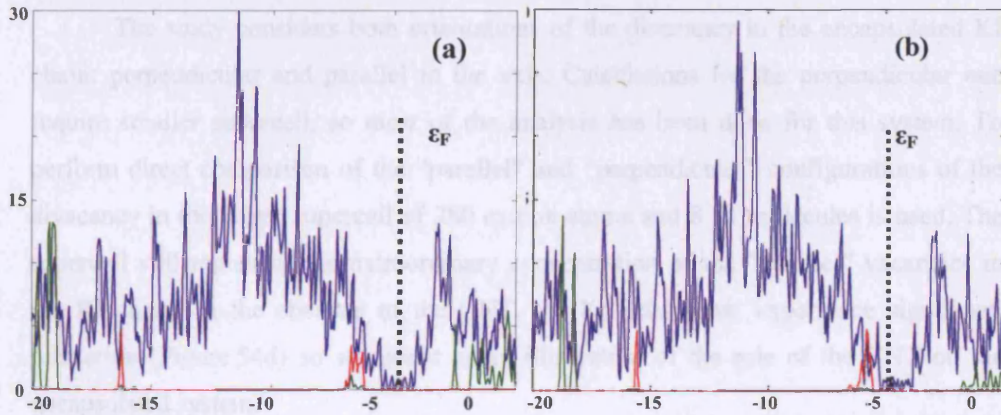


Figure 55. Projected Density of States (PDOS) plotted for C(blue), K(green) and I(iodine). a) KI-filled nanotube with defects; b) KI-filled nanotube with perfect filling.

The analysis of the projected density of states (PDOS) demonstrates that the position of the Fermi level in the CNT also depends on the presence of the filling (Figure 55). Remarkably, not only the absolute position of the Fermi level shifts, but also the relative position of the Fermi level with respect to the features of the CNT PDOS.

The top of the “valence” band of the KI subsystem is separated from the bottom of the conduction band of KI by 4.3 eV, similarly to the bulk. The position of the KI valence band 1.0 eV below the Fermi level prevents resonances between the two systems.

According to the DFT calculations, the encapsulated configuration is favourable by 0.06 eV per KI molecule, which is attributed to the polarization of the CNT. However, little relaxation and no change in the electronic structure of the perfect subsystem has been found.

#### 5.3.1 Electronic structure of filled SW-CNT with defects in the filling

As an example of a possible stronger perturbation to the perfect CNT system, we consider KI chain with a defect formed during the growth. Although disordered fillings are often observed in HRTEM, there is no understanding of the defect’s nature yet. We expect that the neutral divacancy, which is the most frequent defect in the equilibrium bulk, may be formed in the growth process of the KI chain as well. According to the results in section 5.2.2.3, this defect has a formation energy in the KI chain comparable to the formation energy in the KI bulk.

The study considers both orientations of the divacancy in the encapsulated KI chain: perpendicular and parallel to the axis. Calculations for the perpendicular one require smaller supercell, so most of the analysis has been done for this system. To perform direct comparison of the “parallel” and “perpendicular” configurations of the divacancy in the larger supercell of 280 carbon atoms and 8 KI molecules is used. The supercell still represents an extraordinary concentration of the “parallel” vacancies in the KI chain. In the absence of the CNT, the KI subsystem, experience significant relaxation (Figure 54d) so we use it as an illustration of the role of the CNT on the encapsulated system.

Figure 54b-c shows KI structures with divacancies relaxed inside the CNT. The carbon atoms of the CNT are not shown in the figure, for they obstruct the view. The relaxed K-K and I-I distances in these KI structures with divacancies typically increase up to 6% in the neighbourhood of the defect, but the shrinkage by 4% of the K-K



distance is also observed Figure 54b-c. These relaxations in the “defective” structures are much less than in the free-standing chain. We suppose that significant pressure is applied to the walls of the CNT because of the marked relaxation of the free-standing defective KI chains.

Figure 55 compares the partial density of states (PDOS) of (10,10) SWNT with perfect and defective filling. The presence of the defect in such a small supercell, essentially affects the width of the KI valence band. The top of the “valence” band of the KI subsystem is still separated from the bottom of the conduction band of KI by 4.3 eV, which is close to the bulk value. The position of the valence band of the perfect KI chain is 1.0 eV below the Fermi level (black dashed line), which prevents from the charge transfer between the two subsystems. The major difference between PDOS of “ideal” and “defective” KI filling is the width of KI valence band (Figure 55).

In the system with defective filling, the KI valence band shifts downwards approximately by 0.5 eV. This shift might be due to the charge transfer to KI subsystem or due to the effect of the electrostatic potential from the nanotube. The Fermi level of the metallic SWNT shifts upwards by 0.2 eV.

Our DFT calculations do not produce the work function of the system, but if we use the position of the Fermi level as an approximation, then the shift in the Fermi level indicates that a precise scanning probe technique like Kelvin Probe Force Microscopy (KPFM)<sup>278</sup> might be able to differentiate filled/unfilled/defective nanotubes.

The analysis of the band structure, density of states and Mulliken population concludes that no significant charge transfer is expected between the KI and perfect CNT subsystems both for the perfect KI and in the presence of divacancies. The absence of the charge transfer correlates positively with the low-cost sliding of KI along the tube, unchanged ionicity of the KI subsystem ( $\pm 0.57|e|$ ), and the 4.3 eV gap in the KI band structure.

The non-equilibrium methods used in production of the SWNTs as well as previous theoretical investigations with classic MD suggest the presence of defects in the structure of the filling. In this work we evaluate formation energies of a neutral divacancy in the encapsulated chain. These values are obtained in calculations with periodic boundary conditions, so they represent the formation energy per divacancy in the one-dimensional array of divacancies. To estimate the value of the divacancy formation energy at low concentration, we subtract the major contributions to the formation energy: correction due to the dipole-dipole interactions and atomic relaxation.

The sum of the dipole-dipole interaction between divacancies and their images decays rapidly with distance and this correction is neglected for larger unit cells. For 4-times extension of the supercell the relaxation energy is 3 times larger. Therefore we attribute the major effect on the formation energy of the divacancy to insufficient relaxation of the host lattice in the chosen supercell (5.2.2.3).

Analysis of the total energy of the system reveals that the divacancy formation energy is larger for the CNT-encapsulated KI chains than for a free chain. The formation energy of the periodic array of divacancies is 3.54 eV per divacancy for the perpendicular orientation. This number is obtained in calculation with reduced unit cell of 120 carbon atoms and 4 KI molecules and exceeds energy of defect formation (Table 10) in the free chain (3.18 eV) by 0.36 eV.

The difference in the vacancy formation energy can be attributed to the limited relaxation inside the CNT. To validate this hypothesis, one has to remove the effect of the tube without relaxation of the atomic positions. The divacancy formation energy is calculated for the relaxed KI chain configuration in the absence of the CNT. Since the value of the formation energy is 3.5 eV, we conclude that the CNT has very little effect on the electronic part of the divacancy formation energy. We also compare the total energies of divacancies in the two different orientations (parallel and perpendicular to the tube axis) in the larger supercell with 280 carbon atoms. The divacancy parallel to the axis is more favourable as expected from the dipole-dipole interaction between them. The difference in the formation energy amounted to 0.12 eV.

Table 10. Energy of formation for a neutral divacancy in KI-based systems. Divacancy formation energy is calculated with respect to ideal chain (bulk) and a KI molecule. Results are presented for smaller supercell (small SC) and larger supercell (large SC). For KI-SWNT system the results for the larger cell could not be calculated but estimates are provided, based on the relaxation of KI system in large SC. Energies are presented in eV.

<i>System</i>	<i>Bulk KI</i> <i>eV</i>	<i>Free</i> <i>KI-chain</i> <i>(perpen.)</i> <i>eV</i>	<i>KI in</i> <i>m-SWNT,</i> <i>(perpen.)</i> <i>eV</i>	<i>Free</i> <i>KI-chain</i> <i>(parallel)</i> <i>eV</i>	<i>KI in</i> <i>m-SWNT</i> <i>(parallel)</i> <i>eV</i>
Defect Formation Energy (small SC)	3.14	3.18	3.54	3.3 eV	3.42
Relaxation energy (small SC)	0.4	0.4	0.35	0.4	0.4
Relaxation energy (large SC)	–	1.2	–	0.9	–
Defect Formation Energy (large SC)	–	2.38	2.74 (est.)	2.4 eV	2.92 (est.)

To estimate the formation energy calculated in the small unit cells (i.e. for high density of defects) in the case of dilute defects, we calculated the difference in the relaxation energies obtained for the small (4 KI molecules) and 4 times extended unit cell. This correction reduces the formation energies of the “parallel” and “perpendicular” chains to 2.3 eV and 2.6 eV respectively.

The formation energy of a divacancy in the encapsulated KI chain is higher, because of the interaction between the divacancy and the CNT walls and due to the smaller displacements of KI ions. The electronic structure of the defect often depends on the atomic relaxation in the system, hence the encapsulation of the nanosystem with a defect into the CNT can be used for “engineering” of the defect level.

In the case of the perpendicular vacancy the degree of relaxation has an immediate effect on the position of the defect level in the band gap. Particularly, the stronger is the relaxation, the less pronounced is the shift from the valence and conduction bands. Therefore, the separation between HOMO and LUMO orbitals ( $\Delta E^{\text{HOMO-LUMO}}$ ) increases with relaxation. For KI chains with “perpendicular” divacancy modelled with the 8-atom supercell, the ( $\Delta E^{\text{HOMO-LUMO}}$ ) is 4.11 eV, 1.83 eV, and 2.54 eV for the ideal chain, unrelaxed chain with a divacancy, and fully relaxed free chain with a divacancy respectively. Similar effect is observed for the “parallel” orientation of the vacancy.

The presence of the CNT restrains the defective KI from relaxation and creates a system with unique electronic structure, which does not exist in free KI chains. The split of the KI levels, in turn, depends on the degree of the relaxation, hence the position of the level of the defect depends on the radius of the CNT. Therefore, in the experiment it should be possible to tune the position of a defect electron level by changing the chirality of the nanotube.

### 5.3.2 Role of nanotube electronic structure in tube-chain interactions

The change of the chirality is closely related to the electronic structure of the nanotube<sup>6</sup>. For instance, nanotubes with indices (n, n) are metallic, while (n, 0) are insulating or semiconducting.

In the experiment, the solution of carbon SWNT is often a mixture of metallic (m-SWNT) and semiconducting (s-SWNT) nanotubes. A considerable fraction of the low-diameter SWNTs are metallic (10, 10) and semiconducting (14, 0) tubes. The calculation of the electronic structure of s-SWNT is performed using k-grid in the reciprocal space with 16 non-equivalent k-points in a supercell, which is twice larger

( $c = 8.712 \text{ \AA}$ ) than the unit cell ( $c = 4.356 \text{ \AA}$ ). The calculated  $E_{gap} = 0.2 \text{ eV}$  direct band gap qualifies the system as a narrow gap semiconductor. This bandgap is underestimated because DFT-GGA usually reduces the bandgap.

The position of the last occupied molecular orbital differs less than 0.5 eV between ideal semiconducting and metallic systems, which agrees with experimental data on workfunction in SWNTs<sup>119,279</sup> and previous *ab initio* calculations<sup>259,260,280</sup>. When the KI-filling is introduced into the semiconducting tube, the band structure does not change significantly.

However, we are aware of the recent theoretical work<sup>281</sup> on KI in SWNT (10,10), which claimed a significant charge transfer between the subsystems contradicting our result. We do not argue that such behaviour is impossible in the experimental systems, on the contrary, we also expect such behaviour in the case of defective SWNTs. As for the ideal KI chain in an ideal SWNT, charge transfer is “possible” if the band offset between KI and SWNT is underestimated. We have also obtained similar result during preliminary studies of the system. The smaller DZP basis, which was initially chosen, was sufficient to reproduce the electronic structure of both subsystems separately, but failed to reproduce the band offset and resulted in charge transfer between the subsystems. A qualitative indication of the error was the difference ( $6.1-4.4=1.7 \text{ eV}$ ) in the position of the highest occupied state between metallic and semiconducting SWNTs, which exceeded by far corresponding difference in the work function, which is measured experimentally in the range 4.5-5.1 eV<sup>119,279</sup> for various SWNTs. Once the TZP basis set was chosen, the absolute position of the CNT Fermi level returned into the expected range.

This comparison shows the importance of choosing a sufficient basis set, and the necessity to validate the choice by appropriate experimental data. This experience highlights the fact that charge transfer and even spin polarization of the subsystems might be achieved by a sophisticated choice of an insulating filling. On this basis, rubidium iodide (RbI), which has lower workfunction ( $2.2 \text{ eV}$ )<sup>282</sup>, is a system where significant interaction and charge transfer might be expected as a result of intercalation.

#### 5.4 Vibrational analysis of the KI filled SW-CNT

The analysis of the vibrational properties of the KI-filled SWNTs is motivated by the ongoing study of the Raman spectra of the system. This is a preliminary study of the KI:SWNT(10,10) system, therefore we do not perform analysis of the Raman



intensities and concentrate on the effect of the KI filling on the frequencies of the well known Raman-active modes, namely, high frequency tangential modes (G-band) and the low frequency radial breathing mode (RBM) (Figure 56). Both modes are extensively described in the literature and used to deduce parameters of the nanotube<sup>239,240,245,277,283-285</sup>. The two most intensive peaks in the G-mode correspond to displacements along the tube axis (G+) and in the circumferential direction (G-), see (Figure 56).

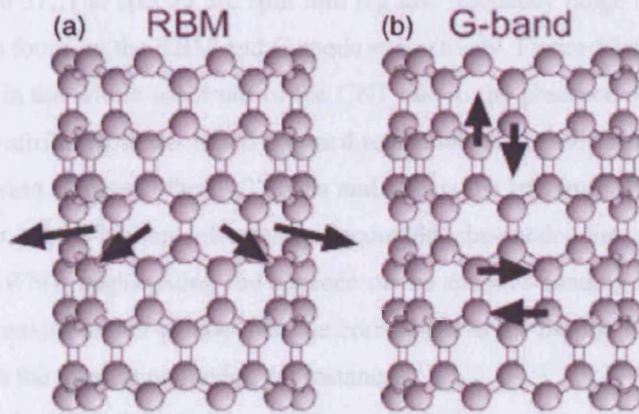


Figure 56. Schematic picture showing the atomic vibrations for (a) the RBM and (b) the G band modes<sup>286</sup>.

In the empty (10,10) CNT, the frequency of the radial breathing mode (RBM) is  $186 \text{ cm}^{-1}$  according to experiment<sup>258</sup> and  $165 \text{ cm}^{-1}$  according to previous theoretical calculation<sup>6</sup>; for the G-band the experimental values are  $1567 \text{ cm}^{-1}$  and  $1593 \text{ cm}^{-1}$  for G- and G+ modes correspondingly.<sup>258</sup>

To address the effect of filling, we use a model of an ideal metallic (10,10) CNT filled with an ideal, slightly strained KI filling (section 5.3). Sensitivity of the main frequencies corresponding to these modes has been demonstrated for several fillings strongly interacting with the host nanotube<sup>283,284</sup> such as alkali metals.

The dynamic matrix of the system is calculated using finite differences with atomic displacements of 0.04 Bohr. Forces on the atoms are calculated using the same *ab initio* method as above. The dynamic matrix is corrected for the under-relaxation, and symmetrised to tackle the case finite residual forces. However, these operations are not sufficient to avoid several non-trivial modes with imaginary eigenvalues. Visual analysis of these modes identifies them as related to the rotation of the CNT, and motion of the KI filling with respect to the CNT.

Since there is no bonding or any other specific site-site interaction and the KI system is very soft, the filling experiences a very low barrier to motion along the SWNT at finite temperatures. In this work we do not investigate this aspect of the problem and do not perform a global optimization of the system. Therefore, we ascribe the presence of the modes with imaginary eigenvalues to the insufficient relaxation of the structure. We neglect them in the further consideration, since their eigenvalues are expected to be much lower than the modes of the interest.

The phonon densities of states (DOS) of the empty and filled SWNTs are presented in Figure 57. The spectra are split into the low frequency range and the high frequency range to focus on the RBM and G-mode respectively. Figure 57 demonstrates a significant shift in the whole spectrum of the CNT due to the presence of the filling. This effect can be attributed to the radial outward relaxation of the tube in the presence of KI. This expansion elongates the C-C bonds and affects the spectrum. However, the subsystems of the KI-SWNT are effectively decoupled: the modes are attributed to either KI or the SWNT, highlighting the absence of the specific bonding between the systems. The few modes which violate this rule correspond to the motion of the system as a whole, such as the translation modes, for instance.

The radial “breathing” mode is one of the examples where the mode of the radial expansion of the nanotube is decoupled from the motion of the filling: in this mode, the displacements of the KI ions are three orders of magnitude less than those of the CNT. The presence of the ionic crystal makes no strong bonds to the wall, but it still affects the frequency of the RBM mode. The magnitude of the shift is sufficient to be detected in Raman spectroscopy.

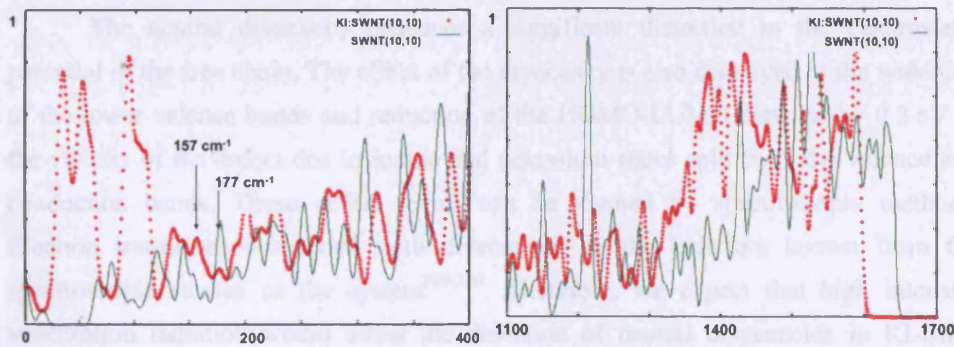


Figure 57. Density of states of the vibrational spectra for the empty and KI-filled individual SWNT(10,10). Left and right graphs zoom into the low and high-frequency regions of the spectrum.

## 5.5 Discussion

### 5.5.1 KI-SWNT interactions

The analysis of the electronic structure calculations for the KI-SWNT system demonstrates no significant charge redistribution or bond formation between the ionic filling and the SWNT. This conclusion follows from several observations: a) the positions of the KI valence and conduction bands are well below or above Fermi level of the SWNT; b) the shape of the PDOS in the KI valence band and band gap in KI subsystem do not change for the encapsulated chain; c) Mulliken analysis reports negligible electron transfer between the KI and SWNT systems; d) there is a low penalty of 0.06 eV for translation of the KI along the nanotube; e) the creation of a perfect encapsulated systems gains only 0.06 eV per KI pair.

As a result of the KI-SWNT interaction, the absolute position of the Fermi level decreases as compared to the empty SWNT. Because DFT-GGA usually promotes delocalization of the wave function, the results of the work indicate that the charge transfer should not happen in experiment with a perfect 2x2 KI filling and perfect SWNT(10,10). In the absence of charge redistribution between the systems, we suggest that the decrease in the workfunction is due to the polarisation of SWNT in the field of the electrostatic potential of the filling.

### 5.5.2 Defects in the free and encapsulated KI chains

The relaxation energy constitutes a significant part, approximately 30%, of the defect formation energy for the soft KI chain. Similar behaviour has been reported in previous atomistic studies of Schottky defects and divacancies in the bulk KI crystal<sup>287,288</sup>. The formation energy of the neutral divacancy depends strongly on the size of the unit cell, i.e. on the concentration of the vacancies in the system.

The neutral divacancy produces a significant distortion to the electrostatic potential of the free chain. The effect of the divacancy is also displayed in the widening of the lower valence bands and reduction of the HOMO-LUMO distance by 0.2 eV in the vicinity of the defect due to iodine and potassium states split from the valence and conduction bands. These defect levels can be studied by spectroscopic methods. Electron transitions associated with divacancies in the bulk are known from the spectroscopic studies of the system<sup>289,290</sup>. Therefore, we expect that high intensity synchrotron radiation would allow the detection of neutral divacancies in KI-filled nanotubes.

For the two orientations of the divacancy in the chain considered in this work we have found no significant difference in the formation energy of the divacancies. The difference remains below 0.1 eV for both the free and encapsulated KI chains. The

formation energy is consistently higher in the encapsulated chain, because of the constrained relaxation of the chain in the presence of the SWNT. Importantly, we have observed no significant charge redistribution due to the formation of the neutral divacancies.

In particular, no electron states are trapped in the divacancy and no charge transfer is detected between the system and SWNT from the comparison of the Mulliken population of the subsystems. For the high concentration of the “perpendicular” divacancies, the position of the KI valence band shifts upwards, closer to the Fermi level of the system. Such shift is also observed in a free chain when the SWNT shield is removed; therefore we associate it with the reduction in the Madelung field on the ionic sites of the KI chain rather than with the interaction between the SWNT and KI.

The major effect of the CNT on a defective filling is the constraint to the relaxation. The effect is especially pronounced for the soft KI chain. The constraints on the relaxation around the defects lead to the modification of the electronic properties of the defect, i.e. the HOMO-LUMO separation in the vicinity of the defect. This separation, if measured, could provide yet another way of determining the radius of a SWNT. On the other hand, the choice of the SWNT radius allows one to tune the optical properties of the KI:SWNT system with defects in the filling.

### 5.5.3 Experimental characterisation of the KI filling inside SWNT

Can one distinguish KI-filled and unfilled single-wall carbon nanotubes (SW-CNT) on an insulating surface by means of NC-AFM? To address this question we analyse the possibility of detecting the electrostatic potential of the KI with an AFM tip having a strong electrostatic potential.

The strongest potential of the KI filling in the 2x2 geometry is expected to be along the edge of the chain. The iodine ions relax outwards and create significant variation in the potential along the “ideal” chain (Figure 58). However, this electrostatic force decays rapidly with the distance from the chain. At the position of the carbon cores the force drops to 0.01 eV/Å and cannot be detected at all by modern low temperature NC-AFM at distances 2-3 Å from the surface of the SWNT, i.e. 7-10 Å from the KI filling.



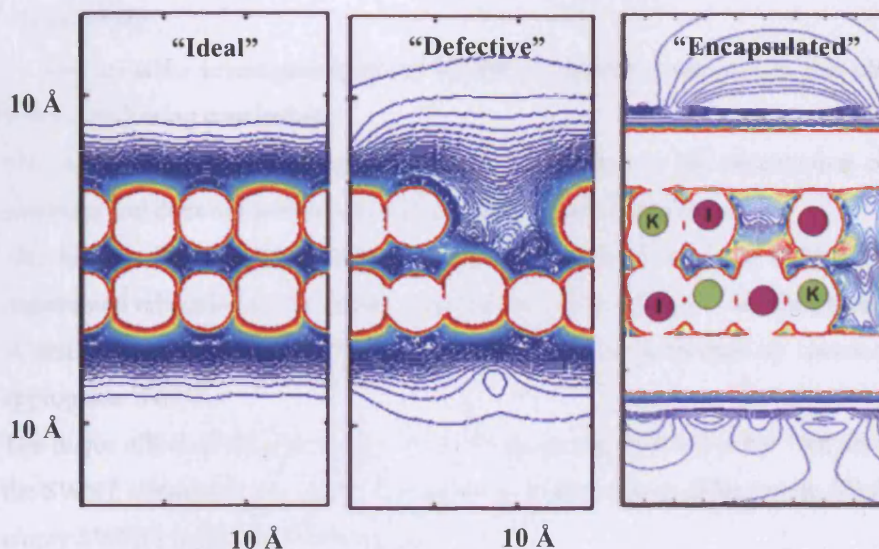


Figure 58. Contour map of the modulus of electrostatic force acting on a probe charge near the edge of the perfect free  $2 \times 2$  KI chain, free  $2 \times 2$  KI chain with a vacancy pair, encapsulated  $2 \times 2$  KI chain with a vacancy pair. The map is constructed from the *ab initio* electrostatic potential. Contour levels start at zero but have different step sizes for the free and for the encapsulated chains: for the free chains the step is 0.08 nN, for the encapsulated chain the step is 0.0016 nN for contours outside the nanotube and 0.16 nN for the contour inside.

We have also have analysed the electrostatic potential of a neutral divacancy in a chain without SWNT. In this case, the corrugations in the potential along the chain are well pronounced and can be detected by NC-AFM at distances of 7 Å and 10 Å from the centre of the “defective” free KI chain (Figure 58).

The metallic SWNT, however, considerably screens the field; as a result, the variation of the electrostatic force acting on the probe charge at 3 Å beyond the nanotube radius does not exceed 0.01 eV/Å (Figure 58). We do not exclude the possibility that filled/unfilled SWNTs can be distinguished by NC-AFM, but the mechanism of the contrast formation will not be the interaction between the electrostatic potential of the tip and the surface. We should not also exclude an indirect effect of the electrostatic potential on D-AFM imaging. Possibly, variations in the position of the Fermi level in the filled tubes can be detected by the KPFM instrument<sup>278,291</sup>.

From the perspective of the Raman scattering experiment, the results of the *ab initio* vibrational study demonstrate, that the presence of the soft ionic filling in the SWNT leads to a red shift of the tube spectrum.



## 5.6 Summary

The *ab initio* investigation of the KI:SWNT system conducted in this chapter leads to the following conclusions:

- The interaction between the subsystems is mainly due to the polarization of the nanotube and does not involve any significant charge redistribution.
- The major effect of the SWNT on the KI electronic structure is due to the constrained relaxation of the atoms in the vicinity of the defect. This allows creation of stable nanostructures and tuning their spectroscopic properties by choosing an appropriate SWNT.
- The major effect of the perfect KI filling on the perfect SWNT is the “red shift” of the SWNT vibrational spectrum. This gives an opportunity to differentiate filled and empty SWNTs by Raman spectroscopy.
- Dynamic Atomic Force Microscopy (D-AFM) might be able to differentiate filled/unfilled semiconducting/metallic SWNTs by the difference in the Fermi level of the system in the Kelvin Probe mode.

## Conclusions

I have studied NC-AFM contrast formation in high-resolution images of insulating surface to support experimental efforts by theoretical studies of the mechanisms of tip-surface interaction. A multi-scale model of NC-AFM imaging was implemented in this work: tip-surface interaction was modeled at atomistic level; equations for the tip motion in the presence of feedback loop were solved numerically; analytic expression for Van-der-Waals interaction was used to account for macroscopic tip-surface interaction.

We started from the analysis of the tip-surface interaction over unreconstructed  $\text{Al}_2\text{O}_3(0001)$  – a “mystical” surface which have not been seen with high resolution, although atomic resolution was achieved at many other insulating surfaces.

It was demonstrated that  $\text{Al}^{3+}$  and  $[\text{O}_3]^{6-}$  groups can be resolved in NC-AFM images of clean unreconstructed  $\alpha\text{-Al}_2\text{O}_3(0001)$  surfaces. Both tip models: oxidized tip model and model of a Si tip with dangling bond, predict significant contrast. Detailed image analysis, i.e. analysis of scanlines or site-dependent force-distance curves, allows identifying sublattices when the tip apex is oxidized. Dangling bond at the apex of the tip allows chemical resolution – interaction of the dangling bond is stronger over the anion site for all surfaces.

The combined results of this work on  $\text{Al}_2\text{O}_3$  and  $\text{MgO}$  agree well with results from our collaborators work<sup>141</sup> on  $\text{TiO}_2(110)$ ,  $\text{CaF}_2$  and  $\text{CaCO}_3$ .

The study advances to systems with single molecules, which are often present even at cleaned insulating surface, sometimes unintentionally, due to the surface contamination from the residual gas or from the bulk.

The presence of a molecule on the surface may reduce the NC-AFM resolution, if the molecule is prone to move or jump to the tip. The study of an individual formate molecule on the  $\text{MgO}(001)$  surface has also demonstrated that the apparent height of the molecule in the CFS mode depends considerably on the strength of the macroscopic interaction. The molecule should attract the tip strongly to be imaged simultaneously with the substrate and yet must be strongly bound to the surface. The higher protrudes the molecule, the stronger level of tip-molecule interaction is required.

The resolution is expected to improve when the whole surface is covered by molecules strongly bound to surface sites, which restricts mobility of individual

molecules and reduces the possibility of tip contamination. The mechanisms of the NC-AFM contrast formation on molecular monolayers (HCOOH on TiO<sub>2</sub>(110)) have been studied with *ab initio* methods following an experimentally observed image<sup>32,147</sup>. The interplay between macroscopic and chemical interactions in the CFS mode results in the interpretation of the dark spots in the image as positions of the highest (CH) group of the adsorbed molecule (HCOO-). The resolution in the image is reduced due to the larger number of tip apex atoms contributing to chemical interaction. However, analysis of the force-distance curves allows differentiating the oxygen and hydroxyl sites of the substrate at low temperatures.

Seeing through the monolayer should not sound too encouraging, for there is a limit to sensitivity of the technique. It has been shown, however, that the presence of a perfect KI filling in an individual SWNT can be detected by Raman spectroscopy of Kelvin Probe microscopy due to the “red shift” in the Raman spectrum and variation of the workfunction of the SWNT respectively. The presence of divacancies in the KI filling can be detected by spectroscopic methods. Moreover, the position of the defect level of the divacancy is related to the radius of the nanotube.

We reach a limit in the attempt to sense KI filling inside SWNT in “non-contact” mode, which was our chosen framework, but D-AFM is not limited to the “non-contact mode” – one can choose appropriate tip, increase the level of tip-surface interaction and find himself in the exciting field of high-resolution D-AFM imaging in “tapping” mode.

## Reference List

1. J. L. Falconer and J. A. Schwarz, *Catalysis Reviews-Science and Engineering* 25, 141-227 (1983).
2. M. Buck and M. Himmelhaus, *Journal of Vacuum Science and Technology A* 19, 2717-2736 (2001).
3. M. Saito, S. Sato, Y. Waseda, *High Temperature Materials and Processes* 17, 117-131 (1998).
4. J. Alsnielsen et al., *Physics Reports-Review Section of Physics Letters* 246, 252-313 (1994).
5. R. Guantes, A. S. Sanz, J. Margalef-Roig, S. Miret-Artes, *Surf.Sci.Rep.* 53, 199-330 (2004).
6. R. Saito, G. Dresselhaus, M. S. Dresselhaus, *Physical Properties of carbon nanotubes* (Imperial College Press, Singapore, 1998).
7. N. S. Tambe and B. Bhushan, *Journal of Physics D-Applied Physics* 38, 764-773 (2005).
8. B. Bhushan and J. A. Ruan, *Journal of Tribology-Transactions of the Asme* 116, 389-396 (1994).
9. G. Binnig, C. F. Quate, Ch. Gerber, *Surf.Sci.* 189, 1-6 (1987).
10. H. G. Hansma, E. Oroudjev, S. Baudrey, L. Jaeger, *Journal of Microscopy-Oxford* 212, 273-279 (2003).
11. M. C. Gallagher, M. S. Fyfield, J. P. Cowin, S. A. Joyce, *Surf.Sci.* 339, 909-913(1995).
12. S. Valeri et al., *Physical Review B* 65, 245410 (2002).
13. S. Schintke et al., *Phys.Rev.Lett.* 87, 276801 (2001).
14. G. Ceballos et al., *Chemical Physics Letters* 359, 41-47 (2002).
15. L. P. Van, O. Kurnosikov, J. Cousty, *Surf.Sci.* 411, 253-271 (1998).
16. S. G. Addepalli, B. Ekstrom, N. P. Magtoto, J. Lin, J. A. Kelber, *Surface-Science* 442, 385-399 (1999).
17. V. V. Afanas'ev, M. Houssa, A. Stesmans, M. M. Heyns, *Journal-of-Applied-Physics* 91, 3079-3084 (2002).
18. H. Miyahara, X. Zou, T. Moriguchi, K. Ogi, *Materials-Transactions* 44, 247-252 (2003).
19. J. M. Shaw and P. F. Seidler, *IBM Journal of Research and Development* 45, 3-6 (2001).
20. S. Wodiunig, J. M. Keel, T. S. E. Wilson, F. W. Zemichael, R. M. Lambert, *Catalysis Letters* 87, 1-5 (2003).
21. F. J. Giessibl and G. Binnig, *Ultramicroscopy* 42-44, 281-289 (1992).
22. A. L. Shluger, A. I. Livshits, A. S. Foster, C. R. A. Catlow, *J.Phys.: Condens.Matter* 11, 295-322 (1999).
23. A. L. Shluger, A. L. Rohl, R. T. Williams, R. M. Wilson, *Physical Review B (Condensed Matter)* 52, 11398-11411 (1995).
24. H. Holscher, U. D. Schwarz, R. Wiesendanger, *Surf.Sci.* 375, 395-402 (1997).
25. R. W. R. Stark, G. Schitter, A. Stemmer, *Ultramicroscopy* 100, 309-317 (2004).
26. J. Kerssemakers and J. T. De Hosson, *Surf.Sci.* 417, 281-291 (1998).
27. J. R. Hahn, H. Kang, S. Song, I. C. Jeon, *Physical Review B (Condensed Matter)* 53, 1725-1728 (1996).
28. M. R. Jarvis, R. Perez, M. C. Payne, *Phys.Rev.Lett.* 86, 1287-1290 (2001).
29. R. García and R. Pérez, *Surf.Sci.Rep.* 47, 197-301 (2002).
30. G. Binnig, C. F. Quate, Ch. Gerber, *Phys.Rev.Lett.* 56, 930 (1986).
31. A. L. Shluger, L. N. Kantorovich, A. I. Livshits, M. J. Gillan, *Physical Review B* 56, 15332 (1997).
32. K. Fukui, H. Onishi, Y. Iwasawa, *Appl.Surf.Sci* 140, 259-264 (1999).
33. L. Nony et al., *Nanotechnology* 15, S91-S96 (2004).
34. E. Reido, E. Gnecco, R. Bennewitz, E. Meyer, H. Brune, *Phys.Rev.Lett.* 91, 0084502 (2003).



35. C. Barth and C. R. Henry, *Phys.Rev.Lett.* 91, art-196102 (2003).
36. C. Barth and C. R. Henry, *Nanotechnology* 1264-1272 (2004).
37. K. Fukui et al., *Phys.Chem.Chem.Phys.* 5, 5349-5359 (2003).
38. F. J. Giessibl, *Reviews of Modern Physics* 75, 949-983 (2003).
39. *Non-contact Atomic Force Microscopy*, Ed. S. Morita (2001).
40. R. Hoffmann, L. N. Kantorovich, A. Baratoff, H. J. Hug, H. J. Guntherodt, *Phys.Rev.Lett.* 92, art-146103 (2004).
41. C. Barth, A. S. Foster, M. Reichling, A. L. Shluger, *J.Phys.: Condens.Matter* 2061-2079 (2001).
42. A. S. Foster, C. Barth, A. L. Shluger, R. M. Nieminen, M. Reichling, *Physical Review B* 66, art-235417 (2002).
43. W. A. Hofer, A. S. Foster, A. L. Shluger, *Reviews of Modern Physics* 75, 1287-1331 (2003).
44. A. L. Shluger, A. L. Rohl, D. H. Gay, R. T. Williams, *J.Phys.: Condens.Matter* 6, 1825 (1994).
45. C. Loppacher et al., *Appl.Phys.A* 66, S215 (1998).
46. F. J. Giessibl, *Appl.Phys.Lett.* 76, 1470-1472 (2000).
47. M. Komiyama et al., *Japanese Journal of Applied Physics Part 2-Letters* 34, L789-L792 (1995).
48. A. I. Livshits, A. L. Shluger, A. L. Rohl, A. S. Foster, *Physical Review B* 59, 2436 (1999).
49. R. Perez, I. Stich, M. C. Payne, K. Terakura, *Appl.Surf.Sci* 140, 320-326 (1999).
50. R. Bennewitz et al., *Appl.Surf.Sci* 188, 232-237 (2002).
51. A. I. Livshits and A. L. Shluger, *Physical Review B* 56, 12482-12489 (1997).
52. C. Barth and M. Reichling, *Surf.Sci.Lett.* 470, L99-L103 (2000).
53. L. N. Kantorovich, A. L. Shluger, A. M. Stoneham, *Phys.Rev.Lett.* 85, 3846-3849 (2000).
54. L. DongWeon et al., *Appl.Phys.Lett.* 84, 1558-1560 (2004).
55. M. Gauthier, R. Perez, T. Arai, M. Tomitori, M. Tsukada, *Phys.Rev.Lett.* 89, art-146104 (2002).
56. G. Couturier, J. P. Aimé, J. Salardenne, R. Boisgard, *J.Eur.Phys.A* 15, 2726-2734 (2002).
57. J. Polesel-Maris, A. S. Piednoir, T. Zambelli, X. Bouju, S. Gauthier, *Nanotechnology* 15, S24-S29 (2004).
58. G. Couturier, R. Boisgard, L. Nony, J. P. Aime, *Review of Scientific Instruments* 74, 2726-2734 (2003).
59. S. P. Jarvis, A. Oral, T.P. Weihs, J. B. Pethica, *Review of Scientific Instruments* 64, (1993).
60. C. Loppacher et al., *Appl.Surf.Sci* 140, 287-292 (1999).
61. T. R. Albrecht, P. Grutter, D. Home, D. Rugar, *Journal-of-Applied-Physics* 69, 668-673 (1991).
62. F. J. Giessibl, H. Bielefeldt, S. Hembacher, J. Mannhart, *Appl.Surf.Sci* 140, 352-357 (1999).
63. A. I. Livshits, A. L. Shluger, A. L. Rohl, *Surf.Sci.* 445, (2000).
64. C. Argento and R. H. French, *Journal-of-Applied-Physics* 80, 6081-6090 (1996).
65. J. M. Soler et al., *J.Phys.: Condens.Matter* 14, 2745-2779 (2002).
66. L. Kleinman, *Physical Review B* 21, 2630 (1980).
67. L. Kleinman and D. M. Bylander, *Phys.Rev.Lett.* 48, 1425 (1982).
68. G. B. Bachelet and M. Schluter, *Physical Review B* 25, 2103-2108 (1982).
69. N. Troullier and J. Martins, *Physical Review B* 43, 1993 (1991).
70. D. Vanderbilt, *Physical Review B* 32, 8412 (1985).
71. J. Junquera and O. Paz, *Physical Review B* 64, 235111 (2001).
72. E. Artacho, D. Sanchez-Portal, P. Ordejon, A. Garcia, J. M. Soler, *Physica-Status-Solidi-B* 215, 809-817 (1999).
73. W. Kohn and L. J. Sham, *Physical Review* 140, 1133 (1965).
74. P. Ordejon, *Physica Status Solidi B* 217, 335-356 (2000).

75. E. Anglada, J. M. Soler, J. Junquera, E. Artacho, *Physical Review B* 66, art-205101 (2002).
76. V. B. Sulimov, P. V. Sushko, A. H. Edwards, A. L. Shluger, A. M. Stoneham, *Physical Review B* 66, art-024108 (2002).
77. P. V. Sushko, A. L. Shluger, C. R. A. Catlow, *Surf.Sci.* 450, 153-170 (2000).
78. M. J. Frisch et al., *Gaussian, Inc., Pittsburgh, PA, 1998* (2004).
79. B. G. Dick and A. W. Overhauser, *Physical Review* 112, 90-103 (1958).
80. A. S. Mysovsky, P. V. Sushko, S. Mukhopadhyay, A. H. Edwards, A. L. Shluger, *Physical Review B* 69, art-085202 (2004).
81. J. S. Braithwaite, P. V. Sushko, K. Wright, C. R. A. Catlow, *J.Chem.Phys.* 116, 2628-2635 (2002).
82. P. V. Sushko, J. L. Gavartin, A. L. Shluger, *J.Phys.Chem.B* 106, 2269-2276 (2002).
83. R. W. Grimes, C. R. A. Catlow, A. M. Stoneham, *Journal of Physics-Condensed Matter* 1, 7367-7384 (1989).
84. P. A. Cox and A. A. Williams, *Surf.Sci.* 175, L782-L786 (1986).
85. V. E. Henrich, G. Dresselhaus, H. J. Zeiger, *Physical Review B* 22, 4764-4775 (1980).
86. L. N. Kantorovich et al., *Faraday Discussions* 114, 173-194 (1999).
87. A. R. Gerson and T. Bredow, *Phys.Chem.Chem.Phys.* 1, 4889-4896 (1999).
88. P. V. Sushko, *Dissertation work* (2000).
89. O. Robach, G. Renaud, A. Barbier, *Surf.Sci.* 401, 227-235 (1998).
90. J. B. Zhou, H. C. Lu, T. Gustafsson, P. Haberle, *Surf.Sci.* 302, 350-362 (1994).
91. L. N. Kantorovich, A. I. Livshits, A. M. Stoneham, *J.Phys.: Condens.Matter* 12, 785-814 (2000).
92. C. Ruberto, Y. Yourdshahyan, B. I. Lundqvist, *Physical ReviewLetters* 88, art. 226101 (2002).
93. P. Guenard, G. Renaud, A. Barbier, S. Gautier, *Surface Review Letters* 5, -324 (1998).
94. Sangster, M. S. L. and Stoneham, A. M. Handbook on interatomic potentials. Harwell report (TP833) . 1980.
95. L. Minervini, M. O. Zacate, R. W. Grimes, *Solid State Ionics* 116, 339 (1999).
96. B. R. Brooks, R. E. Brookolery, M. Karplus, S. Swaminathan, B. D. Olafson, *Journal of Computational Chemistry* 4, 187-217 (1983).
97. D. G. Papageorgiou, I. N. Demetropoulos, I. E. Lagaris, *Computer Physics Communications* 109, 227-249 (1998).
98. R. Baxter, P. Reinhardt, N. Lopez, F. Illas, *Surf.Sci.* 445, 448-460 (2000).
99. B. G. Frederick, G. Apai, T. N. RHODIN, *Physical Review B* 44, 1880-1890 (1991).
100. E. A. Soares, M. A. Van Hove, C. F. Walters, K. F. McCarthy, *Physical Review B* 65, 195405 (2002).
101. R. W. G. Wyckoff, *Crystal Structures* (John Wiley and Sons, ed. 2nd, 1964), p. 40.
102. R. S. Mulliken, *J.Chem.Phys.* 23, 1833-1840 (1955).
103. A. Wander, B. Searle, N. M. Harrison, *Surf.Sci.* 458, 25-33 (2000).
104. A. D. Vita et al., *Physical Review B* 46, 12964-12973 (1992).
105. L. N. Kantorovich, J. M. Holender, M. J. Gillan, *Surf.Sci.* 343, 221-239 (1995).
106. J. R. B. Gomes, N.M.Harrison, F.Illas, *Chemical Physics Letters* 341, 412-418 (2001).
107. G. Renaud, *Surf.Sci.Rep.* 32, 1 (1998).
108. J. Libuda et al., *Surf.Sci.* 318, 61-73 (1994).
109. F. A. Grant, *Review of modern physics* 31, 646-674 (1959).
110. P. Ordejon et al., *RIKEN Review* 42-44 (2000).
111. G. Charlton et al., *Phys.Rev.Lett.* 78, 495-498 (1997).
112. P. J. D. Lindan, N. M. Harrison, M. J. Gillan, J. A. White, *Physical Review B* 55, 15919-15927 (1997).
113. D. Vogtenhuber, R. Podloucky, A. Neckel, S. G. Steinemann, A. J. Freeman, *Physical Review B* 49, 2099-2103 (1994).
114. S. P. Bates, G. Kresse, M. J. Gillan, *Surf.Sci.* 409, 336-349 (1998).
115. U. Diebold, *Surf.Sci.Rep.* 48, 53-229 (2003).
116. F. Montoncello et al., *J.Appl.Phys.* 94, 1501-1505 (2003).
117. J. Chen, L. B. Lin, F. Q. Jing, *Journal of Physics and Chemistry of Solids* 62, 1257-1262 (2001).

118. A. G. Thomas et al., *Physical Review B* 67, art-035110 (2003).
119. S. Suzuki, C. Bower, Y. Watanabe, O. Zhou, *Appl.Phys.Lett.* 76, 4007-4009 (2000).
120. J. A. Rodriguez et al., *Physical Review B* 65, art-235414 (2002).
121. R. A. Evarestov and A. I. Panin, *International Journal of Quantum Chemistry* 88, 472-480 (2002).
122. M. Sushko, *to be published* (2005).
123. D. Erts et al., *Appl.Surf.Sci* 188, 460-466 (2002).
124. R. Bennewitz, A. S. Foster, L. N. Kantorovich, *Physical Review B* 62, 2074 (2000).
125. C. Barth and M. Reichling, *Nature* 414, 54-57 (2001).
126. I. Stich, P. Dieska, R. Perez, *Appl.Surf.Sci* 188, 325-330 (2002).
127. A. Stesmans, V. V. Afanas'ev, M. Houssa, *Journal-of-Non-Crystalline-Solids* 303, 162-166 (2002).
128. J. L. Gavartin and C. C. Matthai, *Materials Science and Engineering B-Solid State Materials for Advanced Technology* 35, 459-462 (1995).
129. D. R. Baer et al., *J.Vac.Sci.Tech.A* 18, 131 (2000).
130. A. Y. Lozovoi, A. Alavi, M. W. Finnis, *Physical Review Letters* 83, 979-982 (2001).
131. C. L. Pang, H. Raza, S. Haycock, G. Thornton, *Physical Review B* 65, 201401 (2002).
132. A. Stierle, F. Renner, R. Streitel, *Physical Review B* 64, 165413 (2001).
133. A. S. Foster, C. Barth, A. L. Shluger, M. Reichling, *Phys.Rev.Lett.* 86, 2373-2376 (2001).
134. M. Ohta, H. Ueyama, Y. Sugawara, S. Morita, *Japanese Journal of Applied Physics Part 2-Letters* 34, L1692-L1694 (1995).
135. S. H. Ke, T. Uda, K. Terakura, *Physical Review B* 65, 125417 (2002).
136. J. Tobik, I. Stich, K. Terakura, *Physical Review B* 63, 245324 (2001).
137. A. A. Jarvis and E. A. Carter, *J.Phys.Chem.B* 105, 4045 (2001).
138. J. Wang, A. Howard, R. G. Egdel, J. B. Pethica, J. S. Foord, *Surf.Sci.* 515, 337 (2002).
139. J. Polesel-Maris, A. Piednoir, T. Zambelli, X. Bouju, S. Gauthier, *Nanotechnology* 14, 1036-1042 (2003).
140. A. S. Foster, A. L. Shluger, R. M. Nieminen, *Nanotechnology* 15, S60-S64 (2004).
141. A. S. Foster et al., *Phys.Rev.Lett.* 92, art-036101 (2004).
142. X. B. Wang and L. S. Wang, *J.Chem.Phys.* 107, 7667-7672 (1997).
143. A. I. Boldyrev and J. Simons, *J.Phys.Chem.* 97, 1526-1532 (1993).
144. C. F. Walters, K. F. McCarty, E. A. Soares, M. A. Van Hove, *Surf.Sci.Lett.* 464, 732-738 (2000).
145. D. Lee et al., *Appl.Phys.Lett.* 84, 1558-1560 (2004).
146. D. W. Lee et al., *Microelectronic Engineering* 67-8, 635-643 (2003).
147. K. I. Fukui, H. Onishi, Y. Iwasawa, *Chemical Physics Letters* 280, 296 (1997).
148. A. Nakasa, U. Akiba, M. Fujihira, *Appl.Surf.Sci* 157, 326-331 (2000).
149. T. Fukuma, T. Ichii, K. Kobayashi, H. Yamada, K. Matsushige, *J.Appl.Phys.* 95, 1222-1226 (2004).
150. T. Ichii, T. Fukuma, K. Kobayashi, H. Yamada, K. Matsushige, *Japanese Journal of Applied Physics Part 1-Regular Papers Short Notes & Review Papers* 43, 4545-4548 (2004).
151. D. Sanvitto, M. De Seta, F. Evangelisti, *Surf.Sci.* 452, 191-197 (2000).
152. J. M. Mativetsky, S. A. Burke, R. Hoffmann, Y. Sun, P. Grutter, *Nanotechnology* 15, S40-S43 (2004).
153. S. Tanaka, H. Suzuki, T. Kamikado, S. Mashiko, *Nanotechnology* 15, S87-S90 (2004).
154. A. L. Shluger, A. L. Livshits, A. L. Rohl, A.S.Foster, *Physical Review, Physical Review B* 59, 2436 (1999).
155. W. A. Hofer, A. S. Foster, A. L. Shluger, *Reviews of Modern Physics* 75, 1287-1331 (2003).
156. D. L. Allara and R. G. Nuzzo, *Langmuir* 1, 45-52 (1985).
157. M. A. Szymanski and M. J. Gillan, *Surf.Sci.* 367, 135-148 (1996).
158. P. Kackell and K. Terakura, *Appl.Surf.Sci* 166, 370-375 (2000).
159. P. Comba and R. Remenyi, *Coordination Chemistry Reviews* 238, 9-20 (2003).
160. H. Yamamoto, N. Akamatsu, A. Wada, K. Domen, C. Hirose, *Journal of Electron Spectroscopy and Related Phenomena* 64-5, 507-513 (1993).

161. K. Domen, N. Akamatsu, H. Yamamoto, A. Wada, C. Hirose, *Surf.Sci.* 283, 468-472 (1993).
162. X. D. Peng and M. A. Barteau, *Catalysis Letters* 7, 395-402 (1991).
163. C. Hirose et al., *Journal of the Chinese Chemical Society* 41, 275-278 (1994).
164. W. T. Petrie and J. M. Vohs, *Surf.Sci.* 259, L750-L756 (1991).
165. H. Nakatsuji, M. Yoshimoto, M. Hada, K. Domen, C. Hirose, *Surf.Sci.* 336, 232-244 (1995).
166. A. L. Magalhaes, S. R. R. S. Madail, M. J. Ramos, *Theoretical Chemistry Accounts* 105, 68-76 (2000).
167. G. Busca, *Catalysis Today* 27, 323-352 (1996).
168. A. Sasahara, H. Uetsuka, H. Onishi, *Langmuir* 19, 7474-7477 (2003).
169. A. Sasahara, H. Uetsuka, H. Onishi, *J.Phys.Chem.B* 105, 1-4 (2001).
170. A. Sasahara, H. Uetsuka, T. A. Ishibashi, H. Onishi, *Appl.Surf.Sci* 188, 265-271 (2002).
171. R. E. Tanner, A. Sasahara, Y. Liang, E. I. Altman, H. Onishi, *J.Phys.Chem.B* 106, 8211-8222 (2002).
172. S. Fujii, U. Akiba, M. Fujihira, *Appl.Surf.Sci* 210, 79-83 (2003).
173. S. Fujii, U. Akiba, M. Fujihira, *Nanotechnology* 15, S19-S23 (2004).
174. T. Uchihashi et al., *Appl.Surf.Sci* 157, 244-250 (2000).
175. T. Uchihashi, T. Okada, Y. Sugawara, K. Yokoyama, S. Morita, *Physical Review B (Condensed Matter)* 60, 8309-8313 (1999).
176. X. L. Xu et al., *Chinese Journal of Chemistry* 20, 899-903 (2002).
177. C. Viorneri et al., *Langmuir* 18, 2582-2589 (2002).
178. R. A. Latour, *Current Opinion in Solid State & Materials Science* 4, 413-417 (1999).
179. G. Hahner, R. Hofer, I. Klingenfuss, *Langmuir* 17, 7047-7052 (2001).
180. D. Guo, W. Xing, Y. B. Shan, T. H. Lu, S. Q. Xi, *Thin Solid Films* 243, 540-543 (1994).
181. M. R. Alexander, G. Beamson, C. J. Blomfield, G. Leggett, T. M. Duc, *Journal of Electron Spectroscopy and Related Phenomena* 121, 19-32 (2001).
182. E. Delamarche and B. Michel, *Thin Solid Films* 273, 54-60 (1996).
183. P. E. Laibinis, J. J. Hickman, M. S. Wrighton, G. M. Whitesides, *Science* 245, 845-847 (1989).
184. A. Ulman, *Chemical Physics* 96, 1533-1554 (1996).
185. B. Bat-Uul, S. Fujii, T. Shiokawa, T. Ohzono, M. Fujihira, *Nanotechnology* 15, 710-715 (2004).
186. A. Sasahara, H. Uetsuka, H. Onishi, *Surf.Sci.* 481, L437-L442 (2001).
187. T. Ohzono and M. Fujihira, *Physical Review B* 62, 17055-17071 (2000).
188. M. de Wild et al., *Molecular Electronics* 1006, 291-305 (2003).
189. A. Badia, R. B. Lennox, L. Reven, *Accounts of Chemical Research* 33, 475-481 (2000).
190. N. Sandhyarani and T. Pradeep, *International Reviews in Physical Chemistry* 22, 221-262 (2003).
191. S. Thevuthasan et al., *Surf.Sci.* 401, 261-268 (1998).
192. Q. G. Wang, J. Biener, X. C. Guo, E. Farfan-Arribas, R. J. Madix, *J.Phys.Chem.B* 107, 11709-11720 (2003).
193. A. Alavi, *Molecular Physics* 71, 1173-1191 (1990).
194. A. Lakhli and C. Girardet, *Surf.Sci.* 241, 400-415 (1991).
195. R. Metzger, C. Werner, A. Spitzer, *Thin Solid Films* 365, 242-250 (2000).
196. M. Freitag, M. Radosavljevic, W. Clauss, A. T. Johnson, *Physical Review B* 62, R2307-R2310 (2000).
197. Z. Dohnalek, R. S. Smith, B. D. Kay, *J.Phys.Chem.B* 106, 8360-8366 (2002).
198. I. A. Krasnov et al., *J.Phys.: Condens.Matter* 12, 1613-1626 (2000).
199. T. Ito, H. Kobayashi, T. Tashiro, *Nuovo Cimento D* 19D, 1695-1705 (1997).
200. W. Jingang, L. Shuben, L. Guoqiang, L. Can, X. Qin, *Appl.Surf.Sci* 81, 37-41 (1994).
201. Y. Yamaguchi, Y. Nagasawa, A. Murakami, K. Tabata, *International Journal of Quantum Chemistry* 69, 669-678 (1998).
202. C. Boas, M. Kunat, U. Burghaus, B. Gumhalter, C. Woll, *Physical Review B (Condensed Matter and Materials Physics)* 68, 75403-1 (2003).
203. C. Ramseyer and C. Girardet, *J.Chem.Phys.* 103, 5767-5775 (1995).



204. M. Ara, A. Sasahara, H. Onishi, H. Tada, *Nanotechnology* 15, S65-S68 (2004).
205. K. Todnem, K. J. Borve, M. Nygren, *Surf.Sci.* 421, 296-307 (1999).
206. J. Z. Larese et al., *Physica B* 226, 221-223 (1996).
207. J. Z. Larese, J. M. Hastings, L. Passell, D. Smith, D. Richter, *J.Chem.Phys.* 95, 6997-7000 (1991).
208. J. L. Anchell, K. Morokuma, A. C. Hess, *J.Chem.Phys.* 99, 6004-6013 (1993).
209. W. Jingang, L. Shuben, L. Guoqiang, L. Can, X. Qin, *Appl.Surf.Sci* 81, 37-41 (1994).
210. C. M. Zicovich-Wilson, R. Gonzalez-Luque, P. M. Viruela-Martin, *THEOCHEM* 67, 153-162 (1990).
211. L. Can and X. Qin, *J.Phys.Chem.* 96, 7714-7718 (1992).
212. K. Fukui and Y. Iwasawa, *Surf.Sci.* 441, 529-541 (1999).
213. Y. Aray, J. Rodriguez, J. Murgich, F. Ruetter, *J.Phys.: Condens.Matter* 5, 211-212 (1993).
214. S. Briquez, C. Girardet, J. Goniakowski, C. Noguera, *J.Chem.Phys.* 105, 678-685 (1996).
215. Y. Ozaki, *Molecular Physics Reports* 31, 72-80 (2001).
216. J. Ahdjoudj, A. Markovits, C. Minot, *Catalysis Today* 50, 541-551 (1999).
217. J. P. Perdew, K. Burke, M. Ernzerhof, *Phys.Rev.Lett.* 77, 3865-3868 (1996).
218. A. S. Foster, O. H. Pakarinen, J. M. Airaksinen, J. D. Gale, R. M. Nieminen, *Physical Review B* 68, art-195410 (2003).
219. M. L. Knotek, *Surf.Sci.* 101, 334-340 (1980).
220. S. A. Chambers et al., *Chemical Physics Letters* 267, 51-57 (1997).
221. P. Kackell and K. Terakura, *Surf.Sci.* 461, 191-198 (2000).
222. P. I. Sorantin and K. Schwarz, *Inorganic Chemistry* 31, 567-576 (1992).
223. A. Sasahara, H. Uetsuka, H. Onishi, *Physical Review B* 64, art-121406 (2001).
224. M. Deleu et al., *Biochimica et Biophysica Acta-Biomembranes* 1513, 55-62 (2001).
225. A. Knoll, R. Magerle, G. Krausch, *Macromolecules* 34, 4159-4165 (2001).
226. T. J. McMaster, M. Berry, A. P. Corfield, M. J. Miles, *Biophysical Journal* 77, 533-541 (1999).
227. S. Morita and Y. Sugawara, *Ultramicroscopy* 91, 89-96 (2002).
228. K. I. Fukui, H. Onishi, Y. Iwasawa, *Chemical Physics Letters* 280, 296 (1997).
229. A. S. Foster et al., *J.Chem.Phys.*, in press.
230. F. J. Giessibl, C. Gerber, G. Binnig, *Journal of Vacuum Science & Technology B (Microelectronics Processing and Phenomena)* 9, 984-988 (1991).
231. M. A. Lantz et al., *Physical Review B* 68, art-035324 (2003).
232. R. D. Antonov and A. T. Johnson, *Phys.Rev.Lett.* 83, 3274-3276 (1999).
233. P. Avouris et al., *Appl.Surf.Sci* 141, 201-209 (1999).
234. S. J. Tans et al., *Nature* 386, 474-477 (1997).
235. J. Lefebvre et al., *Carbon* 38, 1745-1749 (2000).
236. L. Roschier et al., *Appl.Phys.Lett.* 75, 728-730 (1999).
237. M. Ahlskog, R. Tarkiainen, L. Roschier, P. Hakonen, *Appl.Phys.Lett.* 77, 4037-4039 (2000).
238. J. Lefebvre, Y. Homma, P. Finnie, *Phys.Rev.Lett.* 90, art-217401 (2003).
239. A. Hartschuh, H. N. Pedrosa, L. Novotny, T. D. Krauss, *Science* 301, 1354-1356 (2003).
240. M. Y. Sfeir et al., *Science* 306, 1540-1543 (2004).
241. S. Friedrichs et al., *Electron Microscopy and Analysis 2001.Proceedings* 279-282 (2001).
242. R. R. Meyer et al., *Science* 289, 1324-1326 (2000).
243. J. Sloan et al., *Nanotubes and Related Materials.Symposium (Mater.Res.Soc.Symposium Proceedings Vol.633)* 14-31 (2001).
244. M. Paillet et al., *J.Phys.Chem.B* 108, 17112-17118 (2004).
245. A. Jorio et al., *Phys.Rev.Lett.* 90, art-107403 (2003).
246. M. Ashino, A. Schwarz, T. Behnke, R. Wiesendanger, *Phys.Rev.Lett.* 93, art-136101 (2004).
247. J. Sloan et al., *Chemical Physics Letters* 329, 61-65 (2000).
248. M. Wilson, *Chemical Physics Letters* 366, 504-509 (2002).

249. M. Wilson, *J.Chem.Phys.* 116, 3027-3041 (2002).
250. M. Wilson, *Chemical Physics Letters* 397, 340-343 (2004).
251. A. Ilie and M. E. Welland, *Nanotechnology*, in press.
252. M. Monthieux, *Carbon* 40, 1809-1823 (2002).
253. A. Krishnan, E. Dujardin, T. W. Ebbesen, P. N. Yianilos, M. M. J. Treacy, *Physical Review B* 58, 14013-14019 (1998).
254. Z. H. Yao, C. C. Zhu, M. Cheng, J. H. Liu, *Computational Materials Science* 22, 180-184 (2001).
255. G. Dereli and C. Ozdogan, *Physical Review B* 67, art-035416 (2003).
256. A. L. Bassi et al., *Diamond and Related Materials* 12, 806-810 (2003).
257. M. H. Norwood and C. V. Briscoe, *Physical Review* 112, 45-48 (1958).
258. M. S. Dresselhaus, A. Jorio, A. G. Souza Filho, G. Dresselhaus, R. Saito, *Physica B* 323, 15-20 (2002).
259. G. Zhou and Y. Kawazoe, *Physical Review B* 65, art-155422 (2002).
260. G. Zhou, W. H. Duan, B. L. Gu, Y. Kawazoe, *J.Chem.Phys.* 116, 2284-2288 (2002).
261. K. Asaumi, T. Suzuki, T. Mori, *Physical Review B* 28, 3529-3533 (1983).
262. C. H. Panter, *Journal of Physics C-Solid State Physics* 7, 665-668 (1974).
263. A. L. Shluger and J. D. Gale, *Physical Review B* 54, 962-969 (1996).
264. A. B. Kunz, *Journal of Physics and Chemistry of Solids* 31, 265 (1970).
265. P. D. Pathak and N. M. Pandya, *Acta Crystallographica, Section A (Crystal Physics, Diffraction, Theoretical and General Crystallography)* A31, 155-157 (1975).
266. P. D. Schulze and J. R. Hardy, *Physical Review B* 5, 3270 (1972).
267. F. Seitz, *Reviews of Modern Physics* 18, 384-408 (1946).
268. C. R. A. Catlow, J. Corish, K. M. Diller, P. W. M. Jacobs, M. J. Norgett, *Journal of Physics C-Solid State Physics* 12, 451-464 (1979).
269. D. Mapother, H. N. Crooks, R. Maurer, *J.Chem.Phys.* 18, 1231-1236 (1950).
270. J. F. Huang and L. S. Bartell, *J.Phys.Chem.A* 106, 2404-2409 (2002).
271. W. Bollmann, *Crystal Research and Technology* 27, 673-684 (1992).
272. P. D. Schultze and J. R. Hardy, *Physical Review B* 6, 1580 (1972).
273. D. K. Rowell and M. J. L. Sangster, *Journal of Physics C-Solid State Physics* 14, 2909-2921 (1981).
274. R. Jacquemin et al., *Synthetic Metals* 115, 283-287 (2000).
275. A. Hassanien et al., *Appl.Phys.Lett.* 73, 3839-3841 (1998).
276. C. N. Louis and K. Iyakutti, *Physica Status Solidi B* 233, 339-350 (2002).
277. C. Thomsen et al., *Applied Physics A (Materials Science Processing)* A69, 309-312 (1999).
278. C. Maeda, S. Kishimoto, T. Mizutani, T. Sugai, H. Shinohara, *Japanese Journal of Applied Physics Part 1-Regular Papers Short Notes & Review Papers* 42, 2449-2452 (2003).
279. M. Shiraishi and M. Ata, *Carbon* 39, 1913-1917 (2001).
280. J. J. Zhao, J. Han, J. P. Lu, *Physical Review B* 65, art-193401 (2002).
281. C. Y. Yam, C. C. Ma, X. J. Wang, G. H. Chen, *Appl.Phys.Lett.* 85, 4484-4486 (2004).
282. M. N. Pisanias, N. I. Xanthopoulos, S. N. Georga, *Journal of Physics D-Applied Physics* 24, 958-962 (1991).
283. S. M. Bose, S. N. Behera, S. N. Sarangi, P. Entel, *Physica B-Condensed Matter* 351, 129-136 (2004).
284. S. Gupta, M. Hughes, A. H. Windle, J. Robertson, *J.Appl.Phys.* 95, 2038-2048 (2004).
285. P. Lambin, A. Loiseau, C. Culot, L. P. Biro, *Carbon* 40, 1635-1648 (2002).
286. A. Jorio et al., *New Journal of Physics* 5, art.139 (2003).
287. Y. V. G. S. Murti and V. Usha, *Physica B & C* 83B+C, 275-282 (1976).
288. S. Chaudhuri, D. Roy, A. K. Ghosh, *Indian Journal of Physics* 49, 928-938 (1975).
289. Y. N. Pershits and T. A. Kalennikova, *Fizika Tverdogo Tela* 18, 844-846 (1976).
290. Y. N. Pershits and T. A. Kalennikova, *Fizika Tverdogo Tela* 17, 1206-1208 (1975).
291. K. Okamoto, Y. Sugawara, S. Morita, *Japanese Journal of Applied Physics Part 1-Regular Papers Short Notes & Review Papers* 42, 7163-7168 (2003).